LIGHT–MATTER INTERACTIONS IN SEMICONDUCTOR NANOWIRES: LIGHT–EFFECT TRANSISTOR AND LIGHT–INDUCED CHANGES IN ELECTRON–PHONON COUPLING AND ELECTRICAL CHARACTERISTICS

by

Jason Kendrick Marmon

A dissertation submitted to the faculty of
The University of North Carolina at Charlotte
in partial fulfillment of the requirements
for the degree of Doctor of Philosophy in
Nanoscale Science

Charlotte

2016

Approved by:

_____
Dr. Yong Zhang

_____
Dr. Ryan Adams

_____
Dr. Michael A. Fiddy

_____
Dr. Daniel Rabinovich

_____
Dr. Thomas A. Schmedake

_____
Dr. Haitao Zhang

ABSTRACT

JASON KENDRICK MARMON. Light–matter interactions in semiconductor nanowires: Light–effect transistor and light–induced changes in electron–phonon coupling and electrical characteristics. (Under the direction of DR. YONG ZHANG)

This dissertation explores three related embodiments of light–matter interactions at the micro– and nano–scales, and is focused towards tangible device applications. The first topic provides a fundamentally different transistor or electronic switch mechanism, which is termed a light–effect transistor (LET). The LET, unlike exotic techniques, provides a practical and viable approach using existing fabrication processes. Electronic devices at the nanoscale operate within the ballistic regime, where the dominate source of energy loss comes from impurity scattering. As a LET does not require extrinsic doping, it circumvents this issue. Electron–phonon coupling, however, is the second largest source, and it is a pertinent and important parameter affecting electronic conductivity and energy efficiency, such as in LETs. The third topic is laser writing, or the use of a laser to perform post–growth modifications, to achieve specific optical and electrical characteristics.

A LET offers electronic–optical hybridization at the component level, which can continue Moore's law to the quantum region without requiring a FET's fabrication complexity, e.g., physical gate and doping, by employing optical gating and photoconductivity. Multiple independent gates are therefore readily utilized to achieve unique functionalities without increasing chip space. LET device characteristics and novel digital and analog applications, such as optical logic gates and optical amplification, are explored. Prototype cadmium selenide (CdSe) nanowire–based LETs show output and transfer characteristics resembling advanced FETs, e.g., on/off ratios up to ~1.0×10^6 with a source-drain voltage of ~1.43 V, gate-power of ~260 nW, and a

subthreshold swing of ~0.3 nW/decade (excluding losses). The LET platform offers new electronic–optical integration strategies and high speed and low energy electronic and optical computing approaches.

Electron–phonon coupling is typically studied as an intrinsic property, which is particularly important for electronic transport properties at the nanoscale, where controversy and even contradictory experimental and theoretical findings still persist. Zinc telluride (ZnTe) has important uses in optical or laser refrigeration, and the existing studies do not consider extrinsic effects, such as laser–forming tellurium–based species. Nanostructures, with their large surface–to–volume ratios, are more susceptible to extrinsic perturbations that ultimately effect coupling. In this dissertation, ZnTe is studied in bulk, thin film, and nanowire forms with primary focus on the latter. Raman spectroscopy under near resonant excitation is used to extract electron–phonon coupling strengths, which is obtained through the ratio of the first and second order Raman peaks, $R = I_{2LO}/I_{1LO}$ (and is proportional to the Huang–Rhys factor). Laser–formation of tellurium–based species on ZnTe nanowires dynamically altered the ratio R from ~6-7 to 2.4 after laser processing, while tuning the (532 nm) laser power from a few microwatts to 150 microwatts (with constant optical exposure time) did not significantly impact the EPC strength. Other explored effects include size dependence, chemical effects (methanol exposure), and interface effects (e.g., at a gold–nanowire junction). The findings suggest that the previously reported size dependence in ZnTe was extrinsic in nature. Tunable coupling strengths also suggest the possibility of novel electronic and optoelectronic devices.

The electrical characteristic of CdSe nanowire M-S-M devices are shown to be tunable with laser illumination. As with any semiconductor material, sufficiently low optical powers produce stable and reproducible electrical properties, while higher optical

powers and exposure times can induce laser modifications of the material. Drastic modification of electrical characteristics were observed, such as from converting an ohmic response (linear slope change) to rectified characteristics, and modification of both forward and reverse currents. Results suggest the potential to laser write wavelength–specific electronic functions that could be used in applications requiring wavelength discrimination, such as with night vision products. Using a combination of laser modification and device fabrication processes provides the ability to offer a menu of electrical behaviors using the same materials and fabrication processes.

DEDICATION

I dedicate this dissertation to my wife, family, mentors, friends, and to all those who have supported and assisted my pursuit of education.

ACKNOWLEDGEMENTS

Proverbs 19:20 – "listen to advice and accept instruction, that you may gain wisdom in the future." My collective graduate experience include receiving guidance from many individuals to enhance my scientific acumen and technical skill. Prof. Bernadette Donovan–Merkert is both the Nanoscale Science Director and Program Coordinator; she provided valuable guidance and advice. Profs. Yong Zhang, Michael Fiddy, and Haitao Zhang provided direct guidance with different research aspects over the years, while Profs. Glenn Boreman, Raphael Tsu, Stuart Smith, Ed Stokes, Terry Xu, Tom Schmedake, and Ryan Adams provided greatly appreciated technical knowledge through courses and/or conversations. I especially appreciate: conversations and interactions with Drs. James "Jim" Slinkman (IBM/Globalfoundries), Qiuyi Ye (SUNY–Albany, retired), and Nancy Haegel (NREL); Profs. Boreman, Stokes, and H. Zhang granting me permission to use their equipment. Ms. Caroline Kennedy, past Nanoscale Science Assistant Coordinator, and Mr. Mark Clayton, Administrative Assistant for the Optical Sciences and Engineering program, provided tremendous assistance and support with the administrative aspects of graduate study. Prof. H. Zhang and Drs. Robert Hudgins and Lou Deguzman provided instrument training. Dissertation funding came from UNC–Charlotte's Graduate Assistant Support Plan (GASP), Dr. Yong Zhang's Bissell Distinguished Professorship, research assistantships from ARO and the Electrical and Computer Engineering Department, and from teaching assistantships through the Departments of Chemistry and Physics and Optical Science.

1 Thessalonians 5:18 – "give thanks in all circumstances; for this is the will of God in Jesus Christ." There are many reasons to be joyous and to give thanks. I extend deep gratitude and thanks to (in no particular order): (1) Prof. Weilie Zhou's group at the University of New Orelans, Dr. Priyalal Wijewarnasuriya and Dr. Yuanping Chen with

the Army Research Laboratory, and Prof. Haitao Zhang at UNC–Charlotte for providing samples and devices; (2) Friends who brought joy and laughter these past few years. These include Dr. Youfei Jiang, Manu Pashricha, Dr. Yizhan Chen, and Nitish Chandra. (3) Dr. Yong Zhang's research group for conversations, training, and research assistance from Drs. Nali Yue, Liqin Su, Qiong Chen, and Henan Liu. I also thank visiting scholars for useful discussions, such as Profs. Yang, Hu, and Guan. (4) Those who made this doctoral journey possible. During my undergraduate experiences at Beloit College, Profs. George Lisensky and Raman Viswanathan (Chemistry), and Profs. Patrick Polley and Paul Stanley (Physics) both challenged and encouraged intellectual curiosity and scientific growth. Interactions with them helped me understand and form my research interests. Also during that time, both Mr. Devon Wilson and Mr. Nick Ewoldt provided mentorship and academic support (both are currently Assistant Deans at the University of Wisconsin at Madison). During high school, Mr. Hong Chuong, significantly influenced my decision to pursue higher education. (5) Those whom I have not named directly yet played a role in my graduate experiences.

Without family, life would be far less interesting. I sincerely thank my wife, Yanling Lin, as well as, my in–laws, parents, brother, sisters, and my extended family for their support and understanding.

TABLE OF CONTENTS

LIST OF FIGURES

LIST OF TABLES

LIST OF ABBREVIATIONS

0–3D	zero– to three–dimensional
CBM	Conduction band minimum
CVD	Chemical vapor deposition
CW	Continuous wave, e.g., laser power
DFT	Density functional theory
DOS	Density of states
EQE	External quantum efficiency
FET	Field–effect transistor
FLOPS	Floating–point operations per second
HRTEM	High resolution tunneling electron microscopy
IQE	Internal quantum efficiency
LCAO	Linear combination of atomic orbitals
LDA	Local density approximation
LET	Light–effect transistor
MOS/MOSFET	Metal–oxide–semiconductor field–effect transistor
M–S, M–S–M	Metal–semiconductor, and metal–semiconductor–metal
n–LO	n^{th} order longitudinal optical phonon mode
PL	Photoluminescence
SADP	Selected area diffraction pattern
SEM	Scanning electron microscope

SeO_x	Amorphous selenium oxide
SNW	Semiconductor or semiconducting nanowire
TEM	Tunneling electron microscopy
TO	Transverse optical phonon mode
VBM	Valence band maximum
RS	Raman scattering
WZ	Wurtzite (crystal structure)
ZB	Zinc blende (crystal structure)

LIST OF UNITS

μA	microamps
μW	microwatts
cps	counts per second (e.g., optical intensity)
fJ	Femtojoules
mV	millivolt
nA	nanoamps
nW	nanowatt
pA	picoamps
ps	picosecond
pW	picowatts

LIST OF SYMBOLS AND REPRESENTATIONS

ε_0	Vacuum permittivity
ε_r	Relative permittivity of a medium
η_{QE}	Quantum efficiency (equivalent to Ψ).
λg	Optical gate wavelength for a light–effect transistor
Ψ	Electron collection efficiency (equivalent to η_{QE})
$\Psi_{n,k}(r)$	Wave function describing electron motion in a lattice
a, c	Lattice constants
A, B	Two generic inputs into an optical logic gate
$A+B$	Generic output from an optical *OR* logic gate with two inputs
AxB	Generic output from an optical *AND* logic gate with two inputs
$A+(B+C)$	Generic output from an optical *AND–AND* logic gate with three inputs
$Ax(B+C)$	Generic output from an optical *AND–OR* logic gate with three inputs
A_k	Constant(s) in a wave function
C	Generic optical logic gate output
D	Drain contact
d	*d* atomic orbital
E_n	One–electron eigenstate energy

ΔE_{VBM}	Energy difference between valence band maxima of two semiconductors
e	Electronic charge
F	Applied electrical field (used in model by Mott and Gurney)
G	Gate contact
G	Quantum conductance
G_0	Minimum conductance
h	Planck's constant
H_e, H_{ions}	Hamiltonian describing electron (nuclei) motion in a lattice
$H_{e\text{-}ions}$	Hamiltonian containing changes in electronic energy from nuclei displacement relative to equilibrium
H_S	Spin–dependent electronic energy
I_{ds}	Source–drain current
$I_{ds}(t)$	Time–dependent current, e.g., a sine wave
I_{ds}–P_g	Light–effect transistor transfer characteristics
I_{ds}–V_g	Field–effect transistor transfer characteristics
I_{ds}–V_{ds}	Generic transistor output characteristics
k	Index representing a wave vector
L	Spatial dimension, such as nanowire length
m	Carrier's effective mass
P_T	Threshold (optical) gate power for a light–effect transistor

p, P	Electron and ion momentum operators
R_I	The I–th nucleus with atomic number Z_I
$r_{i,}$	Position of the i–th electron
S	Source contact
s	s atomic orbital
S_{FET}	Subthreshold swing for a field–effect transistor
S_{LET}	Subthreshold swing for a light–effect transistor
SD	Source–drain
P_g	Single optical gate power
(P_{g1},P_{g2})	Multiple, simultaneous optical gate powers
$P_g(\lambda_g)$	Optical gate wavelength and power
p	p atomic orbital
R	Current enhancement equation defined for two optical gate inputs in a light–effect transistor
T	Carrier lifetime
$u_k(k,x)$	Bloch function, e.g., part of a wave function
v	Carrier mobility
V	Volts
V_{ds}	Source–drain voltage
$V_{ds}(t)$	Time–dependent voltage
V_T	Threshold gate voltage for a field–effect transistor

$V(x)$	A spatially dependent (x) potential
w	Electron mean free path
x	Lattice translational period
x_0	Distance from the illumination site to the anode electrode
Z_0	Quantum impedance

CHAPTER 1: AN EMERGING ELECTRONIC–OPTICAL DEVICE ERA

"Science and technology revolutionize our lives, but memory, tradition and myth frame our response."
Arthur M. Schlesinger, Jr., 1986 In New York Times Magazine

1.1 Time to Change Paradigms

Our daily lives, from financial data to communications, are entangled in sequences of zeros and ones. The electronic heartbeat of modern electronics is the field–effect transistor (FET), which cycles between electrically insulating ("off") and conductive ("on") states. Despite significant improvements in FET technology, computational performance has remained relatively stagnant since about 2005 due to physical limitations [1-4] imposed by its operation mechanism, such as random dopant fluctuations [5] and gate fabrication complexities [6]. Transistor improvements since then occurred primary through increased transistor densities resulting from reduced gate dimensions, but as their sizes approach the quantum scale, they are plagued by the need for ever greater fabrication complexity and atomically precise doping control [5, 7-10]. Various new technologies [11], such as FinFETs [7, 12], and tunnel–FETs [13], have been developed in recent years to enable the continuation of Moore's law [14], but further development with current technologies are uncertain [15]. This void prompted exploration of other alternatives [16] that include semiconductor nanowire (SNW) –based FETs [17-19], band–to–band tunneling [20, 21], FETs comprised of 2D

materials [22, 23], and FETs with sophisticated gate structures [24], such as multiple independent gates [8, 10] or a gate with embedded ferroelectric material [25]. These possibilities remain within the conventional FET framework, and therefore offer no clear solution to the physical limitations. More exotic approaches, such as all optical and quantum computing, require substantial fundamental research. As a result, no viable and practical rival technology currently exists as FETs approach the end of their contribution to Moore's law [26, 27].

1.2 More Than Moore

At the Solid State Circuits Conference held in San Francisco (from 31 Jan. – 5 Feb. 2016), Mr. William Hold, Intel's Executive Vice–President, announced the end of Moore's law. This sparked the publication of several theses and opinions in *Nature* journals [28, 29], and even an article in *The Economists* "Technology Quarterly" (12 March 2016). But such media attention was observed at least four to five times in the past. Is Moore's law really approaching its end with conventional transistor technologies? Although the rate for reducing the oxide thickness has been slowing recently [30], this statement may seem dubious. This is because modern transistors are a relatively mature technology that have endured many material advances, such as strained silicon and high–κ dielectric gates, and changes in geometry (e.g., FinFETs) and gate configuration (e.g., gate–all–around [31, 32]) to the same basic structure for decades [33]. Their result is the impressive 14–nm–node technology, or minimum feature size such as the device width,, which requires ArF immersion photolithography with multiple patterning [26, 34]. Current doubts regarding continued miniaturization stem from the future transition from 10–nm to 5–nm node technology, which requires moving from deep to extreme ultraviolet photolithography (e.g., a reduction of λ from

193 to 13.5 nm). Power, throughput, and especially mask defects, which are currently below ~50 nm, are critical factors, where for instance, continued reduction in mask defects is required before extreme ultraviolet photolithography could be considered realistic [34]. The method for implementing such drastic changes are unclear and may certainly slow if not cease Moore's law with conventional transistor technologies, but this is not a doom's day prophesy. Rather, it leads to slowed progress in increasing device densities, with negligible improvements to switching performance and increased leakage currents [33]. A shift to a More than Moore strategy, which focuses on creating new functionality at external interfaces using existing technologies, is a stopgap measure for continuing performance increases until the next–generation, transistor technology is identified and implemented. The International Roadmap for Semiconductors (ITRS), which is a technological roadmap decided upon by panels of industry experts, has projected the end of Moore's law by the 2020s followed by Moore than Moore [26]. It is generally expected that a practical and viable next–generation, transistor technology will be available after the year 2030, which could potentially resume Moore's law once again. Finding an alternative solution is becoming more critical as, stated in a joint call for proposals between the National Science Foundation and the Semiconductor Research Corporation, "evolutionary [FET] approaches … are becoming increasingly ineffective" and must be overcome with a "truly holistic … approach" [35]. A majority of transistor candidates, however, remain within conventional frameworks. While this could lead to improvements that may briefly extend Moore's law with conventional technologies, it will not overcome inherent physical limitations or fabrication issues. When considering a drastically different

approach that provides a practical and viable solution to these challenges, it is helpful to consider the reasons behind the transistor's success.

1.3 Transistor Development

While FETs have undoubtedly contributed to developing our digital societies, they are but a single link in a technological chain that must eventually be replaced. The number of switching events per second has increased almost exponentially since the introduction of electrical modulation with electromechanical relays in 1835 [16]. Since then, technology has evolved from electromechanical relays to vacuum tubes, early transistors, and finally, to modern integrated circuits incorporating advanced FETs. Transistors replaced vacuum tubes primarily due to their ability to amplify current, which is why thermal switching (e.g., thermistors) [36-38] did not succeed vacuum tubes. Furthermore, their comparatively lower switching speeds and reduced power consumption were well suited for the rapidly evolving telephone communications industry [37, 38]. In other words, vacuum tube limitations were swapped for those related to FETs because FETs surpassed vacuum tube capabilities in critical areas. Interestingly, FET adoption partially resulted from historical rather than physical reasons. In 1928, Edgar Lilienfield [39, 40] introduced the concept of field–effect conductivity using a thin aluminum foil as an uninsulated gate to modulate current between two conductors, but difficulties with passivating the surface of copper (I) sulfide semiconductors, which lead to a high density of interface states, resulted in irreproducibility and low performance [37, 41-43]. The transistor is credited to W. Shockley, J. Bardeen, and G.L. Pearson [36, 44], who shared the 1956 Nobel Prize in Physics for their reproducible work, that after several configurations, resulted in employing a metal gate to electrostatically modulate current in a p–n junction [45].

Then in 1958, Atalla *et al.* [46, 47] demonstrated excellent surface passivation of silicon with silicon dioxide, which marked the beginning of modern, silicon–based, metal–oxide–semiconductor FET technology, although silicon dioxide surface passivation would later be replaced by high–κ dielectrics and metal gates [33]. It is worth noting that the work of J. Shive [48] proved that electron transport occurred primarily through the body (rather than the surface). Meanwhile, the superior performance of p–n junctions stemmed from improving material quality, such as reducing bulk defects, where post–growth cooling caused boron and phosphorous impurities to diffuse to opposite ends of a silicon ingot [49, 50]. Improved material quality, naturally, yielded superior transistor performance. Growth of high quality materials, for example, is possible down to the quantum scale (e.g., 1–7 nm) for silicon nanowires [51], where the large surface–to–volume ratios of structures with highly reduced dimensions are excellent platforms to exploit surface properties. Why, then, is the same electrostatic paradigm still used when readily available technological tools can overcome the challenges that led to early transistor (p–n junction) adoption?

1.4 Next–Generation Transistor: Electronic–Optical Devices

Just as FET limitations were swapped for vacuum tube deficiencies, a supplanting technology must excel in critical areas that will overcome the physical limitations that lead to a relative stagnation of FET performance. The next link in the technology chain will likely be driven by the ever increasing demand for faster processing speeds, ideally at light speed, the need for further reductions in energy consumption, and a continuation of Moore's law to its physical limit (e.g., the quantum scale). IBM [52] and other

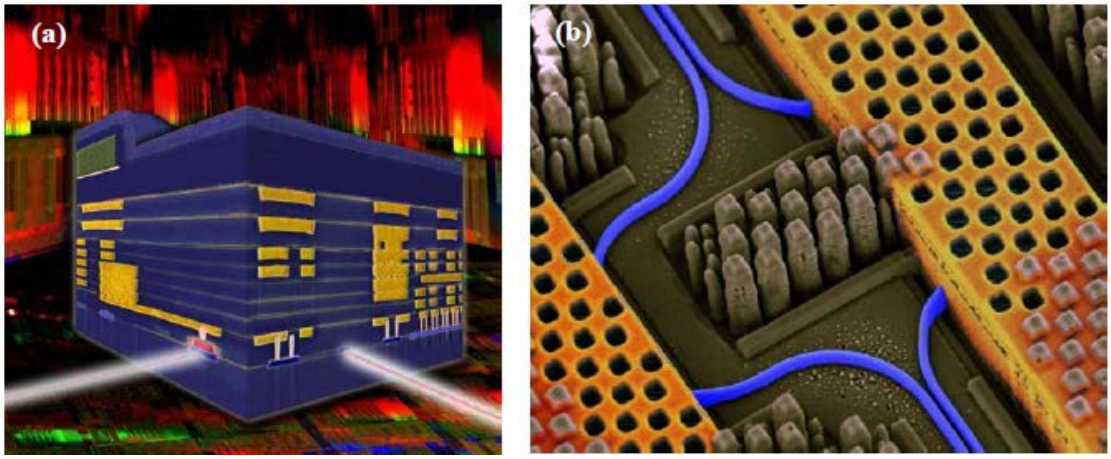

Figure 1.1 An artist's rendition of IBM's silicon nanophotonic transceiver and receiver currently under development. **(a)** The transceiver unit contains: a red photodetector on the lower left side of the cube, an incoming optical beam with optical modulator represented by the blue box on the right side of the cube, and the yellow rectangles represent electronic transistors integrated into its nine conducting layers embedded within the silicon. **(b)** The receiver contains optical waveguides (blue lines), copper conductors to the electronic components (yellow grids). **Courtesy of International Business Machines Corporation, © International Business Machines Corporation**.

companies have adopted electronic–optical devices, which is termed complementary metal–oxide–semiconductor (CMOS) integrated silicon photonics [53], as the next generation transistor technology, Figure 1.1, for two reasons: guided light enables vastly larger data transfer and processing speeds, and electronic–optical devices provide an optical interface that drives electronic functions. As conventional transistors are miniaturized to their limit, they generate enormous (ohmic) heat [54], while their performance is limited by parasitic capacitance from connecting (coper) wires [55] that could support an operating frequencies of, at most, 20 GHz [56, 57]. In principle, optical interconnects [58, 59] or nanophotonic elements [60-62] could overcome these limitations [63, 64], although these concepts requires substantial additional research to realize. The beauty of electronic–optical interfaces is that they provide a natural transition from purely electronic to all–optical computing frameworks. This transition allows development and implementation of new technologies that often require

substantial improvements in multiple supporting industries. Although a single chip microprocessor, which combines electrical and photonic signals, was demonstrated using standard fabrication methods [65], this statement best illustrated by considering the conceptual realization of an electronic–optical circuit.

In realizing computer operation, it is likely that different interfaces for converting an electromagnetic frequency to an electronic signal will be, such as for transitioning between internal and external forms of optical communication. For external communication, high–speed data transmission over long distance communication, such as telecommunications or the internet, could eventually occur with sub–terahertz and terahertz (THz) signals [66], which begin at 300 GHz and are between the microwave and infrared bands, although their propagation distance is currently limited to ~20 mm. External communication could employ on–chip lasers to illuminate a photomixer (sold commercially by the Japanese company NTT–NEL), which produces a THz signal equivalent to the frequency difference between the two illuminating lasers. The same company also sells non–cavity–based, wavelength conversion modules for visible, and near– and mid–infrared radiation. It may be possible to extend the range to the THz, in which case, such a module could act as a receiver and enable rapid conversion between external and internal optical communication frequencies. Within the computer's architecture, a major challenge is integrating global communication, such as board–to–board and chip–to–chip optical interconnects, using ~10–μm–diameter optical fibers with intra–chip communication using waveguides with diameters of ≤0.5 μm [67, 68]. A common method is to use a holographic lens as a fiber–to–waveguide coupler using either on– or off–chip lasers as optical sources [67].

1.5 Dissertation Outline

The intention of this dissertation is to explore next generation switch concepts capable of terahertz switching and beyond with physical (device) dimensions scalable to the quantum regime. The primary focus is on the photoconductive–based, switch mechanism. The ability to tune both optical and electrical behaviors is particularly important for potential implementation in electronic–optical devices, where Appendix I highlights additional merits of a nanowire's large surface–to–volume ratio. Accordingly, this dissertation provides an overview of an intuitive theoretical model based upon *N*–body theory, which is found in standard solid–state physics textbooks [69-71], to support the feasibility of the photoconductive and phonon concepts and to establish the theoretical basis for Raman spectroscopy (Chapter 2). Fundamental concepts behind light–matter interactions, such as enhanced absorption that produces optical amplification, are discussed in Chapter 3. The light–effect transistor (Chapter 4) demonstrates the power of the photoconductive mechanism in a CdSe–nanowire–based device, and its ability to provide functionality not available in either a FET or a photo–diode, e.g., optical logic gates and optical amplification. In Chapter 5, the intrinsic and extrinsic nature of electron–phonon coupling in ZnTe nanowires is explored with continuous wave resonant Raman spectroscopy. The controversial nature of exciton–phonon coupling at the nanoscale requires a thorough investigation to yield additional insight, while other multidimensional ZnTe systems are included to serve as an experimental basis for verifying the accuracy of theoretical results. Demonstrating the dynamic tuning of exciton–phonon coupling could yield novel device applications, and allows for future investigation into its feasibility as a switch mechanism. Chapter 6 demonstrates laser processed tuning of optical and electrical properties in CdSe–

nanowire–based, M–S–M devices, such as altering an ohmic response (e.g., linear slope), converting from nearly linear to rectified characteristics, or modifying the forward current. The source of these electrical changes are explored optically. Finally, Chapter 7 concludes this dissertation, while Chapter 8 provides an outlook into extending and developing this work into other interesting and novel applications.

CHAPTER 2: THEORETICAL FOUNDATIONS

"To say that science is logical is like saying that a painting is paint."
Leon Cooper, 1992 In the Palaces of Memory

2.1 Introduction

Electronic–optical devices ultimately interface both optical and electrical properties. Chapter 2 reviews an intuitive model that links these properties and provides a theoretical foundation for Raman spectroscopy, which is used to probe electron–phonon coupling, while Chapter 3 focuses on device fundamentals, such as carrier drift and recombination involved in the photoconductive mechanism. *N*–body theory is a semi–quantitative treatment of a translationally invariant lattice by decomposing it into a sum of one–electron wave functions, where very different material properties result from changes in atomic locations, bond angles, and interatomic forces (Section 2.1). Adiabatic and other approximations transform hydrogenic–like spatial and force descriptions (Section 2.2) into two electron groups, e.g., core and outer electrons, which results in the creation of three terms that describe electronic, vibrational (phonon), and electron–phonon coupling (Sections 2.3–2.5 respectively). While these terms generally provide numerical values that are correct within an order of magnitude, the primary advantage of this model is the intuition it provides in predicting electrical, optical, and electron–phonon behavior. For example, defects alter one–electron Hamiltonians and could introduce symmetry breaking geometries, where altered carrier mobilities manifest themselves through electrical behavior, and through the appearance of forbidden Raman modes. An important disadvantage of this model is a lack of intuitive

prediction regarding the effect of surface layers. A brief discussion is provided in Section 2.6, while the model's versatility and limitations are outlined in Section 2.7.

2.2 Wurtzite and Zinc–Blend Crystal Lattices

Most II-VI semiconductors crystallize in either hexagonal wurtzite (WZ) or cubic zinc–blende (ZB) lattices at room temperature and pressure [72-74]. Ideal WZ and ZB lattices both possess four tetrahedrally coordinated atoms per unit cell, and for the same material, they only differ in their second–nearest neighbor bond angles [69, 70]. This seemingly small change manifests itself through very different material properties. For example, Raman measurements on WZ and ZB GaAs nanowires revealed different allowed scattering modes (selection rules), polarization dependencies, and strain effects [70, 72, 75], while theoretical investigations corroborated the presence of different electrical, optical, and elastic properties [76]. Figures 2.1A–B respectively illustrate the subtle atomic differences between WZ (left side) and ZB (right side) lattices: (1) left and right "handedness" or chirality, (2) eclipsed and staggered dihedral conformations, and stacking in the (111) direction showing (3) two interpenetrating hexagonal close-packed lattices with AaBb stacking and two interpenetrating face–centered cubic lattices shifted by one quarter length diagonally into the lattice with AaBbCc stacking, where capital and lower case letters represent alternating planes of group II and VI elements [70, 72]. The sum of these differences may be expressed globally in terms of Hermann–Mauguin (Schoenflies) notation, where WZ lattices belong to space group C_{6v}^4 (P63mc), and ZB lattices are assigned to space group $F\bar{4}3m$ (T_d^2) [70, 72]. Bond distances in a unit cell are represented in each lattice dimension with *a*, *b*, and *c*, while W (ZB) lattices are composed of two (one) unique lattice parameter(s): *a* and *c* (only

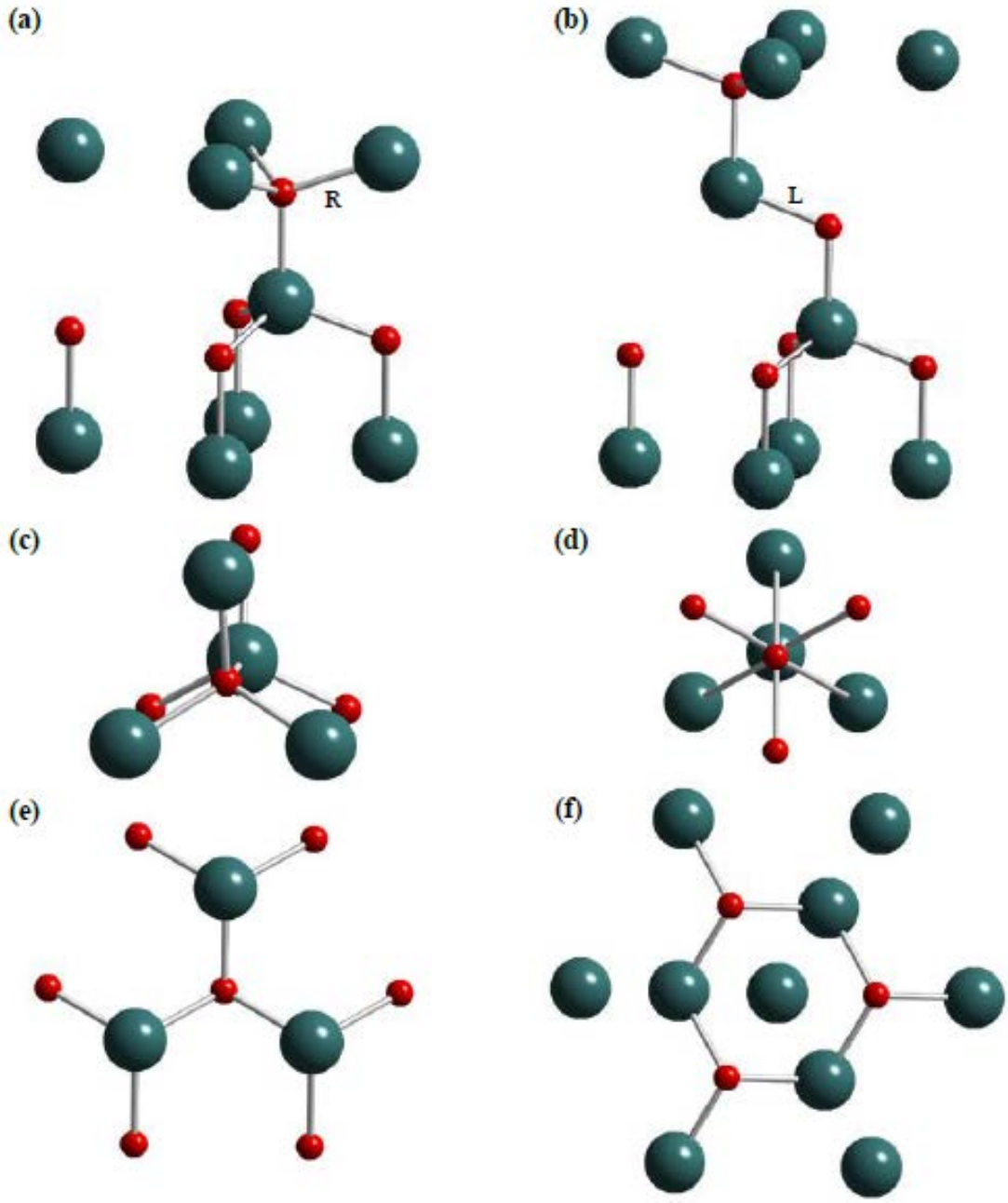

Figure 2.1 Differences between wurtzite (WZ) and zinc blende (ZB) lattices. The red and cyan atoms respectively represent group II and VI atoms, e.g., Cd and Se or Zn and Te for WZ and ZB lattices respectively. For WZ and ZB lattices respectively, the figure illustrates **(a–b)** the right (R) and left (L) handedness of the fourth interatomic bond, **(c–d)** "eclipsed" and "staggered" dihedral conformations, and **(e–f)** layer stacking along the (111) direction.

= 4.30 and c = 7.01 Å (a = 6.10 Å) [77]. For reference, an ideal WZ structure has a c/a ratio of 1.633, while WZ CdSe has a value of 1.630 [70, 78]. Unit–cell vectors describe the spatial location of atoms within a unit cell. ZB and WZ structures have the

following respective unit–cell vectors: $\vec{a}$ = (0,1/2,1/2)*a*, $\vec{b}$ = (1/2,0,1/2)*a*, and $\vec{c}$ = (1/2,1/2,0)*a*; and $\vec{a}$ = (1/2,√3/2,0)*a*, $\vec{b}$ = (1/2,–√3/2,0)*a*, and $\vec{c}$ = (0,0,c/*a*)*a* [70, 72]. Spatial differences between WZ and ZB structures result in different net forces that produce very different material properties.

2.3 Electronic States and Interface Models

The electronic states in a perfect crystal are described by the many–body Hamiltonian (*H*) in Eq. 2.1. Additional details [69, 71, 79, 80] and a purely quantum treatment [78] may be found elsewhere. The terms are, respectfully, the electron and nuclei kinetic energies, interaction energies between two nuclei and between nuclei and electrons, the electron–electron interaction potential energy, and the spin–dependent electronic energy (H_S) that includes spin-orbit interactions, where Σ' indicates summation over pairs with non–identical indices. The electronic states are perturbed by changes in Coulomb interactions and interatomic separation distances, where $r_{i,}$ represents the position of the *i*–th electron, and R_I is the *I*–th nucleus with atomic number Z_I. Other variables include: *p* and *P* are the electron and nucleus momentum operators respectively, ε_0 is the vacuum permittivity, *e* is the electronic charge, *m* (*M)* is the carrier effective mass of the electrons and nuclei respectively, and the value $4\pi\varepsilon_0$ converts from centimeter–gram–seconds (cgs) to standard international (SI) units. Eq. 2.1 is not easily solvable; thus, several approximations, as derived in standard solid–state physics textbooks [69-71], bring meaning to this lengthy equation.

$$H = \sum_i \frac{\hat{p}_i^2}{2m_i} + \sum_j \frac{\hat{P}_j^2}{2M_j} + \frac{1}{2}\sum_{I<J}{}' \frac{Z_I Z_J e^2}{4\pi\varepsilon_0 |\vec{R}_I - \vec{R}_J|} - \sum_{I,i} \frac{Z_I}{4\pi\varepsilon_0 |\vec{R}_I - \vec{r}_i|}$$

$$+ \frac{1}{2}\sum_{i<j}{}' \frac{e^2}{4\pi\varepsilon_0 |\vec{r}_i - \vec{r}_{i'}|} + H_S \qquad (2.1)$$

The adiabatic approximation in Eq. 2.2 separates the electronic states into vibronic,

core electronic (*I*) and outer (valence) electronic (*i*) contributions: H_e (H_{ions}) is a Hamiltonian describing electron (nuclei) motion (first, fourth, and fifth terms for the former, and second through third terms for the latter in Eq. 2.1), and the $H_{e\text{-}ions}$ Hamiltonian contains changes in electronic energy from nuclei displacement relative to equilibrium (which is described interactions between the previous two terms), e.g., electron–phonon interactions [69, 79]. For mathematical convenience, core electrons are assumed to move rigidly, interact through pseudopotentials [81], and display a time–averaged electronic potential [69, 70].

$$H = H_e\left(r_i, R_I\right) + H_{ions}\left(R_I\right) + H_{e-ions}\left(r_i, \delta R_I\right) + H_S \tag{2.2}$$

The adiabatic approximation is justified in textbooks by realizing that, upon application of equal force, ions are much heavier and move more slowly than displaced electrons. The approximation implies that electrons move solely through the outermost atomic orbitals, which can be shown through binding configurations from pure elements to II–VI compounds: $\mathrm{II}\left[\left(n-1\right)d^{10}ns^2\right] + \mathrm{VI}\left[ms^2mp^4\right] \rightarrow \mathrm{II}^{+2}\left[\left(n-1\right)d^{10}ns^0\right] + \mathrm{VI}^{-2}\left[ms^2mp^6\right]$, where n = 5 (4) for Cd (Zn) and m = 2, 3, 4, and 5 for O, S, Se, and Te respectively [82]. The superscript on each orbital represents the number of electrons occupying each orbital energy level. If perfect iconicity is assumed, then ZnTe and CdSe have respective II^{-2}–VI^{+2} binding configurations of $3d^{10}4s^0{+}5p^6$ and $4d^{10}5s^0{+}4p^6$. Roughly speaking, free electrons (holes) in II–VI semiconductors occupy a cation's lowest empty *s*–like (anion's highest occupied *p*–like) energy level [83-85]. Considering only core and outer electronic contributions, rather than each orbital energy, produces values that are within an order of magnitude of experimental results [73]. Despite these limitations, the model provides a qualitative means to correlate structural, electrical, and optical properties.

2.4 Electronic (H_e) Term

The *N*–body H_e Hamiltonian may be solved in a perfect, periodic crystal lattice as a sum of one–electron Hamiltonian. The mean–field approximation is applied to the H_e Hamiltonian, Eq. 2.3, to describe electron motion, and assumes, among other conditions, that a constant potential *V(r)* is equally applied to every electron in a periodic lattice [69, 79]:

$$H_e \Psi_{n,k}(r) = \left\{ \frac{\hat{p}^2}{2m_0} + V(r) \right\} \Psi_{n,k}(r) = E_n \Psi_{n,k}(r) \quad . \tag{2.3}$$

This model is capable of describing several different interactions: (1) covalent bonds resulting from excess charge screening repelling two ions, which results in a stable binding energy; (2) anti–bonding stems from an absence of electrons; (3) ionic interactions occur from electrostatic interactions between ions, with their respective wave functions centered on each ion core, which decreases the binding energy; and (4) metallic behavior is described by reducing the potential to the nearly free electron approximation, e.g., $V(r) \rightarrow 0$. This model can also describe more complex structures. For example, $V(r) = V(r + nx)$ could describe superlattice heterojunctions, where *x* is usually 10–20 times larger than the lattice constant [86].

Describing each unit cell as a sum of wave functions can be computationally demanding, especially when summing single particle wave functions in a large crystal (e.g., with $>10^{23}$ electrons per cubic centimeter [69]), but local details must be retained to sufficiently describe the electronic states. Theoretical models often employ first principles [87] or ab initio [88], and density functional theory (DFT) methods within the local density approximation [89, 90] (LDA). The results are typically expressed in atomic orbital terminology, and are used to describe band gaps and their offsets. This

language expresses aggregated lattice conditions in terms of interactions between *s*, *p*, and *d* atomic orbitals (which are collectively referred to as valence electrons). This treatment accounts for interactions between valence electrons. Figure 2.2A graphically illustrates differences for two different group II cations (A and B) with the same group VI anion (X), which are generically represented as AX and BX. In this case, bonding interactions use valence bands with similar cation and anion symmetries, e.g., Γ_{15v}. The cation's *d*–orbital energies are below the anion's *p*–orbital energies (not shown), which repels the valence band maximum (VBM) upwards energetically. The energy difference between AX and BX, ΔE_{VBM}, is the primary result. Increasing the anion's electronegativity (e.g., from Te to S) increases the *p*–orbital energy, which strengthens *p–d* repulsion to produce an energetically up shifted VBM and shortened bond lengths [73, 87]. Most II–VI compound semiconductors possess similar cation and anion energies and bond distances, which manifest themselves in relatively small valence band offsets [73, 87]. The conduction band minimum (CBM) results primarily from changes in the cation's *s*–orbital energies, while changes in bond distances, such as through applied strain [91-94], can also greatly alter the CBM energy [73, 87]. Figure 2.2B graphically represents band gaps and offsets (relative to vacuum) for bulk CdSe and ZnTe [95]. The resulting band gap energy and lattice constant for common II–VI semiconductors appear in Figure 2.2C. Note that nanowire values can vary significantly from bulk values.

Reciprocal or real lattices, Figure 2.2D, are commonly used in semiconductor physics to visualize a material's electronic structure because its simple representation of three–dimensional symmetry conveniently enables band diagram construction. Reciprocal lattices use *k* and physically represent inverse or reciprocal "real" distances

in a lattice. Convention dictates that high symmetry points and lines within the first Brillouin zone are denoted with Greek letters, while points on the surface use Roman letters, and Γ represents the zone center [69]. Although beyond the scope here, other symmetry points denote higher order features; for example, M represents a saddle point. A highly symmetric crystal, which assumes translational invariance, allows one to represent the electronic states in a reduced zone scheme from $-\pi/a$ to $-\pi/a$. This turns out to be important as k is only conserved for "nearly free" electrons over a multiple of $2\pi/R$, where R is the translational period and a is the lattice constant along k [69, 70]. The vertical axes in Figures 2.2E–F are both energy. Frameworks for expressing energy changes range from molecular orbital (MO) theory [96-99] for single and small molecules to band diagrams [87, 100] for systems with a continuum of states. Band diagrams may be obtained from Eq. 2.2.3 by plotting energy differences across the reciprocal lattice using convention to denote high symmetry features. For example, the [111] direction of an fcc lattice includes the Γ, Λ, and L points [69, 70]. Each allowed electronic state is a direct consequence of electron interactions. Bulk band diagrams for WZ CdSe and ZB ZnTe appear in Figures 2.2E–F, where a major electronic difference is that WZ does not produce the triply degenerate valence band edge found in ZB [76]. Both WZ CdSe and ZB ZnTe are direct gap semiconductors, because their VBMs and CBMs are directly over each other (at the Γ point), with respective bandgaps of 1.74 and 2.254 eV for bulk CdSe and ZnTe [77]. Their shape on a plot of energy vs. k is

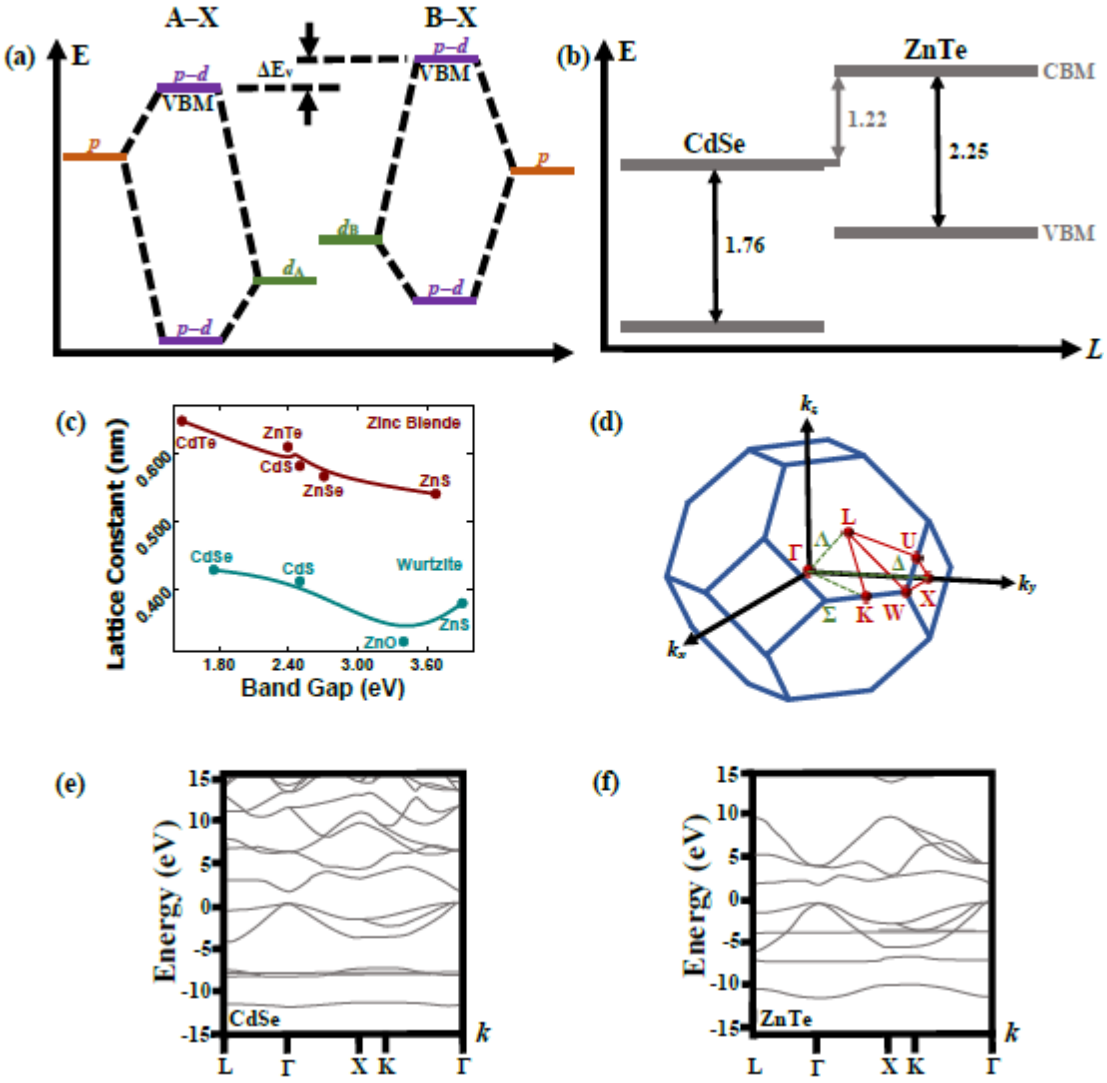

Figure 2.2 Role of *d* orbitals in determining band offsets, which then contribute to different energy levels, lattice constants, and band gaps. **(a)** Role of the cation's *d* states in determining energy level offsets for two generic binary semiconductor heterojunctions labelled as A–X and B–X (after Ref. [73] using the tight–binding approach). **(b)** Band gaps and band offsets for bulk CdSe and ZnTe after Refs. [87, 101, 102], where relative band offsets primarily result from differences on anion *p*–orbitals, while *p*–*d* repulsion is a secondary contribution, e.g., Ref. [102]. **(c)** Room–temperature lattice constants of common wide–bangap, II–VI semiconductors plotted against their zinc–blende and wurtzite bandgaps. The lines are to guide the eye and bulk values are from Refs. [103] and [104]. **(d)** Reciprocal lattice constructed through a Fourier transform of its corresponding Wigner–Seitz lattice. This figure was released into the public domain, e.g., see first Brillouin zone at Wikipedia.org. **(e–f)** Band structures for bulk CdSe and ZnTe respectively calculated using the first–principles orthogonalized linear–combination–of–atomic–orbitals (OLCAO) method within the local–density approximation (see Ref. [100] for additional details). **Copyright 1993 by The American Physical Society.**

often assumed to be perfectly parabolic, which is a mathematically convenient

assumption used to describe electron and hole motion. It is important to realize that this assumption only applies to a small region in *k* space near a high symmetry point [69, 105].

Within the one–dimensional, parabolic band approximation, the force, *F*, experienced by a free carrier is obtained through the derivative of energy, *E*. Assuming identical carrier relaxation times, the relationship is $F\partial x = Fv_d\,\partial t$, $F = \hbar\,\partial k/\partial t$, where ∂x is displacement in the *x* direction, and v_d is group velocity (or electron "flow"). This simple expression has significant implications. Carrier movement is strongly affected by the crystal lattice and material purity. The time interval and distance travelled by a charge carrier between scattering events are respectively referred to as the mean free time, $\tau = \partial t$, and the mean free path, *l* where $l = v_d\,\tau$, assuming that a carrier starts from rest or the ground state, and are typically dominated by collisions with other charge carriers, impurities, lattice imperfections, and lattice vibrations (phonons). The total force represents the sum of internal and external forces acting on the crystal structure. It is generally difficult to account for internal forces, so a charge carrier's effective mass, m^*, is used to represent their collective effect. Both *E* and *k* are related by m^* through $1/\hbar^2\,\partial^2E/dk^2 = 1/m^*$. Under the parabolic assumption, an electron near the bottom (top) of the conduction band will have a negative (positive) acceleration, $\bar{a} = -eE/m^*$, ($\bar{a} = -eE/-m^* = eE/m^*$). This assumption permits determination of the total system energy by simply summing the number of atoms present, where only purely kinetic energy is necessary to account for a particle with constant mass. An interesting result of the parabolic band assumption are energy–dependent density of states (DOS).

The varying dimensions of nanostructures bridge the gap between molecules and bulk materials, where a structure's dimensionality directly affects its available DOS,

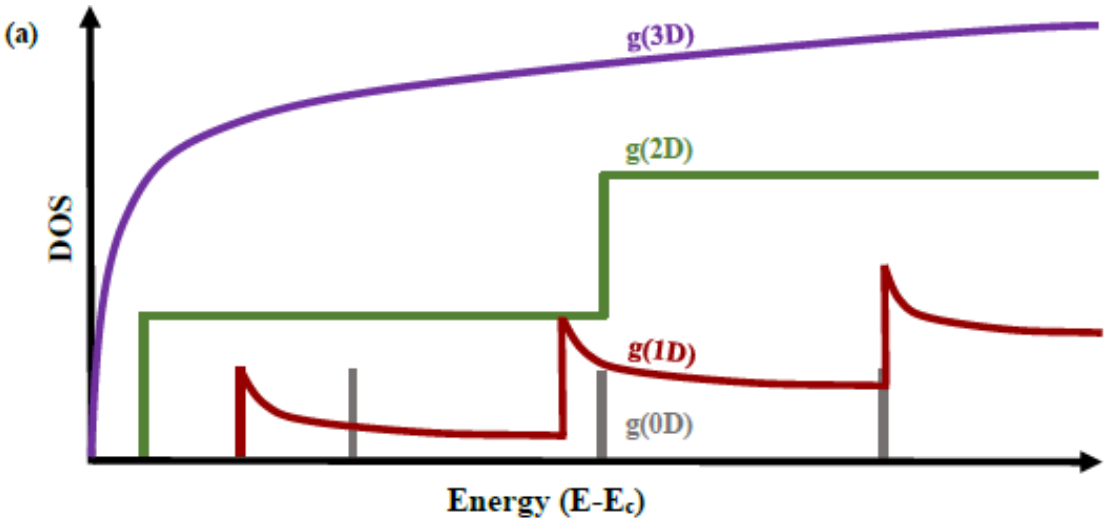

(b)

$$g(E)_{3D} = \frac{1}{2\pi^2}\left(\frac{2m^*}{\hbar^2}\right)^{3/2}\sqrt{E-E_c} \qquad g(E)_{2D} = \frac{m^*}{\pi\hbar^2}$$

$$g(E)_{1D} = \frac{1}{\pi\hbar}\sqrt{\frac{m^*}{2(E-E_c)}} \qquad g(E)_{0D} = \delta E - E_c$$

Figure 2.3 **(a)** Energy dependent density of states (DOS) for 0–3D structures, e.g., bulk, thin films or quantum wells, quantum wires, and quantum dots respectively. E_c is the conduction band edge. **(b)** Their respective equations are represented generically as $g(E)_{nD}$, where n = 0–3. These equations assume that carrier motion within a lattice can be described as a sum of sine and cosine waves, and that $E \geq E_c$, where $\hbar$ is Planck's constant and δ is the Dirac delta function. Image adapted from Ref. [106]. **Copyright 2010 by Oxford University Press**.

Figures 2.3A, and their distribution. The increasingly quantized energy of available states is a direct consequence of increased quantum confinement or the transistion from a continuum to quantized states. Figures 2.3B demonstrates this point through their respective DOS equations, *g(E)*, as commonly derived in standard solid–state text books [69-71]. Progressing from 3– to 0–D systems, the DOS are proportional to, respectively, $E^{1/2}$, E^0 (constant), $E^{-1/2}$, and $\delta(E)$, where δ is the Dirac delta function. The constant energy found in 2D systems implies an abundance of available electronic states at the top of an energy gap. Logically, the systematic $E^{1/2}$ change from 1– to 3–D systems suggests that a unit length along each dimension contributes an equal number of states. Constant energy also allows carrier populations in filled and unfilled electronic states to

be determined by the temperature–dependent, Fermi–Dirac distribution, *f(E)*, given by $1/(1+exp[(\varepsilon-\mu)/k_BT])$, where ε is the single electron energy, μ is the chemical potential (equivalent to the Fermi energy at absolute zero), k_B is Boltzmann's constant, and T is the temperature in Kelvin (K). For 3D (1D) systems, μ/ε decreases (increases) with increasing temperature, and this indicates that a relatively larger number of filled states exist for 1D systems compared to their 3D counterparts (for the same material and temperature), which is consistent with Figure 2.3A.

At an intermediate energy/temperature and for the same material, the 3D DOS, for instance, slowly increases with energy, while about half of the 2D states are occupied. As a practical example, implementing photoconductive mechanisms in a device, such as for photodetectors and solar cells, could be realized at reduced laser powers as dimensionality is reduced. As a result, quantum wires would perform with greater energy efficiency than thin film devices [107-110]. This statement obviously neglects optical absorption, which is discussed in Chapter 3. Nonparabolic bands, as is often the case, would complicate the matter mathematically.

2.5 Vibrational (H_{ion}) Term

The harmonic approximation – also relying upon adiabatic assumptions – describes H_{ion} interactions in terms of $H'(u_{kl})$, Eq. 2.5 [69]. This Hamiltonian accounts for changes in ion k displacement in unit cell l, u_{kl}, with mass M_k as ion(s) in another unit cell, $u_{k'l'}$, remain spatially fixed. In Eq. 2.5, $\Phi(kl,k'l')$ represents the force constant between ions kl and $k'l'$, and the ½ terms accounts for equal distribution over both ions. The force term accounts for both direct ion–ion interactions from Coulombic repulsion and indirect interactions mediated by valence electrons. This equation is then used to calculate the phonon dispersion using the dynamic matrix, $|D_{kk'}(q) - \omega^2\delta_{kk'}|$, which is

obtained from a mass–modified Fourier transform of the force constant [69].

$$H'(u_{kl}) = \frac{1}{2} M_k \left(\frac{du_{kl}}{dt} \right)^2 + \frac{1}{2} \sum_{k'l'} u_{kl} \cdot \Phi\left(kl, k'l'\right) \cdot u_{k'l'} \tag{2.5}$$

Performing a Taylor series expansion decomposes the Hamiltonian into a sum of symmetric (strain), e_{ij}, and antisymmetric, f_{ij}, second–rank tensors. The antisymmetric tensor describes crystal rotations; therefore, vibrational modes arise solely from the strain tensor, where the electronic band shifts from ion displacement, R, as $\delta E_{n,k}/\delta R$. Strain tensor matrices always reduce to a sum of irreducible representations. In the case of ZB structures, the three representations are Γ_1, Γ_3, and Γ_4 (also called Γ_{15}). A matrix with Γ_1 symmetry results in lattice volume dilation because the lattice's strain pattern is equal to the fractional volume change, and Γ_3 (Γ_4) symmetry describes lattice shearing from uniaxial stress applied along the [100] ([111]) direction [69]. Phonons in these matrices can yield longitudinal and transverse modes, where δR is, respectively, parallel or perpendicular to the phonon propagation direction, q. Note that these modes couple electrons to the atomic displacement gradient only when $q \sim 0$, which is the result of Fourier transforms within the long wavelength limit [69].

To more clearly illustrate the meaning of Eq. 2.5, standard solid–state physics textbooks [70] reduce this expression to represent nearest–neighbor atomic interactions for a crystal with one atom in its primitive cell, $M_k (\partial^2 u_s/\partial t^2) = C (u_{s+1} + u_{s-1} - 2u_s)$, where C is the force constant and s and $s\pm1$ denote, respectively, the displaced atomic plane and its nearest neighboring planes, Figure 2.4. Note that assuming a periodic lattice enables reduction to first–order terms without loss of accuracy [78]. This problem is normally solved with a traveling wave solution, $u_{s\pm1} = u \cdot \exp(is\mathit{ka})\exp(\pm i\mathit{ka})$. The resulting

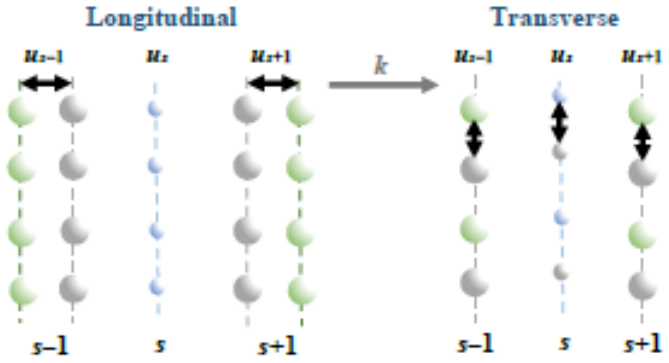

Figure 2.4 Longitudinal and transverse phonon modes result from the displacement of atomic planes parallel and perpendicular to the propagation direction, *k*, respectively. The blue and green circles represent group II and group VI atoms respectively, while the grey circles represent their original (unperturbed locations).

phonon dispersion is given as $\omega^2 = 2C/M_k\,[1 - \cos(ka)]$, which describes the relation between a wave vector and its vibrational frequency, ω. The temperature–dependent, phonon–frequency change or Raman shift, $\Delta\omega(T)$, is the sum of lattice thermal expansion, $\Delta\omega_E(T)$, and anharmonic or "self energy," $\Delta\omega_E(T)$, terms [70]. In this simplification, thermal expansion is an anharmonic or higher order effect that only alters frequencies through the volume–dependent force constant *C*, while the self–energy shift is a function of temperature at constant volume. Note that neither this simplification or Eq. 2.5 well describe lattice thermal expansion below the Einstein temperature around 200 Kelvin [69, 70, 78].

2.6 Electron–phonon ($H_{e–ions}$) Term

The $H_{e–ion}$ Hamiltonian describes electron–phonon interactions. Quantized vibrational mechanical energy, or phonons, are typically associated with heat, and result in inelastic Raman interactions between photons and the lattice. Raman scattering (RS) produces a phonon with a frequency shifted from the incident photon, which contrasts Rayleigh scattering, where a scattered photon has the same energy as the incident photon. Historically, RS was first discovered for liquids in 1928 by C.V. Raman and K.S. Krishnan [111], who were awarded the 1930 Nobel Prize in Physics [112], while

later that year, Gr. Landsberg and L. Mandelstam [113] reported the phenomenon in crystals. The primary role of RS is to probe the perturbation of electronic susceptibility through changes in atomic polarization, where Raman scattering [69, 114], as illustrated in Figure 2.5, involves: (1) absorption of an incoming photon, $\hbar\omega_i$, exciting an electron to a virtual state |a>; (2) emission (absorption) of *a* phonon changed to a state |b>; and (3) return to ground state resulting in photon emission, $\hbar\omega_s$ [115]. Resonant RS [116-123], where the incident photon energy is near the material's band gap, is a sensitive, noncontact, and nondestructive technique for probing both vibrational and electronic features [124-127]. Resonant excitation involves higher order scattering that manifests itself through (*n*–LO) phonon replicas, and physically represent increased inelastic scattering events between an electron with *n* phonons. This is possible because, at room temperature, phonon lifetimes are generally a couple orders of magnitude below that for electrons (e.g., a few ps compared to ~100 ps). It is important to realize that resonant RS requires the sum of wave vectors (*q*) be near zero, while non–resonant conditions probe only $q \sim 0$ contributions [69]. As implied in Figure 2.5, Raman peak intensities and their LO–peak energy separations ($\Delta\omega_{LO}$) directly probe a material's electronic spectrum. Electron–phonon interactions, then, require a holistic view of both excitons and phonons. Their interactions have significant device implications, where increased electron–phonon interactions increase electrical resistance but improve laser refrigeration [128]. A classical treatment [69-71] of RS is first presented before returning to electron–phonon coupling.

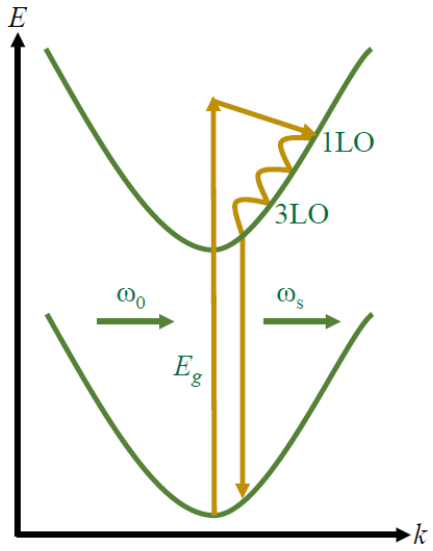

Figure 2.5 Diagram illustrating resonant Raman spectroscopy using an optical electromagnetic frequency, ω_0, near the material's band gap. The processes are described in the text.

RS is typically viewed as a sinusoidal electromagnetic field, Eq. 2.6, interacting with an isotropic medium, where $E(r,t)$ is the electric field strength, $E_i(k_i,\omega_i)$ represents its amplitude, k_i is the incident wave vector, and ω_i is the incident phonon frequency. The isotropic assumption allows the electric susceptibility, χ – a second rank tensor – to be treated as a scalar for mathematical convenience.

$$E(r,t) = E_i(k_i,\omega_i)\cos(k_i \cdot r - \omega_i t) \tag{2.6}$$

Photoexcitation induces sinusoidal polarization, $P(r,t)$, within the medium as shown in Eq. 2.7. The polarization is directly proportional to the electric field's amplitude and even possesses the same frequencies and wave vectors as the incident radiation. Meanwhile, the χ is a dimensionless factor relating the two terms.

$$P(r,t) = P_i(k_i,\omega_i)\cos(k_i \cdot r - \omega_i t) = \chi(k_i,\omega_i)\,E_i(k_i,\omega_i) \tag{2.7}$$

The vibrating medium produces phonons, which Eq. 2.8 represents as atomic displacements, $Q(r,t)$, with frequency ω_m and phonon wave vector q. Thermal or light–induced vibrations will alter the χ, and as a result, RS measures changes in a material's polarizability. The adiabatic approximation enables expansion of the χ with the Taylor

series, Eq. 2.9, which assumes that vibrational amplitudes are typically small compared to the lattice constant, and that electronic frequencies determining χ are much larger than the medium's intrinsic phonon frequencies. The first term in the expanded equation denotes the intrinsic electronic susceptibility (e.g., without thermal fluctuation effects), while the second and higher order terms describe the oscillatory perturbation of the susceptibility by the lattice wave, $Q(r,t)$.

$$Q(r,t) = Q(q,\omega_m)\cos(q\cdot \mathrm{r} - \omega_m \mathrm{t}) \tag{2.8}$$

$$\chi(k_i,\omega_i,Q)Q(r,t) = \chi_0(k_i,\omega_i) + (\partial\chi/\partial Q)_0\, Q(r,t) + \ldots \tag{2.9}$$

Polarization is more clearly expressed by substituting Eq. 2.9 into Eq. 2.7, which yields the mediums polarization, $P(r,t,Q)$, resulting from all allowed vibrational modes, Eq. 2.10, where the second and higher order terms express polarization–induced vibrations in phase with the incident radiation. This relation directly reveals that changes in incident photon energy or wavelength will alter the medium's polarizability, and by extension, the induced phonon population. Phonon occupation is described by the Bose–Einstein distribution function, $N_{ph}(\hbar\omega) = \{\exp[\hbar\omega/(k_B T) - 1]^{-1}\}$, where $\hbar\omega$ is the quantized energy of the phonon oscillator. Furthermore, the electric field's amplitude has a non–linear effect on the polarizability. Expanding Eq. 2.10 reveals a square dependence on both the incident electromagnetic wave's energy and frequency. This is because virtual transitions only need to conserve wave vector (rather than energy) [69]. The second and higher order terms in this equation are collectively represented as $P_{phi}(k_i,\omega_i)$ and are expressed through Eq. 2.11 to reveal two intriguing features.

$$P(r,t,Q) = \{\chi_0(k_i,\omega_i) + (\partial\chi/\partial Q)_0\, Q(r,t) + \ldots\}\{E_i(k_i,\omega_i)\cos(k_i\cdot \mathrm{r} - \omega_i \mathrm{t})\} \tag{2.10}$$

$$P_{phi}(r,t,Q) = \tfrac{1}{2}\,(\partial\chi/\partial Q)_0\, Q(q,\omega_m)\, E_i(k_i,\omega_i t) \times \{\cos[(k_i + q)\cdot \mathrm{r} - (\omega_i + \omega_m)t] + \cos[(k_i - q)\cdot \mathrm{r} - (\omega_i - \omega_m)t]\} \tag{2.11}$$

First, interaction with a single phonon produces two sinusoidal waves, which correspond to Stokes ($k_s = k_i - q$) and anti–Stokes ($k_{As} = k_i + q$) shifted wave vectors. This implies that q ~ 0 or that only zone center (Γ) phonons are involved. The truncated higher order terms contain the Stokes and anti–Stoke shifted wave vectors for higher order phonon modes, except again, only the sum of wave vectors must be approximately zero. Second, phonons are only induced by electromagnetic radiation in Raman active materials or when $(\partial\chi/\partial Q)_0 \neq 0$; otherwise, the modes are termed silent.

The scattered Raman intensity, I_s, is given by Eq. 2.12, where e_i and e_s are the polarization of incident and scattered radiation, and $\Re$ is the Raman tensor described by $(\partial\chi/\partial Q)_0\ Q(\omega_m)$. Finally, assigning a unit wave vector, $\hat{Q} = Q/|Q|$, parallel to the phonon displacement results in Eq. 2.13, where the Raman tensor is a second rank tensor with complex elements including the χ. A subtle result is that Raman scattering can determine both the frequency and symmetry of zone–center phonons.

$$I_s \propto |e_i \cdot \Re \cdot e_s|^2 \tag{2.12}$$

$$\Re = (\partial\chi/\partial Q)_0\, \hat{Q}\ (\omega_m) \tag{2.13}$$

It should now be clear that more vigorous lattice contractions produce larger Raman intensities, where Raman active modes are determined by e_i and e_s and the scattering geometry. These are called selection rules. Returning to ZB structures as an example, such as ZnTe, its irreducible Γ_1, Γ_3, and Γ_4 contributions may be generally assigned as *X*, *Y*, and *Z* respectively, whose respective Raman tensors appear in Eq. 2.14 [69].

$$\Re(X) = \begin{bmatrix} 0 & 0 & 0 \\ 0 & 0 & d \\ 0 & d & 0 \end{bmatrix},\ \Re(Y) = \begin{bmatrix} 0 & 0 & d \\ 0 & 0 & 0 \\ d & 0 & 0 \end{bmatrix},\ \Re(Z) = \begin{bmatrix} 0 & d & 0 \\ d & 0 & 0 \\ 0 & 0 & 0 \end{bmatrix} \tag{2.14}$$

ZB structures are described by a third rank tensor, due to the presence of

Table 2.1 Selection rules for cubic structures under backscatter geometry (refer to text). Additional selection rules are contained in Ref. [69].

Scattering Geometry	Selection Rules	
	TO phonon	LO phonon
$x(y,y)\bar{x}$; $x(z,z)\bar{x}$	0	0
$x(y,z)\bar{x}$; $x(z,y)\bar{x}$	0	$\|d_{LO}\|^2$
$x(y',z')\bar{x}$; $x(z',y')\bar{x}$	0	0
$x(y',y')\bar{x}$; $x(z',z')\bar{x}$	0	$\|d_{LO}\|^2$

electromechanical tensors, and has only one linearly independent, non–zero component denoted as d_{TO} and d_{LO} respectively for transverse optical (TO) and longitudinal optical (LO) phonons [69]. Scattering geometries are composed of a linear combination of *X*, *Y*, and *Z* components, and are generically represented as *A*(*BC*)*D*, where *A* (*D*) is the propagation direction of incident (scattered) radiation, and *B* (*C*) is the polarization direction of incident (scattered) radiation. In the common backscatter configuration, the incident (x) and scattered ($\bar{x}$) directions for the radiation are taken as perpendicular to the medium's surface. It should be noted that these selection rules stem directly from group theory and were rigorously derived by Loudon [129-131] for cubic structures. Table 2.1 summarizes the selection rules for backscatter configuration, while selection rules for additional scattering geometries may be found in Ref. [69]. An intriguing result is that TO and LO modes are rarely both active. In backscatter configuration, TO modes are forbidden, while only LO modes are expected.

While several theories [69, 132-134] exist for electron–phonon coupling, their contributions to the symmetric strain tensor (e.g., e_{ij} in the previous section) are usually described in terms of Fröhlich coupling and deformation potentials. As TO modes are forbidden in ZnTe, LO modes will be the primary focus. Fröhlich coupling describes carrier interactions with longitudinal optical (LO) phonons through macroscopic polarization expressed through Coulombic forces. These forces arise from relative

displacements of oppositely charged ions within a unit cell, Figure 2.6A, and should be partially screened by excitons whose opposite charges provide some cancellation [135]. Mathematically, Eq. 2.15 describes a phonon–induced electric field F and its potential to couple with photons, while Eq. 2.16 represents the oscillating polarization created by the electric field, E_{LO}, assuming a polar crystal with two atoms per unit cell. In these equations, u_{LO} is the phonon amplitude and is defined as the displacement of the positive ion relative to the negative ion, N is the number of unit cells per unit volume in the crystal, μ is the reduced mass given by $1/M_1 + 1/M_2$ where M_1 and M_2 are the masses of each atom in the primitive cell, and ω_{LO} is the LO phonon frequency (e.g., which is calculated or measured using Raman spectroscopy).

$$F = -[4\pi N\mu(\omega_{LO})^2 (1/\varepsilon_\infty - 1/\varepsilon_0)^{1/2}] (4\pi\varepsilon_0)^{-1/2} \quad (2.15)$$

$$E_{LO} = -F\, u_{LO} \quad (2.16)$$

The Fröhlich Hamiltonian, H_{Fr}, is formally defined as the interaction between an electron with charge $|-e|$ and the macroscopic Coulombic potential, φ_{LO}. The mathematical expression is given in Eq. 2.17. Logically, greater changes in phonon amplitudes, or changes in the polarizability, enhances Fröhlich coupling. Other interactions, such as piezoelectric electron–phonon interactions, are excluded but may be treated similarly.

$$H_{Fr} = (-e)\, \varphi_{LO} = (ieF/q)\, u_{LO} \quad (2.17)$$

A more explicit statement is obtained by combining the H_{Fr} with E_{LO}. The result appears in Eq. 2.18, where c_q^+ is a creation operator for the interaction, *c.c.* is the complex conjugate, C_F is defined in Eq. 2.19, and V is the primitive cell's volume. This relationship reveals a dependence not only upon the excitation energy and wavelength,

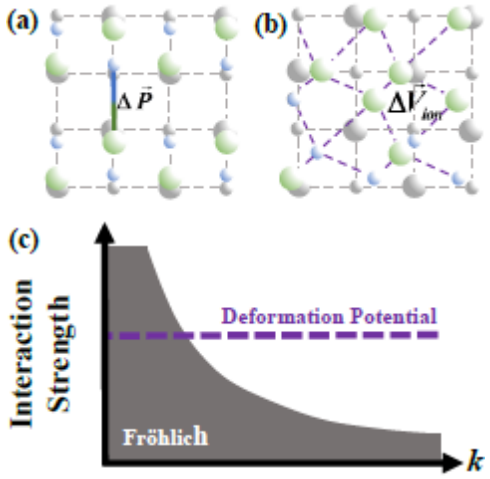

Figure 2.6 Schematic illustration of electron–phonon interactions: optically induced Fröhlich interactions and deformation potentials in a lattice. Grey circles and bonds indicate equilibrium positions, while green and blue circles induced the perturbed and the purple bonds represent altered bond distances. The different sized circles represent alternating planes of group II and IV elements. **(a)** Fröhlich interactions result from the relative displacements of oppositely charged ions within a unit cell, $\Delta\vec{P}$. The resulting momentum changes alter Coulombic forces from their equilibrium values to induce macroscopic polarization within the lattice (blue and green circles). **(b)** Deformation potentials, which are more prominent in nonpolar crystals, result from indirect electron interactions with the altered lattice bond angles and distances, $\Delta\vec{V}_{ion}$. **(c)** Interactive strengths as a function of wave vector *k*. Images adapted from Ref. [135]. **Copyright 2012 by The American Physical Society.**

but also upon the crystal volume. This relationship has found its way into several theoretical treatments, which assume a vanishing H_{Fr} with decreasing nanoparticle diameter [136]. Dielectric constants also affect H_{Fr}, which suggests that changing the supporting substrate could also have an effect.

$$H_{Fr} = \sum_{q} (iC_F/q)\{c_q^{+} \exp[i(q\cdot r - \omega_{LO}t)] - c.c.\} \tag{2.18}$$

$$C_F = e\,[2\pi\hbar\omega_{LO}/(NV)\,(1/\varepsilon_\infty - 1/\varepsilon_0)]^{1/2} \tag{2.19}$$

A more subtle result of the above two equations is that H_{Fr} diverges as q approaches zero.

Deformation potentials stem from local perturbations in bond lengths and angles, Figure 2.6B, and may be induced through increased surface strain [69, 135]. The

deformation potential Hamiltonian describes electron–optical–phonon interactions, $H_{e-OP} = D_{n,k} (\underline{u}/a_0)$, where $D_{n,k}$ is the optical phonon deformation potential for energy bands indexed with n and k, and u is the optical phonon displacement. Because this short range interaction arises from changes in bond lengths and angles, it does not depend upon the phonon's wave vector, but it does affect TO–LO splitting in terms of d. As illustrated in Figure 2.6C, deformation potentials have a relatively constant, finite value of ~10 eV because no potentials exist between conduction–band electrons and optical phonons [137, 138]. In contrast, Fröhlich interaction strengths decrease with increasing wave vector or shorter wavelengths because atoms in the (reciprocal) unit cell are polarized less effectively. Similar trends are observed experimentally, where the deformation potential term demonstrates temperature independence, while Fröhlich interactions result in a reduction of carrier–LO interactions with increased temperatures [135]. Chapter 5 explores electron–phonon interactions experimentally.

2.7 Surfaces and Interfaces

While bulk semiconductor surfaces contain fewer available electronic states, such as $N^{2/3}$ surface states for N bulk states with, for instance, $N_{bulk} = 10^{23}$ atoms per cm^3 [78], the large surface–to–volume ratio found in nanostructures provide abundant surface states that could be exploited for device applications. Surface states also play significant roles in nanostructure properties. Many semiconductors are covered in an amorphous layer or a shell material, such as with oxygen–based surface species [139-142] or core/shell structures [143] respectively. The mechanism behind thin oxide layers is still debated, because neither standard model, such as interfacial defects [50] or metal–induced gap states [144-146], adequately explain all experimental results. Surfaces are typically treated as an ordered, 2D "superlattice" (not to be confused with

repeating quantum well structures) with lattice parameters shifted from the bulk or "substrate" lattice (not to be confused with the supporting substrate). These shifts are represented generically as $X(hkl)(x\times y)R\varphi$, where $X(hkl)$ is the substrate lattice, $x\times y$ represents a superlattice, $\vec{a}_s$, shifted by x relative to the substrate's lattice, $\vec{a}$, given as $\vec{a}_s = x\vec{a}$, R is the superlattice's periodicity, and φ is the superlattice's rotation relative to its substrate lattice [78]. Treating the crystalline surface layers as a translated lattice results in very different electronic states being formed near the surface. Their main effect is to produce electronic and vibrational states in a material's forbidden energy gap [78]. In other words, reconstructed surface states, even those composed of the same material, can act similarly to defects that allow electronic states within a bandgap. Explicit mathematical treatments may be found elsewhere [69-71, 78]. Queisser and Haller [50] reviewed the underappreciated importance of defects and their ability to modify device properties – even in very positive ways. Important examples include controlling electrical conductivity and carrier lifetimes. However, *N*–body theory is not particularly useful for describing amorphous systems, and therefore, has predictive limitations.

2.8 Versatility and Limitations of the *N*–body Approach

This simple model for electronic states in a perfect crystal intuitively correlates fundamental, first–order device physics with optical and electrical properties in homogenous, semiconductor crystals. Supporting examples are provided. First, extrinsic doping [147, 148] replaces lattice atoms – with very different atomic sizes and numbers compared to the host – that alters local carrier mobilities, which is reflected in altered one–electron wave functions in the H_e and H_{ions} Hamiltonians. A sufficiently large dopant concentration could be observed at the macroscopic level, where the

altered electronic states yield very different electrical properties compared to undoped devices [149-151]. A similar argument applies to stoichiometric differences in, for instance, Cd_xSe_{1-x} nanobelts [152], where alterations in group II and VI atomic quantities could affect the electrical performance of nanowire–based transistors [153] and sensors [154]. Second, one could properly reason that the reduced number of electronic states in confined nanostructures would alter optical properties, such as through band structure changes [155-157]. As the diameter or thickness is increased in nanostructures with reduced dimensions, red–shifted absorbance [156-158] is typically observed, which one could view qualitatively as atoms, with global neutrality but local charge, minimizing Coulombic repulsion through maximized bond distances [159]. Section 2.3 covered this topic more explicitly. Third, the $H_{e–ions}$ Hamiltonian suggests that electron–phonon coupling (EPC) can be altered by perturbing the lattice, which is not always realized in the literature. This sometimes results in reporting an assumed "intrinsic" electron–phonon coupling strength that was actually perturbed extrinsically. This not only hints at the possibility of utilizing currently unrealized EPC strategies to produce interesting devices, but literature's typical focus on exciton [82, 160] contributions hints at the potential for further discovery. Extrinsic influence is supported by literature. For example, laser cooling [128] studies on CdS nanobelts suggest that EPC strengths could be dynamically tuned. Chapter 5 investigates both intrinsic and extrinsic methods for tailoring EPC.

Although N–body theory is quite robust, it lacks intuitive prediction and ease of computational implementation regarding (1) surface contributions, (2) geometry–dependent parameters, and (3) resonant features in optical spectra. For example, surface contributions can dominate a nanostructure's optical and electrical properties [161,

162], yet it is not intuitive to predict how surface oxygen species, which are thought to markedly improve the performance of nanowire–based photodetectors [107, 108], will affect the material's properties. This particular example is further complicated by the dynamic chemical process of oxygen desorption under sufficient photo–excitation power densities. An example regarding (2) are geometry–dependent band gap values [163]. Again, an intuitive prediction is not possible and requires computational assistance. As for (3), resonant absorption and photoluminescence features are difficult to unambiguously interpret without theoretical analysis. The frequency–dependent strength of light–matter coupling for interactions among N–1 particles produces an inaccurate interpretation of, for example, photoluminescence stemming solely from bound–exciton recombination (while neglecting ionized–exciton interactions) [164, 165]. Chapter 3 presents a more intuitive illustration of the physical processes involved in light–matter interactions.

2.9 Summary

N–body theory provides the logical framework for this dissertation by relating interacting forces within a lattice to a material's optical and electrical properties. The adiabatic and other applied approximations yield three terms that are the sum of one–electron wave functions throughout a homogenous lattice demonstrating translational symmetry. The resulting H_e, H_{ion}, and H_{e-ion} Hamiltonians describe the electronic, vibrational (phonon), and electron–phonon coupling contributions, where each term is probed experimentally in this dissertation. The theoretical foundation for Raman spectroscopy, in particular, was discussed. Section 2.7 discusses the usefulness and limitations of this semi–quantitative model. For example, the model provides an intuitive framework to predict electrical and electron–phonon coupling changes from

defects, although computational assistance is required for more complicated examples, such as the effect of surface layers and geometry. Theory, however, is constantly evolving. Chapter 5 demonstrates that conventional EPC theory must be further developed to well–describe ZnTe systems, while Chapter 3 presents the fundamentals behind light–matter interactions.

CHAPTER 3: THE LIFEBLOOD OF ELECTRONIC–OPTICAL DEVICES

"The science of today is the technology of tomorrow."
Edward Teller, 1991 Conversations on the Dark Secrets of Physics

3.1 Fundamental Building Blocks

A strong foundational knowledge of light–matter interactions is required to engineer complex device behavior or to design novel functions. Solid–state matter forms the conceptual heart, where electronic–optical devices may use light absorption to produce electrical properties. Light is absorbed when it is in resonance with the electronic structure (Section 3.1), and can experience optical amplification, such as through guided modes [166-168] or stimulated emission [169, 170]. Like devices, matter also possesses loss mechanisms, which result from the different carrier generation and recombination pathways described in Section 3.2. Examples of loss mechanisms include non–radiative recombination (e.g., light–emitting diode), or electrical degradation from defects (e.g., FETs). Phonons also represent losses in the form of heat (e.g., thermoelectric devices), or through reduced electrical performance from enhanced electron–phonon coupling. Incorporating these concepts into a device is the final step. Metal–semiconductor interfaces, which are the backbone of semiconductor physics, are described in Section 3.6, prior to summarizing the chapter in Section 3.7.

3.2 Free Carrier Photogeneration and Recombination

Light absorption is a form of optical perturbation [171], where typically above band gap light waves couple to the lattice to form either highly localized (with respect to the unit cell), Frenkel excitons [172, 173] or more extended, Wannier–Mott excitons [174]. Local photogeneration of free carriers through laser illumination, as illustrated in Figure 3.1A, produces an exciton consisting of an electron–hole pair, where the electron (hole) is excited to the conduction (valence) band. The electric field separates an exciton into a free electron and hole. The photoinduced carrier gradient in the semiconductor induces carrier diffusion, which is dependent upon carrier kinetics, and the laser's penetration depth and illumination wavelength/power. The general diffusion current density is $J_{diffusion} = -qD\,\partial N/\partial x$, where N may be replaced by n or p using the relevant electron or hole diffusion coefficient, $D_{e/h}$. The diffusion gradient, e.g., $\partial n/\partial x$ or $\partial p/\partial x$, obviously increases with a larger number of localized free carriers and decreases with their delocalization along, for example, a nanowire's length (assuming perpendicular illumination). Specific details are extracted from device models, which usually incorporate the surface–recombination velocity [175] to describe trap states, either in the bulk part of the material or surface defects, or absorbed surface species. This model is briefly described before inclusion into a slightly more sophistocated description of $\partial N/\partial x$. In the case of an n–type CdSe nanowire, the kinetic model illustrated in Figure 3.1A (from Ref. [176]) assumes single electron and hole trap states relative to the CBM and VBM for electrons and holes respectively. This model neglects deep–level traps, and appears in Figure 3.1B, where (1) photo–generation creates free carriers along pathway G that may subsequently experience: (2) bimolecular radiative recombination with rate $k_r \sim 10^3$ cm s^{-1}; (3) free electrons combining with trapped holes

at rate $k_n \sim 3.2\text{x}10^2$ cm s^{-1}, (4) free electrons trapped in shallow defects with frequency $k_t^e N_e \sim 10^7$ s^{-1}; (5) holes being trapped in shallow defects with rate $k_t^h N_h \sim 10^{11}$ s^{-1}; and (6) trapped electrons recombining with trapped holes according to $k_S \sim 10$ cm s^{-1} [176]. Recombination of free holes with trapped electrons is excluded because it occurs on a much faster time scale than electron trapping. This model assumes that: (1) carrier photo–generation is limited to the excitation area, where laser excitation is described with a Gaussian intensity distribution, (2) charge carriers are at least partially independent compared to bound excitons, and that (3) time–dependent carrier diffusion is described by the Smoluchowski equation [177], which includes Coulomb interactions experienced by charges from, for example, impurities during diffusion [178, 179].

The rate of photo–generated free carriers, G, is given by $I_{exc}\,\sigma_{abs}/h\nu$, where I_{exc} (σ_{abs}) is the excitation intensity (absorption cross section), and $h\nu$ is the photon energy for monochromatic (single wavelength) illumination [178]. Using single parameters to represent I_{exc} and σ_{abs} is misleading. I_{exc} follows a Gaussian intensity distribution that well describes the positive charge profile in Figure 3.1A, while σ_{abs} is wavelength dependent. The only straight forward variable here is the photon energy, which has an inverse ($1/x$) decay from higher to lower excitation frequency (where x is the carrier displacement). For illustrative purposes, one can imagine carrier buildup through localized photo–generation followed by diffusion from higher concentration at the illumination location to lower carrier concentration further away. The time–dependent carrier concentrations (and diffusion profiles) are described by Equations 3.3–3.4 respectively [178]. In these equations, values for electrons and holes are denoted with subscript e and h respectively, where $\partial N/\partial t$ describes the rate of change in their respective carrier concentrations. Furthermore, bulk mobilities yield D_e and D_h values

of 18.31 and 1.91 $cm^2\ s^{-1}$ respectively [180], while W is the potential energy, $I_{exc}(x)$ describes the spatially dependent laser intensity, R is a general parameter describing carrier recombination using the previously discussed rates, ε_0 (ε_r) is the vacuum (relative) permittivity, r is the nanowire radius, and the indices j and i respectively represent the total number of nanowire segments and the segment illuminated under constant, stationary illumination. Note that Ref. [178] only considered the case when $R = k_{rec}N_eN_h$ although it could, in principle, be generalized to include other recombination pathways.

$$\frac{\partial N_{e(h)}}{\partial t} = D_{e(h)}\frac{\partial^2 N_{e(h)}}{\partial x^2} + \frac{D_{e(h)}}{k_B T}\left(N_{e(h)}\frac{\partial^2 W_{e(h)}}{\partial x^2} + \frac{\partial N_{e(h)}}{\partial x}\frac{\partial W_{e(h)}}{\partial x}\right) + I(x) - R \tag{3.3}$$

$$W_{e(h)}\left(x_j\right) = \frac{\sum_{i\neq j}\left[N_{e(h)}\left(x_i\right) - N_{h(e)}\left(x_i\right)\right]\left[N_h\left(x_i\right) - N_e\left(x_i\right)\right]e^2}{4\pi\varepsilon_0\varepsilon_r r_{ij}} \tag{3.4}$$

Recombination under continuous wave (CW) illumination, or constant laser intensity, represents a long time scale relative to carrier recombination, where steady state carrier generation is assumed, or where a new carrier is generated as soon as one recombines. A steady state assumption, however, does not imply constant recombination rates due to competition between k_r and trap state recombination pathways. Recombination may be measured through the photoluminescence emission intensity, I_{em}, relative to the excitation intensity, I_{ex}. In principle, direct recombination (without trap states) relates these two variables through Eq. 3.5, where P_{abs} is the probability of absorbing an incident photon, P_{rel} is the probability that a photo–excited exciton relaxes to its emitting state (which may not necessarily be the ground state), and P_{em} is the probability of radiative recombination after relaxation [69]. These ideal

photoluminescence conditions produce a Lorentzian spectral shape, $I_{PL}(\hbar\omega)$, given in Eq. 3.6, where $\hbar\omega$ is energy of the emitted photon [69]; obviously, it is only valid for above band gap excitation (e.g., $\hbar\omega > E_g$). Laser heating [181], among other factors, can introduce peak asymmetries that result from a carrier bottleneck, while P_{rel} is strongly influenced by electron–hole pair energies, which is influenced by the laser–power–dependent carrier concentrations [69]. I_{em} is assumed to collectively represent all recombination pathways and their respective rates.

$$I_{em} = P_{abs}\, P_{rel}\, P_{em}\, I_{ex} \tag{3.5}$$

$$I_{PL}(\hbar\omega) = (\hbar\omega - E_g)^{1/2} \exp[-(\hbar\omega - E_g)/(k_B T)] \tag{3.6}$$

Equations 3.7–3.10 approximate carrier recombination at the conduction and valence band edges, which are solved explicitly in Ref. [176] to provide I_{em} values proportional to G^2, $G^{1.5}$, and G for low, moderate, and high laser powers respectively as shown in Table 3.1. These values appear as slopes on the log–log plot of the nanowire's I_{em} versus I_{ex} as shown in Figure 3.1C. The slope reduction with increasing laser power indicates trap state saturation, and subsequent enhancement of direct recombination or k_r. Consider a small bucket. Once the bucket is filled, water can only flow out of it. Similarly, once trap states are completely filled, radiative recombination increases in

Table 3.1 Slopes obtained from log–log slopes of the photoluminescence emission intensity, I_{em}, as a function of the excitation intensity, I_{ex}, and the rate constants proportional to I_{em} for low, intermediate, and high laser powers.

CW Intensity Regime	**Log–log I_{em}–I_{ex} slope**	**$I_{em} \propto$**
low	~2	$k_r G^2/k_t^e N_e k_t^h N_h$
intermediate	~1.5	$k_r G^{1.5}/k_t^h N_h \sqrt{k_n}$
high	~1	G

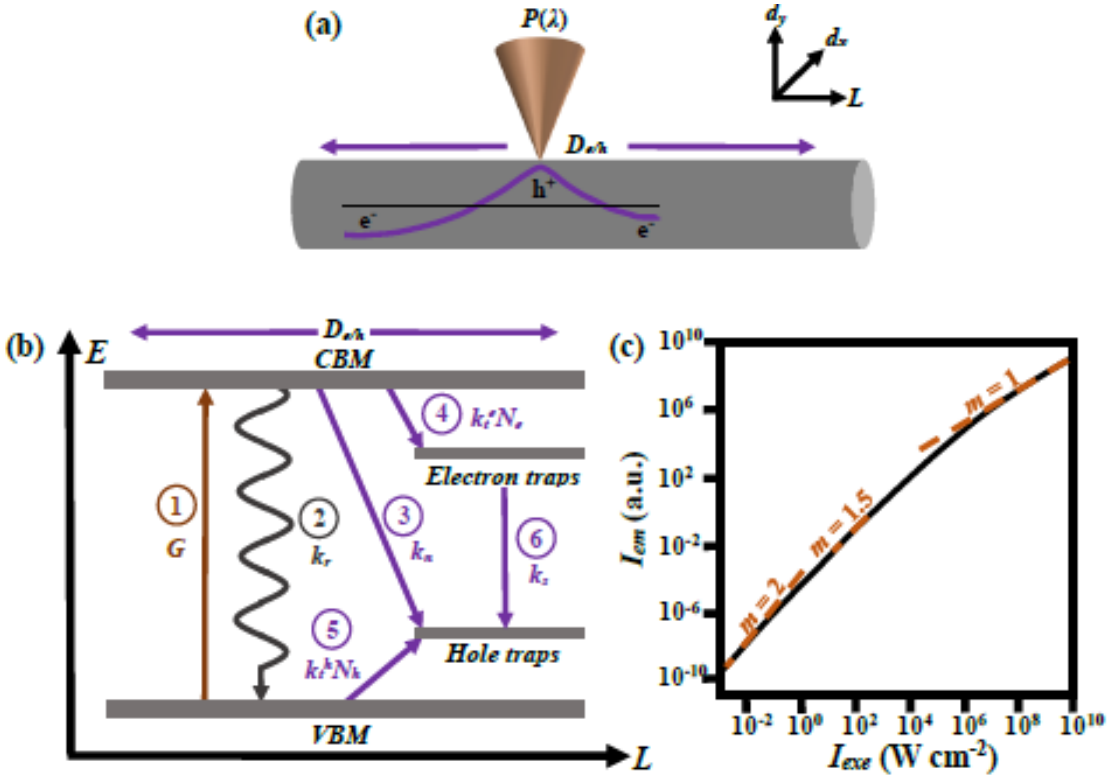

Figure 3.1 Laser–power–dependent photoconductivity is a direct result of the available recombination pathways, e.g., especially trap states, along a nanowire's length, L, and to a much lesser degree, along either of its diameter directions, $d_{x/y}$. **(a)** Optical (laser) illumination, $P(\lambda)$, induces a charge gradient, where, in the case of CdSe, holes collect predominately under the laser spot, while electrons diffuse away from the illumination area. Additional details are contained within Ref. [178]. **(b)** Photogenerated carriers, G, may recombine through several pathways (refer to text), where each pathway has its respective first–order rate constant under steady–state illumination. **(c)** Three laser power regimes are apparent on a log–log plot of the illumination emission intensity, I_{em}, plotted as a function of the excitation intensity, I_{exe}. The slopes, denoted as m, are equivalent to the average rate constant under each illumination condition. (b–c) were adapted from Ref. [176]. **Copyright 2011 by The American Physical Society.**

probability. It is also possible that carrier relaxation to a trap state results in radiative emission less than k_r or the material's bandgap, but this plays a smaller role in high purity materials. Notably, this model excludes interactions between ionized excitons, as well as, other relaxation pathways. Electron–phonon coupling, for example, is small in CdSe and may be neglected in a first approximation, while this would not be true for other materials, such as ZnTe. Electron–phonon coupling will be discussed further in Chapter 5.

3.3 Electrical Resistance: Phonons and Thermal Effects

Light–matter interactions produce carriers that, in the context of devices, are described in terms of their carrier mobility, μ. The carrier mobility is a material quality measure, where multiple recombination pathways produce an averaged value; reduced mobilities, for instance, manifest themselves through increased material resistance. Both the light–effect transistor [182] and resistive memory [183-185] concepts operate by switching between high ("off") and low ("on") resistance states, which are described by changes in the device's net carrier mobilities. A higher mobility implies fewer scattering events, such as on a smooth nanowire surface [186], which yield a larger τ and an increased drift velocity, $v_d = \mu E$ where E is the electric field. This allows more carriers to be collected at the drain contact. Two dominate, temperature–dependent forms of scattering are phonon or lattice scattering, $\mu_{phonon} \propto T^{-3/2}$, and ionized impurity scattering, $\mu_{ionized} \propto T^{3/2}$ [69]. A material's total inverse mobility is the inverse sum of each component or $1/\mu = 1/\mu_{phonon} + 1/\mu_{ionized}$. While both scattering mechanisms alter carrier motion, phonon scattering is an energy relaxation mechanism that couples exciton energy into a phonon wave, which differs from the Coulombic or charge interactions involved with ionized impurity scattering. This type of impurity is termed a deep impurity and demonstrates a highly localized effect that requires computational assistance to estimate within the N–body framework [69]. High quality growth minimizes these effects, although in a device, laser–induced diffusion of the electrode's metal ions into the semiconductor material could turn this into a very real concern if caution is not exercised [150]. Phonons are the most likely source reducing carrier mobilities, and as demonstrated in Section 2.5, are unavoidable. While minimizing these sources of resistances is possible, a holistic view could allow development of novel

devices that utilize these contributions for positive effects, which contrasts the conventional view as a negative effect. For example, phonons are similar to electrons and photons, where wave vectors must be matched for a phonon to traverse across a heterojunction [187]. A photo–conductive device could illuminate a thin material that minimizes phonon transfer to the rest of the device, which could assist with thermal management strategies. However, the relative newness of this field [54, 186] means that such concepts are not yet well explored (or even proposed).

3.4 When Carriers Meet Barriers: Metal–Semiconductor Interfaces

Given a short enough nanowire channel, some carriers will diffuse across the entire channel. Metal contacts are placed on each nanowire end to create a metal–semiconductor (M–S) interface to extract the current. *N*–body theory presented in Chapter 2 properly suggests that such a heterojunction will alter the electrical properties. The light–effect transistor (Chapter 4) employs indium (In) contacts on a CdSe nanowire to form In–CdSe MS junctions at each nanowire end; therefore, this structure will serve as an illustrative example here. Figures 3.2A–B contain, respectively, In and n–type, CdSe energy levels prior to and after forming a contact. In principle, the work function difference between these two materials (Φ_{In} = 4.09 eV and Φ_{CdSe} = 4.9 eV relative to the vacuum level) should produce more ohmic–like than rectified characteristics, as a rectified response requires a large work function difference to form a Schottky barrier [188]. Experimental measurements, however, produce both ohmic and rectified behavior (e.g., see Chapter 6). It is likely that a native surface oxide or amorphous layer also plays a role, such as a thin SeO_x layer (x = 2–3) [189] at the In–CdSe junction, although further investigation is required.

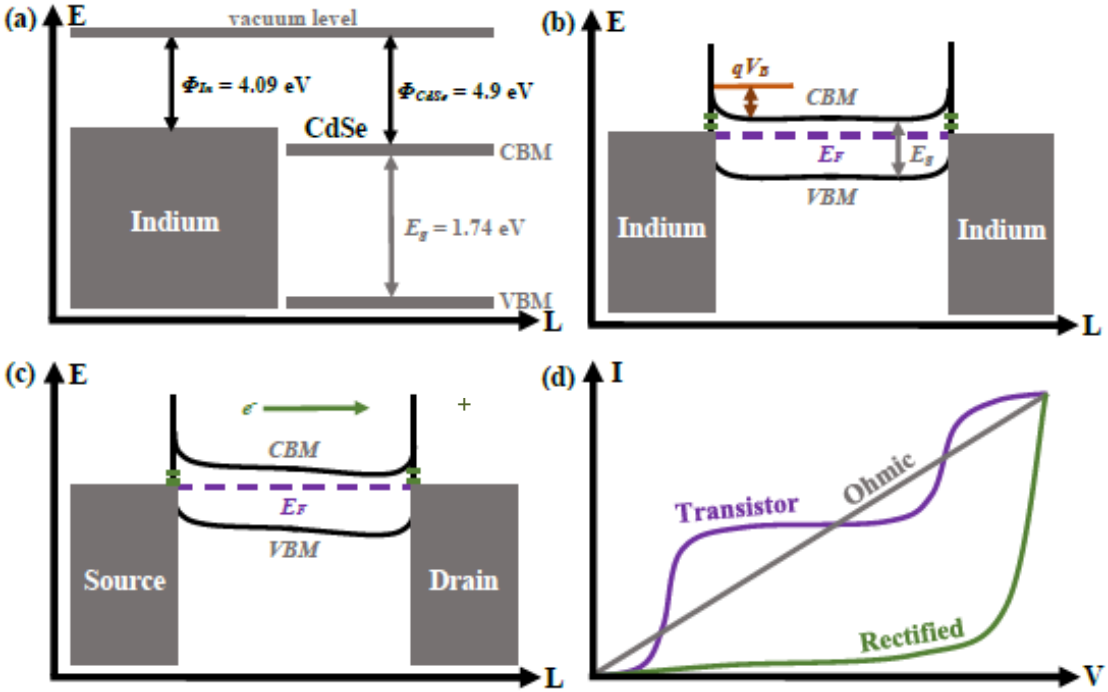

Figure 3.2 In and CdSe energy level diagrams **(a)** before contact, **(b)** after contact, **(c)** under forward bias, and **(d)** fundamental current–voltage characteristics found in resistors (ohmic), diodes (rectified), and transistor–like behavior.

Photo–generation and carrier recombination occurs in the band energy diagrams in Figure 3.2B, although these processes were not duplicated from Figure 3.1 for brevity and clarity. The green lines represent surface states at the In–CdSe interfaces, which strongly influences the M–S interface's energy barrier [190]. An ohmic response possesses far fewer surface states compared to a rectified device, while a rectified device would also possess dissimilar interface state concentrations in order to produce asymmetric characteristics. Increasing surface charges or removing these states, such as through photo–excitation [191] or laser annealing [192] respectively, would alter the M–S barrier, and for reversible processes, a recovery of the electrical processes could be observed. Altering these states, either temporarily (reversibly) or permanently (irreversibly), would alter local potentials, which manifest themselves through altered carrier densities and mobilities. In other words, modifying these states directly alters carrier dynamics and recombination, and if performed in an ideal manner, it could

enhances a device's collection efficiency [193]. The result is observed through the bulk conductance, $G = I_{ds}/V_{ds}$, where I_{ds} and V_{ds} are the source–drain current and voltage respectively (e.g., see Chapter 4). In fact, surface states were manipulated to produce a significantly enhance gain in a zinc–oxide–nanowire–based transistor [108]. Changes in the bulk conductance occur by altering the bulk carrier concentration, n, as described in Equation 3.7, where μ is the carrier mobility, and w, t, and L are the nanowire's width, thickness, and length [194]. The unit of bulk conductivity are siemens, S, which is equivalent to inverse resistance (ohms).

$$G = nq\mu wt/L \tag{3.7}$$

Although a nanowire's dimensions contribute to the conductivity, such as by possessing additional contributing surface and bulk states, these parameters are held constant when examining gentle laser heating of the same device. Therefore at the M–S interfaces, increased carrier mobilities result from reduced trap states, and produce an increased bulk conductance. Thermal annealing of the device can form grain "necks" or connections that restrict bulk current flow, which affects the bulk conductivity.

Figure 3.2C demonstrates the effect of applied bias on the band structure. The positive side attracts electrons and is termed the drain and can be thought of as an electron collection point. Meanwhile, the negative side provides the electrons and is called the source. The vertical energy axis represents increasing electron energy; therefore, the source or negative bias will increase the energy level relative to positive bias. Reverse bias simply reverses the side of the source and drain to produce the mirror image of the illustrated energy level diagram. Figure 3.2D demonstrates possible current versus voltage, I_{ds}–V_{ds}, where the d and s subscripts refer to electrical measurements made across the source and drain contacts. An ohmic response (gray line) is linear, while

a rectified response (green line) begins with a relatively low current followed by a drastic I_{ds} increase. The double plateau structure (purple line) illustrates what Mott and Gurney [195] term the “primary” and “secondary” photo–conductivity region, where the former is discussed in the next section.

3.5 Photoconductivity Model

In the primary photoconductive region, the electron collection efficiency, Ψ, is equivalent to the quantum efficiency, η_{QE}, assuming 100% absorption efficiency, and can be described with either Equations 3.8 or 3.9 for focused or uniform illumination respectively. The purpose is to demonstrate potential electrical (output) characteristic changes from altering the illumination position along a nanowire. Focused (uniform) illumination is when a single point (the entire length) of the nanowire is illuminated. In Equation 3.10, x_0 is the illumination site measured from the anode (cathode) when the carriers are electrons (holes), L is the conducting channel’s length, and w is the electron (hole) mean free path and is related to the applied electrical field, F, or voltage, V, through $w = \mu FT = \mu VT/L$. The variables μ and T are the carrier mobility and carrier lifetime, respectively. Eqs. 3.8 and 3.9 may be compared to provide additional insight into the two typical operation modes.

$$\Psi = w/L\left(1 - e^{-x_0/w}\right) \tag{3.8}$$

$$\Psi = w/L\left[1 - w/L\left(1 - e^{-L/w}\right)\right] \tag{3.9}$$

This theory suggests a continuous photocurrent increase from $V_{ds} = 0$ until saturation at a sufficiently large V_{ds} to produce $w >> L$ and $\Psi \rightarrow 0.5$. This model considers only one

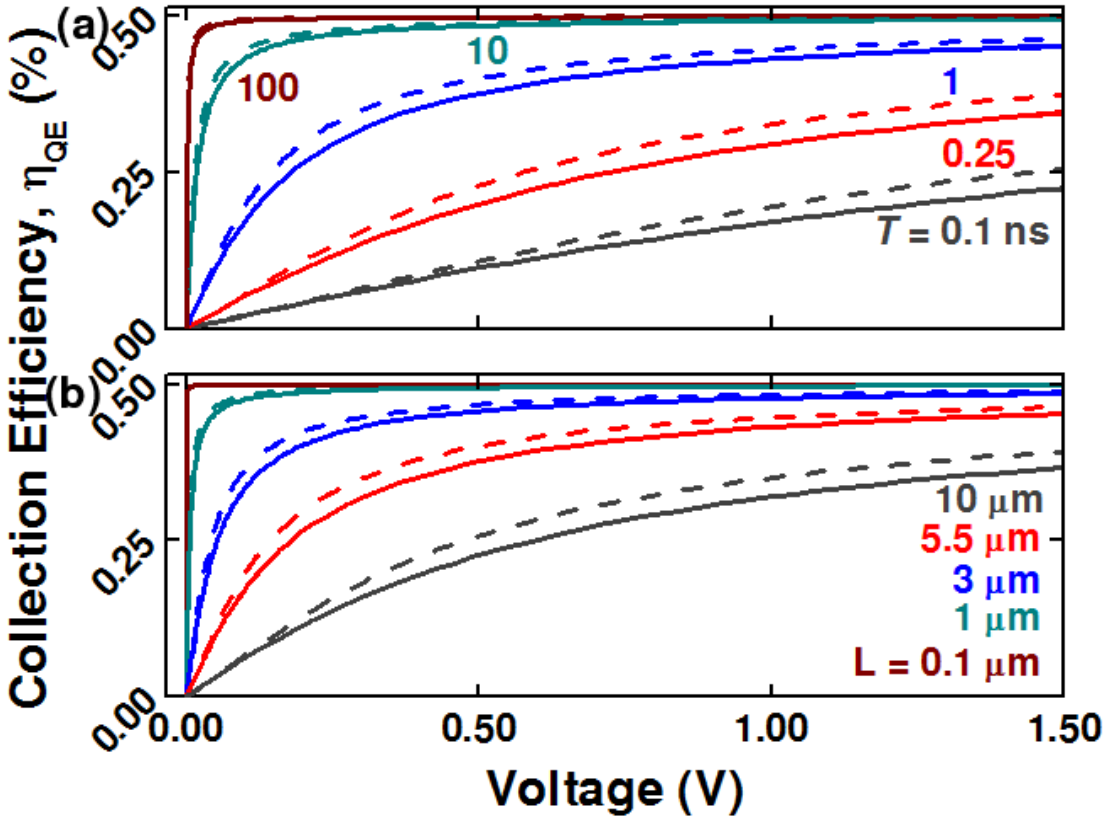

Figure 3.3 Electron collection efficiency, Ψ, or quantum efficiency, η_{QE}, after Mott & Gurney [195], as a function of applied bias for **(a)** different electron lifetimes, T, when L = 5.5 µm, and for **(b)** different nanowire lengths, L , when T = 1 ns, was plotted for focused illumination with x_0/L = 0.5 (dashed lines) and uniform illumination (solid lines) conditions as described by Eqs. 3.14 and 3.15 respectively. Lengths of 5.5 and 10. µm correspond to SNW lengths for two devices used in Chapter 4 (referred to as device 2 or D2 and device 1 or D1 respectively).

carrier type, e.g., electrons, which have an upper efficiency limit of 50%, where η_{QE} is minimized at the anode, but the equation also holds for holes with the exception that η_{QE} is maximized at the anode. Figure 3.3 plots η_{QE} or focused (dashed lines) and uniform (solid lines) illumination conditions as a function of applied voltage with (A) varying T in a realistic carrier lifetime range, e.g. 0.1-100 ns [196], when L = 5.5 µm (the same as D2), and with (B) varying nanowire length from L = 0.1 to 10 µm, assuming T = 1 ns. For focused illumination, x_0/L = 0.5 is assumed. A typical bulk CdSe mobility value [196] of 660 $cm^2\ V^{-1}\ s^{-1}$ is used. Figure 3.3 also indicates that these two illumination modes yield comparable efficiencies, and as a result, either focused or broad–area

illumination could be reasonably implemented into a device, depending on the specific application need. In Figure 3.3A, increasing the electron's mean free path by increasing the mean carrier lifetime resulted in reaching a higher efficiency more rapidly, which suggests the ability to control current production at low applied bias. Figure 3.3B indicates that nanowire length may also control the low bias current, where shorter nanowire devices produce larger currents. Mott & Gurney's classical equations are able to qualitatively reproduce observed LET trends in the low bias region, but this model does not describe (1) the device characteristics in the higher bias region or the second plateau, (2) the ability of surface trap states to alter the τ, or (3) the source–drain voltage offsets (x–axis) in a transistor's output characteristics, e.g., refer to Figure 4.3 in Chapter 4.

Devices are also characterized by their quantum efficiencies, such as their external quantum efficiency (EQE) and internal quantum efficiency (IQE). Both the EQE and IQE describe the number of charge carriers collected, which is represented by the device's drain current divided by the charge of a single electron. The two are related through EQE = $\eta_{abs}(\lambda)$ IQE = $\eta_{abs}(\lambda)\,\eta_{gen}\,\eta_{coll}$, where $\eta_{abs}(\lambda)$ is the wavelength–dependent light absorption efficiency, η_{gen} is the quantum yield for charge carrier generation, and η_{coll} is the photo–generated charge carrier collection efficiency, such as Ψ from the photoconductivity model [197]. The EQE is generally smaller than the IQE.

3.6 Summary

Engineering effective next–generation, electronic–optical devices requires enhancing absorption by coupling the external radiation into the device, and careful consideration of recombination pathways. As a result, the illumination wavelength and power will play direct roles in determining a device's photoconductive response, such

as with the light–effect transistor in Chapter 4. This response is also partially determined by the M–S interface details, such as the existence of a native oxide or an amorphous layer. A holistic view of device fabrication and the involved processes are required to develop electronic–optical devices that could far exceed FET capabilities.

CHAPTER 4: LIGHT–EFFECT TRANSISTOR

"You never change things by fighting the existing reality. To change something, build a new model that makes the existing model obsolete."
R. Buckminster Fuller, 1982 Critical Path

4.1 Next Generation Transistors

As basic electronics building blocks, a field-effect transistor's (FET's) primary switching function is widely used in both logic and memory chips. A typical FET is a three–terminal device consisting of source (*S*), drain (*D*), and gate (*G*) contacts – where the *S–D* conductivity is modulated to realize on and off states by applying a voltage or an applied electric field through *G* [198]. Although FETs have evolved structurally from early planar to their current 3D geometries in parallel with the continual shrinkage of its lateral size, the basic operating principle remains the same. This has led to ever greater fabrication complexity, and ultimately to challenges in gate fabrication and doping control [5, 7-10]. Various new technologies, such as FinFETs [7, 12], and tunnel–FETs [13], have been developed in recent years to enable the continuation of Moore's law [14], but further development with current technologies are uncertain [15]. Other options are being explored as alternatives, which include semiconductor nanowire (SNW) based FETs [17-19], FETs comprised of 2D materials [22, 23], and FETs with sophisticated gate structures [24], such as multiple independent gates [8, 10] or a gate with embedded ferroelectric material [25]. There is, however, no clear pathway for overcoming a FET's intrinsic physical limitations [1-3] dictated by its operation mechanism, such as random dopant fluctuations [5] and gate fabrication complexities [6], and no viable rival technology currently exists. We offer a competitive

alternative with additional unique functionalities. The light–effect transistor (LET) is a two-terminal device composed of a metal–semiconductor–metal (M–S–M) structure, where each M–S junction serves as either the *S* or *D* contact, and the two contacts are separated by a nanostructure–based channel. Figure 4.1 contrasts SNW–based LET and FET structures to reveal the apparent structural simplicity offered by a LET – no physical gate is required. A LET's operation mechanism is distinctly different from a FET in two regards: (1) the *S*–*D* conductivity is solely modulated by light or an optical frequency electromagnetic field, which contrasts a FET's electrostatic control through an applied DC voltage, and (2) current carriers are generated through optical absorption rather than by thermal activation of dopants. In other words, a LET employs optical gating based upon the well–known photoconductive mechanism [195] that has typically been of interest in photo–detection. Inherent advantages stem from a LET's simplistic architecture, which include (1) eliminating gate fabrication complexity, and (2) avoiding difficulties with doping control. These attributes remove the two primary challenges or intrinsic limitations for down scaling conventional FETs to the quantum regime [199], and they offer the potential for reduced fabrication costs. While a LET's most basic application emulates a FET when it operates under single beam illumination (as in a photo-detector), it offers functions not readily achievable by either a FET [200] or a photo-detector [108, 201], when it operates differently than a typical photo-detector (e.g., when responding to multiple independent light beams).

Light–induced electrical conductivity changes are a well–known phenomenon typically used for photo–detection. In fact, SNW devices structurally similar to our LET have been investigated as photo-detectors [108, 201]. At first glance, it may appear that a LET simply employs a photo–detector's switching function to emulate a

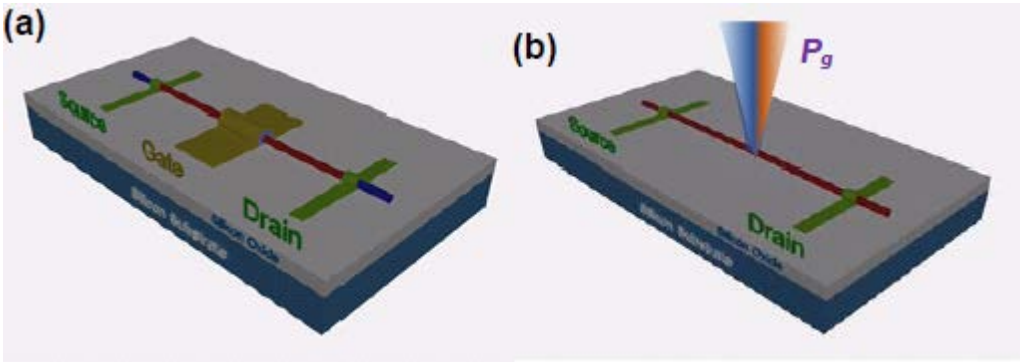

Figure 4.1 Schematic comparison between a semiconductor–nanowire–based (SNW-based) field–effect transistor (FET) and a light–effect transistor (LET). **(a)** A FET is a three terminal device where the source–drain, *S–D*, current, is driven by an *S–D* voltage and may be modulated through a gate (*G*) voltage applied through its *G* contact. **(b)** A LET is a two terminal device where the *S–D* current is modulated with one or multiple independently controlled light beams fused together through an optical combiner. Color codes are SNWs in red, *S* and *D contact in green*, *G* contact in yellow, and the gate dielectric (under the *G* contact) in blueish–gray. The blue–colored SNW tips past the *S* and *D* contacts indicate different FET doping types along the conducting SNW channel. It is assumed that these devices are resting upon an insulating substrate.

FET. In reality, most photo–detectors lack desirable FET-like characteristics and are therefore unsuitable for LET use. It is therefore important to understand the differences between a photo–detector, LET, and FET to appreciate the LET's novelty. Photo–detection typically relies upon a p–n–junction–based device, because it usually offers superior performance over a simpler M–S–M device based on the photoconductive mechanism. This arises from the M–S–M structure typically requiring a larger bias to drive carriers through the *S* region [195, 198]. Note that a p–n–junction–based photo–detector has a distinctly different I–V characteristic under illumination than a photoconductive-based one, and only the latter can offer a light I–V resembling that of a FET with gate voltage on. The photoconductive mode's disadvantage is eased through reduced device dimensions, as demonstrated by SNW–based photo–detectors [108, 201], and the LET application in this work. Its structural simplicity should provide further advantages at the genuine nanoscale. We note that photo–detector structures that are difficult to dope may also employ an M–S–M structure [195, 198]. Therefore,

a LET does not employ a new device structure or mechanism. Its novelty stems from its stringent electrical and optical characteristics that can (1) replicate the basic switching function of the modern FET with competitive (and potentially improved) characteristics, and (2) enable new functionalities not available in modern FETs nor offered by conventional photo–detectors. While under single–beam illumination, a LET yields a high on/off ratio under optical gating, which resembles a FET under gate–voltage control or a photo–detector with high photoconductive gain. Despite this similarity, a LET should be characterized with a pertinent FET parameter known as "subthreshold swing," which measures how much gate action is required to turn the device on, and is normally not of interest in photo–detection applications. Under simultaneous multi–beam illumination, which is usually irrelevant for photo–detection, the multiple independent gating capability enables a LET to demonstrate previously unreported functions, such as optical logic (*AND* and *OR*) gates and optical amplification as an analog application. In contrast, multiple independent gating has been a very challenging task for FETs [8]. These unique functionalities are of great interest for optical computing and novel optical detectors. To summarize, LET novelty, in comparison to photo-detectors, is two–fold. First, LETs are characterized electrically in a very different manner than photo–detectors, as photo–detectors are not typically explored for the electronic functions found in a FET. Second, LETs utilize their multi-beam response while a photo–detector does not. In comparison to FETs, a LET's gating mechanism is distinctly different from a FET's, which easily enables a LET's multi–gate capability, and allows a LET to offer functions beyond those in a typical FET. Furthermore, a LET's frequency response or switching speed is limited by the carrier transit time through its conducting channel. While this effect is shared with a FET, a

FET's response is limited by its gate capacitance.

In this chapter, CdSe SNWs [95, 143] are employed to demonstrate the LET concept and functions (Appendix II contains additional information). First, the material and devices are characterized. Then, single–beam optical gating effects are explored with different wavelengths and laser powers, e.g., $P_g(\lambda_g)$, which are manifested in both *output characteristic* (I_{ds}–V_{ds}) and *transfer characteristic* (I_d–P_g). Finally, LET operation is demonstrated by applying multiple independent beams to demonstrate novel device functions, which are not achievable in conventional FETs, such as, optical logic gates and optical amplification.

4.2 Nanowire and Device Characterization

Figure 4.2 provides material and device characteristics. Figure 4.2A displays an SEM image of a 10–μm–long, CdSe SNW (device 1 or D1) with indium (In) contacts forming M–S junctions at each end. The uniform single-crystalline CdSe SNW was grown in wurtzite phase along the [0001] axis with a diameter of ~80 nm, as revealed by the low magnification transmission electron microscopy (TEM) image in Figure 4.2B, with the selected area diffraction pattern (SADP) as inset, and Figure 4.2C's high–resolution TEM (HRTEM) image showing a 0.69 nm inter-planar spacing. The gold catalyst at the SNW end (Figure 4.2B) suggests the vapor–liquid–solid growth mechanism [202]. The CdSe–SNW's laser–power–dependent photoluminescence (PL), Figure 4.2D, shows a strong emission peak at 1.78 eV that matches CdSe's bandgap energy [103]. The inset overlays a PL map upon an optical image to demonstrate relatively homogenous SNW emission, and by extension, homogenous material quality across the SNW channel. In Figure 4.2E, the output characteristic, *S–D* current I_{ds} vs. *S–D* voltage V_{ds}, is demonstrated for the device with and without light illumination

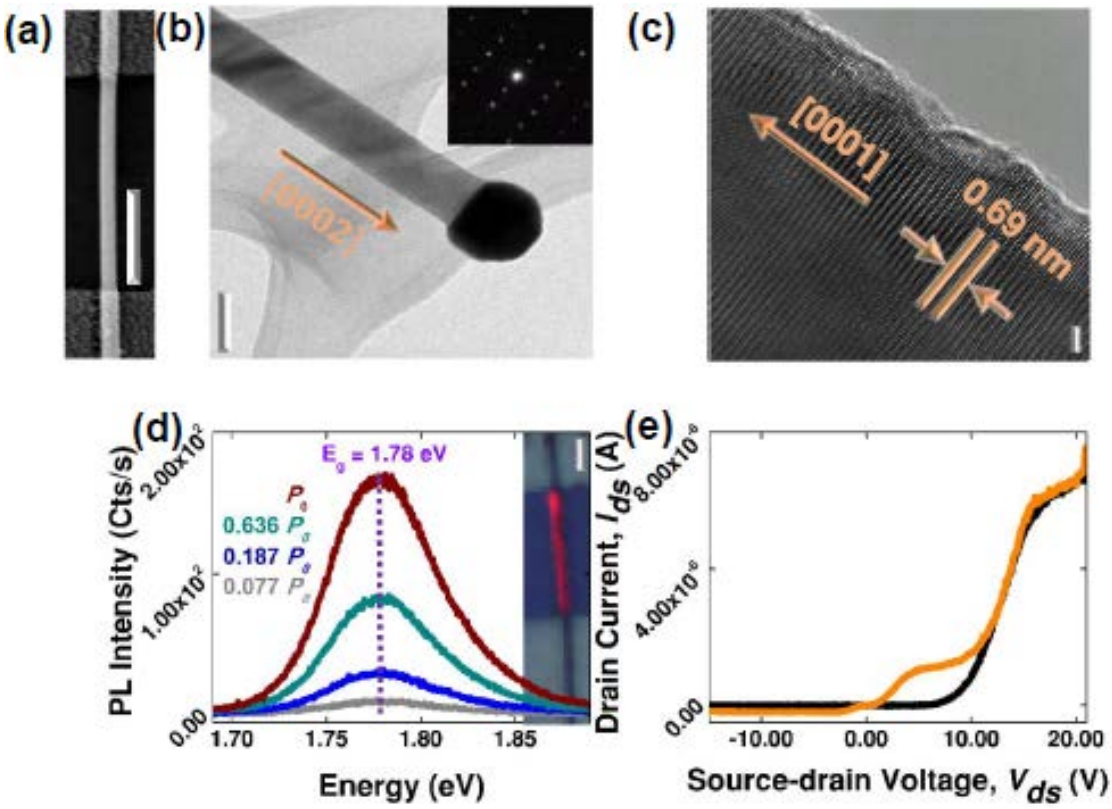

Figure 4.2 LET characterization. **(a)** SEM image of a typical In–CdSe–In device (2 µm scale bar). **(b)** TEM (100 nm scale bar) with SAED inset, and **(c)** HRTEM image (2 nm scale bar) of a representative CdSe nanowire. The TEM results indicate single crystalline CdSe with well-ordered lattice plane spacing of 0.69 nm along the [0001] growth direction. **(d)** PL spectra obtained under 442 nm excitation at different powers (P_0 = 1.5 µW). Inset contains PL map overlaid upon an optical image of D1 (4 µm scale bar). (E) Source–drain current, I_{ds}, as a function of source–drain voltage, V_{ds}, under dark (black line) and halogen light illumination (orange line) conditions.

using a halogen light, where illumination optically modulates or "gates" the electrical conductivity between dark ("off") and illuminated ("on") states. The I_{ds} *vs.* V_{ds} curves for these two states clearly resembles those of a FET's off and on states [198], respectively, especially when V_{ds} < ~7 V.

4.3 Output and Transfer Characteristic

Results for two devices, device 1 (D1) and device 2 (D2) with lengths of ~10 and ~5.5 µm and similar diameters (~80 nm), are presented to illustrate general LET properties, and to demonstrate the potential for characteristic tuning and optimization. The two devices were fabricated in essentially the same way.

Device dark currents reveal negligible reverse bias current and rectification (diode-like behavior) under forward bias, e.g. Figure 4.2E. LET operation occurs under forward bias for both devices. Rectification is indicative of asymmetric In/CdSe contacts for both devices, where one M–S junction is close to ohmic and the other forms a Schottky contact [203]; large asymmetric contacts are desired as they drastically reduce the dark current or off state and thereby improve the on/off ratio. The Schottky barrier largely determines the turn–on voltage, $V_{D,on}$, which is ~8 V for D1 and > 21 V for D2. For instance, D2 shows nearly resistive behavior up to V_{ds} = 21 V with I_{ds} reaching only ~15 pA, compared to D1's range from ~1 nA to ~4 µA over 1-21 V. The vast difference between the two devices might stem from a thin SeO_x layer ($x = 2–3$) [189] at the In–CdSe interface, although the details require further study. These results hint that dark or off state parameters can be controlled through M–S contact engineering.

Representative LET output characteristics are shown in Figures 4.3A–D for D1 and in Figures 4.3E–F for D2, respectively, to exemplify how LET performance depends on the gate power/wavelength, illumination condition, and device variation. D1 exhibits two well–separated plateaus, respectively, starting at V_{ds} ~ 4–5 V and ~14–18 V depending on the gate wavelength and power. For example, the second plateau's onset is at ~14–15 V for 633 nm illumination but shifts to ~16–18 under 442 nm excitation. Two tunable plateaus can potentially offer two distinct, customizable on states. For D2, the first and second plateau are comparatively not well separated, and both 532 nm and halogen illumination have their first plateau at ~2 V with respective power–dependent, second plateaus at ~6–7.5 V (532 nm) and ~5–5.75 V (halogen). Each plateau appears at respectively lower V_{ds} values than in D1, and because of the

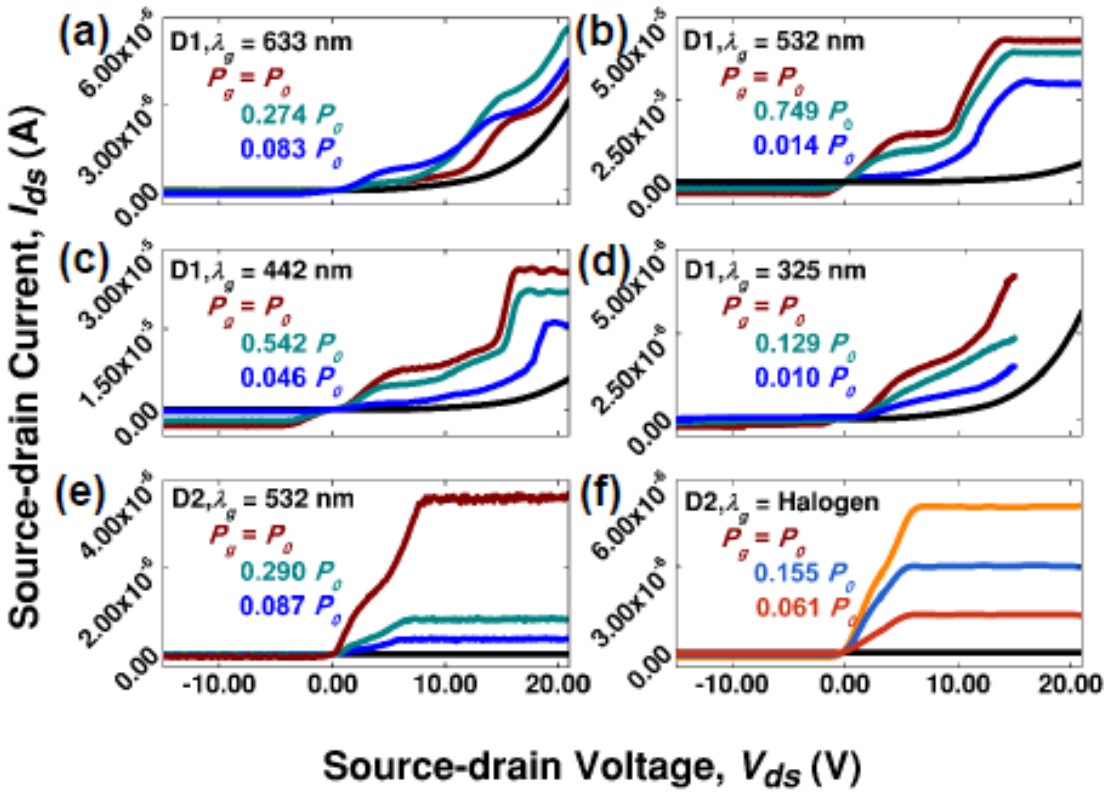

Figure 4.3 LET output characteristics: Source–drain current, I_{ds}, as a function of the applied source–drain voltage, V_{ds} with varying gate power, P_g, and wavelength, λ_g, for two devices (D1 and D2). **(a–d)** are for D1 under 633, 532, 442, and 325 nm illumination with P_0 values of 1.40, 2.07, 2.38, and 2.25 µW respectively, while **(e–f)** are for D2 under 532 nm and halogen excitation with respective P_0 values of 1.38 and 69.1 µW. The dark current is represented as black lines.

extremely low dark current, the long second plateau extends to the highest V_{ds} measured. For D1, the maximum on/off ratios typically occur at V_{ds} < 5 V, and vary from 10^2 to 10^4 depending on the gate power and wavelength. For instance, Figure 4.3B contains on/off ratios of ~5x10^4 and ~2x10^4 at V_{ds} = 1.43 and 4.95 V, respectively, when $P_g(532nm) \approx$ 2 µW. The on/off ratios for D2 in Figure 4.3E are ~1.0x10^6 and ~1.1x10^6 at V_{ds} = 1.43 and 4.95 V when $P_g(532nm) \approx$ 2.6 µW. When $P_g(halogen) \approx$ 69 µW in Figure 4.3F, the on/off ratios are ~6x10^5 and ~1x10^6 at V_{ds} = 1.43 and 4.95 V, respectively.

Differences between D1 and D2 indicate that a LET's characteristics may be tuned and optimized through material and device engineering. A large M–SNW contact barrier is generally desirable for producing small off state currents over the operation range, and can be optimized to maximize the on/off ratio. Note that current levels for different "gate" wavelengths in Figs. 3A–D showed considerable variations, which is fundamentally due to wavelength–dependent, light–matter interaction effects, e.g. absorption and carrier dynamics, and illumination conditions, e.g., power density and beam size. This feature offers the unique LET advantage of flexibility in achieving gate functions compared to FETs.

The transfer characteristics allow extraction of several performance metrics. A FET's threshold gate voltage, V_T, and subthreshold swing, S_{FET}, are respectively defined as the onset of a linear region in the I_{ds}–V_g curve (i.e. voltage-controlled resistor behavior), and as the inverse linear slope on a semi-log I_{ds}–V_g plot [7]. Their physical interpretations, respectively, are the gate voltage required for device operation and the gate voltage increment to induce an order of magnitude current change below V_T. A small S_{FET} value implies a small energy or power consumption to turn on or operate a FET. Figure 4.4 contains D1's and D2's transfer characteristics, which in general, resemble a FET's transfer characteristics, e.g., increasing I_{ds} as the gate power P_g increases under constant V_{ds}, except a LET replaces V_g with P_g. A LET's threshold gate power, P_T , then, corresponds to the onset of a linear I_{ds}–P_g region for a given λ_g, and S_{LET} is its subthreshold swing. Significantly, FETs usually do not operate in the "subthreshold swing" region, while a LET can employ this range to realize optical logic gates and for an interesting optical amplification effect. Taking D2's I_{ds} vs. P_g curves, Figure 4.4E, with λ_g = 532 nm as examples, typical P_T and S_{LET} values at $V_{ds} = 1.43$

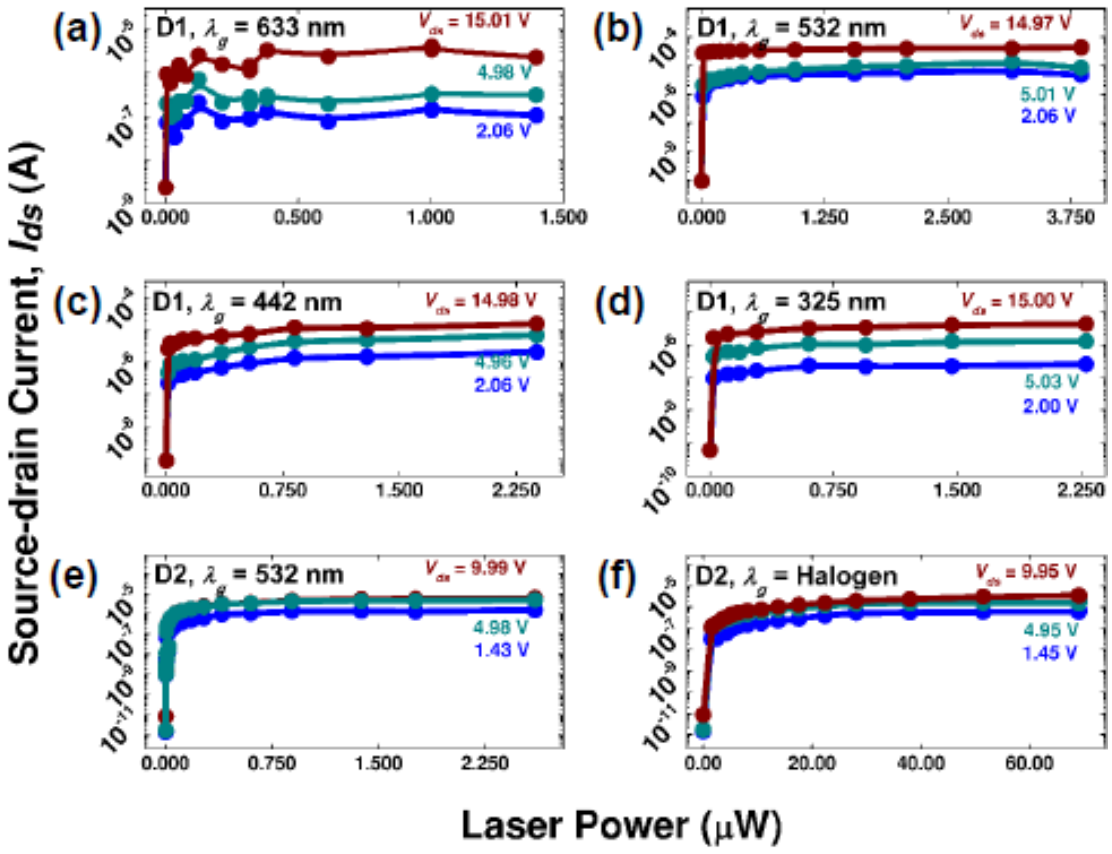

Figure 4.4 LET transfer characteristics: Source–drain current, I_{ds}, as a function of laser power under different source–drain voltages, V_{ds}. **(a-d)** are for device D1, while **(e-f)** are for device D2 using the same conditions as in Figure 4.3.

(4.98) V are, respectively, ~30. (~30.) nW, and ~2.8 (~2.5) nW/decade. For reference, advanced FETs have respective V_T and S parameters of 100–200 mV, and ~70–90 mV/decade [204]. At V_{ds} =1.43 V, P_g = 0.11 μW yields $I_{ds} \approx$ 0.35 μA, and a LET dynamic power consumption of ~0.5 μW, which is comparable to advanced FETs [205]. A LET's off–state energy consumption can be very low. For instance, the dark current is ~1 pA at V_{ds} = 1.43 V with a corresponding off power consumption of ~1.5 pW, which is lower than a FET of similar length [205]. Section 4.6 provides additional comparison and discussion of transistor metrics.

4.4 Application Demonstrations

LET transfer characteristics are used to illustrate the underlying principles for a few important applications. D2's 532 nm illumination characteristics, Figure 4.4E, are re–plotted on a double log scale in Figure 4.5A, with only V_{ds} = 1.43 and 4.98 V shown for clarity, to more clearly portray the three major operating regions: super–linear (dark gray region), linear (medium gray), and sub–linear/saturation (light gray). Different regions can offer different unique applications, as the examples highlighted below.

(1) *AND logic gate and Voltage amplifier:* Figure 4.5B demonstrates single beam illumination as a hybrid *AND* logic gate, which replicates the most basic FET logic function [198, 206], using electrical input A = V_{ds} and optical input B = P_g with output denoted as *AxB*. This is achieved when V_{ds} = 5V and P_g is modulated between 0 and 2.60 μW. One–beam operation could also act as a current source or voltage amplifier when operating in the output characteristic's saturation region, or even when utilizing a LET's two distinct on states (e.g. the first and second plateaus in Figure 4.3B) to realize two–level logic gate and voltage amplifier functions. Furthermore, two LET devices may be combined in parallel or series to respectively create universal *NOR* and *NAND* logic gates, as shown in Figure AIII.1 with their corresponding truth tables.

(2) *Multi–independent–gate capability:* An important LET advantage is multi–independent–gate operation, where optical gates do not increase device dimensions. As an example, two–beam operation is demonstrated with independently controlled uniform illumination with halogen light and focused illumination from a 532 nm laser, denoted as P_{g1} and P_{g2} respectively. Illumination by either individual light beam produces its corresponding transfer characteristics, e.g. I_{ds} *vs.* P_g in Figure 4.4, while

two–beam illumination results in a 3D I_{ds} vs. (P_{g1},P_{g2}) plot (Figure AIII.2A). However, the two–beam response fundamentally reflects the linearity of the single–gate response shown in Figure 4.5A. To more clearly show this effect, a current enhancement factor R is introduced by converting $I_{ds}(P_{g1},P_{g2})$ to $R(P_{g1},P_{g2})$, where $R = I_{ds}(P_{g1},P_{g2}) /[I_{ds}(P_{g1}) + I_{ds}(P_{g2})]$. Figure AIII.1A's data were converted with this definition and the corresponding R values are displayed in Figure 4.5C's contour plot. Using the LET response characteristics in Figure 4.5A and Figure 4.5C, we demonstrate a few distinctly different LET functions that are not readily achievable using a FET, and can be realized with a single LET device. Figures 4.5D–G demonstrate dual–gate applications in three important $R(P_{g1},P_{g2})$ regions illustrated in Figure 4.5C. Additionally, the nonlinear response under 633 nm is also extended to two beam illumination with the addition of halogen light (Figure AIII.3).

(2a) *Optical amplification:* This occurs in Figure 4.5A's super–linear or subthreshold swing region and yields a region where $R >> 1$, for instance, $R \approx 9–11$ in Figure 4.5C. Figure 4.5D yields single–beam–induced currents of $I_{ds,\ 532nm} \approx 11$ nA (dark cyan line) and $I_{ds,\ halogen} \approx 37$ nA (orange line), while simultaneous illumination produced ~11 times their sum with a $I_{ds,\ 2beam} \approx 525$ nA (royal blue line). If the laser beam is viewed as a weak optical signal to be measured, and the halogen light (~1.6 μW) as a gate signal, an amplification factor of $m \approx 48$ is obtained. Optically–induced amplification of a LET's electronic signal replicates three–terminal photo–transistor function, e.g. a bipolar transistor with a semi–transparent electrode [207], where a small base–emitter bias leads to photo–current amplification. This feature may find broad application in weak optical signal detection.

(2b) *Optical AND logic gate*: Results shown in Figure 4.5D can also be used for important optical logic operations, such as that in Figure 4.5E. Two individually applied optical gates, with inputs of *A* and *B* respectively, produce two low current or off states represented as *(1,0)* or *(0,1)* in addition to the *(0,0)* off state (not shown for clarity). Only under simultaneous illumination does output *C* produce the on or *(1,1)* state. LET–enabled optical logic operations could lead to new optical or quantum computing approaches [208].

(2c) *Optical summation*: Sum operations can be realized in Figure 4.5C's linear response region, e.g. R = 1, as illustrated in Figure 4.5F. In this figure, $P_{g1,532nm}$ and $P_{g1,halogen}$ generate two independent signals of 2.00 and 0.32 μA, while simultaneous illumination produces a current of 2.43 μA, approximately their numerical sum. This region is convenient for producing multiple states, such as for memory devices.

(2d) *Optical OR logic gate:* Current saturation is achieved when R = ½, and can function as an optical *OR* logic gate, Figure 4.5G. When $A = P_{g1}(532nm)$ = 0.63 μW and $B = P_{g2}(halogen)$ = 69.1 μW, individual illumination as *(1,0)* and *(0,1)* states or dual illumination as the *(1,1)* state all produce comparable I_{ds} values; all three on states contrast the off state with pA–level I_{ds} denoted as *(0,0)* (not shown for clarity). A single LET could perform more complex logic functions concurrently by combining V_{ds} control with dual optical gate ability, such as a three–terminal *AND* gate with output *AxBxC*, or with simultaneous *AND* and *OR* gates with *Ax(B+C)* output. Truth tables for these logic operations and their proposed symbols are provided in Appendix III (Figure AIII.4). It is significant that a single LET can realize complex logic functions that typically require multiple FETs, but could require fewer devices to perform identical or enhanced functionality. Thus LETs offer an additional pathway for achieving high

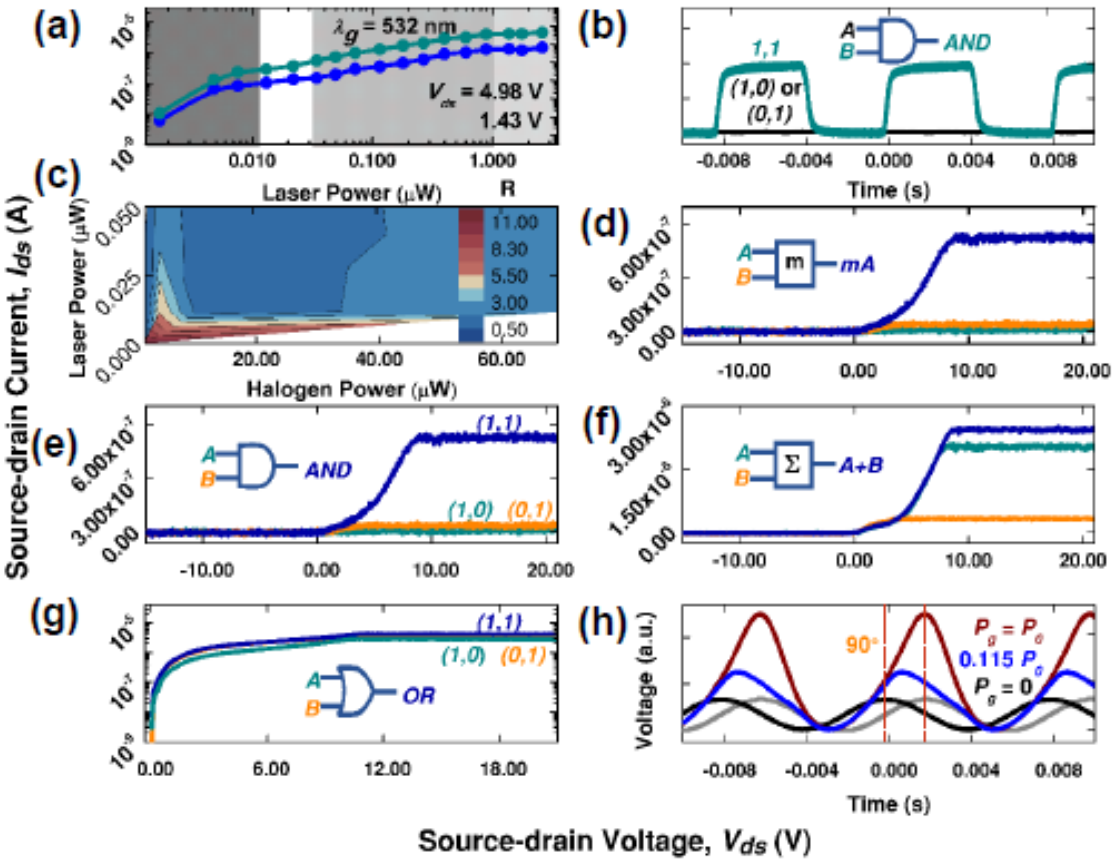

Figure 4.5 Selected LET functionality demonstrations using D2. The axes are source–drain current, I_{ds}, vs. source–drain voltage, V_{ds}, except where noted otherwise. **(a)** Log–log plot of I_{ds} vs. P_g curves under 532 nm excitation with V_{ds} values of 1.43 and 4.98 V, where the three shaded areas are visual guides for distinguishing the super–linear (dark gray), linear (medium gray), and saturation (light gray) regions used to demonstrate LET behaviors and applications in (b–h). **(b)** Optically modulated *AND* logic gate where A= V_{ds} (5.00 V) and B=modulated P_g*(532nm)* (up to 2.60 μW in amplitude). Dark line: V_{ds} = 5 V and P_g = 0; green line: V_{ds} = 5 V and P_g is modulated. **(c)** Various operation regions, according to ratio R (see text for definition), achievable with two-beam illumination under a fixed V_{ds} of 5.0 V. **(d)** A typical R >> 1 operation point, with P_{g1}*(532nm)* = 2 nW and P_{g2}*(halogen)* = 1.57 μW, used as a demonstration of optical amplification; and **(e)** contains the same data as (d) but used as a demonstration of an optical AND gate instead. **(f)** A typical $R \approx 1$ operation point, with P_{g1}*(532nm)* = 0.63 μW and P_{g2}*(halogen)* = 0.7 μW, used as a demonstration of summation operation. **(g)** A typical $R \approx ½$ operation point, with P_{g1}*(532nm)* = 0.63 μW and P_{g2}*(halogen)* = 69.1 μW, used as an optical *OR* logic gate. **(h)** LET operation under electrical modulation of V_{ds}*(t)*, while varying P_g (P_0 = 2.60 μW). The outputs I_{ds}*(t)* were measured through a sampling resistor. The input is shown in gray (normalized to the black P_g = 0 output curve).

device densities on a single chip.

(3) *Differentiator and Optically gated phase tuner*: Complementary to the above mentioned functions, LETs can also be used as a differentiator under zero or low P_g, and as a phase tuner as P_g is increased. Figure 4.5H shows the $I_{ds}(t)$ vs. $V_{ds}(t)$ curves for different P_g values, where $V_{ds}(t)$ is a sine wave modulation with an amplitude of 5.0 V and a DC offset to remove the negative portion. The $I_{ds}(t)$ curve exhibits a 90° phase delay with respect to $V_{ds}(t)$ when $P_g = 0$, which indicates that the device functions as a differentiator by converting a sine wave into a cosine wave; increasing P_g results in a tunable phase shift that gradually approaches zero, e.g. at $P_g = 2.6$ μW. This effect can be understood as changing the LET's impedance by varying the gate power.

4.5 LET Operation Mechanism

The I_{ds}–V_{ds} curves in Figure 4.3 may be understood qualitatively with the photo–conductivity model proposed by Mott and Gurney [195]. The first plateau could be associated with the "primary photoconductivity" which produces current as a result of photo–generated electrons and holes flowing through the nanowire under applied bias. A steady state condition is formed when just enough external carriers entering the nanowire through the electrodes replenish those leaving the device. Under single point illumination and uniform illumination, the collection efficiency, Ψ, is approximately described by Equations 3.14 and 3.15 respectively. It is worth restating that this theory suggests a continuous photocurrent increase from $V_{ds} = 0$ until saturation at a sufficiently large V_{ds} to produce $w >> L$ and $\Psi \rightarrow 0.5$ (see Figure 3.5 for simulated Ψ vs. V_{ds} curves). If all photons are absorbed, the sum of the collection efficiencies of both electrons and holes will yield a quantum efficiency, η_{QE}, defined as $I_{ph}/(eN_{ph})$, where I_{ph} is the photo-induced current, and N_{ph} is the number of absorbed photons. When current saturation occurs, $\eta_{QE} = 100\%$. For instance, absorbing 2 μW of 620 nm

light with η_{QE} = 100% yields a 1 μA current. As V_{ds} approaches $V_{D,on}$, a major Schottky barrier reduction [203, 209] allows excess carriers to enter the nanowire through the electrodes, which then produce a drastic I_{ds} increase that allows $\eta_{QE} >> 1$. The detailed operation mechanism is likely much more complex than that described by the simple photoconductive mode, and deserves further investigation.

Significantly, the collection efficiency is expected to improve drastically at low V_{ds} with nanometer–length devices (Figure 3.5), which should further reduce the static power consumption and provide lower V_{ds} than those demonstrated here. The maximum applied laser power is about 3 μW and corresponds to a power density of ~0.60 W/mm^2, which is less than that delivered by an efficient light–emitting diode [210]. The gate power actually used is only about 10% of the applied power because the laser spot size is considerably larger than the nanowire diameter (see Appendix III for energy loss estimates). Reducing the beam size closer to the SNW's diameter could reduce P_g by at least a factor of 10 [211], and as is well established in FET devices, reducing the channel length can further reduce the required V_{ds} (Figure AIII.5). Enhanced efficiency and reduced energy consumption could significantly reduce thermal issues plaguing nanoscale FET-containing electronics devices. We note that FETs possess a thermal dynamic limit of $S_{LET} \geq$ (kT/q) ln(10) = 60 mV/decade at 300 K, whereas for LET, S_{LET} is extrinsic in nature through w's dependence on the carrier density, which in turn depends on the defect density. Thus, S_{LET} can be significantly improved by shortening the conduction channel, perfecting the material quality, and by choosing materials with strong absorption.

4.6 Pathways to Further Miniaturization and Integration

A LET's structural simplicity removes potential obstacles that FETs face for further down scaling. A LET shares the same limit of a FET, that is, the nanostructure dimensions practically achievable, e.g. 1–7 nm for Si nanowires [51], but LETs do not require complex and sophisticated fabrication steps for physical gates and doping. In general, ballistic transport theory suggests that commercially viable currents could be achieved in quantum structures [212]. Quantum conductance, which limits 1–D ballistic transport, is given by $G = nG_0$, where $G_0 = 2e^2/h$ is the minimum conductance and n are integers representing quantized energy levels. This equation [213] yields a maximum quantum impedance for the conducting channel of $Z_0 = 1/ G_0 = 12.9$ kΩ. The on-state energy consumption could be as low as ~13 nW/LET when $I_{ds} = 1$ μA, and the required minimal V_{ds} would only be 13 mV (not including the voltage drop over the M–S junctions). Given the highly localized nature of the 1–D energy density of states, LET conductivity is expected to be quantized, and thus, tunable using different photon energies.

Industry may employ at least two basic illumination modes in an integrated LET circuit depending on the application: (1) uniform, broad–area illumination over a high–density, LET array with SNWs, or (2) separated light beams directed to individual or small groups of LETs through, for instance, sharp fiber tips or nanoscale emitters embedded on the same chip. For either mode, multiple light sources of the same or different wavelength(s) and/or intensities can be combined into one beam but controlled independently. Because so little light is actually absorbed by nanostructure–based devices, as will be discussed in the next section, engineering enhanced optical absorption is important for developing next generation electronic–optical devices.

4.7 Major Electrical Advances and Novel Functionality

A LET's contribution is two–fold: it not only represents a major electrical advance for application of the photo–conductive phenomenon to an electronics device, but it also offers functionality not available in either FETs or photo–detectors. The former is highlighted through direct comparison of LET with FET and photo–detector performance metrics in Table 4.1. Photo–detector architectures can employ an M–S–M structure, which possess a large dark current typically on the order of 100 nA [214, 215]. For example, an on/off ratio of 10^4 would require high current (1 mA) and illumination power (2 mW) [215]. As a result, photo–detectors are typically explored only in the linear responsivity regime rather than as a transistor, and thus, threshold power and subthreshold swing parameters are not applicable to these devices. While, at first glance, all LETs may appear to function as photo–detectors, the differences between photo–detector and LET dark currents manifest themselves through drastic differences in electrical performance. For example, an n–type, GaAs:Fe photo–detector with M–S–M architecture requires 2 mW of optical power to produce an on/off ratio of ~10^4, while in comparison, a LET (D2) only required 30 nW of applied power or ~3 nW of absorbed power to produce an on/off ratio of $6x10^5$–$1.1x10^6$ at V_{ds} = 1.43 (4.98)

Table 4.1 Comparison of important transistor metrics between photo–detectors [215, 216], LETs [182], and advanced FETs [26, 204]. LET values were obtained from D2 using $P_g(532nm)$ = 1.28 μW and V_{ds} = 1.43 (4.98) V. For LETs, the upper value is for the "applied power," while the lower value, or the actually absorbed power, is estimated in Appendix III. FET subthreshold swings, *S*, are the theoretical limits for conventional and FinFET devices respectively.

Parameter	Photo–detector	LET	FET
on/off ratio	~10^4	~10^5–10^6	~10^6
V_t/P_t	NA	30. (30.) nW (applied) ~3 nW (actual)	100–200 mV
S	NA	2.8 (2.5) nW/decade ~0.3 nW/decade	~70–90 mV/decade (limits)

V. Appendix III provides additional details and parameters for these estimates, and for convenience, Table 4.1 reproduces the previously stated FET parameters.

Comparing switch energies or the amount of energy needed to perform a switching event is another important metric. In this case, carriers are being switched between insulating off states and conductive on states through either electrostatic or photo–conductive gating in FETs and LETs respectively. The measurement system prevented a direct measurement of the switching time, although it may be reasoned that LETs can have lower switching energies than modern FETs. Most direct band gap semiconductors possess room temperature carrier lifetimes on the order of 100 ps without an applied bias e.g., Ref. [217], where applying a bias, especially for a short conducting channel length, reduces the transit time by more quickly wiping out free carriers. CdSe has a maximum or saturation velocity similar to gallium arsenide (approximately $2x10^7$ cm/s [218]) which is a factor of 5 smaller than graphene. Graphene, however, does not possess a bandgap and cannot be turned off. The potential to operate as low as 13.5 mV/LET (see Appendix III) with picosecond times scales suggest that semiconductor–based, M–S–M, LET technology could function as a "millivolt switch" [219] with a THz (10^{12}) clock frequency that is more than 100 times faster than the current technology [219]. More impressively, estimates based upon D2's performance suggest this function could be implemented with lower total switch energies, by up to 4–5 orders of magnitude, than found in advanced FETs.

The fraction of laser power actually absorbed by a nanostructure is estimated through the ratio of nanowire diameter to the light's spot size (or projected area). In the case of an optical microscope, the spot size is estimated by the optical diffraction limit of $1.22\lambda/N.A.$, where λ is the excitation wavelength and *N.A.* is the numerical aperture

of the microscope's objective lens. As a numerical example, a 50x long working distance (LWD) objective lens (*N.A.* = 0.55) has an area of ~279 μm^2 (although a laser may only illuminate a much smaller area), while a CdSe nanowire with an 80 nm diameter and 10 μm length has an aspect ratio (width/length) of ~0.008. Illumination under 632.8, 532.0, and 441.6 nm results in actual power absorption estimates of 5.18, 6.16, and 7.43% respectively. For 441.6 nm light, this implies that a nanowire could absorb only 74.3 nW from an "applied power" of 1.00 μW; this estimate ignores potential reflection from transparent oxide layers on a thick substrate (e.g., ~300 thick SiO_2 on Si). Accounting for a laser's Gaussian intensity distribution, rather than assuming a uniform distribution, would further reduce these values.

Table 4.2 compares the switch energy from optical action, which only applies to photo–detectors and LETs, and the electrical contribution – assumptions and parameters are discussed in Appendix III. A photo–detector's large dark current makes it an impractical transistor requiring a large total switch energy of 70. fJ/switch to produce a low on/off ratio. They cannot compete with advanced FETs capable of delivering a 10^6 on/off ratio with total switch energies ranging from 0.1 to 1.0 fJ/switch [26]. A LET's (D2's) pico–amp–level dark current yielded up to a 10^6 on/off ratio while only requiring 0.061 fJ/switch or 61 aJ/switch (atto = 10^{-18}). It is remarkable that the unoptimized LET devices explored here produced comparable metrics to advanced FETs while requiring far less energy. The vast majority of the total switch energy in D2 stems from the electrical action, which can be reduced through device optimization, such as by further reducing the channel length and optimizing the contacts. When considering a LET's potential, it is useful to consider two cases. The first uses quantum conductance theory, while the second is based upon optical efficiency and represents

Table 4.2 (Total) switch energy comparison from optical and electrical action are provided for photo–detectors (with M–S–M architecture), advanced FETs, and LETs. Assumptions and parameters are discussed in Appendix III.

Parameter	Photo–detector	LET	FET
on/off ratio	~10^4	~10^5–10^6	~10^6
V_t/P_t	NA	30. (30.) nW (applied) ~3 nW (actual)	100–200 mV
S	NA	2.8 (2.5) nW/decade ~0.3 nW/decade	~70–90 mV/decade (limits)

the lower limit. Quantum conductance theory from the previous section suggests that a LET could be operate with as little as 2.6 aJ/switch using readily available fabrication technologies. In considering the lower limit, one could imagine optically gating a ribbon–like structure with (x,y,z) dimensions of (20nm, 2 nm, 10 nm). The assumptions from Chapter 1 yield δE_L = 2.30 zJ (zepto = 10^{-21}), which when combined with the electrical action given by $\delta E_{ds} = I_{ds}^2 Z_0 \tau$ = 0.13 zJ, produces a total switch energy of 2.43 zJ. This represents 6–7 orders of magnitude improvement over that offered by advanced FET technologies, but further advances could be made. A value of G = 1,000 was obtained from D2 (Figure AIII.7), but it is likely that an optimized device could yield an even higher gain. As the gain increases, the total switch energy will continue to decrease ($P_L \propto E_{ph}/G$). It is also useful to note that the optical source will also alter the total switch energy through η, which is dependent upon CdSe's wavelength–dependent, absorption coefficient.

A LET also offers functions not readily achievable by either a FET [200] or a photo–detector [108, 201] when it operates differently than a typical photo–detector (e.g., when responding to multiple independent light beams). Example applications were presented in Section 4.3. The addition of multiple optical beams is a significant advancement because LETs easily achieve multi–gate capability that has been difficult for FETs to achieve. Although additional optical gates do not consume valuable chip

real estate, further research is required to implement them onto a chip. Chapter 1 provided three possible scenarios: an a–NSOM array, matching nanoscale emitters, and modification of holographic optical interconnect technology. The potential of the LET platform make these endeavors worth pursuing. As a final note, a CdSe/ZnTe structure may further improve LET performance while lowering the total switch energy. Ref. [143] demonstrated enhanced photo–currents for CdSe/ZnTe nanowire arrays, while Figure 8.2 clearly show minute dark current changes. This suggests that a CdSe/ZnTe–based LET could be capable to achieving on/off ratios far greater than 10^6, while the associated increase in gain would further reduce the total switch energy.

4.8 Conclusions

The LET concept presents a drastically different approach for FET–based IC technologies by using an all optical, rather than a physical gate mechanism. A LET explores the well–known photoconductivity attribute of a semiconductor that is naturally and commonly used for photo–detection. Digital and analog applications are demonstrated, which are typically only achievable with transistors, and provides functions that FETs cannot achieve. Most significantly, the LET gate function can provide much greater flexibility than a FET, including tunable gate properties and multiple independent gates. Notably, a LET can continue Moore's law without the FET complications and limitations associated with gate fabrication and doping control through: (1) a simple device architecture to potentially reduce fabrication costs; (2) feasible down scaling to the quantum level; (3) efficient, multi-functional ability in a single device; and (4) operation at low energy consumption, which negate thermal issues plaguing nanoscale electronics devices. The general LET operation principle is independent of a particular material system, thus, when applied to silicon, the existing

silicon–based, microelectronic and photonic technologies can be readily adopted by LET technology. The LET concept can also be extended to develop other light–effect devices.

CHAPTER 5: ELECTRON–PHONON COUPLING IN MULTIDIMENSIONAL ZnTe SYSTEMS

"The most exciting phrase to hear in science, the one that heralds new discoveries, is not 'Eureka!' (I found it!) but 'That's funny …'."
Isaac Asimov, 1992 Attribution in *UNIX "Fortune" software*

5.1 Introduction

The first and most important step is to address the common misperception that EPC is purely an intrinsic material property [220] – what I call the intrinsic mantra – despite the long known extrinsic effects of impurities in semiconductors [134, 221-223], and thermal heating in molecules [224-227]. Extrinsic effects, such as the presence of Te–based surface aggregates on ZnTe nanowires [142], are typically excluded during analysis of EPC. Logically, impurities modify the electronic spectrum by altering the potential experienced by a free electron traversing a crystal lattice, which also changes the force constants within the Hookean framework used to derive phonon dispersion curves. The EPC "strength" is typically reported in terms of the Huang–Rhys parameter (S), which, like the Hirsch index [228], is a single value composite but related to the dimensionless displacement between ground– and excited–state potential energy minima (Δ). Typically, $S = \Delta^2/2$ (at low temperature) [229]. The Δ term is strongly affected by Fröhlich interactions in polar semiconductors [230], and ultimately arises from lattice perturbations, such as changes in bond distances, bond angles, and interatomic forces that alter coupling and overlap between electronic and vibrational wave functions. Although vibrational states are less sensitive to dimensional change

than the well–known, quantum–confinement–induced, band–gap shifts [231-235], they too should produce dramatically different vibrational spectrums for different lattice and surface conditions [69, 70, 84]. Limited experimental investigations suggest that EPC could be influenced by stoichiometric ratio [236-238], surface and bulk defect concentrations [134, 221, 239], laser power (e.g., photo-generated carrier concentration) [240, 241], thermal/laser heating [224-226, 239, 242-244], geometry or dimension [245], size [246], strain [247-251], polarization [252], and surface modifications and interface additions [253-259]. These many contributing factors suggest that numerous potential methods exist for tailoring EPC–based device behaviors.

Inconsistent optical measurements [136, 260] and contradictory theoretical frameworks [235, 260-267], which are typically verified against experimental results, have only sustained the murkiness enveloping EPC at the nanoscale. The second step is the careful design and systematic experimental investigations into the actual intrinsic, EPC strength, but especially in regards to size dependence. Widely studied CdSe nanocrystals, for example, produced conflicting theoretical and experimental reports of size–dependent [268, 269], inverse size–dependent [258, 270, 271], and size–*in*dependent [262, 272] EPC strengths [136]. Khambhampati *et al.*[269] attributed these conflicting results to using different experimental and theoretical methods to measure and calculate EPC strengths [260, 269]. Theoretical issues are discussed subsequently. Continuous–wave (CW) –based methods, such as resonant Raman spectroscopy (RRS) [116-123], are thought to more accurately resolve longitudinal–optical (LO) phonon modes, which yield slightly larger S values (e.g., the I_{2LO}/I_{1LO} is increased by a few tenths), while femtosecond (fs) –based methods, such as time and frequency domain pump–probe measurements, better resolve high frequency acoustic and intrinsic modes

[136, 260, 273]. The reasoning is that CW–based techniques primarily probe extrinsically photo–generated, charge–trapped excitons, while the shorter time scales involved with fs–based methods exclude this extrinsic effect, and primarily yield information on intrinsic LO phonon modes [260, 274-276]. One may naturally question the plausibility of this statement. It is well–known that laser illumination of intrinsically n–type, CdSe nanowires produces a small hole concentration under the laser beam, while electron populations decreases further away from the illumination site [178]. While exciton concentrations are controllable, to a degree, through laser power, the accumulation of charge–trapped excitons will be minimized at sufficiently low laser powers, and could yield nearly intrinsic values. Meanwhile, both CW– and fs–based techniques likely possess some similarities. For example, heating–induced phonon peak asymmetries could, in principle, alter the EPC strength obtained with either technique [225, 277-282]. Both techniques are also susceptible to laser–induced damage, which is often ignored during EPC strength analysis but it could have an effect. This possibility may be evaluated by assuming that nanowires experience higher excitation densities (due to smaller volumes) and lower thermal conductivities that produce increased laser–induced temperatures, as demonstrated with silicon nanowires [225, 280, 281], which could result in partial phase changes [283]. Logically, laser–induced phase changes should alter the measured EPC strength. It appears that the potential of laser–based methods are greatly underappreciated for their potential to probe extrinsic EPC behavior, such as by varying the laser power. For example, Fröhlich interactions [69, 284] were altered through both temperature, which is controllable through laser power, and different dielectric materials incorporated into an organic–based, field–effect transistor [285]. This also implies that a sufficiently low laser power could

measure (nearly) intrinsic EPC strengths. CW RRS, which is the focus here, is a fast, highly sensitive, and nondestructive technique [286-289] affected by vibrational [290], thermal [291, 292], and carrier [293-295] behaviors, and should therefore be susceptible to influences beyond charge–trapped excitons. This technique could carefully probe a system to provide comprehensive and accurate measurements of both extrinsic and intrinsic EPC contributions at the nanoscale.

Third, a comprehensive, multidimensional study on a prototypical system would provide experimental verification for theoretical approaches. A general lack of consensus manifests itself through either employing very different frameworks, such as the configuration coordinate (CC) and momentum conservation (CM) models [132, 296], or by incorporating different assumptions to describe similar physical systems. Widely studied CdSe quantum–dot models are an excellent example, where the model by: (1) Schmitt–Rink, Miller, and Chemla [264] supports size–dependent EPC behavior by assuming hole localization on each ion while ignoring valence–band mixing; (2) Nomura and Kobayashi [263] accounts for moderate EPC strengths by including valence–band mixing and nonparabolicity but they also employ an independent phonon model; and (3) Klein and group [262] demonstrates size–independence with the common adiabatic approximation. These frameworks are usually validated against experimental data, which, as previously discussed, contains its own set of issues that contributes to these very different theoretical frameworks. All of these models, however, possess inherent deficiencies compared to a first–principles approach, which predicts more realistic electronic and phononic structures along with their coupling [297, 298]. While first–principle methods are readily available [299-304], it has yet to be applied to semiconductor nanostructures, while semiconductor systems

[305-308], in general, have received only infrequent and limited attention. And the existing theoretical EPC investigations are spread across very different material systems, e.g., different doping conditions and geometries, which undoubtedly limits insight into the underlying physical processes and has even contributed to producing contradictory findings. Relative to other compound semiconductors, zinc telluride (ZnTe) systems are ideal for exploring EPC–related phenomenon due to their relatively large *S* parameter [82, 142], which makes measuring EPC strength variations less ambiguous. Several reports exist for ZnTe material systems, and consist of superlattice [309-326], quantum dot/well [242, 326-335], nanowire [142, 336, 337], thin film/epilayer [243, 244, 312, 338-347], and bulk [348-352] structures and heterostructures [353, 354]. The many different conditions further highlights the need for a consistent, multidimensional study on a single material system. Furthermore, ZnTe's diverse optoelectronic applications could potentially enable widespread EPC optimization, such as in core–shell photovoltaic devices [95, 143, 355], lasers [356, 357], light–emitting diodes [358-360], and electro–optic detectors [361] and terahertz emitters [362].

For the first time, CW RRS probes extrinsically tunable EPC in multidimensional ZnTe systems – namely bulk, thin film, and nanowire samples – and (less ambiguously) investigates intrinsic size–dependence in ZnTe nanowires. Bulk, thin film, and nanowire samples are characterized structurally and optically before intrinsic EPC values are determined. Then, EPC is intrinsically altered through different stoichiometric ratios, laser heating and ablation, and surface and interface modifications, while non–ablative laser heating, strain, polarization, and size dependencies had no discernable influence. Laser ablation produced Te–based surface aggregates that tuned

EPC over a factor of 2.4, where the exclusion of this effect likely resulted in a previous report [142] claiming that ZnTe nanowires display size–dependent EPC strengths. Methanol exposure and interface effects, such as an Au–ZnTe junction, altered EPC strengths, and demonstrate the potential for optical bar codes and cross–reactive (e.g., chemical) sensors [363-365] based upon this concept.

5.2 Reducing Dimensionality: Structural and Optical Characterization

While multidimensional ZnTe systems were probed optically, the primary focus of this work is on nanowires, which are characterized in Figure 5.1. The uniform, single–crystalline ZnTe SNW was grown in zinc–blende phase along the [210] axis with a diameter of ~280 nm, as revealed by the low magnification TE image in Figure 5.1A. The SADP as inset and Figure 5.1B's HRTEM image, which displays a 0.35 nm inter–planar spacing, indicate high quality, single crystalline material. Elemental analysis was performed on a similar nanowire with a 500 nm diameter in Figure 5.1C, where elemental maps of Si, Zn, and Te, in Figures 5.1D–F respectively, indicate the presence of ZnTe that distinctly contrasts the underlying silicon (Si) substrate (with an ~300–nm–thick, silicon dioxide layer). The elemental maps were collected with the energy dispersive x–ray capability in a SEM. This same technique was also used to measure the stoichiometric ratios of samples (as shown in Figure 5.3), and has typical uncertainties of ±1-2% (depending upon surface roughness). Samples B2-B4 were sent out for analysis with Rutherford Backscattering Spectrometry (RBG performed at EAG Laboratories). This technique has a 1% uncertainty for Zn and Te and a 0.5% uncertainty for Cd. Samples B2-B3 were found to have 1:1 stoichiometric ratios, which is consistent with dispersive x-ray capabilities. Both techniques yielded a consistent Cd impurity concentration of ~2.5%.

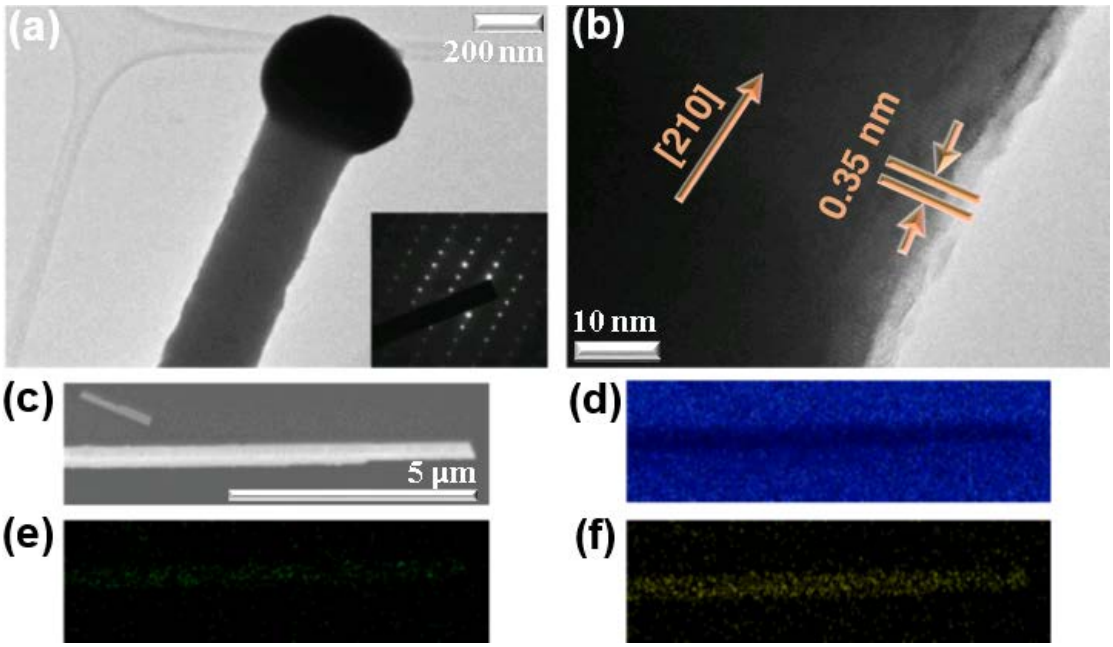

Figure 5.1 Structural characterization of an ~200 nm diameter ZnTe nanowire with TEM and SEM. **(a–b)** TEM image with diffraction pattern as inset. An oxide or amorphous layer is visible on the nanowire's surface. **(c)** SEM image of a different nanowire, and elemental analysis showing **(d–f)** Si (blue), Zn (green), and Te (yellow).

Table 5.1 Bulk ZnTe and thin film sample summary including the Zn/Te ratio measured with energy–dispersive spectroscopy in SEM (SEM) and Rutherford Backscattering Spectrometry (RBG) (obtained from EAG Laboratories for B2-B4 only). Thin film parameters include the FWHM measured with x–ray diffraction, growth/nucleation temperatures.

Sample	Comment	Zn:Te SEM/RBG	FWHM (arcsec)	Nucleation/Growth Temperature (ºC)
B1	Raman Standard	1.0	—	—
B2	ZnTe(100)	0.97/1.0	—	—
B3	ZnTe(100)	0.94/1.0	—	—
B4	ZnTe(110) ~2.4% Cd	0.97/0.95	—	—
TF1	ZT022411N	0.95	72.0	300/280
TF2	ZT022811N	0.96	74.0	300/320
TF3	ZT030211N	0.92	79.0	300/340
TF4	ZT030311N	0.94	86.0	300/360
TF5	ZT030711N	0.94	85.0	300/260
TF6	ZT031611N	0.93	83.0	320/300
TF7	ZT031711N	0.92	83.0	280/300
TF8	ZT031811N	0.93	83.0	340/300

Defects [221, 239] and stoichiometry [237, 238] are known to alter PL and Raman spectra from that of high quality or intrinsic ZnTe. Four (4) bulk, nine (9) thin film, and

many nanowire structures were characterized structurally and optically, but only representative samples are included in this section for visual clarity. These bulk samples are meant to probe stoichiometric differences induced by defects or, for one bulk sample (B4), by cadmium (Cd) impurities. Representative PL and RRS spectra for ZnTe in bulk, thin film, and nanowire forms are plotted in Figures 5.2A–B, 5.2C–D, and 5.2E–F respectively. Samples are summarized in Table 5.1. As the bulk number increases (e.g., B1 to B4), so does the number of defects or impurities, while the thin film spectra are grouped by growth conditions, where either the growth or nucleation temperature was held constant while varying the other temperature. These spectra were collected with 1.62–2.64 μW of 532 nm light, which is far below the typical laser powers employed for ZnTe (e.g., 170 μW for similarly sized ZnTe nanowires), where size–dependent EPC was reported [142]. While, as a general note, the Raman shifts are provided on the figures, Appendix IV contains additional Raman information for the displayed spectra, such as the Raman peak positions, integrated intensities, and the full width at half maximum (FWHM) values. In Figure 5.2, exciton emission at 2.25 eV did not shift appreciably among the different ZnTe systems explored, and the emission intensity was increasingly quenched as dimensionality was reduced. Quenched emission likely stems from reduced optical interaction volumes as dimensions shrink, although defects could play a role in the bulk samples, while strong quantum confinement is unlikely due to relatively weak shifts in the peak energies overall, e.g., < 15 meV, which is especially supported by negligible shifts in peak energies among the nanowires in Figure 3E (with diameters of 84, 223, and 340 nm). The nanowires were measured on a TEM grid to mitigate potential substrate effects. In contrast, the Raman spectra yielded appreciable shifts, which will be discussed subsequently.

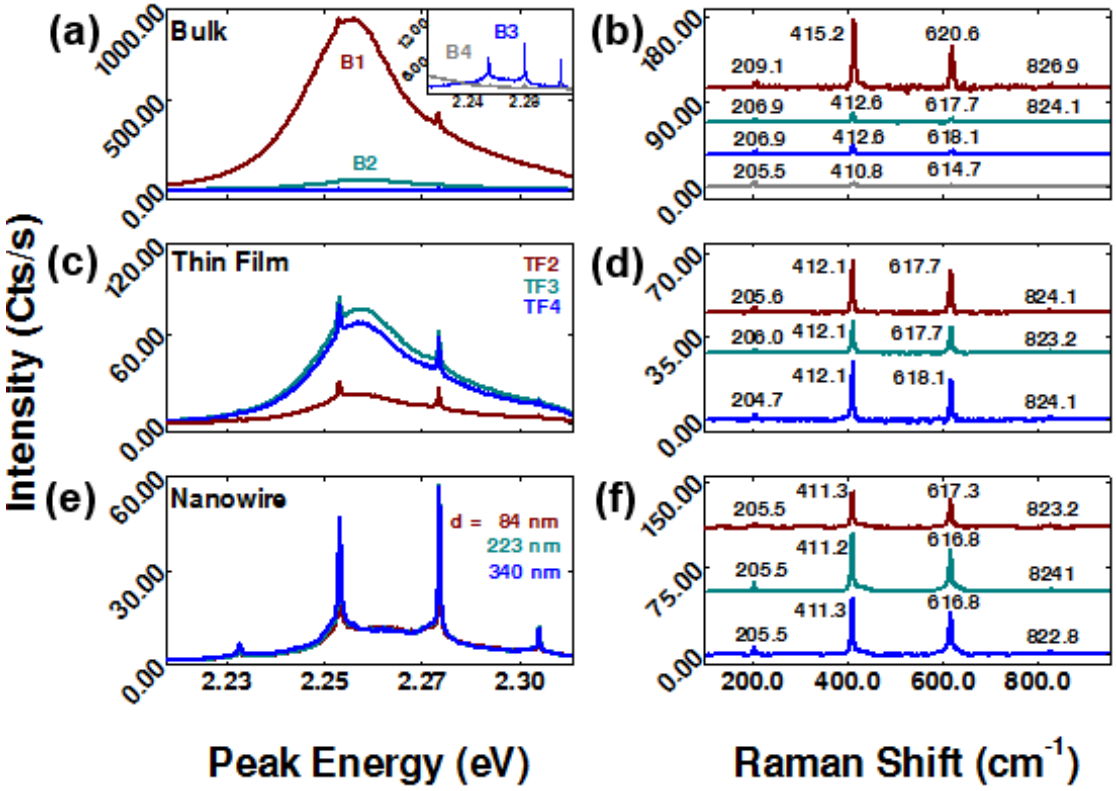

Figure 5.2 PL and Raman characterization of ZnTe in **(a–b)** bulk, **(c–d)** thin film, and **(e–f)** nanowire forms respectively. Bulk and thin film samples are summarized in Table 5.1. The Raman spectra (right column) were obtained by subtracting the PL contribution from spectra in the left column. Spectra were collected with 1.62–2.64 μW of 532 nm light; the nanowires are on a TEM grid.

Generally, the I_{2LO} is dominate followed, in order of decreasing intensity, by the I_{3LO}, I_{1LO}, and I_{4LO} peaks. The exception is the bulk sample with 2.46% Cd impurities, which demonstrates the classic impurity signature [134, 222, 223] with a dominant I_{1LO} with decreasing intensities as follows: I_{2LO}, I_{3LO}, and I_{4LO}. Bulk ZnTe Raman peaks are expected at 205, 410, 615, and 820 cm^{-1} [352]. The bulk Raman spectra in Figure 5.2B demonstrated a Raman shift of the 1LO peak from 209.1 cm^{-1}, for high quality bulk with an ~1:1 Zn:Te ratio (sample B1), to 206.9 cm^{-1} for samples containing bulk defects (B3 with a 0.94:1 Zn:Te ratio), such as substitutional and interstitial defects. Introduction of ~2.5% Cd impurities yielded a 0.97:1 Zn:Te ratio (B4), which further down–shifted the 1LO peak to 205.5 cm^{-1}. Recall that these values are consistent with

the RBS ratios of 1:1 for B1–B3 and 0.95:1 for B4. Similar Raman trends were also observed for the 2–4 LO peaks as observed in Figure 5.2B. The thin film samples altered growth parameters to produce the stoichiometric ratio rather than relying upon defects and impurities alone. Their Raman spectra in Figure 5.3D shows some variation in Raman shift, but a clear trend in a particular direction was not observed. These thin film samples have Zn:Te stoichiometric ratios of 0.95, 0.93(9), and 0.94(4) for TF2, TF3, and TF4 samples respectively. The nanowire spectra in Figure 5.2F also demonstrated mostly negligible Raman shifts. Overall, Figure 5.2 highlights the impact of stoichiometric ratio on Raman peak positions, which ranges from minor for high quality samples (e.g., B1) to drastic for defect and impurity containing samples (e.g., B2–4).

Figure 5.3 plots the I_{2LO}/I_{1LO} as a function of stoichiometric ratio for bulk and thin film samples. The dark cyan and blue circles represent thin films grown while varying the growth and nucleation temperatures respectively (see Table 5.1). Raman spectra were collected on both the front surface and cleave–edge of B1 (B1–FS and B1–CE respectively). The mean values, with error bars represented by the standard deviation from the mean value, decreased in the following order: B1–FS (10.8±2.5) > B1–CE (7.7±0.6) > B2 (3.7± 2.0) > B3 (2.0±0.2) > B4 (0.8±0.5). These are composite values for N = 5 measurements collected at five different sample locations (refer to Appendix IV for averages at individual measurement sites), and therefore represent sample inhomogeneity, such as from spatial variations in defect concentrations. Using B2 as an example, one measurement location generated a low I_{2LO}/I_{1LO} uncertainty (e.g., 2.5±0.1 or 4.0%), while the composite value over five different spatial locations was much larger (3.7± 2.0). For reference, Figure AIV.1A demonstrates an I_{TO}/I_{1LO} of

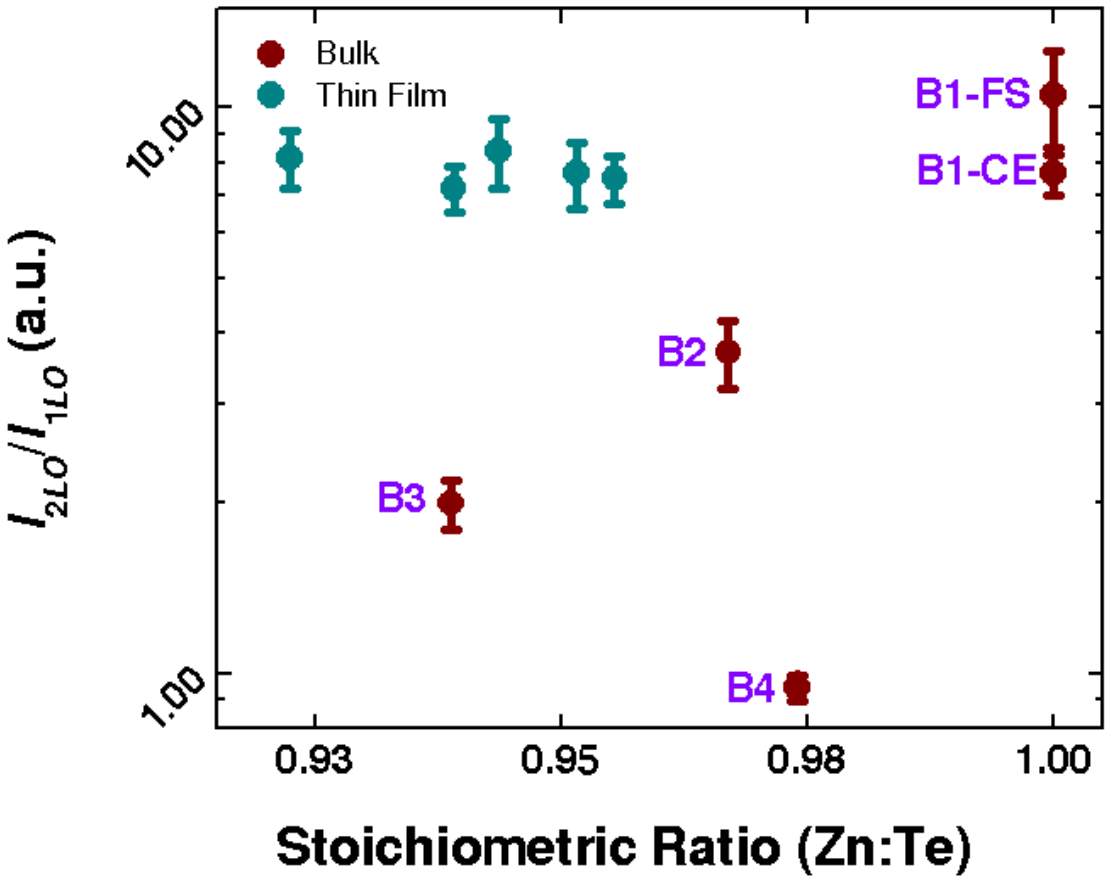

Figure 5.3 Stoichiometric dependence of I_{2LO}/I_{1LO} for bulk ZnTe and ZnTe thin films. For comparison purposes, stoichiometric ratios obtained with x-ray dispersive capabilities are shown. Only thin film samples with varied growth temperature are shown, while those that varied the nucleation temperature produced identical results within the shown error bars. Raman spectra were collected with 1.62–2.64 μW of 532 nm light. The mean values, with error bars represented by the standard deviation from the mean, decreased in the following order: B1–FS (10.8±2.5) > B1–CE (7.7±0.6) > B2 (3.7± 2.0) > B3 (2.0±0.2) > B4 (0.8±0.5). Composite values from N = 5 measurements collected at five different sample locations (see Appendix IV for individual site means and ranges). B1 was obtained from N = 10 measurements at the same measurement location.

1.5±0.05 (N = 30) for a prototypical sample (GaP) under similar conditions. Note that B2's I_{2LO}/I_{1LO} uncertainty at each measurement site is similar to that measured for the prototypical sample. An exception must be noted for B1–FS, where its I_{2LO}/I_{1LO} value was obtained from N = 10 measurements at the same measurement location. The 1LO is expected to be nearly forbidden based on an excitonic theory treating free–exciton–phonon coupling [134] for a perfect crystalline sample, where a small perturbation can

result in a large deviation from the intrinsic value that is very difficult to measure accurately. B1's error bars could reflect this possibility or the effect of the polished front surface, and the difficulty in extracting the peak area of its strongly forbidden 1LO peak (Figure AIV.1B), while B4 highlights the impact of defects and impurities on the integrated peak area ratios (Figure AIV.1C). It is well–known [134] that impurities increase the I_{1LO} at the expense of the I_{2LO}. Figure IV.1C not only demonstrates this point, but its associated table also indicates an impact on higher order ratios. The origin of the large I_{2LO}/I_{1LO} range requires additional investigation with a larger range of defect and impurity types and concentrations, where exploring additional impurity types is important, as other impurities can impact the I_{2LO}/I_{1LO} [366] very differently than for the Cd impurities observed in B4.

The effect of defects in bulk samples suggests that nanowires should be similarly impacted. Figure 5.4 contains PL and Raman spectra for ZnTe nanowires supported by a TEM grid. The shoulder may be from surface optical (SO) phonons [142], although this is beyond the scope of this dissertation. The PL intensity and similarity in Raman shoulders allow differentiation, rather broadly, into groups with similar and different optical characteristics. Figures 5.4A–B reproduces Figures 5.2E–F for convenience. Again, these three nanowires, with diameters of 84, 223, and 340 nm, display similar PL and Raman shapes with negligible Raman shifts. Figures 5.4C–D contain nanowires with similar diameters of 75, 225, and 335 nm, although the 2LO shoulders are very different. The shoulder contribution analysis are a topic of further study (beyond this dissertation). Different SO contributions to the 2LO peak corresponds with appreciable differences in peak position, such as the 1LO of the 75 and 335 nm diameter nanowires being positioned at 206.7 to 207.1 cm^{-1} respectively, and very different coupling

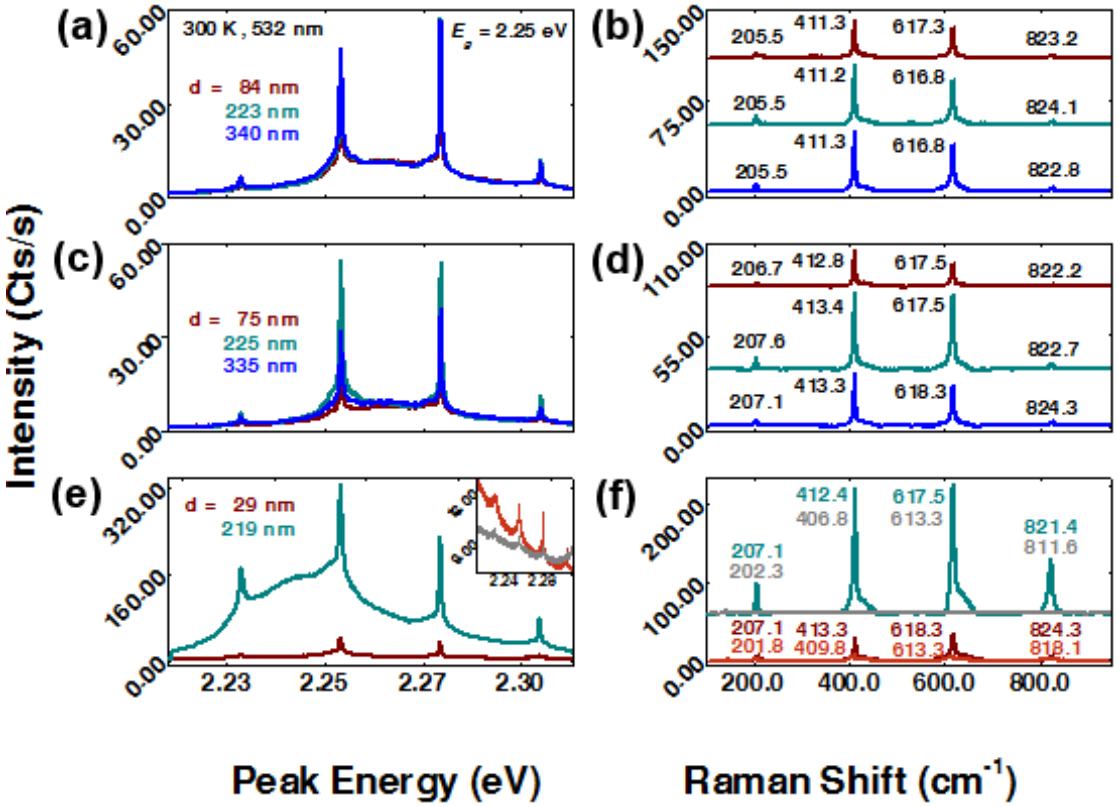

Figure 5.4 PL and Raman characterization of ZnTe nanowires with **(a–b)** similar, and **(c–d)** dissimilar surface optical phonon contributions to the 2LO peak. Spectra were collected with 1.62–2.06 μW of 532 nm light. **(e–f)** PL and Raman spectra of two different diameter nanowires, which collected under 25.2 μW (wine and dark cyan lines) and 186.0 μW (reddish–orange and gray lines) of 532 nm light respectively, indicate that laser heating the same nanowires drastically alters the PL peak energy, Raman shifts and the ratios of integrated phonon peak areas (e.g., I_{2LO}/I_{1LO}). All nanowires are supported by a TEM grid.

strengths. For example, the dissimilar group had I_{2LO}/I_{1LO} values of 7.43 (75 nm), 8.45 (225 nm), and 6.41 (335 nm), while the similar group had relatively consistent values of 7.27 (84 nm), 7.25 (223 nm), and 6.90 (340 nm). Although these nanowires were grown using chemical vapor deposition after Ref. [367] and then dispersed in methanol, defect variation from growth or through different degrees of surface passivation from methanol exposure could contribute to the observed optical differences. A method to further evaluate the effects of altered surface states is through the laser–formation of tellurium–based species [140, 141, 243]. Figures 5.4E–F provide respective PL and Raman spectra for two nanowires with 29 and 219 nm diameters both measured under

25.2 and 186.0 μW of 532 nm light. Under the lower laser power, the 219 nm nanowire displays red–shifted PL emission (by < 50 meV) relative to emission collected under ~2 μW, while the Raman shifts are similar to the 335 nm diameter nanowire in Figure 5.4D. Increasing the laser power strongly red–shifted the PL emission outside of the measured range. A similar effect was produced by Te clusters in ZnSe [368], while surface conditions are known to alter the optical properties of these clusters [369]. The Raman shifts showed tremendous down–shifts, such as a decrease of the 1LO from 207.1 to 202.3 cm^{-1} (for the 219 nm diameter nanowire) and large reductions in the integrated peak areas and their intensity ratios (refer to Appendix IV for values). This certainly cautions against using only Raman shifts in size–dependent EPC strengths, e.g., Ref. [142].

The ability for surface conditions to strongly modify the integrated Raman intensity ratios implies that EPC strengths possess both intrinsic and extrinsic contributions. It is reasonable to investigate the intrinsic value for ZnTe nanowires. Figure 5.5 measures the integrated Raman intensity ratios as a function of nanowire diameter from 29 to 390 nm, where the nanowires are supported by a TEM grid or silicon (Si) substrate (with an ~300–nm–thick, silicon–dioxide, surface layer). The different supports enable investigation into substrate effects, which is important as the impact of the surrounding dielectric environment is infrequently investigated, e.g., Refs. [370, 371]. The Raman spectra were collected with low, 532 nm laser powers (e.g., 1.62–2.06 μW) to avoid laser forming surface species. Although different surface conditions, such as defects, contribute to the scattered values, consistent averages are observed with only minor differences between nanowires on the TEM grid and Si substrate. The average I_{2LO}/I_{1LO}, I_{3LO}/I_{2LO}, and I_{4LO}/I_{3LO} values for nanowires supported

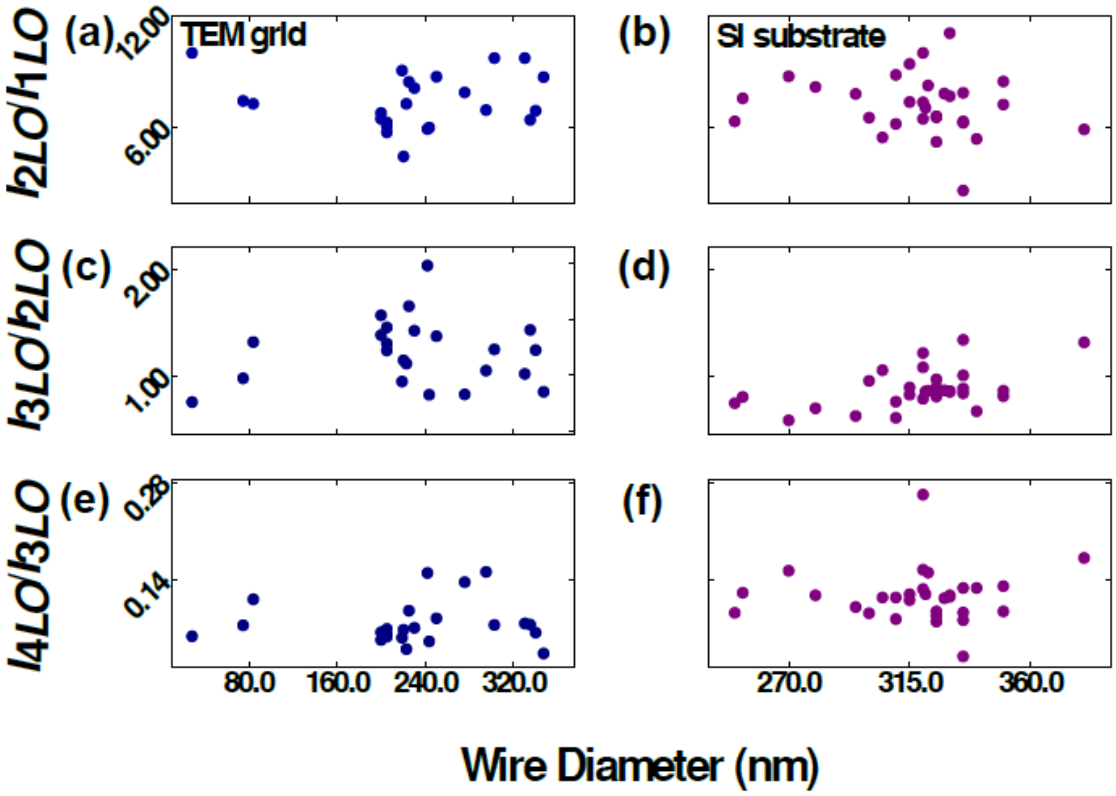

Figure 5.5 Integrated phonon peak areas, e.g., $I_{(n+1)LO}/I_{nLO}$, as a function of wire diameter with different supporting materials. I_{2LO}/I_{1LO}, I_{3LO}/I_{2LO}, and I_{4LO}/I_{3LO} when supported by grid **(a, c, e)** a TEM and **(b, d, f)** silicon (Si) substrate respectively. Spectra were collected with 1.62–2.06 μW of 532 nm light. The average I_{2LO}/I_{1LO}, I_{3LO}/I_{2LO}, and I_{4LO}/I_{3LO} values for nanowires supported by a TEM grid/Si substrate are 6.2±1.3/7.4±1.5, 1.2±0.3/0.9±0.2, and 0.37±0.32/0.08±0.03 respectively.

by a TEM grid/Si substrate are 6.2/7.4, 1.2/0.9, and 0.37/0.08 respectively. The slightly higher I_{2LO}/I_{1LO} values for nanowires on the Si substrate could be closer to intrinsic values, where nanowires possessed fewer defects as a whole. Relationships between higher order integrated intensity ratios are usually not explored, and experienced greater differences than the I_{2LO}/I_{1LO} values. For example, the I_{3LO}/I_{2LO} was a factor of 5.2/8 smaller than the I_{2LO}/I_{1LO} for nanowires supported on the TEM grid/Si substrate respectively, while the I_{4LO}/I_{3LO} was a factor of 15/7.5 smaller than the I_{3LO}/I_{2LO}. Overall, a clear size–independence was observed over a broad range of nanowire diameters. In principle, normalizing each integrated peak area by a nanowire's square diameter should yield a slope with an identical value. Figure AIV.2 plots, for example, I_{2LO}/d^2 as

a function of I_{1LO}/d^2 along with the higher order ratios, where the slope should match the average value in Figure 5.5. While values for nanowires on the TEM grid yielded similar results as those shown in Figure 5.5, very different values were obtained for the nanowires on Si substrate. The I_{2LO}/I_{1LO}, I_{3LO}/I_{2LO}, and I_{4LO}/I_{3LO} values for the Si substrate/TEM grid in Figures AIV.2B–C (under 2.05/1.62 μW of 532 nm light respectively) are 9.7/0.9, 0.8/4.0, and 0.070.18, while nanowires on Si substrate in Figure AIV.2C, which were measured under a higher laser power (25.2 μW), produced values of 7.8, 2.2, and 0.13 respectively. Further investigation is required to ascertain the origin of these differences. A point of future study is to determine if diameter normalization is a more sensitive measure of surface conditions and substrate effects and to verify findings with a larger sample population (especially at lower diameters). The higher order intensity ratios, however, do not change appreciably for many of the effects that will be explored, and thus, these values are placed in Appendix IV.

5.3 Laser Heating Effects

Laser–power–dependent effects on EPC strengths are not usually explored, and existing investigations typically yield information for bulk [372, 373] and surface [373-376] contributions for below bandgap (transparent) or ablative illumination conditions. These reports do not relate laser heating to EPC strength, e.g., Refs. [243], [244], [282] and [373]. The laser powers used in CW–based techniques are typically justified when an estimated surface temperature is below the bulk melting temperature. This simple justification may be inadequate. For instance, Uzan *et al.*[377] demonstrated strong surface decomposition on CdTe crystals well below the bulk decomposition temperature (e.g., decomposition occurred at 850 K instead of at the bulk value of 1314 K). Their results are quite illustrative despite neglecting, at least directly, carrier and

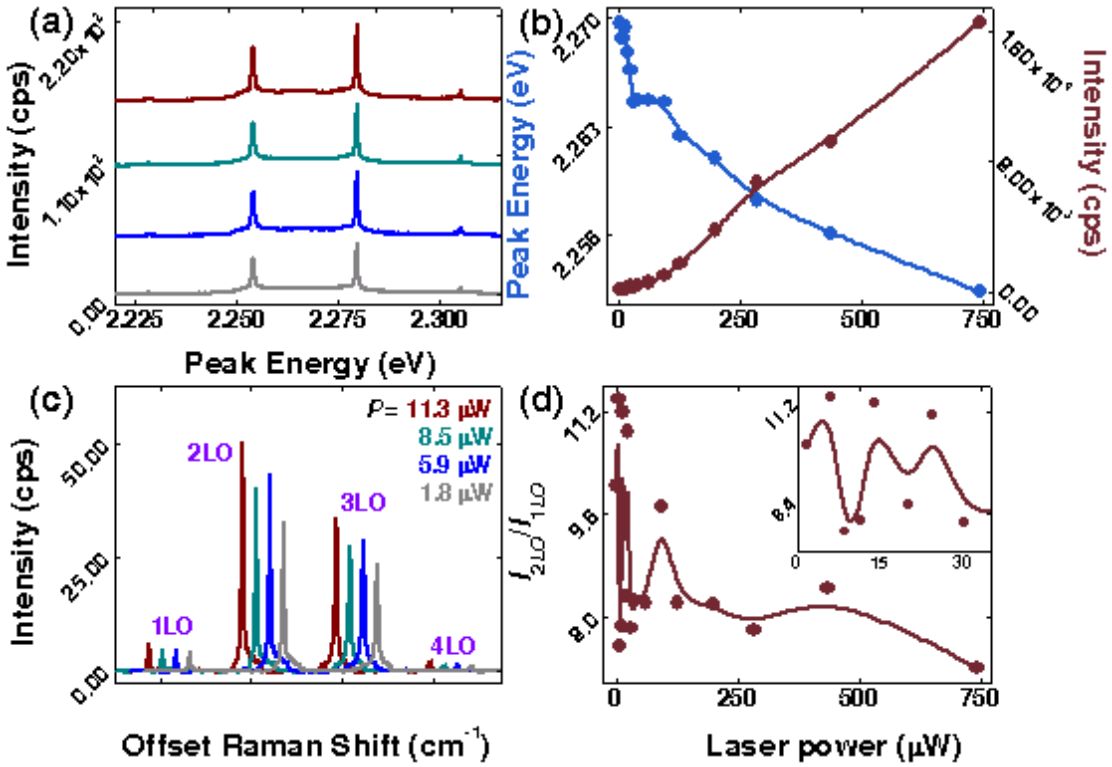

Figure 5.6 Power–dependent EPC strengths obtained with 532 nm light**. (a)** Power–dependent PL spectra that result in modification of **(b)** peak energies and emission intensities. **(c)** Raman spectra at low power demonstrate undulating peak intensities as indicated with the black wave above the 2LO peak. **(d)** Power–dependent I_{2LO}/I_{1LO} values demonstrate undulations at low laser power and become more linear at higher laser powers, e.g., > ~100 μW.

surface strain contributions [282, 376, 378, 379]. To address this literature gap and to reveal important effects, laser–power–dependent effects are explored using high quality B1. Figure 5.6 uses nearly resonant (532 nm) excitation to yield PL and Raman spectra in Figures 5.6A–B respectively. PL emission shows a linear increase in intensity with increasing laser power, while the peak energy red–shifted slightly. The Raman spectra reveals relatively linear intensity changes at higher laser powers, while at the lower powers shown in Figure 5.6C, undulating Raman intensities are observed (as illustrated by the black line above the 2LO peaks). This behavior directly impacts the coupling strengths graphed in Figure 5.6D. The 532 nm laser powers are steady with fluctuations within 0.27% across the optical power range used. For example, three different power

measurements (N = 10) yielded 2.00±0.005, 29.78±0.08, and 153.72±0.41 μW, while for silicon, peak area variations of < 3–4% were measured. For high quality ZnTe, however, I_{2LO}/I_{1LO} uncertainties of ±0.6 were observed for the unpolished, B1–CE. Although further investigation is required, it is possible that power fluctuations alone may not entirely account for the observed oscillatory behavior at very low optical powers.

Laser heating effects under low and higher laser powers are performed in ambient and under nitrogen gas flow to explore the impact of heating on coupling strengths. Sample B2 is chosen to avoid the large coupling strength variations observed in ZnTe RS for B1–FS. In Figure 5.7, B2 is first measured with 2.60 μW of 532 nm laser light to establish a baseline, followed by 194.4 μW, and measured again under 2.60 μW to examine spectral recovery in both ambient and nitrogen atmospheres. Dark cyan and wine lines represent the initial conditions in Figure 5.7A- B, for nitrogen and ambient conditions respectively, while the gray and reddish–orange lines were collected after laser heating. Heating times are reported in terms of the number of successive 100 s spectra collected (with the external shutter closing briefly every 10 s). The spectra were measured consecutively, where the next was initiated immediately after the previous one finished. In Figures 5.7A–B, both environments produced a 0.7 cm^{-1} Raman down shift after laser heating relative to the initial values (all collected with 2.60 μW), while the absolute Raman and PL emission intensities did not show appreciable variation. Measurement sites under ambient and N_2 conditions were collected very near each other, but the slight spatial difference may account for the minor difference in peak energy and emission intensity between the two sites. While Figure 5.6 suggests the possibility of heating effects at low optical powers, Figure 5.7C displays only benign

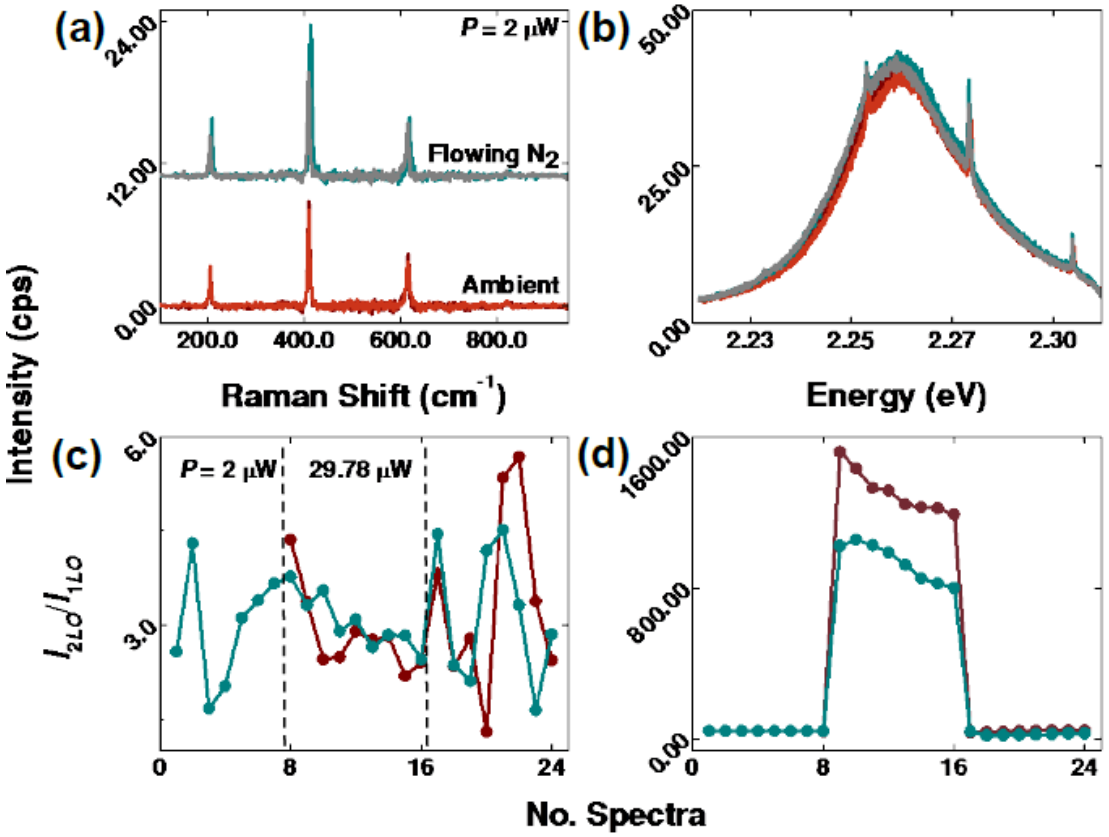

Figure 5.7 Laser heating's impact on EPC strength. **(a–b)** Raman and PL spectra under ambient and flowing nitrogen (N_2) gas conditions during initial measurement with 2.60 μW of 532 nm light (wine and dark cyan lines). After laser heating with 194.4 μW of 532 nm light, the spectra were collected again under 2.60 and 29.8 μW. **(c–d)** I_{2LO}/I_{1LO} and PL emission intensity as a function of the number of 100 s spectra collected. Spectra were collected with 2.60 μW for spectra numbers 1–8 and 17–24, while 29.8 μW was for spectra numbers 9–16 for nitrogen and ambient conditions (dark cyan and wine colored lines respectively).

changes in the I_{2LO}/I_{1LO}. The I_{2LO}/I_{1LO} was 4.0±0.2 (N = 10 measurements). Thermal effects do not appear to play a significant role at these low optical powers.

Exploring the effects of higher optical powers, such as laser–forming Te–based, surface aggregates, and the subsequent impact on coupling strength is also useful. The optical image for a large, 1.3–μm–diameter wire appears in Figures 5.8A. Raman spectra are collected under 157.5 μW of 532 nm light, heated for t = 5 s with 2.53 mW, and then measured again using 157.5 μW. Higher optical powers are acceptable as larger diameter wires possess higher thermal conductivities, although 2.53 mW is about

an order of magnitude higher than the ~0.1 mW required to laser–form Te in bulk CdTe (see Figure IV.4). This cycle of low power measurements followed by laser heating is repeated for an elapsed heating time of 125 s. PL emission in Figure 5.8B reveals negligible changes in the peak energy. This could imply the presence of a small amount of laser-formed Te relative to the interaction volume. The quenched emission results from a reduced material volume, e.g., from ablation and laser–formed, Te–based species. As shown in Figure 5.8C, these Raman changes stem from a drastic I_{1LO} reduction coupled with a less severe I_{2LO} decrease, and corresponded with the appearance of Te–related Raman peaks [139-141, 380] that shifted from 137.9 to 143.7 cm^{-1}. While the 2– and 3–LO peaks present a stable up–shift in peak position with increased heating times, the 1– and 4–LO peak positions fluctuated in opposite directions. Interestingly, the fluctuating Raman peak positions appear to correspond with reduced integrated peak areas, while the stable shifts occurred with increasing peak areas. Using t = 110 and 125 s as an example, the Te–related peak area (at ~141 cm^{-1}) increased from 43.3 to 47.0 cm^{-1} cps, while the 1– and 2–LO peak areas respectively decreased from 108.3 to 54.0 cm^{-1} cps and from 246.7 to 141.0 cm^{-1} cps. Subsequent heating (t > 110 s) forms stable, Te–based, surface deposits, which is supported by stable I_{2LO}/I_{1LO} values, and broadening of the Te–related peak, which is expressed through a decreased peak area from 211.8 to 154.5 cm^{-1} cps (at ~161 cm^{-1}). The extracted I_{2LO}/I_{1LO} values are plotted in Figure 5.8D. Laser heating varied the I_{2LO}/I_{1LO} by ±1 until t < 90 s. After $t \approx$ 90–110 s, the I_{2LO}/I_{1LO} reduced from 6.2±0.91 (N = 21 measurements) to 2.4±0.2 (N = 4). An intermediate data point exists with an I_{2LO}/I_{1LO} of 4.3. Reduced coupling strength at t > 110 s is consistent with an unrecovered PL intensity. As for an underlying mechanism, it is quite possible that the drastic

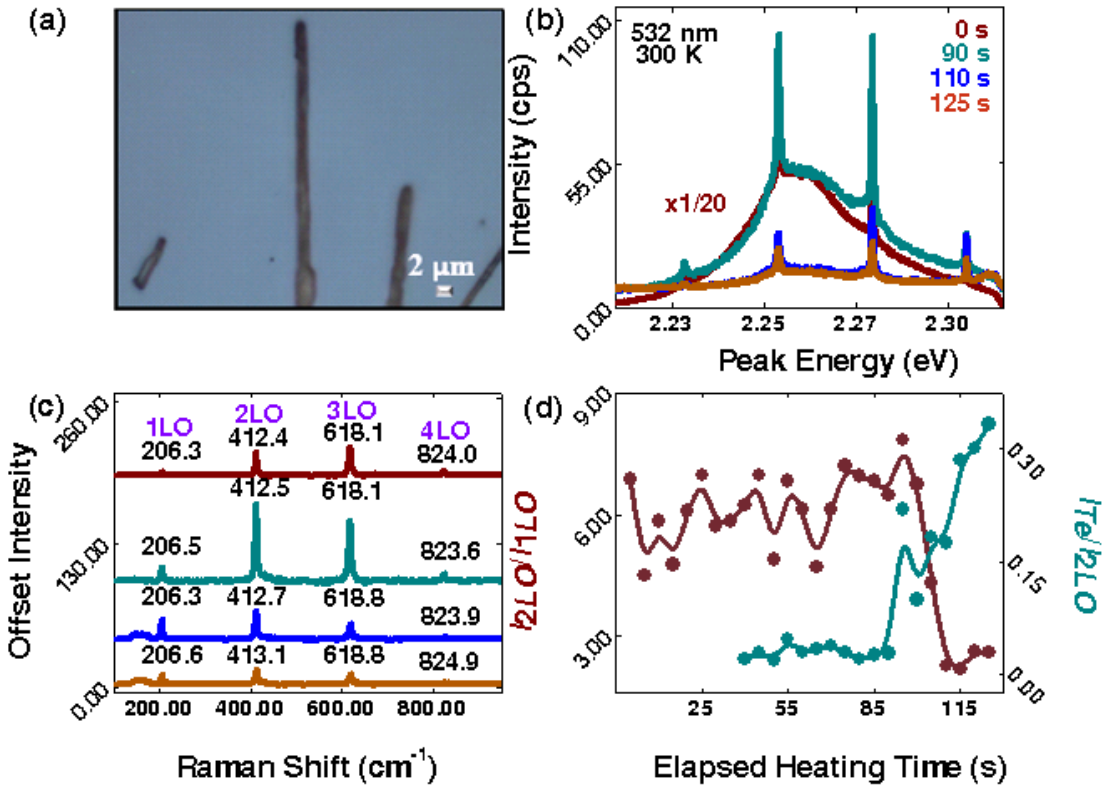

Figure 5.8 Modulating EPC strength through laser formation of Te–based species on a large ZnTe wire with a diameter of 1.3 µm. **(a)** Optical image of the large wire (2 µm scale bar). **(b)** I_{2LO}/I_{1LO} as a function of 5 s heating intervals under 2.53 mW of 532 nm light, while initial and post laser–heated, Raman measurements were obtained with 157.5 µW of laser power. Temporal evolution of **(c)** PL and **(d)** Raman spectra with laser heating.

modulation results from laser–formation of Te–based species that experience partial ablation during the formation process from t = 90–110 s. After this time, the surface deposit becomes stable, which is signaled through a broadened Te–related peak. This is also when the I_{2LO}/I_{1LO} reduces below its initial value (of ~6-7) to ~2.4. Interestingly, this value is similar to that reported for size–dependent values in ZnTe nanowires with diameters ranging from 90 to 250 nm [142]. The results in Figure 5.8 demonstrate that not accounting for extrinsic effects, such as the laser–formation of surface species, can lead to erroneous conclusions regarding size–dependence. This is because smaller diameter wires possess reduced thermal conductivities compared to larger ones, which

could produce an erroneous size dependence from laser heating different wire diameters (to varying degrees) using the same laser power and heating times. If the I_{2LO}/I_{1LO} can indeed be taken as a reliable measure of the electron–phonon coupling strength, this result indicates a relatively simple way to tune this property by a large magnitude, and more surprisingly, without the need for nanoscale dimensions.

5.4 Strain and Polarization

Strain and polarization could be practical methods for modifying EPC coupling, such as by bending a flexible substrate or by inserting a polarizer into the illumination path. Relatively few reports, however, explore the impact of strain [248-250] and polarization [252] on EPC strength, although one example applied elastic strain to preferentially enhance the I_{2LO} in ZnO nanowires [249]. Figure 5.9A displays a bent ZnTe nanowire with a diameter of 300 nm and a bend radius over 34 μm. Various sites were measured from the nanowire end to the bend near its center. The numbered measurement sites are proxy values for the nanowire's radius of curvature (induced by the bend), which is related to strain, because extracting this parameter from optical images introduced unnecessarily large uncertainties. In a future study, an SEM image will be employed to extract this parameter. Regardless, Figure 5.9B shows strain independence of the I_{2LO}/I_{1LO} term (where higher order ratios are included in Appendix IV). Raman measurements were collected with polarized, 532 nm light with and without a polarizer, while no appreciable changes were observed in coupling strengths between the two conditions. The polarizer measured an electric field that is vertical with respect to the optical image in Figure 5.9A and is referred to as "vertical polarization." The Raman and PL spectra in Figures 5.9C–D respectively show that vertical polarization does, as expected, reduce the absolute intensities, while the ratio

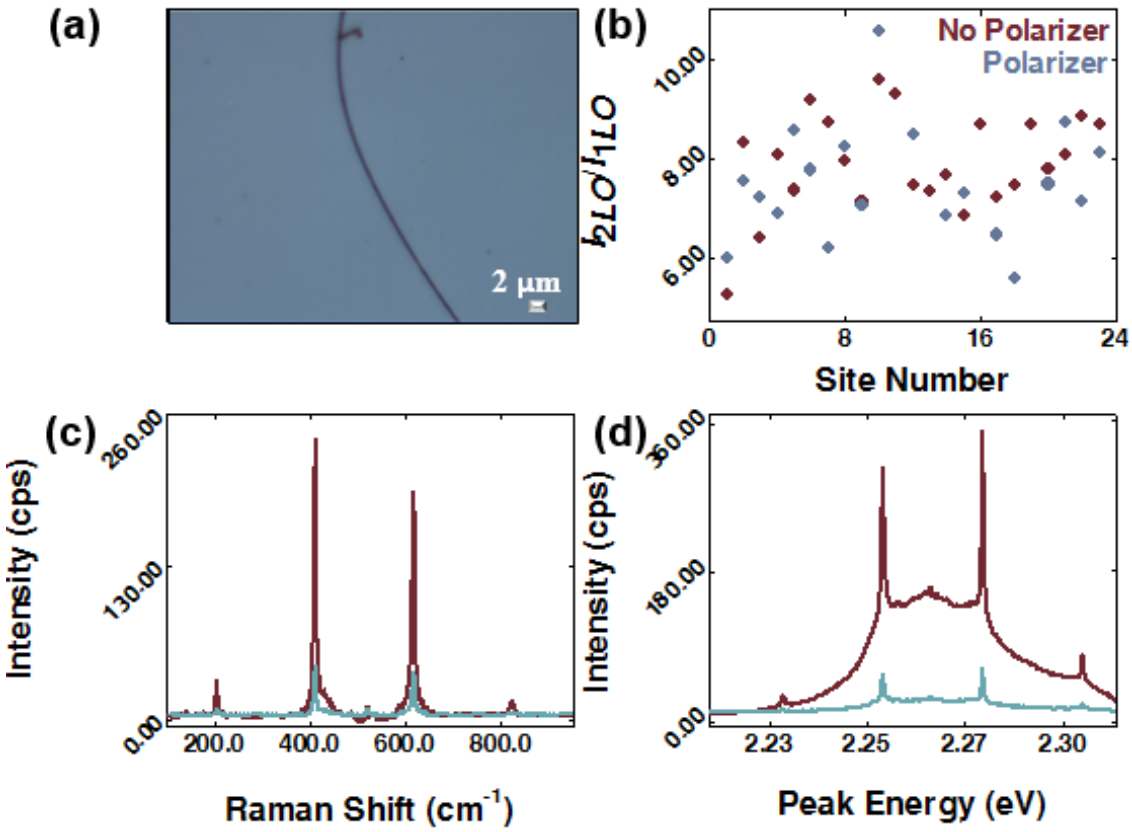

Figure 5.9 EPC strength dependence on both strain and polarization. **(a)** Optical image of the bent ZnTe nanowire (2 μm scale bar). It possesses a 300 nm diameter, a bend radius over 34 μm with a 23° bend relative to the vertical axis. **(b)** I_{2LO}/I_{1LO} as a function of the measurement site ranging from the nanowire end to the bend at its center. Representative **(c)** Raman and **(d)** PL from site number 11. Light blue and wine lines represent values obtained with and without a vertical polarized laser in the beam path. The laser is vertically polarized with respect to the optical image, which when combined with the bent nanowire, varies both the curvature (strain) and polarization.. Raman spectra were collected with 0.354 μW of 532 nm light.

of integrated peak areas is not significantly altered. A more conclusive, future study will examine: (1) both the vertical and horizontal polarization components, and (2) a greater range of bend curvatures and nanowire diameters. But for now, it appears that EPC strengths may be both polarization and strain independent in ZnTe nanowires.

5.5 Interface and Surface Effects

Sensitivity to laser–formed, Te–based species suggests that EPC strengths may also be extrinsically tuned in other ways. This section explores the effect of Au–ZnTe junctions and the impact of methanol exposure on EPC strengths. Figures 5.10A–B

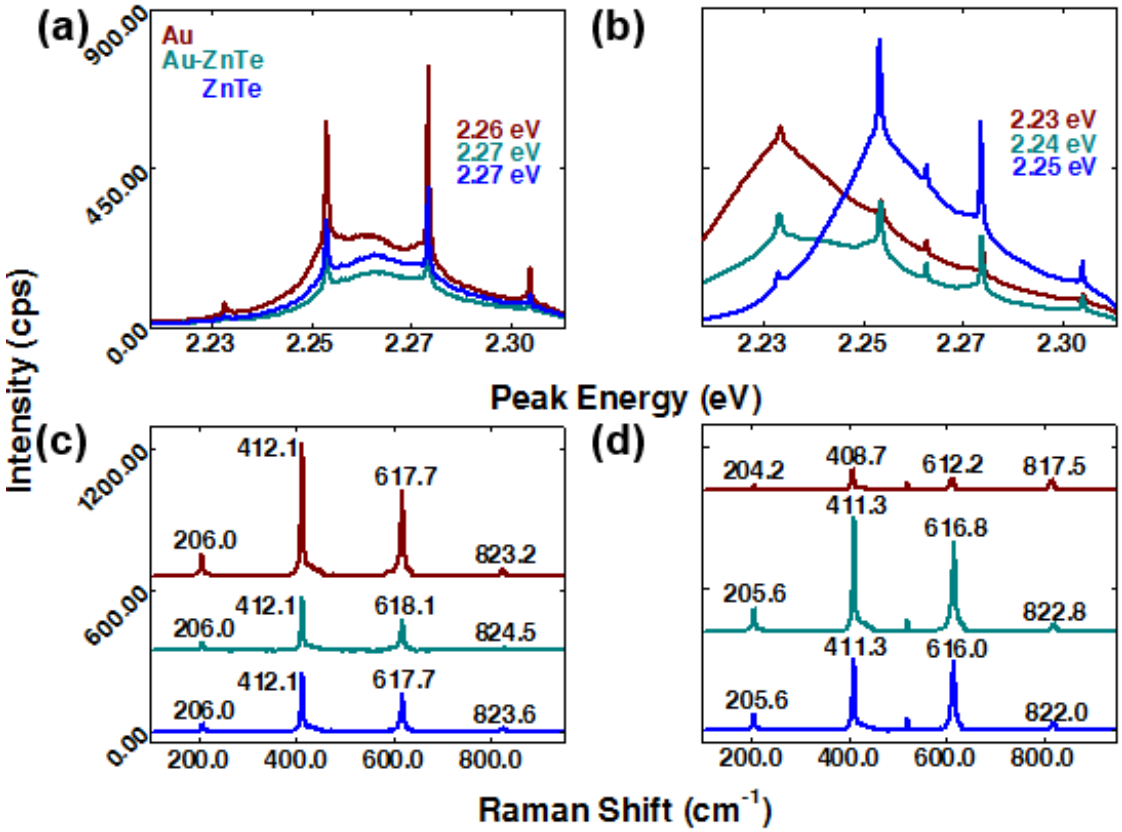

Figure 5.10 Raman and PL spectra measured at the Au sphere, Au–ZnTe interface, and ZnTe nanowire body for two different nanowires. Left (right) column for nanowire 1 (2). **(a–b)** PL emission and **(c–d)** Raman spectra for Au–ZnTe junctions with similar and dissimilar PL spectra. Spectra were collected with 24.3 μW of 532 nm light.

contain PL spectra for two different nanowires that demonstrate two distinct behaviors: similar and dissimilar peak energies measured for the two different nanowires in Figures 5.10A–B respectively, which suggests, respectively, the presence of a high quality nanowire and a nanowire containing a relatively larger defect concentration. The similar spectra show very little shift in the peak energies (e.g., up to ~10 meV), while the dissimilar spectra displayed shifts up to ~20 meV (relative to each other). For the similar spectra, the nanowire body (wine line) and the Au–ZnTe junction (light brown line) had identical peak energies, while energy. Conversely for the dissimilar spectra, all three measurement locations displayed different peak energies (see figure for values). The corresponding Raman spectra are in Figures 5.10C–D respectively.

The higher quality sample demonstrates negligible 1– and 2–LO Raman shifts, while the two highest order LO peaks were up shifted relative to the Au–ZnTe interface. Very different I_{2LO}/I_{1LO} values were measured at the Au sphere, Au–ZnTe junction, and ZnTe body, which were 4.7, 14.8, and 7.5 respectively. The higher order ratios of integrated intensities, however, did not change much across these sites. For the dissimilar group in Figure 5.10B, Raman up shifts were observed for the Au–ZnTe junction and the nanowire body relative to the Au sphere. Interestingly, no significant changes in any of the ratios of integrated peak areas were observed across these three locations. The I_{2LO}/I_{1LO} for the Au, Zu–ZnTe and ZnTe sites for the similar/dissimilar groups are 4.7/4.9, 14.8/4.2, and 7.5/4.7 respectively. While the enhancement at the Au–ZnTe junction suggests electromagnetic enhancement of first and second order phonon interactions, the latter results suggest that the mechanism is likely more complex. Further investigation is required to unravel its intricacies.

Meanwhile, methanol exposure probes the sensitivity of coupling strength to surface conditions. Figures 5.11A–B plots PL emission and Raman spectra respectively before and after exposing B1 to methanol. Methanol not only quenched PL emission (without inducing a shift in peak energy), but it also upshifted the first three LO peaks, while the 4LO was down shifted by 0.1 cm^{-1}. For example, the 1LO peak was shifted from 206.1 to 206.5 cm^{-1}. Methanol also drastically reduced the I_{2LO}/I_{1LO} from 11.4 to 1.9, while the higher order ratios did not change appreciably. These findings highlight the ability to tune EPC strengths at material interfaces and surfaces, which have tangible applications, such as optical bar codes and sensors, respectively.

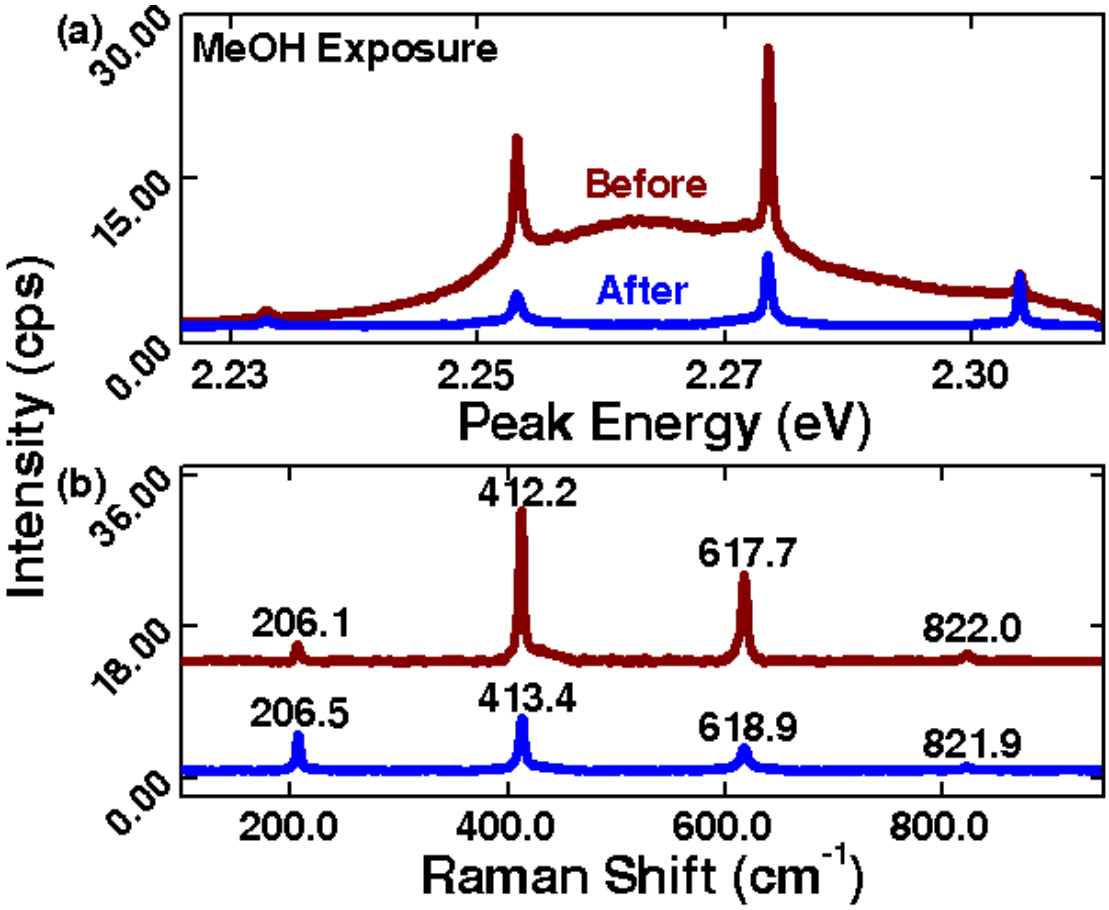

Figure 5.11 Impact of methanol exposure on EPC strength. **(a)** PL emission and **(b)** Raman spectra before and after exposing high quality bulk ZnTe (RS) to methanol. Spectra were collected with 2.31 μW of 532 nm light.

5.6 Discussion

The standard model [132, 133], which is used to calculate or extract EPC strengths from experimental measurements, yields Eq. 5.1, which relates S to the I_{2LO}/I_{1LO}. In this equation, E_{ex} (μ) is the electronic transition energy (dipole transition), ω_0 (n ω_{LO}) is the emitted photon (n–LO phonon) energy, and Γ is the electronic state's homogenous linewidth (typically assumed to minimally impact S) [132, 133]. Using material parameters in Appendix IV, Eq. 5.1 yields a calculated S_{bulk} value of 3.2 [142], which corresponds to an I_{2LO}/I_{1LO} of ~1.6. This model, which is routinely applied to nanowire

systems [142, 246, 270, 381], does not adequately describe the high quality ZnTe systems explored here.

$$\left|\frac{I_{2LO}}{I_{1LO}}\right| = \frac{S}{2}\frac{\left(E_{ex}+\hbar\omega_{LO}-\hbar\omega_0\right)^2+\Gamma^2}{\left(E_{ex}+2\hbar\omega_{LO}-\hbar\omega_0\right)^2+\Gamma^2} \tag{5.1}$$

The high quality bulk sample (B1) demonstrated a high mean I_{2LO}/I_{1LO} value with a large range, (e.g., 12.9±10.0 and 17.9±9.7), while the high quality thin film and nanowire systems possessed average I_{2LO}/I_{1LO} values ranging from 7.14–15.6 and ~5–9. Defects and impurities were able to drastically reduce these values. For example, bulk values experienced a reduction in I_{2LO}/I_{1LO} to 1.5–3.5, while one thin film sample, which was not presented here, displayed the classic impurity signature and yielded an I_{2LO}/I_{1LO} of 1.43. Figure 5.8 even demonstrated the ability to change the I_{2LO}/I_{1LO} from 7 to 3 by laser–forming surface species. These altered values more closely reflects the value calculated for high quality bulk ZnTe (e.g., S = 3.2). This is an important and significant finding that warrants a revisiting of theoretical frameworks and a reinterpretation of previous experimental findings. Appendix IV provides an extended discussion regarding the standard model including limitations potentially contributing to the discrepancy between theoretical and experimental coupling strengths.

The S factor derived experimentally using Eq. 5 .1 is often compared to the theoretical value $S = \Delta^2$, where Δ^2 can be evaluated using the formula below only when Fröhlich interactions are considered: the EPC constant, δ^2, given in Eq. 5.2, where μ is the reduced mass and $\hbar\Omega_{LO}$ is the n–LO phonon energy [134].

$$\delta^2 = \frac{e^2}{\sqrt{2\mu}\hbar^{1.5}\Omega_{LO}^{0.5}}\left(\frac{1}{\varepsilon_\infty}-\frac{1}{\varepsilon_0}\right) \tag{5.2}$$

An alternative theory, which accounts for the exciton kinetic energy, suggests that LO scattering in bulk ZnTe is nearly forbidden, while the 2LO scattering is relatively much stronger, because the 2LO is independent of the exciton kinetic energy [134]. The theory also implies that the breakdown of the crystal translational symmetry by the defects can significantly enhanced the 1LO scattering. Although this understanding could explain the reduction in the I_{2LO}/I_{1LO} ratio, the strong enhancement observed in Figure 5.8 cannot be explained by this theory. As no theory currently accounts for EPC at interfaces, interpreting the laser–formation of Te–based species is not clear. These systems also displayed drastic Raman shifts that further imply a change in the coupling constant. For example, laser heating the 29–nm– and 1.3–μm–diameter wires produced 1LO shifts from 207.1 to 201.8 cm^{-1} and from 206.9 to 206.4 cm^{-1} respectively. The different degrees of change could imply a concentration dependence but this possibility requires further exploration. Methanol exposure and an Au–ZnTe interface also altered the coupling strength, which according to this theoretical framework, implies the ability to alter interactions with intermediate Raman scattering states.

The relative intensities of nLO are temperature dependent. These dependencies for the 1LO and *n*–LO modes (with $n > 2$) are given by $S_1 = I_{1LO}/I_{2LO} \propto T^{(L1-L2)}$ and $S_n = I_{nLO}/I_{2LO} \propto B_n(1+1.5\gamma_n T)$, where: T is the crystal lattice temperature, L is an exponent describing the probability of the n^{th} order phonon–assisted annihilation, and B_n and γ_n are constants [134]. Laser induced heating could potentially contribute to the observe variation in I_{2LO}/I_{1LO} , but apparently inadequate to explain the large change as shown in Fig. 5.8(b). An extension of this work could involve exploring the thermal influence of EPC on the ratio of integrated areas for the 1LO anti–Stokes and Stokes peaks, which is a commonly used method to determine local temperatures [279].

While this work is an important guide that demonstrates several methods for extrinsically perturbing EPC strengths in multidimensional ZnTe systems, an accurate theoretical analysis is needed to unveil the complexities of the underlying physical mechanisms. Such a study would greatly assist in opening interesting pathways for engineering EPC strengths for device (or other) applications. Furthermore, the ability to extrinsically modify coupling strengths extends beyond ZnTe systems. Appendix IV demonstrates coupling strength tuning for CdSe nanowires.

5.7 Conclusions

At the nanoscale, EPC strengths are controversial and even yield contradictory theoretical and experimental results. This investigation employed CW resonant Raman spectroscopy using a 1.60 μW to 0.25 mW of 532 nm light to explore nearly intrinsic and extrinsic contributions to coupling strengths in multidimensional ZnTe systems. Size–independent EPC strength were revealed for the investigated bulk, thin film, and nanowire samples, although extrinsic influences enabled the tuning of this parameter. For example, laser–forming Te–based species on ZnTe nanowires altered the I_{2LO}/I_{1LO} from an initial value of ~7 to ~32, and after sufficient Te was formed, the value was reduced to ~3. This observation explains the supposedly size–dependent EPC strengths previously reported for ZnTe nanowires, where the erroneous size–dependence likely results from each diameter possesses a different thermal conductivity and rate of Te formation. Defect concentration in bulk and thin film samples also altered the EPC strength. Laser power also had an effect, where undulations in I_{2LO}/I_{1LO} were observed below ~200 μW of 532 nm light, and demonstrates the ability to quickly and reproducibly tune EPC strengths. Other effects were also explored. Methanol exposure modified the coupling strength, while an enhanced coupling strength was measured at

Au–ZnTe interfaces compared to the same nanowire's body. Both strain and laser polarization had negligible effects on coupling strength, although a more thorough investigation is required.

CHAPTER 6: LASER PROCESSED TUNING OF SEMICONDUCTOR NANOWIRES

"An experiment is a question which science poses to nature, and a measurement is the recording of Nature's answer."
Max Planck, 1949 The Meaning and Limits of Exact Science (Science, Vol. 110, Issue 2857, pgs. 319-327)

6.1 Introduction

Lasers are widely used in materials processing. Examples include laser cutting, scribing, welding and laser machining [382-384], while laser modification or "processing" with both pulsed [385, 386] and continuous–wave (CW) [387] lasers in the ambient environment or under a gaseous atmosphere are employed to create embedded devices and circuits with stable, laser–patterned electrical properties [388]. Two general effects are observed during laser modification: (1) material ablation that may also alter the crystal structure at the illumination site, or (2) laser–induced transformation of the crystal structure without ablating the material [389-391]. Ablative methods include material removal or transfer, such as by laser–etching surface material [392] (e.g., laser micromachining), and material transfer from source to substrate [393-395]. Laser–induced transformations could be used to laser process, for instance, graphene on a (single or multi–layer) sheet of graphite oxide [396]. Important material systems include transforming silicon from an amorphous to a polycrystalline structure [389] or even to single crystalline material [390, 397], and converting silicon carbide to graphene [391]. Ablative processes tend to require high optical power densities, such as above megawatts per square centimeter. Similarly, laser processing performed of

nanostructures typically use sub–10–mW powers, which produce similar power densities because of tight focusing, and are investigated using limited laser wavelengths, such as in the ultraviolet regime [398] or in visible wavelengths for limited material systems, e.g., Ref. [399]. Investigations with very low laser powers, such as sub–milliwatt and microwatt powers, are limited, e.g., Ref. [192], but further study is required to enhance and expand this technique's capabilities [398, 400], such as by enabling the laser modification of a variety of surface geometries (e.g., form factors). Low laser powers yield a third laser processing regime where the (3) "gentle" alteration of semiconductor surface states [401-403] does not alter the underlying crystal structure, and can be accomplished through, for example, modifying the surface defect concentration or configuration via laser annealing. This regime effectively expands the laser processing concept to semiconductor surface states [404], and offers the potential to dynamically tune a material's electronic and optical properties through spatially controlled, laser–induced temperature changes. The primary focus here is on the gentle regime although partial surface ablation on SNW's will be briefly explored.

Fabricating electronic devices continues to be divided between high spatial resolution and high throughput techniques. For example, conventional photolithography [405] and electron–beam lithography [406] both offer sub–10–nm spatial resolutions, but these techniques employ masks and vacuum systems that result in high costs. Other methods were developed to reduce costs – such as imprint lithography [407, 408], soft lithography [409], dip–pen lithography [410, 411], micro–contact printing [412, 413], and inkjet printing [414] – but these methods typically require masks or contaminate device surfaces [415]. In contrast, maskless and inkless laser processing offers a robust, cost–effective, and high throughput technique with low

laser exposure times, rapid laser positioning, and sub–micron spatial resolution [398, 416]. The laser processing effects in (1–3) can be evaluated for device applications. Laser ablation is not typically used in device applications, although partial ablation should provide permanent changes in electronic characteristics. Obviously, ablative processes are not suitable in device applications requiring reprocessing capabilities as the device would eventually be destroyed. “Laser pruning” [417], or slight surface ablation, controllably removed surface layers, which also altered the stoichiometric ratio (in the illuminated area). This process increased rectification of the electrical characteristics while also increasing the reverse current, which is not desirable in, for example, transistor applications. Another common example of laser ablation is oxygen incorporation [243, 418] into the surface layer, where laser–formed, oxygen–based surface species [139-141, 419] alter both optical and electrical properties, e.g., Ref. [417]. Meanwhile, gentle laser treatments have been exploited for tangible electronics applications. Examples of altering the electronic performance of nanowire– [192] and thin–film–based [420, 421] transistors include increasing the source–drain current [192], and reducing the threshold voltage [192] and leakage current [422, 423]. In general, both laser processing regimes are of interest for laser modification of electronic characteristics for specific device applications.

A critical and necessary improvement for advancing laser processing is the ability to laser process multi–component systems using effects in (1–3) to provide a menu of electrical responses that could potentially emulate both simple and complex functions. Progressing towards this goal ultimately involves generalizing the underlying mechanisms behind ablative and gentle laser processing beyond the limited materials systems and dimensions investigated, which include semiconductor oxides [424],

multi–ferroic thin films [422], graphene sheets [417], and ternary II–VI semiconductor nanowires (SNWs) [418]. Cadmium selenide (CdSe) is an ideal candidate for two reasons. First, it is one of the few demonstrated SNW's with a low dark current [182], which is important for achieving desired functions in optically addressable devices. Second, it provides an opportunity to study a complex native surface oxide or amorphous layer (e.g., SeO_x where x = 2–3 [189]), which contrasts binary oxides, such as zinc oxide [192], which are typically explored with gentle laser processing. Findings could be quickly incorporated into broad, CdSe–based applications, such as solar cells [95, 425-427], photodetectors [143], lasers [428], field–effect transistors [429, 430], and light–effect transistors (LETs) [182]. In this work, ablative and gentle laser processing is demonstrated to provide static and dynamically tunable optical and electrical characteristics for an optically addressable, M–S–M devices employing CdSe SNWs [95, 143]. Findings may also be applied to other material systems with reduced dimensionality, such as ultrathin films. More specifically, gentle laser processing demonstrates the potential to temporarily alter electrical properties, while ablative processing not only alters the dark current, but it further probes the relationship between the crystal structure, native oxide layer, and optical and electrical properties. Gentle laser processing is demonstrated with and without bias–assistance under two different illumination sources to demonstrate the versatility of laser processing with low laser powers. The altered optical and electrical properties are correlated with structural changes to unravel the underlying mechanisms.

6.2 Laser Modified Electrical Characteristics

As with any semiconductor–based device, low optical powers produce stable and consistent optical and electrical measurements as observed in Figure 4.3. A LET's

electrical functionality may be laser modified and depends on the optical source's wavelength and power, and the exposure or illumination time, $P_w(\lambda_w,t)$. Note that the *g* and *w* subscripts clearly differentiate optical gating from laser processing functions. The exact power threshold between optical gating and laser processing functions depends upon the material quality, nanowire diameter, and laser parameters. For example, the material quality can play an important role in material ablation [431]. Laser modification of the surface, such as by laser annealing surface trap states [432], can also alter laser–power–dependent carrier kinetics [176] that manifest themselves in altered electronic characteristics [176]. The flexibility offered by laser processing stems from a combination of device fabrication, as discussed in Section 3.5, and laser processing conditions. Given In's and CdSe's similar work functions, an In–CdSe interface should, in principle, produce an ohmic response [198]. However, varied electrical responses [190] are possible and result from variations in M–S junction details [190] and oxidation [433]. In this work, the nanowire body is laser processed to produce a large menu of electronic functions. Figure 6.1A contains a 3D, device schematic illustrating laser modification on the conducting channel (CdSe SNW). Two different laser power effects are observed: (1) the lower or "gentle" optical powers reversibly modifies the optical and electrical properties through modifying the SNW's suface, while not altering its underlying crystal structure; while (2) higher optical powers irreversibly alters the optical and electrical properties, because sufficiently high powers or prolonged exposure times, even at lower powers, could lead to material ablation. In other words, gentle laser processing produces transient responses that eventually recover to near their initial values, while irreversible processing produces

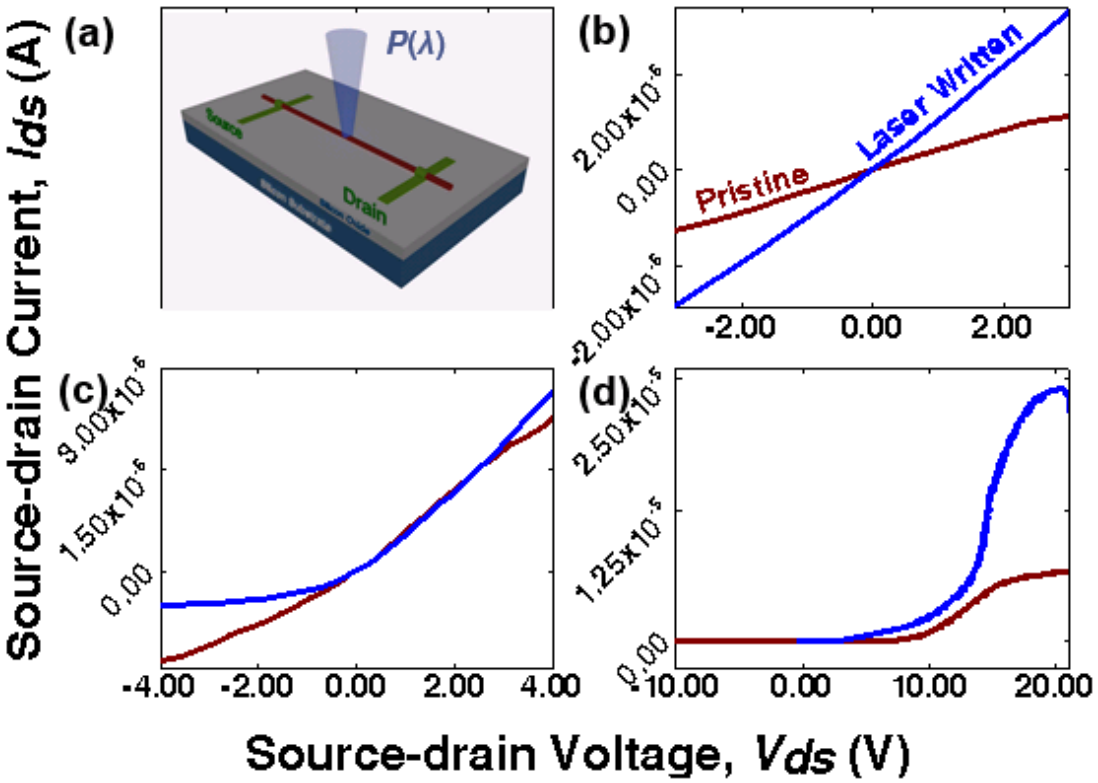

Figure 6.1 Demonstration of irreversible laser processing of output or I_{ds}–V_{ds} characteristics. **(a)** $P_w(\lambda_w,t)$ conditions are chosen to laser write the conducting channel composed of a CdSe nanowire. The SNW is in red, and the *S* and *D* contacts are in green. Dark current changes were achieved through partial ablation of the CdSe SNW channel in three different In–CdSe–In devices. Modifications in electrical behavior include: **(b)** increasing the ohmic response (e.g., the linear slope), **(c)** converting nearly ohmic behavior to a rectified response by reducing the reverse current, and **(d)** increasing the forward current. Although the dark current was altered in these demonstrations, similar but recoverable photo–currents are achievable with lower laser powers (while dark current changes are negligible).

permanent changes. Figure 6.1B–D offers a few demonstrations of irreversible modifications, although this chapter will primarily focus on reversible modifications. The dark current (I_{ds}–V_{ds}) modifications were performed through a 50x long–working–distance objective lens (*N.A.* = 0.50) using (B) P_w = 2.98 mW (t = 10 s), although similar results were obtained on a different device (not shown) with = 20.20 mW (t = six, 10 s pulses), (C) $P_w(532nm)$ = 0.366 mW, (t = four, 100 s pulses), and (D) exposure to P_w = 3.82 μW for several minutes (e.g., 5–10 min.). The SNW channel was illuminated near its center in each case, while care was taken to avoid modifying the

M–S junction. While the dark current changes in Figure 6.1 resulted from lightly ablating the SNW channel on three different devices, similar photocurrent characteristic changes are also observed, with negligible dark current modification, for laser processing with gentle optical conditions. Gentle conditions are the primary focus here. Figure 6.1 demonstrates the flexibility offered by laser processing M–S–M structures, which include: (1) altering the ohmic response (linear slope change, Figure 6.1B), (2) conversion of an ohmic response to rectified characteristics, such as through reduction of the reverse current (Figure 6.1C), and (3) enhanced forward current (Figure 6.1D). This flexibility, which is obtained from the same materials and fabrication processes, offers the possibility of low–cost device fabrication for a broad array of electronic applications.

Gentle laser processing of a LET highlights important device effects that are displayed in Figure 6.2. These consist of: (1) the nearly complete reversibility of the device's output characteristics; (2) bias–assisted laser processing, or the simultaneous application of gentle laser processing with applying electrical bias or voltage with a low sweep rate (e.g., ~500 ms/mV), produces very different output characteristics than processing with only an optical source; and (3) the ability to laser–process wavelength–dependent, electrical responses. The flexibility of laser–modified and bias–assisted devices are illustrated in Figures 6.3A–B with operation under halogen and 532 nm light respectively. The gray lines represent the dark currents, which do not change appreciably, even after gentle laser processing (not included in Figure 6.2B for clarity). In Figure 6.2A, LET operation with $P_g(Halogen)$ = 36.1 μW before gentle laser processing is represented with the orange line, while the dark orange line demonstrates the enhanced current obtained immediately after laser processing with $P_w(532\ nm)$ =

3.5 μW (changes occur on the order of seconds). The blue line represents a nearly complete recovery to initial values, which was collected using the same P_g(*Halogen*) value a few minutes after laser processing. The initial or pristine response (orange line) demonstrates a single slope leading to a current plateau, while the laser–modified response produced two distinct slopes leading to the first plateau, which shortened the current plateau. As a result, the plateau's V_{ds} onset shifted from ~2.25 to ~9.75 V. These changes affect device operation. For example, the two slopes indicate little to negligible I_{ds} enhancement at low operating voltages, e.g., $V_{ds} \leq 3.5$ V, while a near doubling and tripling of the I_{ds} was observed at $V_{ds} = 3.82$ V (from 1.04 to 2.00 μA) and $V_{ds} = 9.04$ V (from 1.05 to 3.48 μA) respectively. The reverse current also increased from –0.16 to –0.50 μA at $V_{ds} = -1.48$ V. The stable, laser–processed response demonstrates near recovery of the I_{ds}–V_{ds} "shape" (blue line), or a transition from two slopes back to only one, which also lengthened the current plateau. After recovery, the current plateau is slightly shorter than the initial response, and it also possesses a slightly enhanced forward current, e.g., from 1.04 to 1.58 μA and from 1.05 to 1.66 μA at $V_{ds} = 3.82$ and 9.04 V respectively, and a reduced reverse current, e.g., from –0.16 to –0.12 μA at $V_{ds} = -1.48$ V. As will be shown later with photoluminescence measurements, the incomplete recoverability likely stems from laser–annealing deep–level defects.

Gentle, bias–assisted laser processing is demonstrated in Figure 6.2B, where the same P_w(*532nm*) = 3.5 μW is employed while sweeping V_{ds} from –21.00 to + 21.00 V at a low sweep rate (~500 ms/mV). The I_{ds}–V_{ds} "shape" transition from a double to a triple plateau is attractive for devices requiring multiple I_{ds} operation points, such as in

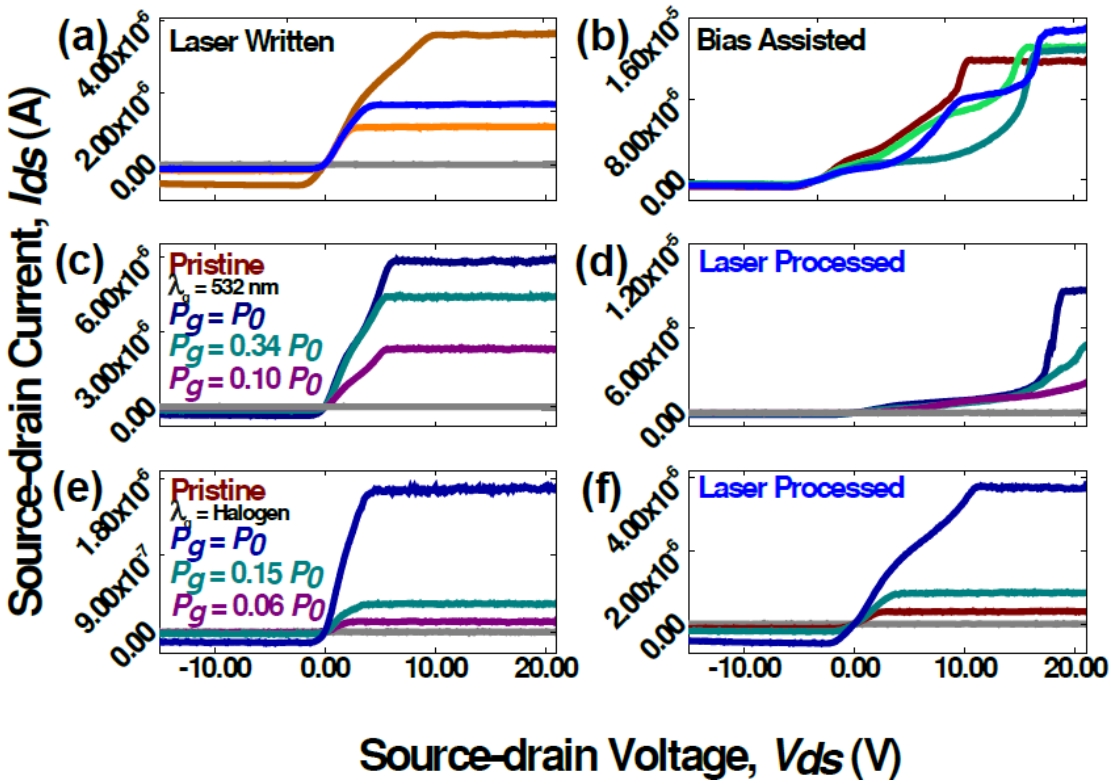

Figure 6.2 Demonstration of gently (or reversibly) laser–processing a LET's output characteristics. **(a)** Optical gating with $P_g(Halogen)$ = 69.1 μW before (orange line), immediately after (dark orange line), and several hours after (blue line) modification with $P_w(532nm) \approx 3.5$ μW, where electrical changes were observed after seconds of exposure to 532 nm light. The picoamp–level dark current (gray line) was not appreciable altered by laser processing. **(b)** Bias–assisted laser modification using the same P_w as (a) but with $P_g(532nm)$ = 2.60/2.22 μW before/after laser processing, while V_{ds} was swept from -21.00 to 21.00 V at a rate of ~500 ms mV^{-1}. Output characteristics for the same pristine and laser–processed device was collected using **(c–d)** $P_g(532nm)$ = 2.60/2.22 μW and **(e–f)** $P_g(Halogen)$ = 69.1/69.1 μW before/after laser processing with $P_w(532nm) \approx 3.5$ μW respectively. Although the optical gate powers before and after modification differ slightly, the same fractional P_0 values are used before and after.

multi–level memory and logic applications. The I_{ds}–V_{ds} curves were measured immediately after (bright green line) and 10 min. after (cyan line) laser processing the device's CdSe SNW. After 7–8 hours in air, a reproducible response (blue line) was observed that is qualitatively similar to the (bright green) curve measured immediately after laser processing the device. The long stabilization times, and conversion from a triple plateau, to highly rectified behavior, and back to a triple plateau could result from oxygen desorption [434]. Bias–assisted laser processing is demonstrated to illustrate

the potential to laser–tune different electrical response from that obtained with only laser illumination, but it will not be investigated further. Figures 6.3C–F explore the potential of gently laser processing a device to display specific, electrical characteristics when optically gated with 532 nm and halogen light. The effects of laser tuning LET output characteristics in Figures 6.3C–D and Figures 6.3E–F, respectively, were obtained with $P_g(532nm)$ = 2.60/2.22 μW and $P_g(Halogen)$ 36.1/36.1 μW before/after gentle laser modification with $P_w(532nm) \approx 3.5$ μW. LET operation with 532 nm light demonstrated altered output characteristics from two current plateaus to highly rectified after laser processing, although these values nearly recovered to their initial values after 7–8 hours in air (e.g., see Figure 6.2A for halogen recovery). The laser–modified curves in Figure 6.2D presented a small, first plateau at ~2 V, which was similar to the pristine device's V_{ds} onset of its current plateau, but with a greatly reduced I_{ds} relative to the pristine device. For example, the I_{ds} decreased from 1.50 to 0.17 μA and from 4.56 to 0.60 μA at V_{ds} = 1.43 V and 4.93 V respectively. A decrease in the reverse bias was also observed, where the I_{ds} experienced a three–fold reduction from –0.35 to –0.11 μA when V_{ds} = –1.48 V. Halogen operation, which illuminates a broader device area, produced both similar and contrasting features. When $P_g(halogen)$ = 63.1μW before/after laser processing, as displayed in Figures 6.3E–F respectively, the V_{ds} onset of halogen's first plateau also did not shift appreciably after laser processing, while the second plateau's V_{ds} onset shifted to ~9.75 V. As before, this reduced (increased) the I_{ds} slightly at relatively low (high) voltage, where $V_{ds} \approx 3.5$ V served as an approximate threshold between these effects. This trend is also apparent in device operation. As examples, the I_{ds} relative to pristine operation decreased from 6.97 to 6.09 μA at V_{ds} = 1.43 V and increased from 1.67 to 1.96 μA when V_{ds} = 4.93 V.

A tripling of the reverse bias was also observed, e.g., from –0.12 to –0.43 μ A at V_{ds} = –1.48 V. The relatively weak changes under halogen illumination primarily results from broad–area illumination of the SNW, where only one spot was gently modified with the 532–nm laser. This explains the negligible I_{ds}–V_{ds} differences at low optical powers, while at the highest power, the origin of a second slope is unclear, but it is a result of laser modification.

The differences between LET operation with 532 nm and halogen sources in Figures 6.3C–F demonstrate combined wavelength– and illumination–area dependent changes in LET operation before and after laser processing. To decouple wavelength and illumination–area effects, LET operation was performed on a different device, with a 10. μm long SNW, before and after gentle laser processing using λ_g = 633, 532, and 442 nm (Figure AV.2). These finding generally support those observed in Figure 6.2, where either increased rectification or altered first and second current plateaus were observed, e.g., a change in the V_{ds} onset and I_{ds} values. This implies that 532 nm light operation, as shown in Figures 6. 3C–D, is representative of focused optical sources, although different illumination sources, as previously demonstrated in Ref. [182], can tailor the current plateau's V_{ds} onset, and the on/off ratios through I_{ds} changes. An interesting observation was obtained with λ_g = 633 nm in Figure AV.2, where a transition from non–linear output characteristics to a more linear laser–power dependence was observed after laser processing the SNW with $P_w(532nm)$ = 3.6 μW (and similar P_g operation before and after laser processing). Relationships between $P_g(\lambda_g)$–dependent photoluminescence (PL) emission for the devices appear in Figure AV.3. As expected, an increased I_{ds} (at V_{ds} = 0 V) resulted in reduced PL emission, which stems from trap filling and free carrier diffusion from the measurement location;

however, no direct correlation was observed between the non–linear electrical behavior and the relatively linear, laser–power–dependent, PL emission for λ_g = 633 nm. Additional investigation, which is beyond the scope of this dissertation, is required to determine the source of this behavior.

A LET's output responses also manifest themselves in transfer characteristics (Figure AV.4), or I_{ds} vs. $P_g(\lambda_g)$ as an analog to a FET's I_{ds} vs. gate voltage (V_g) curves, and a LET's unique multi–optical–gate functionality, such as when two optical beams are used to simultaneous gate a LET (Figure AV.5). The relationship between output and transfer characteristics are straightforward, where an increase in I_{ds} for a given V_{ds} increases the on/off ratio. Laser–processed electrical responses; however, are more complex for multi–gate behavior. Dual optical gating with $P_{g,1}(532nm)$ and $P_{g,2}(Halogen)$ drastically altered the multi–gate function (Figure AV.5). A current amplification ratio, R, was obtained by taking the ratio of the current measured under both optical sources to that of the summed current produced through independent illumination with each optical source. The pristine device demonstrated optical amplification at low laser powers with a maximum R of ~10, which yielded an implied gain of ~15 [182], while the amplification factor decreased to near zero as the power of either optical gate was increased. After laser processing the device with $P_g(532nm)$ $\approx$ 3.5 μA, the maximum R was reduced by about one order of magnitude to ~1.5, while optical amplification was observed over a smaller power range. This implies that multi–optical–gate functionality can may be modified, although an enhancement is preferable. This concept could be extended to laser processing a photo–detector's responsivity, which could be useful in night vision and other applications requiring performance

discrimination of select, low–power optical frequencies, while minimizing effects from background frequencies.

6.3 Unraveling the Mechanisms: Laser Modified Optical Properties

The electronic changes created through gentle and irreversible laser processing also altered optical properties, which can yield mechanistic information or function as optical feedback in a manufacturing environment. Figures 6.4 presents PL and Raman spectra obtained after gentle and irreversible laser processing of single CdSe SNWs through a 100x objective lens (*N.A.* = 0.9). While both gentle and irreversible laser–processing regimes did not alter PL peak energies appreciably, laser processing did alter the PL intensity and Raman features. PL showed increased and decreased exciton emission intensities, which hints at the possibility of two different mechanisms. Figure 6.3A shows initial PL emission collected with P_0 = 167.6 μW of 532 nm light, where the PL emission intensity was altered with $P_g(532nm)$ = 397 μW after 300 s and 900 s of elapsed laser heating (in 100 s intervals). The PL intensities increased up to a maximum of 300 s (elapsed time), while the fourth, 100 s series marked a reduction in intensity, which eventually dropped below its initial value after 600s of elapsed heating. Further heating continuously reduced PL emission to 1200 s of elapsed exposure, at which point, the emission experienced nearly complete quenching. Negligible deep level emission (~1.5 cps) was observed ranging from ~1.33–1.53 eV, but this feature will be discussed subsequently. In Figure 6.3B, a CdSe SNW was gently illuminated using $P_w(532nm)$ = 0.366 mW (t = 0.5 s), while the PL spectra was collected with 2.07 μW of 532 nm light. The PL intensity increased by ~1000 cps (from 3,894.5 to 4,885.7 cps), while the peak energy displayed negligible change and remained centered around

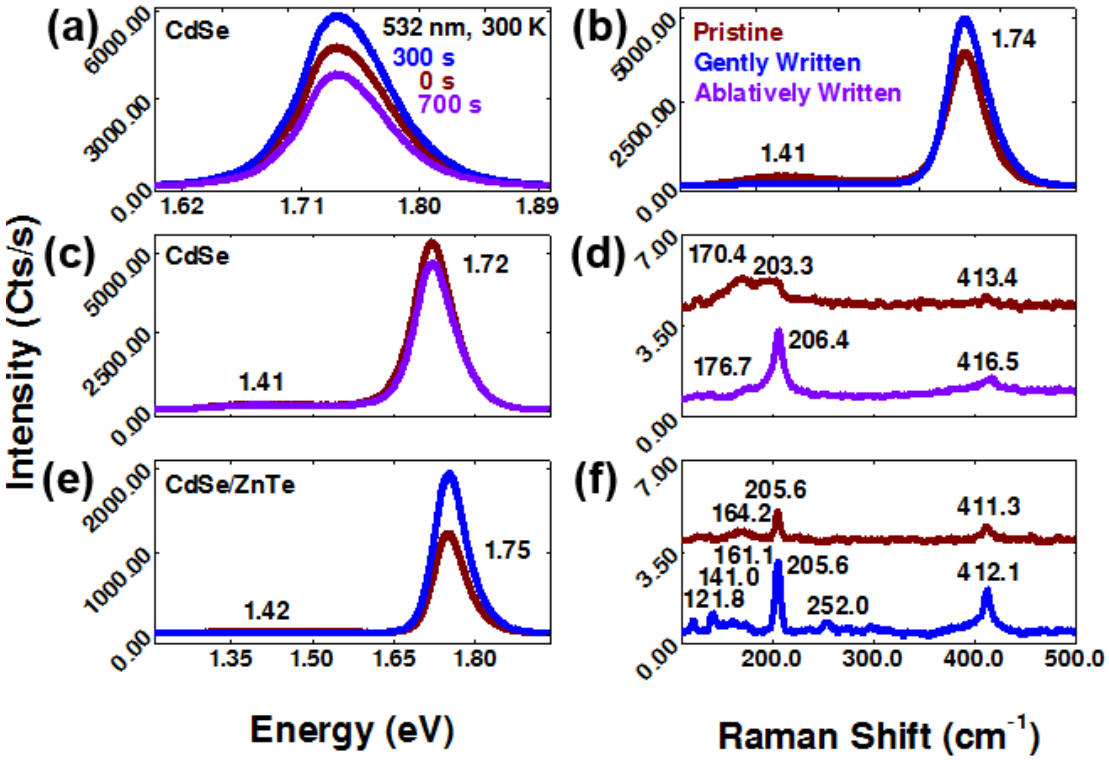

Figure 6.3 Optical investigation into laser processed single CdSe and CdSe/ZnTe SNWs. **(a)** PL emission as a function of the number of t = 100 s exposures to $P_w(532nm)$ = 0.397 mW, while PL emission was collected with 167.6 μW of 532 nm light. **(b)** Enhanced PL emission from a single CdSe SNW using $P_w(532nm)$ = 0.366 mW (t = 0.5 s), while the PL spectra was collected with 2.07 μW of 532 nm light. The Raman spectra (not shown) displays negligible peak shifts and intensity changes. **(c–d)** PL and Raman spectra were collected for the same pristine and irreversibly laser–processed, CdSe SNW using $P_w(532nm)$ = 0.366 mW, while the optical spectra were collected with 2.07 μW of 532 nm light. The laser–processed PL and Raman spectrum were collected after t = 0.25 s and four, 100 s exposures to P_w respectively. To gain additional insight, **(e–f)** an all–wurtzite, CdSe/ZnTe SNW [95] was laser processed using $P_w(532nm)$ = 0.366 mW (t = 0.25 s) for both PL and Raman spectra.

1.74 eV. Figure AV.6 demonstrates the reproducibility of the measurements and indicates that this intensity change is significant. Deep–level emission was also observed at ~1.4 eV, which is magnified for convenience in Figure AV.7, and displayed undulations with spacing of ~20 meV under 532 nm excitation. The oscillatory PL emission has been observed in silicon, and was removed after laser annealing [401, 403]. While their origin is still being debated, surface phonons may be involved. Figure AV.8 explores ultraviolet illumination of different semiconductor systems, where

undulations with spacings of 50–60 meV were observed in different material systems. The observed generalized PL behavior could imply the presence of common origins. Gentle laser processing (annealing) in Figure 6.3A not only completely dampened the oscillations, which simultaneously produced enhanced exciton emission, but the dominate ~1.4 eV peak transformed into two peaks located at 1.42 and 1.49 eV. This double peak structure was previously observed in CdSe quantum dots and is attributed to surface states [435]. Altering the peak structure and intensity of the deep–level emission peak, while simultaneously enhancing exciton emission, both hint at the laser modification of defect states or configurations. The corresponding Raman spectra was not collected on this SNW, but similar spectra reveal negligible changes at such low laser powers.

Ablative laser processing is explored next, where its contrast with gentle laser processing yields additional mechanistic insight. A single CdSe SNW was partially ablated with four, 100 s exposures to $P_w(532nm)$ = 0.366 mW (t = 100 s), while the optical spectra were collected with 2.07 μW of 532 nm light. Figures 6.4C–D contain the respective Raman and PL spectra for this SNW. While laser ablation reduced the exciton PL emission in Figure 6.3C, which stems from a reduced material volume, no change was detected in either the exciton peak energy at 1.72 eV or the nature of the deep–level PL emission, e.g., in terms of peak structure or its oscillatory behavior. The pristine Raman spectra displayed in Figure 6.3D reveals a broad peak at 170.4 cm^{-1}, as well as, CdSe's first and second order, longitudinal optical (1– and 2–LO) phonon peaks at 203.3 and 413.3 cm^{-1} respectively. Irreversible laser processing shifted the broad peak to 176.7 cm^{-1} and the two LO peaks to 206.4 and 416.5 cm^{-1} respectively. To understand the Raman spectra in Figure 6.3D, bulk CdSe modes (at 300 K) are

provided for reference, and include two transverse optical (TO) phonon modes located at 166 and 169 cm^{-1} respectively, whereas the 1LO peak is located at 209 cm^{-1}, while the anisotropy typically found in nanostructures allows weak observance of the normally forbidden, 2LO peak at ~419 cm^{-1} [69, 436]. Experimental measurements [95] collected on a CdSe thin film revealed down–shifted 1LO and 2LO peaks at 205.8 and 411.9 cm^{-1} respectively. Interestingly, laser processing CdSe's 1LO phonon peak resulted in significant enhancement of its 1LO peak as its (typically assigned) TO peak completely disappeared. Laser–removal of the broad feature defies expectation: both single crystalline and polycrystalline CdSe are expected to contain similar Raman peaks but with different TO and LO intensity ratios [189]. The reproducibility of this result was explored in the partially ablated device in Figure 6.1C. Raman spectra were collected across this device (Figure AV.9), where spectra obtained at pristine and lightly ablated sites were similar to those in Figure 6.3D. These findings correlate optical and electrical properties, while structural changes were examined for a partially ablated SNW using TEM (Figure AV.10). The main finding is the laser–induced formation of a polycrystalline surface layer with the same lattice spacing as the underlying single crystalline material. As only the nanowire body (and not M–S junction) was modified, it is likely that trapped charges in grain boundary "necks" or connections restrict carrier flow [194], and could produce the enhanced rectification observed in Figure 6.1C.

The optical spectra in Figures 6.3A–D raise important questions: (1) what is the origin of the broad Raman feature, and (2) why does the broad peak's disappearance enhance CdSe's 1LO peak? While it is difficult to answer these questions based solely upon these optical spectra and structural investigation, laser processing a CdSe/ZnTe (core/shell) SNW yields additional information. Note that the CdSe core templates shell

growth so that a ZnTe shell with wurtzite structure is formed instead of its typical zinc–blende structure [95]. The CdSe/ZnTe SNW was laser processed with $P_w(532nm)$ = 0.366 mW (t = 0.25 s), while the optical spectra were collected with 2.07 μW. Structural investigations using TEM revealed no surface damage or alteration of the crystal structure (Figure AV.11), although optical changes could possibly occur from surface state modification or altering the ZnTe spheres on the SNW surface. The PL spectra in Figure 6.3E revealed enhanced PL emission at 1.75 eV after laser processing. The overall intensity is less than half of the CdSe core, which cannot be explained solely by differences in SNW size and laser power. The ZnTe shell was previously found to enhance carrier separation and reduce exciton emission relative to the bare CdSe core [95], which would increase the number of carriers diffusing away from the measurement site. The PL spectra revealed no change in deep–level emission at ~1.4 eV in regards to the oscillatory peak spacing or peak structure, which contrasts the results achieved with gentle laser processing. This suggests some protection by the ZnTe shell, while intensity reduction of the ~1.4 eV with a simultaneous increase exciton emission suggests that defect states were laser annealed. The corresponding Raman spectra appears in Figure 6.3F, where up to only the 2–LO peak was observed. As both CdSe and ZnTe have similar Raman peak positions, it is not straightforward to decouple their individual contributions. The lack of 3– and 4–LO peaks are probably due to the very thin (~1 nm) ZnTe shell, and a dominate CdSe contribution to the Raman signal. The 2LO peak shifted from 411.3 to 412.1 cm^{-1}, while the 1LO peak did not shift. Other interesting occurrences were also observed. First, the broad feature moved to a lower Raman shift or from 164.2 to 161.1 cm^{-1}. While the broad peak did shift, its peak shape and size were unaltered, which further suggests that the ZnTe shell

offered some protection from laser processing. Second, three new peaks appeared. The two peaks at 121.8 and 141.0 cm^{-1} resulted from laser–forming tellurium–based species [140, 141, 243]. This attribution is supported by the dominant 1LO Raman intensity relative to the 2LO intensity observed after laser processing, which is a well–known, resonant Raman signature for detecting impurities [134, 380]. The 252.0 cm^{-1} peak could originate from laser–formed, amorphous selenium [437]. While the Raman shifts suggests that the broad feature is sensitive to surface features, this hypothesis may be further evaluated at another interface.

Figures 6.4A–B respectively compares Raman spectra of CdSe and CdSe/ZnTe SNWs either at the middle (wine line) of the SNW body or at the Au–SNW interface (light green line). The Raman spectra were collected with 207.5 μW of 532 nm light. The CdSe SNW displays the broad feature and the 1LO peak at 166.9 and 196.7 cm^{-1} respectively. At the Au–CdSe interface, the broad feature was not observed, while the 1LO up–shifted to 207.8 cm^{-1}. A similar effect is observed for the CdSe/ZnTe SNW, where the ZnTe shell provides a greatly enhanced Raman signal. The broad peak appears at 164.7 cm^{-1} with the 1– and 2–LO peaks at 206.0 and 410.4 cm^{-1} respectively, while at the Au–CdSe/ZnTe interface, the broad feature was not observed, and the 1– and 2–LO peaks drastically up–shifted to 237.4 and 481.4 cm^{-1} respectively. The source of this up shift is not known and requires further investigation (e.g., see Chapter 5), while Figure AV.13 demonstrates reproducible measurements for Au–CdSe/ZnTe SNWs. Surface sensitivity is further supported by laser processing CdSe and CdSe/ZnTe SNWs, which produced similar Raman features but with the broad feature shifted in the opposite directions. Figures 6.3–6.4 demonstrates that this broad peak is sensitive to surface conditions, which include the presence of a shell material, thermal

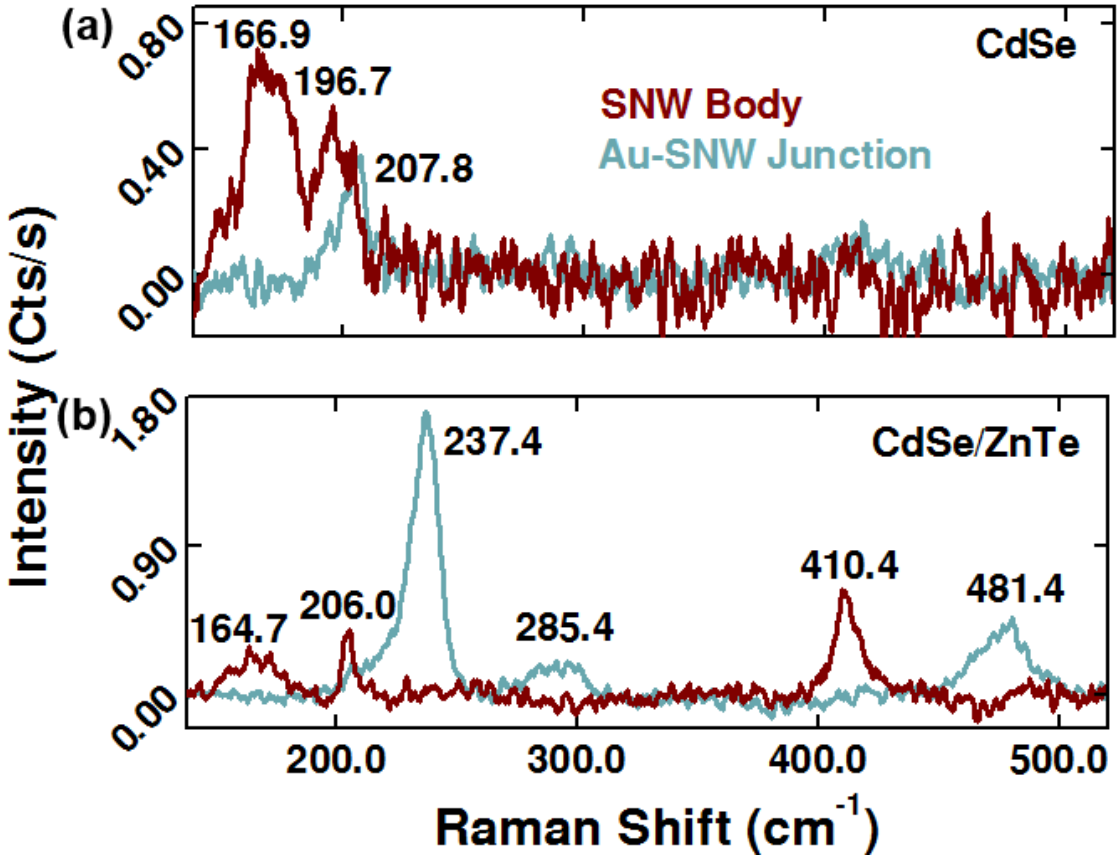

Figure 6.4 Raman effect of the SNW body and at the Au–SNW junction for **(a)** CdSe and **(b)** CdSe/ZnTe SNWs. The Raman spectra were collected with 207.5 μW of 532 nm light.

oxide, ablation, and laser–formed surface species. The oscillatory deep–level (PL) emission may suggest that the broad peak results from the presence of oxygen, where Au or polycrystalline layers prevent oxygen passivation, although the origin could be more complex. Furthermore, a holistic view of Figures 6.3–6.4 highlights optical relationships that can be correlated to electronic changes. A practical implementation is as optical feedback to indicate when the desired electrical changes have been achieved, while further investigation is required to develop this finding into interesting applications. For example, reversibly tuning this peak could enable a dynamic switching function that enables wavelength–selective electrical characteristics. It may also be possible to laser process circuit functions. One could imagine processing material shapes with and without this broad peak for transistor–like and rectified

electrical behaviors. If other fundamental electronic characteristics could also be developed, then it would be, in principle, possible to laser process circuit behavior using the same materials and fabrication processes. This is indeed a profound implication that deserves continued exploration.

6.4 Conclusions

Laser processing is a fast, cost–effective, and high–throughput technique capable of modifying electrical responses for a variety of devices and form factors. Two general mechanisms are used to laser modify SNWs: optical powers that produce what is termed here as gentle (e.g., reversible and non–destructive) and irreversible changes in electrical properties. These effects were explored structurally, optically, and electrically in LETs. As previously demonstrated, these devices have wavelength–dependent, output characteristics in terms of their on/off ratios through I_{ds} changes, and V_{ds} onsets of their current plateaus. Gentle laser processing provided another means to dynamically tune these parameters, which produce increased rectification under focused illumination, or enhanced I_{ds} with increased V_{ds} onsets for broad–band and uniform illumination (with halogen light). It is important to note that gentle laser processing did not appreciably alter the dark current. Their electrical responses experienced near complete recovery to initial values after several minutes, where the unrecovered component results from laser annealing defect states or configurations. This conclusion is supported by two observations. First, reduced deep–level PL emission at ~1.4 eV occurred with simultaneous enhancement of exciton emission at ~1.7 eV (with constant peak energy before/after laser processing). Second, deep–level emission displayed oscillatory behavior with a peak spacing of ~20 meV, where gentle laser processing transformed the peak structure from a single dominant peak at 1.41 eV

to two dominate peaks with the second at 1.49 eV. Both of these finding, as previously mentioned, are linked to surface state effects. Raman spectra revealed little change after exposure to such low laser powers (e.g., 3.2–3.6 μW) and did not yield additional information. Irreversible laser processing was permanently achieved through laser ablation, which drastically altered the dark current, which include altering the ohmic response or linear slope, conversion from ohmic to rectified behavior, and alteration of the forward dark current. Structural investigations reveal laser–formation of a polycrystalline CdSe layer with an identical lattice spacing as the underlying single crystalline material. The polycrystalline structure could trap charges at grain boundaries or "necks," which accounts for the altered dark currents (e.g., see Section 3.5). PL spectra revealed decreased exciton emission from reduced material volume, while the nature of the deep–level emission was unaltered. The corresponding Raman spectra revealed complete laser–removal of a broad Raman feature at ~160–170 cm^{-1}, and occurred with simultaneous enhancement of the 1LO peak. This defies expectation, where the TO and LO modes in single and polycrystalline CdSe are expected to produce different intensity ratios. Furthermore, assignment as a TO mode does not explain the preferential 1LO enhancement resulting from surface damage. In order to yield additional information, an all–wurtzite, CdSe/ZnTe SNW was laser modified. While CdSe's exciton emission increased at the expense of quenched deep–level emission, which once again supports the laser annealing of defects, no oscillatory behavior was observed. Furthermore, Raman spectra revealed the appearance of peaks related to laser–formed Te (from the ZnTe shell) at 121.8 and 141.0 cm^{-1}. Amorphous selenium was also observed after laser heating at 252.0 cm^{-1}. Structural investigations revealed no surface damage or alteration of the underlying crystal structure. Interestingly, the

size and shape of the broad Raman peak did not change, which implies some protection from the ZnTe shell. Furthermore, its Raman shift was in the opposite direction of the ablatively modified CdSe SNW. It appears that the broad feature is sensitive to surface conditions, which include the presence of a shell material, thermal oxide, ablation, and laser–formed surface species. These findings suggest that the broad peak may be related to surface phonons rather than TO modes. Finally, changes in optical properties could be used as an optical feedback mechanism in a fabrication process. The optimal choice is PL emission because this technique is generally much quicker than Raman spectroscopy.

CHAPTER 7: CONCLUSIONS

"Some people do not like to think. If one thinks, one must reach conclusions."
Helen Keller, 1967 In Helen Keller: Her Socialist Years

7.1 Towards an Electronic–Optical Device Era

This dissertation revealed conceptual foundations that, when viewed holistically, demonstrate important aspects for device operation, fabrication, and design. In general, the following concepts were illustrated: (1) the ability to perform practical and viable electrical switching based upon the photoconductive phenomenon for optically driven analog and digital applications; (2) modulation of electron–phonon coupling strengths over broad ranges to enhance nanoscale device performance, which could lead to novel devices and applications; and (3) laser processed tuning of specific optical and electrical properties on a nanowire–based device, which provides a robust pathway for inexpensively and reliably fabricating integrated devices and circuits.

The LET concept presents a drastically different conceptual approach to FET–based IC technologies by using an all optical, rather than a physical gate mechanism. A LET utilizes the well–known photoconductivity attribute of a semiconductor that is naturally and commonly used for photo-detection. Not only is LET function competitive with FET performance, and offers digital and analog applications typically only available with transistors, but it also provides functions not achievable in FETs. A LET's most significant feature is its multi–optical–gate, which can provide much

greater flexibility than a FET, such as tunable gate properties and multiple independent gates that enable further increases in chip density. A LET could potentially operate in the ballistic transport regime by overcoming limitations associated with a FET's gate fabrication and doping control, which suggests that it could continue Moore's law to the quantum scale. These features are achieved through: (1) a simple device architecture that potentially reduces fabrication costs; (2) feasible down scaling to the quantum level; (3) efficient, multi–functional ability in a single device; and (4) operation with low energy consumption or total switch energy, which minimizes thermal issues plaguing nanoscale electronics devices. Prototype CdSe–nanowire–based LETs demonstrated output and transfer characteristics resembling advanced FETs, e.g., on/off ratios up to ~1.0×10^6 with a source–drain voltage of ~1.43 V, gate-power of ~260 nW, and a subthreshold swing of ~0.3 nW/decade (excluding losses). This work offers new electronic–optical integration strategies and electronic and optical computing approaches. LET operation principles are independent of a particular material system, thus, when applied to silicon, existing silicon–based microelectronic and photonic technologies can be readily adapted for LET technology. The LET concept can also be extended to develop other light–effect devices and circuits.

Electron–phonon coupling is typically assumed to be a static material property that greatly affects electronic transport at the nanoscale. Despite continued investigation, controversy and even contradictory experimental and theoretical findings are still reported, which stem from different theoretical assumptions and experimental techniques. Resolving these issues could improve device optimization. As examples, a high coupling strength has great potential in laser cooling applications, while a low coupling strength reduces energy losses and improves efficiency in electronic devices,

while tunable coupling strengths suggest the ability to realize novel electronic and optoelectronic devices. Electron–phonon coupling strength were obtained through the ratio of the second to first order Raman peaks, $R = I_{2LO}/I_{1LO}$ (proportional to the Huang–Rhys factor), which were collected from Raman spectra under nearly resonant conditions. Although coupling strength modulation was observed for zinc–blend, ZnTe bulk, thin film, and nanowire structures, the dynamically tunable range was greatest for nanowires. This is expected as a nanostructure's larger surface–to–volume ratios are more susceptible to extrinsic perturbations that ultimately effect the coupling strength. Laser–formation of tellurium–based species on ZnTe nanowires, which was ignored in a previous diameter–dependent study on ZnTe nanowires, dynamically altered *R* from 7 to an impressive 32 on the same nanowire! *R* was eventually reduced to 5 after forming a sufficient Te concentration, while tuning the (532 nm) laser power from a few microwatts to 150 microwatts yielded a more modest dynamic range of 7 to 11. Other explored effects include size dependence, chemical effects (methanol exposure), and interface effects (e.g., at a gold–nanowire junction). These findings suggest potential use as sensors and bar codes, where, for instance, a bar code could be comprised of alternating gold and ZnTe nanowire segments. The ability to tune a material's coupling strength has significant and far reaching implications. For example, by assuming that the observed changes are an intrinsic, nanoscale effect, then interpreting coupling strength as a static material property is inappropriate for ZnTe. This work also prompts a revisiting of conventional theoretical frameworks and a reinterpretation of previous experimental findings.

Laser processed tuning of specific optical and electronic properties for nanostructure–based device properties provide an inexpensive, flexible, and high–

throughput technique, where the same materials and device fabrication processes could provide a menu of device function. Laser modification of optical and electrical properties in a LET's metal–semiconductor–metal (In–CdSe–In) structure was explored. While LETs offer reproducible operation with optical gate powers ranging from a few picowatts to ~3 microwatts, higher optical powers, as with any semiconductor material, induces optical and electrical changes that enables the laser modification of specific device properties. Intermediate powers produced reversible output characteristics, while higher powers produced irreversible structural changes, which respectively correlate with either transient or permanent modifications of the device's optical and electrical properties. Drastic irreversible modification of the electrical characteristics included converting an ohmic response (linear slope change) to rectified characteristics, and modification of both forward and reverse currents. No structural changes were observed after reversible (gentle) laser processing. Meanwhile, irreversible changes permanently altered both the dark and photo–currents, and corresponded with the laser formation of polycrystalline CdSe at the ablation site. Optically, both deep–level photoluminescence (~1.4 eV) and a Raman peak at ~160–170 cm^{-1} disappeared while "sharpening" CdSe's first order longitudinal optical (1LO) phonon peak. The optical characterization power densities, which are low compared to typical milliwatt values for similarly sized nanowires, revealed, for the first time, these features in single–crystalline, CdSe nanowires, and merits further investigation.

In this dissertation work, first, the conceptual foundations for a new device era (e.g., electronic–optical devices) was demonstrated with the LET, which illustrates the viability and competitiveness of the photoconductive phenomenon. Second, the LET platform not only mimics a FET's electronic characteristics using a lower total switch

energy, but it also provides novel functionality, such as optical logic gates and optical amplification, not found in either photo–detectors or FETs. Third, a combination of defect and dynamically tunable electron–phonon coupling strengths minimizes impurity scattering and phonon interactions respectively. This implies that a LET could operate effectively at the quantum scale. Fourth, laser processed tuning of electronic and optical characteristics enables flexible device and circuit design using the same materials and fabrication processes, although this technique could potentially be extended to other material systems and fabrication processes. Finally, a glance into device functionality potentially offered by electronic–optical devices is briefly discussed in Chapter 8. This chapter's purpose is to inspire further discovery and innovation. Perhaps this dissertation could inspire changes that manifest themselves though an altered technological reality, where one day, our modern computers will be viewed as ancient relics of an age relying upon the binary modulation of electrical signals.

CHAPTER 8: OUTLOOK – REALIZING AN ELECTRONIC–OPTICAL DEVICE ERA

"Never underestimate the power of thought; it is the greatest path to discovery."
Idowu Koyenikan, 2016 Wealth for All:
Living a Life of Success at the Edge of Your Ability

8.1 Inspiring the Future

Even with a long, constantly evolving, scientific body of knowledge – with books, journals, and online repositories serving as storage media – nature's complexity ensures that there is indeed more to discover. While this dissertation has directly challenged conventional thinking, the intention of this last chapter is to motivate further scientific and technological development, and to inspire novel concepts. Natural questions are to inquire into the next steps for research, and perhaps, to ponder how a mere dissertation can assist in realizing a very different reality than the one enveloping us now. These questions will be addressed by considering multi–level logic, extended laser–processed tuning, and progressing towards all–optical computing through contactless, 3D devices and circuits. Additionally, Appendix VI contains additional work on piezoelectric–related devices, which could also be implemented as electronics devices.

8.2 LET–based Logic Applications

The LET concept could be further developed immediately by using multiple devices to construct *universal* logic gates, e.g., the *NOR* and *NAND* logic gates shown in Figure AIII.1, which when combined, can mimic any existing logic gate function. Logic gates are general purpose, Boolean–based devices used to construct circuits that

can be used in applications ranging from controlling water sprinklers to providing an automated emergency shutoff function. A LET also has other immediate applications. A single LET could function as either a conventional (Boolean) or non–Boolean adder. The addition of bits, or 0's and 1's, is the core principle behind Boolean logic. Conventional adder circuits employ several transistors in a rather intensive process. Despite a LETs very different operational principles, it is electrically similar to n–type, metal–oxide–semiconductor (MOS)FETs, and could leverage these existing circuits to reduce the number of required transistors and computation times [438]. This is particularly advantageous as large and complex transistor networks, which are required for binary switches, produce slower raw switching speeds [439, 440]. A more interesting direction, however, is multi–level logic, which vastly increases data processing capability. This requires a shift in thinking from transistor density, where each device performs binary switching, to considering the computational density of multi–level switching. The primary impediment to realizing multi–level switching is the lack of a true multi–state device, where only limited successful implementations have been realized, e.g., current–mode CMOS devices [439]. A LET offers multi–level logic functions by merely changing the optical gate power, and again, it may be implemented in existing circuits designed for n–type MOSFETs [441].

8.3 Laser–processed Tuning of Electrical and Optical Properties

Chapter 6 demonstrated laser–processed tuning of CdSe's electrical and optical properties and their subsequent modulation with light. Ohmic and rectified characteristics, which form two fundamental electronic elements, were demonstrated. In terms of technological development, the next step is to use laser processing to achieve more complex electrical behavior in a single nanowire device, such as a LET,

and to correlate electrical and optical behavior to obtain foundational knowledge beyond that in Chapter 6. This dissertation demonstrated the ability to laser process a single spot on a nanowire, while laser processing multiple spots could produce more complex electrical characteristics. The next phase would extend these results to an ultrathin film, which could be thought of as a 2D circuit board for applying and extending the 1D carrier behaviors observed in nanowires. The ultrathin film's surface could be portioned into different regions, where each region is laser processed to perform an assigned electronic function. This is conceptually similar to wiring conventional electronic elements, but with carrier diffusion length replacing metallic leads. It would be interesting to observe how these different regions modify carrier behavior both under dark and illuminated conditions. Carrier behavior could be investigated optically with μ–Raman, μ–PL, μ–reflectance, μ–transmission, and μ–LBIC (laser beam–induced current). Figure 8.1 demonstrates these techniques in a thin film solar [442], where correlative imaging of a surface feature reveals defect different types of defects from the different forms of spatially–resolved, characterization techniques. These techniques will highlight differences that produced different PL intensities in Chapter 6, while collaborations could be established to quantify carrier behavior through relevant parameters [443], investigate near–field effects [444], or to perform additional characterization on a device, such as with scanning probe microscopy [445, 446]. This research trajectory has important potential applications: (1) contactless, 3D, optoelectronic integrated circuits with potential for significantly enhanced device densities (e.g., Refs., [447, 448]), (2) optoelectronic bar codes and sensors (e.g., Refs. [363, 449, 450]), (3) photo–conductive, neuromorphic devices (e.g., Ref. [451, 452]), and (4) further progression towards all optical computing.

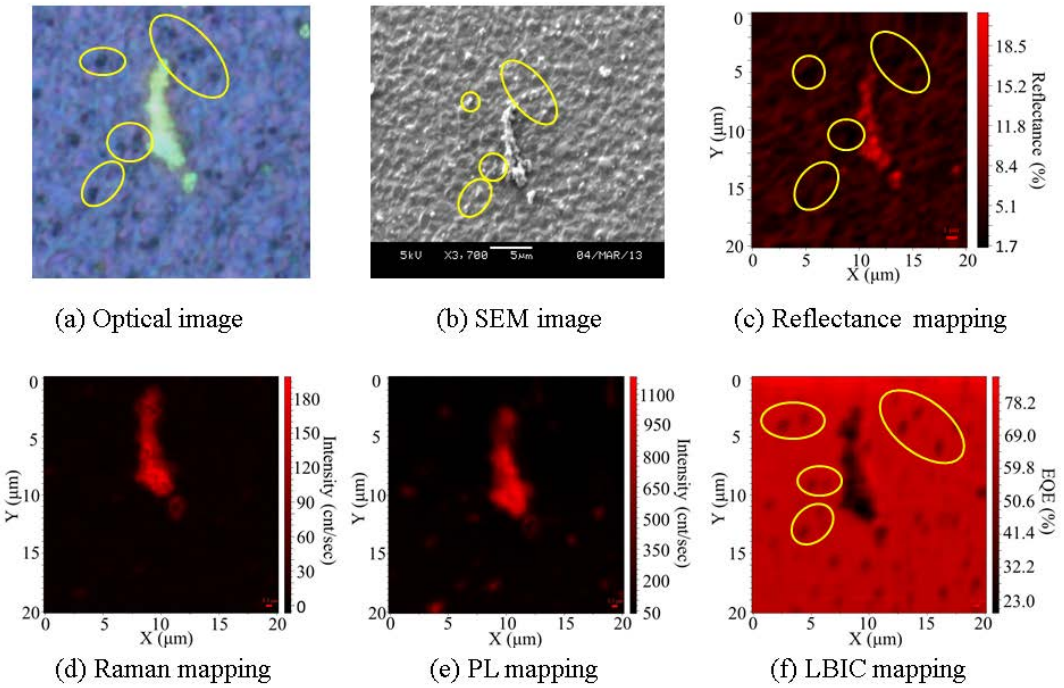

Figure 8.1 Demonstration of correlative, spatially–resolved, characterization techniques performed on a CZTS thin–film solar cell [442]. (a) Optical image, (b) SEM image, (c) reflectance mapping, (d–e) Raman mapping, and (f) LBIC mapping of a surface feature.

If the second research phase could be achieved, then laser processing can produce simple and complex electrical characteristics, e.g., (1–2) above. From a fundamental perspective, a bar code represents spatial signal variations, which could be achieved through gentle (reversible) and irreversible laser processing of ZnTe nanowires. For example, irreversibly laser–forming tellurium–based species alters both the Raman spectra and ZnTe's electron–phonon coupling strength. Forming an alternating pattern of ZnTe and Te–based surfaces could modulate the optical properties similar to a bar code. Applications require the encoding of more complex information could combine PL and Raman peak positons, integrated line intensities, and electron–phonon coupling strengths. Correlated tuning of the optical and electronic properties could also yield a practical sensor. Sensors are typically not very selective, and thus, unique optotelectronic signal patterns could be used as a fingerprint to identify specific

chemical and biological signatures (e.g., Refs. [363, 449, 450]).

Completion of the second research phase could also realize neuromorphic circuits that mimic the current spikes found in neurological systems such as the human brain, and are used, for example, in event–driven computing applications. The LET can act as a differentiator, where the derivative of a square wave produces spikes on each edge of the square. Sufficient optical power can return the wave form to its original square shape, while lower powers can reduce or completely remove the current plateau connecting the two spikes. While a LET operating under dark conditions provides a rather “rough” imitation of a neuromorphic circuit, it does illustrate proof of concept. Exploring the effects of laser processing on time–dependent electronic effects (as in Figure 4.5H) could reveal improved neuromorphic mimicry. Finally, if the last research phase is realized, then optical–electrical–optical conversions enables receipt, electrical processing, and transmission of optical signals without metallic contacts limiting device or circuit performance [447]. This would represent a major advancement towards all–optical computing. The emitted optical signal strength, however, would determine the success of such a circuit. For example, PL emission is typically much stronger than Raman emission in most materials. Imagine patterning an arbitrary array of semiconductor material, where each array element possesses a different electrical function represented in Figure 8.3. These elements absorb light and convert it to an electrical signal, perform electrical processing, followed by converting the electrical signal to light through carrier recombination and phonon–assisted luminescence. The optical signal could be reabsorbed by a neighboring element to form a circuit. The foundations for this concept are in literature. For example, a molecule–based, FET demonstrated light–emission [453]. However, no correlated study between optical and

electrical behavior exists, which is necessary to determine mechanisms to optically encode and transmit electrically processed signals.

REFERENCES

[1] D.J. Frank, R.H. Dennard, E. Nowak, P.M. Solomon, Y. Taur, H.S.P. Wong, Device scaling limits of Si MOSFETs and their application dependencies, Proceedings of the IEEE, 89 (2001) 259-288.

[2] W. Haensch, E.J. Nowak, R.H. Dennard, P.M. Solomon, A. Bryant, O.H. Dokumaci, A. Kumar, X. Wang, J.B. Johnson, M.V. Fischetti, Silicon CMOS devices beyond scaling, IBM Journal of Research and Development, 50 (2006) 339-361.

[3] K. Bernstein, D.J. Frank, A.E. Gattiker, W. Haensch, B.L. Ji, S.R. Nassif, E.J. Nowak, D.J. Pearson, N.J. Rohrer, High-performance CMOS variability in the 65-nm regime and beyond, IBM Journal of Research and Development, 50 (2006) 433-449.

[4] T.N. Theis, P.M. Solomon, In quest of the "next switch": Prospects for greatly reduced power dissipation in a successor to the silicon field-effect transistor, Proceedings of the IEEE, 98 (2010) 2005-2014.

[5] T. Shinada, S. Okamoto, T. Kobayashi, I. Ohdomari, Enhancing semiconductor device performance using ordered dopant arrays, Nature, 437 (2005) 1128-1131.

[6] H.T. Ng, J. Han, T. Yamada, P. Nguyen, Y.P. Chen, M. Meyyappan, Single crystal nanowire vertical surround-gate field-effect transistor, Nano Letters, 4 (2004) 1247-1252.

[7] I. Ferain, C.A. Colinge, J.-P. Colinge, Multigate transistors as the future of classical metal-oxide-semiconductor field-effect transistors, Nature, 479 (2011) 310-316.

[8] T. Ernst, Controlling the polarity of silicon nanowire transistors, Science, 340 (2013) 1414-1415.

[9] D.M. Fried, J.S. Duster, K.T. Kornegay, High-performance p-type independent-gate FinFETs, IEEE Electron Device Letters, 25 (2004) 199-201.

[10] M. De Marchi, D. Sacchetto, S. Frache, J. Zhang, P.E. Gaillardon, Y. Leblebici, G. De Micheli, Ieee, Polarity control in double-gate, gate-all-around vertically stacked silicon nanowire FETs, IEEE International Electron Devices Meeting (IEDM), (2012).

[11] T. Skotnicki, J.A. Hutchby, T.J. King, H.S.P. Wong, F. Boeuf, The end of CMOS scaling: Toward the introduction of new materials and structural changes to improve MOSFET performance, IEEE Circuits & Devices, 21 (2005) 16-26.

[12] X.J. Huang, W.C. Lee, C. Kuo, D. Hisamoto, L.L. Chang, J. Kedzierski, E. Anderson, H. Takeuchi, Y.K. Choi, K. Asano, V. Subramanian, T.J. King, J. Bokor, C.M. Hu, Sub-50 nm p-channel FinFET, IEEE Transactions on Electron Devices, 48 (2001) 880-886.

[13] A.M. Ionescu, H. Riel, Tunnel field-effect transistors as energy-efficient electronic switches, Nature, 479 (2011) 329-337.

[14] G.E. Moore, Cramming more components onto integrated circuits, Electronics, 38 (1965) 114–117.

[15] ITRS, Updates to the International Technology Roadmap for Semiconductors (ITRS), 2012.

[16] CMOS and beyond: Logic switches for terascale integrated circuits, Cambridge University Press, Cornwall, 2015.

[17] Y. Cui, Z.H. Zhong, D.L. Wang, W.U. Wang, C.M. Lieber, High performance silicon nanowire field effect transistors, Nano Letters, 3 (2003) 149-152.

[18] C. Thelander, P. Agarwal, S. Brongersma, J. Eymery, L.F. Feiner, A. Forchel, M. Scheffler, W. Riess, B.J. Ohlsson, U. Goesele, L. Samuelson, Nanowire-based one-dimensional electronics, Materials Today, 9 (2006) 28-35.

[19] J. Appenzeller, J. Knoch, M.I. Bjork, H. Riel, H. Schmid, W. Riess, Toward Nanowire Electronics, IEEE Transactions on Electron Devices, 55 (2008) 2827-2845.

[20] S. Banerjee, W. Richardson, J. Coleman, A. Chatterjee, A new 3-terminal tunnel device, IEEE Electron Device Letters, 8 (1987) 347-349.

[21] J. Appenzeller, Y.M. Lin, J. Knoch, P. Avouris, Band-to-band tunneling in carbon nanotube field-effect transistors, Physical Review Letters, 93 (2004) 196805.

[22] H. Ko, K. Takei, R. Kapadia, S. Chuang, H. Fang, P.W. Leu, K. Ganapathi, E. Plis, H.S. Kim, S.Y. Chen, M. Madsen, A.C. Ford, Y.L. Chueh, S. Krishna, S. Salahuddin, A. Javey, Ultrathin compound semiconductor on insulator layers for high-performance nanoscale transistors, Nature, 468 (2010) 286-289.

[23] C. Zhou, X. Wang, S. Raju, Z. Lin, D. Villaroman, B. Huang, H.L.-W. Chan, M. Chan, Y. Chai, Low voltage and high on/off ratio field-effect transistors based on CVD MoS2 and ultra high-k gate dielectric PZT, Nanoscale, 7 (2015) 8695-8700.

[24] T.N. Theis, P.M. Solomon, It’s Time to Reinvent the Transistor!, Science, 327 (2010) 1600-1601.

[25] S. Salahuddin, S. Datta, Use of negative capacitance to provide voltage amplification for low power nanoscale devices, Nano Letters, 8 (2008) 405-410.

[26] ITRS, International Technology Roadmap for Semiconductors (ITRS), 2013.

[27] M.M. Waldrop, The chips are down for Moore's law, Nature, 530 (2016) 144-147.

[28] W.M. Waldrop, More than Moore, Nature, 11 (2016) 145-147.

[29] C. Toumey, Less is Moore, Nature Nanotechnology, 11 (2016) 2-3.

[30] H. Wong, H. Iwai, On the scaling of subnanometer EOT gate dielectrics for ultimate nano CMOS technology, Microelectronic Engineering, 138 (2015) 57-76.

[31] N. Singh, A. Agarwal, L.K. Bera, T.Y. Liow, R. Yang, S.C. Rustagi, C.H. Tung, R. Kumar, G.Q. Lo, N. Balasubramanian, D.L. Kwong, High-performance fully depleted silicon-nanowire (diameter <= 5 nm) gate-all-around CMOS devices, IEEE Electron Device Letters, 27 (2006) 383-386.

[32] N. Singh, K.D. Buddharaju, S.K. Manhas, A. Agarwal, S.C. Rustagi, G.Q. Lo, N. Balasubramanian, D.-L. Kwong, Si, SiGe Nanowire Devices by Top-Down Technology and Their Applications, IEEE Transactions on Electron Devices, 55 (2008) 3107-3118.

[33] S.E. Thompson, R.S. Chau, T. Ghani, K. Mistry, S. Tyagi, M.T. Bohr, In search of "forever," continued transistor scaling one new material at a time, IEEE Transactions on Semiconductor Manufacturing, 18 (2005) 26-36.

[34] M. Neisser, S. Wurm, ITRS lithography roadmap: 2015 challenges, Advanced Optical Techniques, 4 (2015) 235-240.

[35] National Science Foundation Call for Proposals, Energy-efficient computing: From devices to architectures (E2CDA) in, National Science Foundation, 2016, NSF/SRC Call for Proposals.

[36] W.S. Gorton, The genesis of the transistor (Reprinted from Bell Telephone Laboratories Memorandum for Record, December 27, 1949), Proceedings of the IEEE, 86 (1998) 50-52.

[37] M. Riordan, L. Hoddeson, C. Herring, The invention of the transistor, Reviews of Modern Physics, 71 (1999) S336-S345.

[38] I.M. Ross, The invention of the transistor, Proceedings of the IEEE, 86 (1998) 7-28.

[39] J.E. Lilienfeld, Method and apparatus for controlling electric currents, U.S. Patent, 1930.

[40] J.E. Lilienfeld, Electric current control mechanism,Canadian Patent, 1925.

[41] J.B. Johnson, More on the solid‐state amplifier and Dr. Lilienfeld, Physics Today, (1964) 60-62.

[42] B.E. Crawford, The invention of the transistor, in, University of Vermont, October 1991.

[43] W.H. Brattain, W. Shockley, Density of surface states on silicon deduced from contact potential measurements, Physical Review, 72 (1947) 345-345.

[44] R.G. Arns, The other transistor: Early history of the metal-oxide-semiconductor field-effect transistor, Engineering Science and Education Journal, 7 (1998) 233-240.

[45] W. Shockley, The theory of p-n junctions in semiconductors and p-n junction transistors, Bell System Technical Journal, 28 (1949) 435-489.

[46] M.M. Atalla, E. Tannenbaum, E.J. Scheibner, Stabilization of silicon surfaces by thermally grown oxides, Bell System Technical Journal, 38 (1959) 749-783.

[47] M.M. Atalla, Surface stabilization of silicon by thermally grown oxides, Journal of the Electrochemical Society, 105 (1958) C252-C252.

[48] J.N. Shive, The double-surface transistor, Physical Review, 75 (1949) 689-690.

[49] W.F. Brinkman, D.E. Haggan, W.W. Troutman, A history of the invention of the transistor and where it will lead us, IEEE Journal of Solid-State Circuits, 32 (1997) 1858-1865.

[50] H.J. Queisser, E.E. Haller, Defects in semiconductors: Some fatal, some vital, Science, 281 (1998) 945-950.

[51] B. Weber, S. Mahapatra, H. Ryu, S. Lee, A. Fuhrer, T.C.G. Reusch, D.L. Thompson, W.C.T. Lee, G. Klimeck, L.C.L. Hollenberg, M.Y. Simmons, Ohm's Law Survives to the Atomic Scale, Science, 335 (2012) 64-67.

[52] IBM, Silicon Integrated Nanophotonics, 2012. Available: http://researcher.watson.ibm.com/researcher/view_group.php?id=2757.

[53] W. Green, S. Assefa, A. Rylyakov, C. Schow, F. Horst, Y. Vlasov, CMOS integrated silicon nanophotonics: Enabling technology for exascale computational systems, in: SEMICON, Tokyo, Japan, 2010.

[54] E. Pop, S. Sinha, K.E. Goodson, Heat generation and transport in nanometer-scale transistors, Proceedings of the IEEE, 94 (2006) 1587-1601.

[55] A. Dixit, A. Kottantharayil, N. Collaert, M. Goodwin, M. Jurezak, K. De Meyer, Analysis of the parasitic S/D resistance in multiple-gate FETs, IEEE Transactions on Electron Devices, 52 (2005) 1132-1140.

[56] E. Mohammad, A. Alduino, T. Thomas, H. Braunisch, D. Lu, J. Heck, A. Liu, I. Young, B. Barnett, G. Vandentop, R. Mooney, Optical interconnect system integration for ultra-short-reach applications, Intel Technology Journal, 8 (2004) 115-127.

[57] M. Salib, M. Morse, M. Paniccia, Opportunities and integration challenges for CMOS-compatible silicon photonic and optoelectronic devices, in: 2004 1st IEEE International Conference on Group Iv Photonics, Hong Kong, China, 2004, pp. 1-3.

[58] R.K. Kostuk, J.W. Goodman, L. Hesselink, Optical imaging applied to microelectronic chip-to-chip interconnections, Applied Optics, 24 (1985) 2851-2858.

[59] M.R. Feldman, C.C. Guest, T.J. Drabik, S.C. Esener, Comparison between electrical and free space optical interconnects for fine-grain processor arrays based on interconnect density capabilities, Applied Optics, 28 (1989) 3820-3829.

[60] D.K. Gramotnev, S.I. Bozhevolnyi, Plasmonics beyond the diffraction limit, Nature Photonics, 4 (2010) 83-91.

[61] W. Bogaerts, R. Baets, P. Dumon, V. Wiaux, S. Beckx, D. Taillaert, B. Luyssaert, J. Van Campenhout, P. Bienstman, D. Van Thourhout, Nanophotonic waveguides in silicon-on-insulator fabricated with CMOS technology, Journal of Lightwave Technology, 23 (2005) 401-412.

[62] Y. Vlasov, W.M.J. Green, F. Xia, High-throughput silicon nanophotonic wavelength-insensitive switch for on-chip optical networks, Nature Photonics, 2 (2008) 242-246.

[63] M. Asghari, A.V. Krishnamoorthy, Silicon photonics: Energy-efficient communication, Nature Photonics, 5 (2011) 268-270.

[64] T. Barwicz, H. Byun, F. Gan, C.W. Holzwarth, M.A. Popovic, P.T. Rakich, M.R. Watts, E.P. Ippen, F.X. Kaertner, H.I. Smith, J.S. Orcutt, R.J. Ram, V. Stojanovic, O.O. Olubuyide, J.L. Hoyt, S. Spector, M. Geis, M. Grein, T. Lyszczarz, J.U. Yoon, Silicon photonics for compact, energy-efficient interconnects, Journal of Optical Networking, 6 (2007) 63-73.

[65] C. Sun, M.T. Wade, Y. Lee, J.S. Orcutt, L. Alloatti, M.S. Georgas, A.S. Waterman, J.M. Shainline, R.R. Avizienis, S. Lin, B.R. Moss, R. Kumar, F. Pavanello, A.H. Atabaki, H.M. Cook, A.J. Ou, J.C. Leu, Y.-H. Chen, K. Asanovic, R.J. Ram, M.A. Popovic, V.M. Stojanovic, Single-chip microprocessor that communicates directly using light, Nature, 528 (2015) 534-538.

[66] S. Koenig, D. Lopez-Diaz, J. Antes, F. Boes, R. Henneberger, A. Leuther, A. Tessmann, R. Schmogrow, D. Hillerkuss, R. Palmer, T. Zwick, C. Koos, W. Freude, O. Ambacher, J. Leuthold, I. Kallfass, Wireless sub-THz communication system with high data rate, Nature Photonics, 7 (2013) 977-981.

[67] R. Soref, The past, present, and future of silicon photonics, IEEE Journal of Selected Topics in Quantum Electronics, 12 (2006) 1678-1687.

[68] P.-K. Shen, A. Hosseini, X. Xu, Y. Hei, Z. Pan, R.T. Chen, Multiple-input multiple-output enabled large bandwidth density on-chip optical interconnect, Journal of Lightwave Technology, (2016) Accepted.

[69] P.Y.C. Yu, Manuel, Fundamentals of Semicondcutors: Physics and Material Properties, Springer, New York, 2005.

[70] C. Kittel, Introduction to Solid State Physics (3rd ed.), Wiley & Sons, New York, 1967.

[71] N.W.M. Ashcroft, N. David, Solid State Physics, Holt, Rinehart and Winston, New York, 1976.

[72] C.Y. Yeh, Z.W. Lu, S. Froyen, A. Zunger, Zinc-blende-wurtzite polytypism in semiconductors, Physical Review B, 46 (1992) 10086-10097.

[73] J. Mukesh, II-VI semiconductor compounds, World Scientific, New Jersey, 1993.

[74] M.C. Tamargo, II-VI Semiconductor Materials and their Applications, Taylor and Francis, Inc., New York, 2002.

[75] I. Zardo, S. Conesa-Boj, F. Peiro, J.R. Morante, J. Arbiol, E. Uccelli, G. Abstreiter, A. Fontcuberta i Morral, Raman spectroscopy of wurtzite and zinc-blende GaAs nanowires: Polarization dependence, selection rules, and strain effects, Physical Review B, 80 (2009) 245324.

[76] I. Vurgaftman, J.R. Meyer, L.R. Ram-Mohan, Band parameters for III-V compound semiconductors and their alloys, Journal of Applied Physics, 89 (2001) 5815-5875.

[77] D. Strauch, Semiconductors - New data and updates for several III-V (including mixed crystals) and II-VI compounds, in: Landolt-Börnstein - Group III Condensed Matter, Springer/Verlag, Berlin Heidelberg, 2012.

[78] M.S.P. Rogalski, Stuart B., Solid State Physics, Overseas Publishers Association, Singapore, 2000.

[79] D.E. Gomez, M. Califano, P. Mulvaney, Optical properties of single semiconductor nanocrystals, Physical Chemistry Chemical Physics, 8 (2006) 4989-5011.

[80] W. Shockley, Energy band structures in semiconductors, Physical Review, 78 (1950) 173-174.

[81] M.L. Cohen, T.K. Bergstre, Band structures and pseudopotential form factors for 14 semiconductors of Diamond and Zinc-blend structures, Physical Review, 141 (1966) 789-796.

[82] X. Xu, Q. Zhang, J. Zhang, Y. Zhou, Q. Xiong, Taming excitons in II-VI semiconductor nanowires and nanobelts, Journal of Physics D-Applied Physics, 47 (2014) 394009.

[83] M. Shahmohammadi, J.D. Ganiere, H. Zhang, R. Ciechonski, G. Vescovi, O. Kryliouk, M. Tchernycheva, G. Jacopin, Excitonic diffusion in InGaN/GaN core-shell nanowires, Nano letters, 16 (2016) 243-249.

[84] C.F. Klingshirn, Semiconductor Optics, Springer, Berlin, 2012.

[85] D. Yu, C.J. Wang, P. Guyot-Sionnest, n-type conducting CdSe nanocrystal solids, Science, 300 (2003) 1277-1280.

[86] R. Tsu, Superlattice to Nanoelectronics, in, Elsevier, New York, NY, USA, 2011.

[87] S.H. Wei, A. Zunger, Band offsets and optical bowings of chalcopyrites and Zn-based II-VI alloys, Journal of Applied Physics, 78 (1995) 3846-3856.

[88] S. Albrecht, L. Reining, R. Del Sole, G. Onida, Ab initio calculation of excitonic effects in the optical spectra of semiconductors, Physical Review Letters, 80 (1998) 4510-4513.

[89] S.Z. Karazhanov, P. Ravindran, A. Kjekshus, H. Fjellvag, B.G. Svensson, Electronic structure and optical properties of ZnX (X=O, S, Se, Te): A density functional study, Physical Review B, 75 (2007) 155104.

[90] O. Zakharov, A. Rubio, X. Blase, M.L. Cohen, S.G. Louie, Quasi-particle band structures of 6 II-VI Compounds - ZnS, ZnSe, ZnTe, CdS, CdSe, and CdTe, Physical Review B, 50 (1994) 10780-10787.

[91] D. Shiri, Y. Kong, A. Buin, M.P. Anantram, Strain induced change of bandgap and effective mass in silicon nanowires, Applied Physics Letters, 93 (2008) 073114.

[92] B. Wei, K. Zheng, Y. Ji, Y. Zhang, Z. Zhang, X. Han, Size-dependent bandgap modulation of ZnO nanowires by tensile strain, Nano Letters, 12 (2012) 4595-4599.

[93] G. Signorello, S. Karg, M.T. Bjoerk, B. Gotsmann, H. Riel, Tuning the light emission from GaAs nanowires over 290 meV with uniaxial strain, Nano Letters, 13 (2013) 917-924.

[94] J. Greil, A. Lugstein, C. Zeiner, G. Strasser, E. Bertagnolli, Tuning the electro-optical properties of germanium nanowires by tensile strain, Nano Letters, 12 (2012) 6230-6234.

[95] K. Wang, S.C. Rai, J. Marmon, J. Chen, K. Yao, S. Wozny, B. Cao, Y. Yan, Y. Zhang, W. Zhou, Nearly lattice matched all wurtzite CdSe/ZnTe type II core-shell nanowires with epitaxial interfaces for photovoltaics, Nanoscale, 6 (2014) 3679-3685.

[96] R.S. Mulliken, Electronic population analysis on LCAO-MO molecular wave functions .1., Journal of Chemical Physics, 23 (1955) 1833-1840.

[97] R.S. Mulliken, Electronic population analysis on LCAO-MO molecular wave functions .2. Overlap populations, bond orders, and covalent bond energies, Journal of Chemical Physics, 23 (1955) 1841-1846.

[98] R.S. Mulliken, Electronic population analysis on LCAO-MO molecular wave functions .3. Effects of hybridization on overlap and gross AO populations, Journal of Chemical Physics, 23 (1955) 2338-2342.

[99] R.S. Mulliken, Electronic population analysis on LCAO-MO molecular wave functions .4. Bonding and antibonding in LCAO and valence-bond theories, Journal of Chemical Physics, 23 (1955) 2343-2346.

[100] M.Z. Huang, W.Y. Ching, Calculation of optical-excitatons in cubic semiconductors .1. Electronic-structure and linear response, Physical Review B, 47 (1993) 9449-9463.

[101] S.H. Wei, S.B. Zhang, A. Zunger, First-principles calculation of band offsets, optical bowings, and defects in CdS, CdSe, CdTe, and their alloys, Journal of Applied Physics, 87 (2000) 1304-1311.

[102] E.T. Yu, M.C. Phillips, J.O. McCaldin, T.C. McGill, Measurement of the CdSe/ZnTe valence band offset by x-ray photoelectron spectroscopy, Journal of Vacuum Science & Technology B, 9 (1991) 2233-2237.

[103] O. Madelung, Semiconductors: Data Handbook, in, Springer, New York, NY, USA, 2004.

[104] S. Kasap, P. Capper, Springer Handbook of Electronic and Photonic Materials, Springer Science+Business Media, Inc., New York, 2006.

[105] J.M. Luttinger, Fermi surface and some simple equilibrium properties of a system of interaction fermions, Physical Review, 119 (1960) 1153-1163.

[106] M. Fox, Optical Properties of Solids, Oxford University Press, Oxford, 2010.

[107] L. Hu, J. Yan, M. Liao, L. Wu, X. Fang, Ultrahigh external quantum efficiency from thin SnO2 nanowire ultraviolet photodetectors, Small, 7 (2011) 1012-1017.

[108] C. Soci, A. Zhang, B. Xiang, S.A. Dayeh, D.P.R. Aplin, J. Park, X.Y. Bao, Y.H. Lo, D. Wang, ZnO nanowire UV photodetectors with high internal gain, Nano Letters, 7 (2007) 1003-1009.

[109] M.D. Kelzenberg, S.W. Boettcher, J.A. Petykiewicz, D.B. Turner-Evans, M.C. Putnam, E.L. Warren, J.M. Spurgeon, R.M. Briggs, N.S. Lewis, H.A. Atwater, Enhanced absorption and carrier collection in Si wire arrays for photovoltaic applications, Nature Materials, 9 (2010) 239-244.

[110] X. Li, Y. Zhan, Enhanced external quantum efficiency in rectangular single nanowire solar cells, Applied Physics Letters, 102 (2013) 021101.

[111] C.V. Raman, K.S. Krishnan, A new type of secondary radiation, Nature, 121 (1928) 501-502.

[112] Y. Zhou, Nobel Lectures: Physics 1922 – 1941, 1st Edition, Elsevier Publishing Company, New York, 1965.

[113] G. Landsberg, L. Mandelstam, Über die lichtzerstreuung in kristallen, Zeitschrift für Physik, 50 (1928) 769-780.

[114] A. Garcia-Cristobal, A. Cantarero, C. Trallerogíner, M. Cardona, Excitonic model for 2nd-order resonant Raman scattering, Physical Review B, 49 (1994) 13430-13445.

[115] L. Bornstein, Numerical Data and Functional Relationships in Science and Technology, in: O.W. OMadelung, H.; Schulz, M. (Ed.), Springer, Berlin, 1982.

[116] J.F. Scott, R.C.C. Leite, T.C. Damen, Resonant Raman effect in semiconductors, Physical Review, 188 (1969) 1285-1290.

[117] R.C.C. Leite, J.F. Scott, Resonant surface Raman scattering in direct-gap semiconductors, Physical Review Letters, 22 (1969) 130-132.

[118] M.V. Klein, S.P.S. Porto, Multiple-phonon-resonance Raman effect in CdS, Physical Review Letters, 22 (1969) 782-784.

[119] R.C.C. Leite, S.P.S. Porto, Enhancement of Raman cross section in CdS due to resonant absorption, Physical Review Letters, 17 (1966) 10-12.

[120] A. Pinczuk, E. Burstein, Raman scattering from InSb surfaces at phonon energies near E1 energy gap, Physical Review Letters, 21 (1968) 1073-1075.

[121] R.C.C. Leite, J.F. Scott, T.C. Damen, Multiple phonon resonant Raman scattering in CdS, Physical Review Letters, 22 (1969) 780-782.

[122] J.F. Scott, T.C. Damen, R.C.C. Leite, W.T. Silfvast, Resonant Raman effect in indirect gap semiconductor gallium phosphide, Solid State Communications, 7 (1969) 953-955.

[123] Y. Oka, M. Cardona, Resonance Raman scattering of excitonic polaritons by LO and acoutic phonons in ZnTe, Solid State Communications, 30 (1979) 447-451.

[124] A.C. Ferrari, J. Robertson, Interpretation of Raman spectra of disordered and amorphous carbon, Physical Review B, 61 (2000) 14095-14107.

[125] S. Krimm, J. Bandekar, Vibrational spectroscopy and conformation of peptides, polypeptides, and proteins, Advances in Protein Chemistry, 38 (1986) 181-364.

[126] M.S. Dresselhaus, G. Dresselhaus, R. Saito, A. Jorio, Raman spectroscopy of carbon nanotubes, Physics Reports-Review Section of Physics Letters, 409 (2005) 47-99.

[127] S.M. Nie, S.R. Emery, Probing single molecules and single nanoparticles by surface-enhanced Raman scattering, Science, 275 (1997) 1102-1106.

[128] J. Zhang, D. Li, R. Chen, Q. Xiong, Laser cooling of a semiconductor by 40 kelvin, Nature, 493 (2013) 504-508.

[129] R. Loudon, Theory of first-order Raman effect in crystals, Proceedings of the Royal Society of London Series A-Mathematical and Physical Sciences, 275 (1963) 218-232.

[130] R. Loudon, Raman effect in crystals, Advances in Physics, 13 (1964) 423-482.

[131] R. Loudon, Theory of resonant Raman effect in crystals, Journal De Physique, 26 (1965) 677-683.

[132] R. Merlin, G. Guntherodt, R. Humphreys, M. Cardona, R. Suryanarayanan, F. Holtzberg, Multiphonon processes in YbS, Physical Review B, 17 (1978) 4951-4958.

[133] A.P. Alivisatos, T.D. Harris, P.J. Carroll, M.L. Steigerwald, L.E. Brus, Electron-vibration coupling in semiconductor clusters studied by resonant Raman spectroscopy, Journal of Chemical Physics, 90 (1989) 3463-3468.

[134] S. Permogorov, Optical emission due to exciton scattering by LO phonons in semiconductors, in: E.I. Rashba, M.D. Struge (Eds.) Excitons, North Holland Publishing Company, New York, 1982, pp. 177-203.

[135] A. Chernikov, V. Bornwasser, M. Koch, S. Chatterjee, C.N. Boettge, T. Feldtmann, M. Kira, S.W. Koch, T. Wassner, S. Lautenschlaeger, B.K. Meyer, M. Eickhoff, Phonon-assisted luminescence of polar semiconductors: Frohlich coupling versus deformation-potential scattering, Physical Review B, 85 (2012) 035201.

[136] A.M. Kelley, Electron-phonon coupling in CdSe nanocrystals, Journal of Physical Chemistry Letters, 1 (2010) 1296-1300.

[137] W. Potz, P. Vogl, Theory of optical-phonon deformation potentials in tetrahedral semiconductors, Physical Review B, 24 (1981) 2025-2037.

[138] S.H. Park, S.L. Chuang, Comparison of zinc-blende and wurtzite GaN semiconductors with spontaneous polarization and piezoelectric field effects, Journal of Applied Physics, 87 (2000) 353-364.

[139] A.S. Pine, G. Dresselhaus, Raman scattering in paratellurite, TeO_2, Physical Review B, 5 (1972) 4087-4093.

[140] H. Wu, C. Cao, J. Si, T. Xu, H. Zhang, H. Wu, J. Chen, W. Shen, N. Dai, Observation of phonon modes in epitaxial PbTe films grown by molecular beam epitaxy, Journal of Applied Physics, 101 (2007) 103505.

[141] B. Zhang, C. Cai, H. Zhu, F. Wu, Z. Ye, Y. Chen, R. Li, W. Kong, H. Wu, Phonon blocking by two dimensional electron gas in polar CdTe/PbTe heterojunctions, Applied Physics Letters, 104 (2014) 161601.

[142] Q. Zhang, J. Zhang, M.I.B. Utama, B. Peng, M. de la Mata, J. Arbiol, Q. Xiong, Exciton-phonon coupling in individual ZnTe nanorods studied by resonant Raman spectroscopy, Physical Review B, 85 (2012) 085418.

[143] S.C. Rai, K. Wang, J.J. Chen, J.K. Marmon, M. Bhatt, S. Wozny, Y. Zhang, W.L. Zhou, Enhanced broad band photodetection through piezo-phototronic effect in CdSe/ZnTe core/shell nanowire array, Advanced Electronic Materials, 1 (2015) 1400050.

[144] V. Heine, On general theory of surface states and scattering of electrons in solids, Proceedings of the Physical Society of London, 81 (1963) 300-310.

[145] V. Heine, Theory of surface states, Physical Review, 138 (1965) A1689-A1696.

[146] D. Kalkstei, P. Soven, Greens function theory of surface states, Surface Science, 26 (1971) 85-99.

[147] S.C. Erwin, L.J. Zu, M.I. Haftel, A.L. Efros, T.A. Kennedy, D.J. Norris, Doping semiconductor nanocrystals, Nature, 436 (2005) 91-94.

[148] A. Sahu, M.S. Kang, A. Kompch, C. Notthoff, A.W. Wills, D. Deng, M. Winterer, C.D. Frisbie, D.J. Norris, Electronic impurity doping in CdSe nanocrystals, Nano Letters, 12 (2012) 2587-2594.

[149] M. Joseph, H. Tabata, H. Saeki, K. Ueda, T. Kawai, Fabrication of the low-resistive p-type ZnO by codoping method, Physica B, 302 (2001) 140-148.

[150] Z. He, J. Jie, W. Zhang, W. Zhang, L. Luo, X. Fan, G. Yuan, I. Bello, S.-T. Lee, Tuning electrical and photoelectrical properties of CdSe nanowires via indium doping, Small, 5 (2009) 345-350.

[151] S. Lany, A. Zunger, Anion vacancies as a source of persistent photoconductivity in II-VI and chalcopyrite semiconductors, Physical Review B, 72 (2005) 035215.

[152] J. Lu, C. Sun, M. Zheng, N. Mathews, H. Liu, S. Chen Gin, X. Zhang, S.G. Mhaisalkar, S.C. Haur, Facile one-step synthesis of CdS_xSe_{1-x} nanobelts with uniform and controllable stoichiometry, Journal of Physical Chemistry C, 115 (2011) 19538-19545.

[153] J.J. Hou, F. Wang, N. Han, F. Xiu, S. Yip, M. Fang, H. Lin, T.F. Hung, J.C. Ho, Stoichiometric effect on electrical, optical, and structural properties of composition-tunable InxGa1-xAs nanowires, ACS Nano, 6 (2012) 9320-9325.

[154] P. Gali, G. Sapkota, A.J. Syllaios, C. Littler, U. Philipose, Stoichiometry dependent electron transport and gas sensing properties of indium oxide nanowires, Nanotechnology, 24 (2013) 225704.

[155] W.W. Yu, L.H. Qu, W.Z. Guo, X.G. Peng, Experimental determination of the extinction coefficient of CdTe, CdSe, and CdS nanocrystals, Chemistry of Materials, 15 (2003) 2854-2860.

[156] H. Yu, J.B. Li, R.A. Loomis, P.C. Gibbons, L.W. Wang, W.E. Buhro, Cadmium selenide quantum wires and the transition from 3D to 2D confinement, Journal of the American Chemical Society, 125 (2003) 16168-16169.

[157] H. Yu, J.B. Li, R.A. Loomis, L.W. Wang, W.E. Buhro, Two- versus three-dimensional quantum confinement in indium phosphide wires and dots, Nature Materials, 2 (2003) 517-520.

[158] J. Cibert, P.M. Petroff, G.J. Dolan, S.J. Pearton, A.C. Gossard, J.H. English, Optically detected carrier confinement to one and zero dimension in GaAs quantum-well wires and boxes, Applied Physics Letters, 49 (1986) 1275-1277.

[159] A.J. Houtepen, D. Vanmaekelbergh, Orbital occupation in electron-charged CdSe quantum-dot solids, Journal of Physical Chemistry B, 109 (2005) 19634-19642.

[160] C.-H. Cho, C.O. Aspetti, M.E. Turk, J.M. Kikkawa, S.-W. Nam, R. Agarwal, Tailoring hot-exciton emission and lifetimes in semiconducting nanowires via whispering-gallery nanocavity plasmons, Nature Materials, 10 (2011) 669-675.

[161] Y. Zhou, F. Wang, W.E. Buhro, Large exciton energy shifts by reversible surface exchange in 2D II-VI nanocrystals, Journal of the American Chemical Society, 137 (2015) 15198-15208.

[162] O. Chen, Y. Yang, T. Wang, H. Wu, C. Niu, J. Yang, Y.C. Cao, Surface-functionalization-dependent optical properties of II-VI semiconductor nanocrystals, Journal of the American Chemical Society, 133 (2011) 17504-17512.

[163] V. Protasenko, D. Bacinello, M. Kuno, Experimental determination of the absorption cross-section and molar extinction coefficient of CdSe and CdTe nanowires, Journal of Physical Chemistry B, 110 (2006) 25322-25331.

[164] S.W. Koch, M. Kira, G. Khitrova, H.M. Gibbs, Semiconductor excitons in new light, Nature Materials, 5 (2006) 523-531.

[165] W. Hoyer, C. Ell, M. Kira, S.W. Koch, S. Chatterjee, S. Mosor, G. Khitrova, H.M. Gibbs, H. Stolz, Many-body dynamics and exciton formation studied by time-resolved photoluminescence, Physical Review B, 72 (2005) 075324.

[166] M.L. Brongersma, Y. Cui, S. Fan, Light management for photovoltaics using high-index nanostructures, Nature Materials, 13 (2014) 451-460.

[167] E. Garnett, P. Yang, Light trapping in silicon nanowire solar cells, Nano Letters, 10 (2010) 1082-1087.

[168] Z. Yu, A. Raman, S. Fan, Fundamental limit of nanophotonic light trapping in solar cells, Proceedings of the National Academy of Sciences of the United States of America, 107 (2010) 17491-17496.

[169] H.S. Rong, A.S. Liu, R. Jones, O. Cohen, D. Hak, R. Nicolaescu, A. Fang, M. Paniccia, An all-silicon Raman laser, Nature, 433 (2005) 292-294.

[170] R.L. Espinola, J.I. Dadap, R.M. Osgood, S.J. McNab, Y.A. Vlasov, Raman amplification in ultrasmall silicon-on-insulator wire waveguides, Optics Express, 12 (2004) 3713-3718.

[171] J.C. Slater, W. Shockley, Optical absorption by the alkali halides, Physical Review, 50 (1936) 705-719.

[172] J. Frenkel, On the transformation of light into heat in solids. I, Physical Review, 37 (1931) 17-44.

[173] J. Frenkel, On the transformation of light into heat in solids. II, Physical Review, 37 (1931) 1276-1294.

[174] G.H. Wannier, The structure of electronic excitation levels in insulating crystals, Physical Review, 52 (1937) 191-197.

[175] W. Shockley, Electrons and holes in semiconductors, D. Van Nostrand Company, Inc., New York, 1950.

[176] F. Vietmeyer, P.A. Frantsuzov, B. Janko, M. Kuno, Carrier recombination dynamics in individual CdSe nanowires, Physical Review B, 83 (2011) 115319.

[177] M.V. von Smoluchowski, Drei vorträge über diffusion, brownsche bewegung und koagulation von kolloidteilchen, Physik Zeit, 17 (1916) 557-585.

[178] S. Schafer, Z. Wang, R. Zierold, T. Kipp, A. Mews, Laser-induced charge separation in CdSe nanowires, Nano Letters, 11 (2011) 2672-2677.

[179] D.N. Petsev, N.D. Denkov, Diffusion of charged colloidal particles at low volume fraction - theoretical model and light scattering experiments, Journal of Colloid and Interface Science, 149 (1992) 329-344.

[180] C. Canali, F. Nava, Ottavian.G, C. Paorici, Hole and electron drift velocity in CdSe at room temperature, Solid State Communications, 11 (1972) 105-107.

[181] S. Kouteva-Arguirova, T. Arguirov, D. Wolfframm, J. Reif, Influence of local heating on micro-Raman spectroscopy of silicon, Journal of Applied Physics, 94 (2003) 4946-4949.

[182] J.K. Marmon, S.C. Rai, K. Wang, W. Zhou, Y. Zhang, Light-effect transistor (LET) with multiple independent gating controls for optical logic gates and optical amplification, Frontiers in Physics, 4 (2016) 1-10.

[183] R. Waser, M. Aono, Nanoionics-based resistive switching memories, Nature Materials, 6 (2007) 833-840.

[184] A. Sawa, Resistive switching in transition metal oxides, Materials Today, 11 (2008) 28-36.

[185] R. Waser, R. Dittmann, G. Staikov, K. Szot, Redox-Based Resistive Switching Memories - Nanoionic Mechanisms, Prospects, and Challenges, Advanced Materials, 21 (2009) 2632-2663.

[186] E. Pop, Energy dissipation and transport in nanoscale devices, Nano Research, 3 (2010) 147-169.

[187] N. Li, J. Ren, L. Wang, G. Zhang, P. Haenggi, B. Li, Colloquium: Phononics: Manipulating heat flow with electronic analogs and beyond, Reviews of Modern Physics, 84 (2012) 1045-1066.

[188] R.T. Tung, Recent advances in Schottky barrier concepts, Materials Science & Engineering R-Reports, 35 (2001) 1-138.

[189] D.P. Masson, D.J. Lockwood, M.J. Graham, Thermal oxide on CdSe, Journal of Applied Physics, 82 (1997) 1632-1639.

[190] Z.-M. Liao, K.-J. Liu, J.-M. Zhang, J. Xu, D.-P. Yu, Effect of surface states on electron transport in individual ZnO nanowires, Physics Letters A, 367 (2007) 207-210.

[191] W.I. Hamdi, S. Darwish, Evaluation of the interface state density from light-induced effects on I-U characteristics of Schottky diodes, Physica Status Solidi a-Applied Research, 143 (1994) 457-461.

[192] J. Maeng, S. Heo, G. Jo, M. Choe, S. Kim, H. Hwang, T. Lee, The effect of excimer laser annealing on ZnO nanowires and their field effect transistors, Nanotechnology, 20 (2009) 095203.

[193] A. Creti, M. Anni, M. Zavelani-Rossi, G. Lanzani, G. Leo, F. Della Sala, L. Manna, M. Lomascolo, Ultrafast carrier dynamics in core and core/shell CdSe quantum rods: Role of the surface and interface defects, Physical Review B, 72 (2005) 125346.

[194] S.R. Morrison, Semiconductor gas sensors, Sensors and Actuators, 2 (1982) 329-341.

[195] N.F. Mott, R.W. Gurney, Electronic processes in ionic crystals, Oxford University Press, London, 1940.

[196] X.Y. Wang, L.H. Qu, J.Y. Zhang, X.G. Peng, M. Xiao, Surface-related emission in highly luminescent CdSe quantum dots, Nano Letters, 3 (2003) 1103-1106.

[197] A. Armin, R.D. Jansen-van Vuuren, N. Kopidakis, P.L. Burn, P. Meredith, Narrowband light detection via internal quantum efficiency manipulation of organic photodiodes, Nature Communications, 6 (2015) 6343.

[198] S.M. Sze, K.K. Ng, Physics of Semiconductor Devices, Wiley & Sons, New York, 2007.

[199] D.K. Ferry, Materials science - Nanowires in nanoelectronics, Science, 319 (2008) 579-580.

[200] H.S.P. Wong, Beyond the conventional transistor, IBM Journal of Research and Development, 46 (2002) 133-168.

[201] H. Kind, H.Q. Yan, B. Messer, M. Law, P.D. Yang, Nanowire ultraviolet photodetectors and optical switches, Advanced Materials, 14 (2002) 158-160.

[202] R.S. Wagner, W.C. Ellis, The vapor-Liquid-Solid Mechanism of Crystal Growth, Applied Physics Letters, 4 (1964) 89–90.

[203] W. Shockley, G.L. Pearson, Modulation of conductance of thin films of semi-conductors by surface charges, Physical Review, 74 (1948) 232-233.

[204] C.-M. Kyung, Nano devices and circuit techniques for low-energy applications and energy harvesting, Springer, New York, 2015.

[205] E.J. Nowak, Maintaining the benefits of CMOS scaling when scaling bogs down, IBM Journal of Research and Development, 46 (2002) 169-180.

[206] Y. Huang, X.F. Duan, Y. Cui, L.J. Lauhon, K.H. Kim, C.M. Lieber, Logic gates and computation from assembled nanowire building blocks, Science, 294 (2001) 1313-1317.

[207] J.N. Shive, The properties of germanium phototransistors, Journal of the Optical Society of America, 43 (1953) 239-244.

[208] R.S. Tucker, The role of optics in computing, Nature Photonics, 4 (2010) 405-405.

[209] R.T. Tung, The physics and chemistry of the Schottky barrier height, Applied Physics Reviews, 1 (2014) 011304.

[210] Y.J. Zhao, S. Tanaka, C.C. Pan, K. Fujito, D. Feezell, J.S. Speck, S.P. DenBaars, S. Nakamura, High-Power Blue-Violet Semipolar (2021) InGaN/GaN Light-Emitting Diodes with Low Efficiency Droop at 200 A/cm2, Applied Physics Express, 4 (2011) 082104.

[211] P.J. Schuck, A. Weber-Bargioni, P.D. Ashby, D.F. Ogletree, A. Schwartzberg, S. Cabrini, Life beyond diffraction: Opening new routes to materials characterization with next-generation optical near-field approaches, Advanced Functional Materials, 23 (2013) 2539-2553.

[212] O. Kurniawan, M.-F. Ng, W.S. Koh, Z.Y. Leong, E. Li, Simplified model for ballistic current-voltage characteristic in cylindrical nanowires, Microelectronics Journal, 41 (2010) 155-161.

[213] R. Landauer, Spatial Variation of currents and fields due to localized scatterers in metallic conduction, IBM Journal of Research and Development, 1 (1957) 223-231.

[214] S.Y. Chou, M.Y. Liu, Nanoscale tera-hertz metal-semiconductor-metal photodetectors, IEEE Journal of Quantum Electronics, 28 (1992) 2358-2368.

[215] E.H. Bottcher, D. Kuhl, F. Hieronymi, E. Droge, T. Wolf, D. Bimberg, Ultrafast semiinsulating InP:Fe-InGaAs:Fe-InP:Fe MSM photodetectors: Modeling and performance, IEEE Journal of Quantum Electronics, 28 (1992) 2343-2357.

[216] Z. Marks, B. Van Zeghbroeck, High-speed nanoscale metal-semiconductor-metal photodetectors with terahertz bandwidth, Optical and Quantum Electronics, 42 (2011) 771-776.

[217] P. Wiesner, U. Heim, Dynamics of exciton-polariton recombination in CdS, Physical Review B, 11 (1975) 3071-3077.

[218] S. Adachi, Handbook on Physical Properties of Semiconductors, Springer US, 2007.

[219] M.M. Waldrop, The chips are down for Moore’s law, Nature, 530 (2016) 145.

[220] Bulyanitza, (in Russian), Fizika i Technika Poluprovodnikov, St.-Petersburg, 4 (1970) 1273.

[221] V.J.F. Mazurczyk, H.Y., Effects of optical phonons in the impurity photoconductivity of ZnTe, Physics Letters, 26A (1968) 220-221.

[222] E.I. Rashba, Optical spectra of phonons bound to impurity centers, Zhurnal Eksperimentalnoi I Teoreticheskoi Fiziki, 71 (1976) 319-329.

[223] A.A. Gogolin, E.I. Rashba, Mechanism of strong resonant 1LO Raman scattering, Solid State Communications, 19 (1976) 1177-1179.

[224] P. Gurtler, E.E. Koch, Temperature dependence of the exciton-phonon coupling in the strong coupling limit - Results for solid nitrogen, Chemical Physics, 49 (1980) 305-309.

[225] K.W. Adu, H.R. Gutierrez, U.J. Kim, P.C. Eklund, Inhomogeneous laser heating and phonon confinement in silicon nanowires: A micro-Raman scattering study, Physical Review B, 73 (2006) 155333.

[226] H.M. Cheng, K.F. Lin, H.C. Hsu, C.J. Lin, L.J. Lin, W.F. Hsieh, Enhanced resonant Raman scattering and electron-phonon coupling from self-assembled secondary ZnO nanoparticles, Journal of Physical Chemistry B, 109 (2005) 18385-18390.

[227] M.R. Silvestri, J. Schroeder, Pressure-tuned and laser-tuned Raman scattering in II-VI semiconductor nanocrystals - Electron-phonon coupling, Physical Review B, 50 (1994) 15108-15112.

[228] J.E. Hirsch, An index to quantify an individual's scientific research output, Proceedings of the National Academy of Sciences of the United States of America, 102 (2005) 16569-16572.

[229] K. Huang, A. Rhys, Theory of light absorption and non-radiative transistions in F-centers, Proceedings of the Royal Society of London Series a-Mathematical and Physical Sciences, 204 (1950) 406-423.

[230] M. Brewster, O. Schimek, S. Reich, S. Gradecak, Exciton-phonon coupling in individual GaAs nanowires studied using resonant Raman spectroscopy, Physical Review B, 80 (2009) 201314(R).

[231] A.D. Yoffe, Low-dimensional systems: quantum size effects and electronic properties of semiconductor microcrystallites (zero-dimensional systems) and some quasi-two-dimensional systems, Advances in Physics, 51 (2002) 799-890.

[232] D.J. Norris, A.L. Efros, M. Rosen, M.G. Bawendi, Size dependence of exciton fine structure in CdSe quantum dots, Physical Review B, 53 (1996) 16347-16354.

[233] D.J. Norris, M.G. Bawendi, Measurement and assignment of the size-dependent optical spectrum in CdSe quantum dots, Physical Review B, 53 (1996) 16338-16346.

[234] A.I. Ekimov, F. Hache, M.C. Schanneklein, D. Ricard, C. Flytzanis, I.A. Kudryavtsev, T.V. Yazeva, A.V. Rodina, A.L. Efros, Absorption and intensity-dependent photoluminescence measurements on CdSe quantum dots - assignment of the 1st electronic transitions, Journal of the Optical Society of America B-Optical Physics, 10 (1993) 100-107.

[235] S. Sapra, D.D. Sarma, Evolution of the electronic structure with size in II-VI semiconductor nanocrystals, Physical Review B, 69 (2004) 125304.

[236] M.R. Salvador, M.W. Graham, G.D. Scholes, Exciton-phonon coupling and disorder in the excited states of CdSe colloidal quantum dots, Journal of Chemical Physics, 125 (2006) 184709.

[237] A. Ashrafi, Stoichiometry enhanced exciton-phonon interactions in ZnO epilayers, Journal of Physics D-Applied Physics, 41 (2008) 195415.

[238] T. Voss, C. Bekeny, L. Wischmeier, H. Gafsi, S. Boerner, W. Schade, A.C. Mofor, A. Bakin, A. Waag, Influence of exciton-phonon coupling on the energy position of the near-band-edge photoluminescence of ZnO nanowires, Applied Physics Letters, 89 (2006) 182107.

[239] L.L. Yang, Q.X. Zhao, M. Willander, J.H. Yang, I. Ivanov, Annealing effects on optical properties of low temperature grown ZnO nanorod arrays, Journal of Applied Physics, 105 (2009) 053503.

[240] A.M. Poujade, H.J. Albany, Carrier-concentration dependence of electron-phonon scattering in Te-doped GaSb at low temperature, Physical Review, 182 (1969) 802-807.

[241] B. Liao, B. Qiu, J. Zhou, S. Huberman, K. Esfarjani, G. Chen, Significant reduction of lattice thermal conductivity by the electron-phonon interaction in silicon with high carrier concentrations: A First-Principles study, Physical Review Letters, 114 (2015) 115901.

[242] E. Zielony, E. Placzek-Popko, A. Henrykowski, Z. Gumienny, P. Kamyczek, J. Jacak, P. Nowakowski, G. Karczewski, Laser irradiation effects on the CdTe/ZnTe quantum dot structure studied by Raman and AFM spectroscopy, Journal of Applied Physics, 112 (2012) 063520.

[243] E.M. Larramendi, G. Berth, V. Wiedemeier, K.P. Huesch, A. Zrenner, U. Woggon, E. Tschumak, K. Lischka, D. Schikora, Intensity enhancement of Te Raman modes by laser damage in ZnTe epilayers, Semiconductor Science and Technology, 25 (2010) 075003.

[244] V. Wiedemeier, G. Berth, A. Zrenner, E.M. Larramendi, U. Woggon, K. Lischka, D. Schikora, In situ characterization of ZnTe epilayer irradiation via time-resolved and power-density-dependent Raman spectroscopy, Semiconductor Science and Technology, 26 (2011) 105023.

[245] S. Acharya, D.D. Sarma, Y. Golan, S. Sengupta, K. Ariga, Shape-dependent confinement in ultrasmall zero-, one-, and two-dimensional PbS nanostructures, Journal of the American Chemical Society, 131 (2009) 11282-11283.

[246] R.P. Wang, G. Xu, P. Jin, Size dependence of electron-phonon coupling in ZnO nanowires, Physical Review B, 69 (2004) 113303.

[247] M.A. Tamor, J.P. Wolfe, Drift and diffusion of free exictons in Si, Physical Review Letters, 44 (1980) 1703-1706.

[248] R. Chen, Q.-L. Ye, T.C. He, T. Wu, H.D. Sun, Uniaxial tensile strain and exciton-phonon coupling in bent ZnO nanowires, Applied Physics Letters, 98 (2011) 241916.

[249] S. Yang, X. Tian, L. Wang, J. Wei, K. Qi, X. Li, Z. Xu, W. Wang, J. Zhao, X. Bai, E. Wang, In-situ optical transmission electron microscope study of exciton phonon replicas in ZnO nanowires by cathodoluminescence, Applied Physics Letters, 105 (2014) 071901.

[250] A. Sharma, S. Dhar, B.P. Singh, C. Nayak, D. Bhattacharyya, S.N. Jha, Surface strain engineering through Tb doping to study the pressure dependence of exciton-phonon coupling in ZnO nanoparticles, Journal of Applied Physics, 114 (2013) 214309.

[251] Z.-M. Liao, H.-C. Wu, Q. Fu, X. Fu, X. Zhu, J. Xu, I.V. Shvets, Z. Zhang, W. Guo, Y. Leprince-Wang, Q. Zhao, X. Wu, D.-P. Yu, Strain induced exciton fine-structure splitting and shift in bent ZnO microwires, Scientific Reports, 2 (2012) 452.

[252] A. Sedhain, J. Li, J.Y. Lin, H.X. Jiang, Probing exciton-phonon interaction in AlN epilayers by photoluminescence, Applied Physics Letters, 95 (2009) 061106.

[253] L.J. McKimmie, C.N. Lincoln, J. Jasieniak, T.A. Smith, Three-Pulse Photon Echo Peak Shift Measurements of Capped CdSe Quantum Dots, Journal of Physical Chemistry C, 114 (2010) 82-88.

[254] A.V. Baranov, Y.P. Rakovich, J.F. Donegan, T.S. Perova, R.A. Moore, D.V. Talapin, A.L. Rogach, Y. Masumoto, I. Nabiev, Effect of ZnS shell thickness on the phonon spectra in CdSe quantum dots, Physical Review B, 68 (2003) 165306.

[255] V.M. Dzhagan, M.Y. Valakh, O.E. Raevska, O.L. Stroyuk, S.Y. Kuchmiy, D.R.T. Zahn, The influence of shell parameters on phonons in core-shell nanoparticles: A resonant Raman study, Nanotechnology, 20 (2009) 365704.

[256] F. Comas, C. Trallero-Giner, N. Studart, G.E. Marques, Interface optical phonons in spheroidal dots: Raman selection rules, Physical Review B, 65 (2002) 073303.

[257] H. Lange, M. Artemyev, U. Woggon, T. Niermann, C. Thomsen, Experimental investigation of exciton-LO-phonon couplings in CdSe/ZnS core/shell nanorods, Physical Review B, 77 (2008) 193303.

[258] T.A. Nguyen, S. Mackowski, H.E. Jackson, L.M. Smith, J. Wrobel, K. Fronc, G. Karczewski, J. Kossut, M. Dobrowolska, J.K. Furdyna, W. Heiss, Resonant spectroscopy of II-VI self-assembled quantum dots: Excited states and exciton-longitudinal optical phonon coupling, Physical Review B, 70 (2004) 125306.

[259] D.A. Luh, T. Miller, J.J. Paggel, T.C. Chiang, Large electron-phonon coupling at an interface, Physical Review Letters, 88 (2002) 256802.

[260] D.M. Sagar, R.R. Cooney, S.L. Sewall, E.A. Dias, M.M. Barsan, I.S. Butler, P. Kambhampati, Size dependent, state-resolved studies of exciton-phonon couplings in strongly confined semiconductor quantum dots, Physical Review B, 77 (2008) 235321.

[261] A.L. Efros, A.I. Ekimov, F. Kozlowski, V. Petrovakoch, H. Schmidbaur, S. Shumilov, Resonance Raman spectroscopy of electron-hole pairs - polar phonon coupling in semiconductor quantum microcrystals, Solid State Communications, 78 (1991) 853-856.

[262] M.C. Klein, F. Hache, D. Ricard, C. Flytzanis, Size dependence of electron-phonon coupling in semiconductor nanospheres - The case of CdSe, Physical Review B, 42 (1990) 11123-11132.

[263] S. Nomura, T. Kobayashi, Exciton LO-phonon couplings in spherical semiconductor microcrystallites, Physical Review B, 45 (1992) 1305-1316.

[264] S. Schmitt-Rink, D.A.B. Miller, D.S. Chemla, Theory of the linear and nonlinear optical-properties of semiconductor microcrystals, Physical Review B, 35 (1987) 8113-8125.

[265] T. Takagahara, Electron-phonon interactions and excitonic dephasing in semiconductor nanocrystals, Physical Review Letters, 71 (1993) 3577-3580.

[266] T. Takagahara, Electron-phonon interactions in semiconductor nanocrystals, Journal of Luminescence, 70 (1996) 129-143.

[267] D.V. Melnikov, W.B. Fowler, Electron-phonon interaction in a spherical quantum dot with finite potential barriers: The Frohlich Hamiltonian, Physical Review B, 64 (2001) 245320.

[268] R. Rodriguez-Suarez, E. Menendez-Proupin, C. Trallero-Giner, M. Cardona, Multiphonon resonant Raman scattering in nanocrystals, Physical Review B, 62 (2000) 11006-11016.

[269] P. Kambhampati, Unraveling the the structure and dynamics of excitons in semiconductor quantum dots, Accounts of Chemical Research, 44 (2011) 1-13.

[270] G. Scamarcio, V. Spagnolo, G. Ventruti, M. Lugara, G.C. Righini, Size dependence of electron-LO-phonon coupling in semiconductor nanocrystals, Physical Review B, 53 (1996) 10489-10492.

[271] H. Lange, M. Mohr, M. Artemyev, U. Woggon, T. Niermann, C. Thomsen, Optical phonons in colloidal CdSe nanorods, Physica Status Solidi B-Basic Solid State Physics, 247 (2010) 2488-2497.

[272] V.M. Dzhagan, M.Y. Valakh, A.E. Raevskaya, A.L. Stroyuk, S.Y. Kuchmiy, D.R.T. Zahn, Size effects on Raman spectra of small CdSe nanoparticles in polymer films, Nanotechnology, 19 (2008) 305707.

[273] E.I.G. Rashba, Z.S., Anisotropic dimensional effects in semiconductors and semimetals, Soviet Physics Uspekhi, 19 (1976) 361-386.

[274] F.W. Wise, Lead salt quantum dots: The limit of strong quantum confinement, Accounts of Chemical Research, 33 (2000) 773-780.

[275] T.D. Krauss, F.W. Wise, Raman-scattering study of exciton-phonon coupling in PbS nanocrystals, Physical Review B, 55 (1997) 9860-9865.

[276] T.D. Krauss, F.W. Wise, Coherent acoustic phonons in a semiconductor quantum dot, Physical Review Letters, 79 (1997) 5102-5105.

[277] A. Compaan, M.C. Lee, G.J. Trott, Phonon populations by nanosecond-pulsed Raman scattering in Si, Physical Review B, 32 (1985) 6731-6741.

[278] E.G. Gamaly, A.V. Rode, Physics of ultra-short laser interaction with matter: From phonon excitation to ultimate transformations, Progress in Quantum Electronics, 37 (2013) 215-323.

[279] R. Tsu, J.G. Hernandez, Temperature dependence of silicon Raman lines, Applied Physics Letters, 41 (1982) 1016-1018.

[280] S. Piscanec, M. Cantoro, A.C. Ferrari, J.A. Zapien, Y. Lifshitz, S.T. Lee, S. Hofmann, J. Robertson, Raman spectroscopy of silicon nanowires, Physical Review B, 68 (2003) 241312(R).

[281] R. Gupta, Q. Xiong, C.K. Adu, U.J. Kim, P.C. Eklund, Laser-induced Fano resonance scattering in silicon nanowires, Nano Letters, 3 (2003) 627-631.

[282] D. Ristau, Laser-induced damage in optical materials, CRC Press, New York, 2015.

[283] K. Yonemitsu, K. Nasu, Theory of photoinduced phase transitions in itinerant electron systems, Physics Reports-Review Section of Physics Letters, 465 (2008) 1-60.

[284] H. Frohlich, Theory of the superconducting state .1. The ground state at the absolute zero of temperature, Physical Review, 79 (1950) 845-856.

[285] I.N. Hulea, S. Fratini, H. Xie, C.L. Mulder, N.N. Iossad, G. Rastelli, S. Ciuchi, A.F. Morpurgo, Tunable Frohlich polarons in organic single-crystal transistors, Nature Materials, 5 (2006) 982-986.

[286] R. Petry, M. Schmitt, J. Popp, Raman Spectroscopy - A prospective tool in the life sciences, Chemphyschem, 4 (2003) 14-30.

[287] D. Graf, F. Molitor, K. Ensslin, C. Stampfer, A. Jungen, C. Hierold, L. Wirtz, Spatially resolved raman spectroscopy of single- and few-layer graphene, Nano Letters, 7 (2007) 238-242.

[288] A.C. Ferrari, J.C. Meyer, V. Scardaci, C. Casiraghi, M. Lazzeri, F. Mauri, S. Piscanec, D. Jiang, K.S. Novoselov, S. Roth, A.K. Geim, Raman spectrum of graphene and graphene layers, Physical Review Letters, 97 (2006) 187401.

[289] J.X. Cheng, X.S. Xie, Coherent anti-Stokes Raman scattering microscopy: Instrumentation, theory, and applications, Journal of Physical Chemistry B, 108 (2004) 827-840.

[290] A. Zumbusch, G.R. Holtom, X.S. Xie, Three-dimensional vibrational imaging by coherent anti-Stokes Raman scattering, Physical Review Letters, 82 (1999) 4142-4145.

[291] S. Perichon, V. Lysenko, B. Remaki, D. Barbier, B. Champagnon, Measurement of porous silicon thermal conductivity by micro-Raman scattering, Journal of Applied Physics, 86 (1999) 4700-4702.

[292] G.S. Doerk, C. Carraro, R. Maboudian, Single Nanowire Thermal Conductivity Measurements by Raman Thermography, ACS Nano, 4 (2010) 4908-4914.

[293] F. Cerdeira, M. Cardona, Effect of carrier concentration on Raman frequencies of Si and Ge, Physical Review B, 5 (1972) 1440-1454.

[294] G. Irmer, V.V. Toporov, B.H. Bairamov, J. Monecke, Determination of the charge carrier concentration and mobility in n-gap by Raman spectroscopy, Physica Status Solidi B-Basic Research, 119 (1983) 595-603.

[295] Z.C. Zhang, B.B. Huang, Y.Q. Yu, D.L. Cui, Electrical properties and Raman spectra of undoped and Al-doped ZnO thin films by metalorganic vapor phase epitaxy, Materials Science and Engineering B-Solid State Materials for Advanced Technology, 86 (2001) 109-112.

[296] Y.G. Zhang, W.; Struge, M.D., Phonon sidebands of excitons bound to isoelectronic impurities in semiconductors, Physical Review B, 47 (1993) 6330-6339.

[297] S. Mukhopadhyay, D.A. Stewart, First-principles study of the phonon dispersion and dielectric properties of wurtzite InP: Role of In 4d electrons, Physical Review B, 89 (2014) 054302.

[298] A. Alkauskas, B.B. Buckley, D.D. Awschalom, C.G. Van de Walle, First-principles theory of the luminescence lineshape for the triplet transition in diamond NV centres, New Journal of Physics, 16 (2014) 073026.

[299] X. Gonze, B. Amadon, P.M. Anglade, J.M. Beuken, F. Bottin, P. Boulanger, F. Bruneval, D. Caliste, R. Caracas, M. Cote, T. Deutsch, L. Genovese, P. Ghosez, M. Giantomassi, S. Goedecker, D.R. Hamann, P. Hermet, F. Jollet, G. Jomard, S. Leroux, M. Mancini, S. Mazevet, M.J.T. Oliveira, G. Onida, Y. Pouillon, T. Rangel, G.M. Rignanese, D. Sangalli, R. Shaltaf, M. Torrent, M.J. Verstraete, G. Zerah, J.W. Zwanziger, ABINIT: First-principles approach to material and nanosystem properties, Computer Physics Communications, 180 (2009) 2582-2615.

[300] S.J. Clark, M.D. Segall, C.J. Pickard, P.J. Hasnip, M.J. Probert, K. Refson, M.C. Payne, First principles methods using CASTEP, Zeitschrift Fur Kristallographie, 220 (2005) 567-570.

[301] V.I. Anisimov, F. Aryasetiawan, A.I. Lichtenstein, First-principles calculations of the electronic structure and spectra of strongly correlated systems: The LDA+U method, Journal of Physics-Condensed Matter, 9 (1997) 767-808.

[302] X. Gonze, J.M. Beuken, R. Caracas, F. Detraux, M. Fuchs, G.M. Rignanese, L. Sindic, M. Verstraete, G. Zerah, F. Jollet, M. Torrent, A. Roy, M. Mikami, P. Ghosez, J.Y. Raty, D.C. Allan, First-principles computation of material properties: the ABINIT software project, Computational Materials Science, 25 (2002) 478-492.

[303] M.D. Segall, P.J.D. Lindan, M.J. Probert, C.J. Pickard, P.J. Hasnip, S.J. Clark, M.C. Payne, First-principles simulation: ideas, illustrations and the CASTEP code, Journal of Physics-Condensed Matter, 14 (2002) 2717-2744.

[304] D.J. Tannor, B. Marten, R. Murphy, R.A. Friesner, D. Sitkoff, A. Nicholls, M. Ringnalda, W.A. Goddard, B. Honig, Accurate first principles calculation of molecular charge distributions and solvation energies from ab initio quantum mechanics and continuum dielectric theory, Journal of the American Chemical Society, 116 (1994) 11875-11882.

[305] B. Monserrat, R.J. Needs, Comparing electron-phonon coupling strength in diamond, silicon, and silicon carbide: First-principles study, Physical Review B, 89 (2014) 214304.

[306] S. Ponce, G. Antonius, P. Boulanger, E. Cannuccia, A. Marini, M. Cote, X. Gonze, Verification of first-principles codes: Comparison of total energies, phonon frequencies, electron-phonon coupling and zero-point motion correction to the gap between ABINIT and QE/Yambo, Computational Materials Science, 83 (2014) 341-348.

[307] T. Gunst, T. Markussen, K. Stokbro, M. Brandbyge, First-principles method for electron-phonon coupling and electron mobility: Applications to two-dimensional materials, Physical Review B, 93 (2016) 035414.

[308] S. Sadasivam, U.V. Waghmare, T.S. Fisher, Electron-phonon coupling and thermal conductance at a metal-semiconductor interface: First-principles analysis, Journal of Applied Physics, 117 (2015) 134502.

[309] M. Siakavellas, A.G. Kontos, Y.S. Raptis, Strain characterization of epitaxially-grown superlattices by Raman spectroscopy, 2002.

[310] J. Nieto-Jalil, R. Perez-Alvarez, Optical phonons in II-VI quantum wells, Physica Status Solidi a-Applications and Materials Science, 164 (1997) 699-708.

[311] V.S. Bagaev, L.K. Vodop'yanov, V.S. Vinogradov, V.V. Zaitsev, S.P. Kozyrev, N.N. Mel'nik, E.E. Onishchenko, G. Karczewski, Electronic states and vibration spectra of CdTe/ZnTe quantum dot superlattices, Physics of the Solid State, 46 (2004) 173-175.

[312] R. Vogelgesang, A.J. Mayur, M.D. Sciacca, E. Oh, I. Miotkowski, A.K. Ramdas, S. Rodriguez, G. Bauer, Raman and infrared spectroscopy of optical phonons in II-VI alloys, epilayers and superlattices, Journal of Raman Spectroscopy, 27 (1996) 239-247.

[313] J. Menendez, A. Pinczuk, J.P. Valladares, R.D. Feldman, R.F. Austin, Resonance Raman scattering in CdTe-ZnTe superlattices, Applied Physics Letters, 50 (1987) 1101-1103.

[314] S. Nakashima, Y. Nakakura, H. Fujiyasu, K. Mochizuki, Raman scattering from ZnTe-ZnSe strained-layer superlattices, Applied Physics Letters, 48 (1986) 236-238.

[315] S. Nakashima, A. Wada, H. Fujiyasu, M. Aoki, H. Yang, Resonant Raman scattering in ZnTe-ZnSe strained layer superlattices, Journal of Applied Physics, 62 (1987) 2009-2011.

[316] L.H. Shon, K. Inoue, K. Murase, H. Fujiyasu, Y. Yamazaki, Raman probing of ZnTe-ZnS strained layer supperlattices, Solid State Communications, 62 (1987) 621-625.

[317] T. Fromherz, F. Hauzenberger, W. Faschinger, M. Helm, P. Juza, H. Sitter, G. Bauer, Confined transverse optical phonons in ultrathin CdTe/ZnTe superlattices, Physical Review B, 47 (1993) 1998-2002.

[318] M.K. Jackson, R.H. Miles, T.C. McGill, J.P. Faurie, Raman scattering determination of strain in CdTe/ZnTe superlattices, Applied Physics Letters, 55 (1989) 786-788.

[319] E. Oh, A.K. Ramdas, T. Fromherz, W. Faschinger, G. Bauer, H. Sitter, Confined and propagating phonons in ultrathin CdTe/ZnTe superlattices, Physical Review B, 48 (1993) 17364-17367.

[320] Y. Jin, Y.T. Hou, S.L. Zhang, J. Li, S.X. Yuan, G.G. Qin, Interface vibrational mode in CdSe/ZnTe superlattices, Physical Review B, 45 (1992) 12141-12143.

[321] R. Sugie, H. Ohta, H. Harima, S. Nakashima, H. Fujiyasu, Raman scattering of interface modes in ZnTe-CdSe superlattices, Journal of Applied Physics, 80 (1996) 5946-5950.

[322] J. Cui, H.L. Wang, F.X. Gan, Longitudinal optical phonon modes in a ZnSe-ZnTe strained-layer superlattice, Journal of Applied Physics, 72 (1992) 1521-1524.

[323] J. Frandon, M.A. Renucci, N. Briot, O. Briot, R.L. Aulombard, Confinement and strain effects on phonons in a ZnSe-ZnTe superlattice, Superlattices and Microstructures, 14 (1993) 71-78.

[324] J. Cui, H.L. Wang, F.X. Gan, A.H. Li, The study of phonons and lattice strains in ZnSe-ZnTe and ZnS-ZnSe strained-layer superlattices by Raman and fari-infrared reflectivity, Journal of Crystal Growth, 111 (1991) 811-815.

[325] H. Ozaki, D. Suzuki, K. Imai, K. Kumazaki, Photoluminescence and Raman scattering of ZnSe-ZnTe superlattices, Physica Status Solidi a-Applied Research, 133 (1992) 523-532.

[326] Y.T. Hou, Y. Jin, M.Y. Shen, S.L. Zhang, J. Li, S.X. Yuan, Raman scattering of a CdTe/ZnTe superlattice and quantum wells, Superlattices and Microstructures, 12 (1992) 69-71.

[327] M. Gilic, N. Romcevic, M. Romcevic, D. Stojanovic, R. Kostic, J. Trajic, W.D. Dobrowolski, G. Karczewski, R. Galazka, Optical properties of CdTe/ZnTe self-assembled quantum dots: Raman and photoluminescence spectroscopy, Journal of Alloys and Compounds, 579 (2013) 330-335.

[328] N. Pelekanos, J. Ding, Q. Fu, A.V. Nurmikko, S.M. Durbin, M. Kobayashi, R.L. Gunshor, Hot-exciton luminescence in ZnTe/MnTe quantum wells, Physical Review B, 43 (1991) 9354-9357.

[329] V.S. Vinogradov, G. Karczewski, I.V. Kucherenko, N.N. Mel'nik, P. Fernandez, Raman spectra of structures with CdTe-, ZnTe-, and CdSe-based quantum dots and their relation to the fabrication technology, Physics of the Solid State, 50 (2008) 164-167.

[330] S.L. Zhang, Y.T. Hou, M.Y. Shen, J. Li, S.X. Yuan, Multiphonon Raman scattering resonant with 2 kinds of excitons in a (CdTe)2(ZnTe)4/ZnTe short-period-superlattice multiple quantum well, Physical Review B, 47 (1993) 12937-12940.

[331] R.P. Stanley, J.F. Donegan, J. Hegarty, R.D. Feldman, R.F. Austin, Dynamics of excitons in CdxZn1-xTe/ZnTe quantum wells, Journal of Luminescence, 52 (1992) 109-122.

[332] A. Abdi, T.B. Hoang, S. Mackowski, L.M. Smith, H.E. Jackson, J.M. Yarrison-Rice, J. Kossut, G. Karczewski, Probing the excited state distributions of CdTe/ZnTe self-assembled quantum dots using resonant Raman scattering, Applied Physics Letters, 87 (2005) 183104.

[333] E. Oh, A.K. Ramdas, N. Samarth, H. Luo, J.K. Frurdyna, Magnetic and vibrational raman scattering from II-VI magnetic quantum wells - ZnTe/Cd1-xMnxSe and ZnTe/MnSe, Physical Review B, 47 (1993) 7288-7294.

[334] D. Lee, J.E. Zucker, A.M. Johnson, R.D. Feldman, R.F. Austin, Raman scattering resonant with excitons in CdZnTe/ZnTe multiple quantum wells, Applied Physics Letters, 59 (1991) 75-77.

[335] N. Pelekanos, Q. Fu, A.V. Nurmikko, S. Durbin, J. Han, O. Sungki, D. Menke, M. Kobayashi, R.L. Gunshor, Spectroscopy in CdTe/MnTe and ZnTe/MnTe single quantum wells - New binary wide gap II-VI heterostructures, Journal of Crystal Growth, 101 (1990) 628-631.

[336] W. Szuszkiewicz, J.F. Morhange, E. Dynowska, E. Janik, W. Zaleszczyk, A. Presz, G. Karczewski, T. Wojtowicz, Raman spectroscopy of MBE-grown ZnTe and $Zn_{1-x}Mn_xTe$ nanowires, in: B. Perrin, B. Bonello, A. Devos, J.Y. Duquesne, C. Rossignol (Eds.) 12th International Conference on Phonon Scattering in Condensed Matter, 2007.

[337] W. Szuszkiewicz, J.-F. Morhange, E. Janik, W. Zaleszczyk, G. Karczewski, T. Wojtowicz, Raman spectroscopy of MBE-grown ZnTe-based nanowires, in: E.M. Sheregii, W. Gebicki, Y.M. Azhniuk (Eds.) Physica Status Solidi C - Current Topics in Solid State Physics, Vol 6, No 9, 2009, pp. 2047-2052.

[338] J. Camacho, A. Cantarero, I. Hernandez-Calderon, L. Gonzalez, Raman spectroscopy and photoluminescence of ZnTe thin films grown on GaAs, Journal of Applied Physics, 92 (2002) 6014-6018.

[339] R.J. Thomas, M.S. Boley, H.R. Chandrasekhar, M. Chandrasekhar, C. Parks, A.K. Ramdas, J. Han, M. Kobayashi, R.L. Gunshor, Raman and modulated-reflectivity spectra of a strained pseudomorphic ZnTe epilayer in InAs under pressure, Physical Review B, 49 (1994) 2181-2184.

[340] M.A. Foad, M. Watt, A.P. Smart, C.M.S. Torres, C.D.W. Wilkinson, W. Kuhn, H.P. Wagner, S. Bauer, H. Leiderer, W. Gebhardt, High-resolution dry etching of zinc telluride: Characterization of etched surfaces by X-ray photoelectron spectroscopy, photoluminescence and Raman scattering, Semiconductor Science and Technology, 6 (1991) A115-A122.

[341] G. Kudlek, J. Gutowski, Analysis of strain and impurity distribution in II-VI epilayers with optical methods, Journal of Luminescence, 52 (1992) 55-69.

[342] D.N. Talwar, Z.C. Feng, P. Becla, Impurity-induced phonon disordering in $Cd_{1-x}Zn_xTe$ ternary alloys, Physical Review B, 48 (1993) 17064-17071.

[343] O.I. Olusola, M.L. Madugu, N.A. Abdul-Manaf, I.M. Dharmadasa, Growth and characterisation of n- and p-type ZnTe thin films for applications in electronic devices, Current Applied Physics, 16 (2016) 120-130.

[344] A.R. Balu, V.S. Nagarethinam, A. Thayumanavan, K.R. Murali, C. Sanjeeviraja, M. Jayachandran, Effect of thickness on the microstructural, optoelectronic and morphological properties of electron beam evaporated ZnTe films, Journal of Alloys and Compounds, 502 (2010) 434-438.

[345] H.P. Wagner, S. Lankes, K. Wolf, W. Kuhn, P. Link, W. Gebhardt, Spectroscopic investigations of donor and acceptor states in n-doped and p-doped ZnTe epilayers, Journal of Crystal Growth, 117 (1992) 303-308.

[346] J.H. Lee, K.S. Jang, C.S. Shin, H.L. Park, T.W. Kim, Structural and optical properties in ZnTe/GaAs strained heterostructures grown by temperature gradient vapor transport deposition, Journal of Applied Physics, 75 (1994) 8216-8218.

[347] S. Nam, J. Rhee, B.S. O, K.S. Lee, Y.D. Choi, Resonance Raman scattering in high-quality ZnTe epilayers grown by hot-wall epitaxy, Journal of the Korean Physical Society, 32 (1998) 82-86.

[348] M.D. Frogley, D.J. Dunstan, W. Palosz, Combined Raman and transmission spectroscopy of ZnTe under pressure, Solid State Communications, 107 (1998) 537-541.

[349] M.J. Seong, I. Miotkowski, A.K. Ramdas, Isoelectronic impurities in II-VI semiconductors: ZnTe doped with Ca, Sr, and Ba, Physical Review B, 59 (1999) 12911-12916.

[350] J. Camacho, I. Loa, A. Cantarero, K. Syassen, High-pressure Raman study of zincblende, cinnabar, and Cmcm phases of ZnTe, High Pressure Research, 22 (2002) 309-313.

[351] M.J. Seong, H. Alawadhi, I. Miotkowski, A.K. Ramdas, S. Miotkowska, Role of electronegativity in semiconductors: Isoelectronic S, Se, and O in ZnTe, Physical Review B, 62 (2000) 1866-1872.

[352] Z.C. Feng, S. Perkowitz, P. Becla, Multiple phonon overtones in ZnTe, Solid State Communications, 78 (1991) 1011-1014.

[353] M.P. Halsall, D. Wolverson, J.J. Davies, B. Lunn, D.E. Ashenford, Ga2Te3 and tellurium interfacial layers in ZnTe/GaSb heterostructures studied by Raman scattering, Applied Physics Letters, 60 (1992) 2129-2131.

[354] C.T. Chou, J.L. Hutchison, D. Cherns, M.J. Casanove, J.W. Steeds, R. Vincent, B. Lunn, D.A. Ashenford, An ordered Ga2Te3 phase in the ZnTe/GaSb interface, Journal of Applied Physics, 74 (1993) 6566-6570.

[355] J. Schrier, D.O. Demchenko, L.-W. Wang, Optical properties of ZnO/ZnS and ZnO/ZnTe heterostructures for photovoltaic applications, Nano Letters, 7 (2007) 2377-2382.

[356] L.D. Deloach, R.H. Page, G.D. Wilke, S.A. Payne, W.F. Krupke, Transition metal-doped zinc chalcogenides: Spectroscopy and laser demonstration of a new class of gain media, IEEE Journal of Quantum Electronics, 32 (1996) 885-895.

[357] F. Blanchard, L. Razzari, H.C. Bandulet, G. Sharma, R. Morandotti, J.C. Kieffer, T. Ozaki, M. Reid, H.F. Tiedje, H.K. Haugen, F.A. Hegmann, Generation of 1.5 mu J single-cycle terahertz pulses by optical rectification from a large aperture ZnTe crystal, Optics Express, 15 (2007) 13212-13220.

[358] T. Tanaka, Y. Kume, M. Nishio, Q.X. Guo, H. Ogawa, A. Yoshida, Fabrication of ZnTe light-emitting diodes using Bridgman-grown substrates, Japanese Journal of Applied Physics Part 2-Letters, 42 (2003) L362-L364.

[359] K. Sato, M. Hanafusa, A. Noda, A. Arakawa, M. Uchida, T. Asahi, O. Oda, ZnTe pure green light-emitting diodes fabricated by thermal diffusion, Journal of Crystal Growth, 214 (2000) 1080-1084.

[360] K. Sato, T. Asahi, M. Hanafusa, A. Noda, A. Arakawa, M. Uchida, O. Oda, Y. Yamada, T. Taguchi, Development of pure green LEDs based on ZnTe, Physica Status Solidi a-Applied Research, 180 (2000) 267-274.

[361] Q. Wu, M. Litz, X.C. Zhang, Broadband detection capability of ZnTe electro-optic field detectors, Applied Physics Letters, 68 (1996) 2924-2926.

[362] T. Loffler, T. Hahn, M. Thomson, F. Jacob, H.G. Roskos, Large-area electro-optic ZnTe terahertz emitters, Optics Express, 13 (2005) 5353-5362.

[363] K.J. Albert, N.S. Lewis, C.L. Schauer, G.A. Sotzing, S.E. Stitzel, T.P. Vaid, D.R. Walt, Cross-reactive chemical sensor arrays, Chemical Reviews, 100 (2000) 2595-2626.

[364] T.A. Dickinson, J. White, J.S. Kauer, D.R. Walt, A chemical-detecting system based on a cross-reactive optical sensor array, Nature, 382 (1996) 697-700.

[365] U. Tisch, H. Haick, Nanomaterials for cross-reactive sensor arrays, Mrs Bulletin, 35 (2010) 797-803.

[366] W. Stadler, D.M. Hofmann, H.C. Alt, T. Muschik, B.K. Meyer, Optical investigations of defects in Cd1-xZnxTe, Physical Review B, 51 (1995) 10619-10630.

[367] M.I.B. Utama, M. de la Mata, Q. Zhang, C. Magen, J. Arbiol, Q. Xiong, The Growth of Ultralong ZnTe Micro/Nanostructures: The Influence of Polarity and Twin Direction on the Morphogenesis of Nanobelts and Nanosheets, Crystal Growth & Design, 13 (2013) 2590-2596.

[368] T. Yao, M. Kato, J.J. Davies, H. Tanino, Photoluminescence of excitons bound at Te isoelectronic traps in ZnSe, Journal of Crystal Growth, 86 (1988) 552-557.

[369] S. Xu, C. Wang, Y. Cui, Influence of ligand and solvent on characters of ZnTe clusters, Journal of Molecular Structure, 938 (2009) 133-136.

[370] E.J. Juarez-Perez, R.S. Sanchez, L. Badia, G. Garcia-Belmonte, Y.S. Kang, I. Mora-Sero, J. Bisquert, Photoinduced Giant Dielectric Constant in Lead Halide Perovskite Solar Cells, Journal of Physical Chemistry Letters, 5 (2014) 2390-2394.

[371] H.S. Tan, N. Mathews, T. Cahyadi, F.R. Zhu, S.G. Mhaisalkar, The effect of dielectric constant on device mobilities of high-performance, flexible organic field effect transistors, Applied Physics Letters, 94 (2009).

[372] S.C. Jones, P. Braunlich, R.T. Casper, X.A. Shen, P. Kelly, Recent progress on laser-induced modifications and intrinsic bulk damage of wide-gap optical materials, Optical Engineering, 28 (1989) 1039-1068.

[373] F.K.P. Mirzoev, V.Ya.; Shelepin, L.A., Laser control of processes in solids, SUpspekhi Fizichenskikh Nauk, 39 (1996) 1-29.

[374] J. Reif, High power interaction with the surface of wide bandgap materials, Optical Engineering, 28 (1989) 1122-1132.

[375] F. Costache, M. Henyk, J. Reif, Modification of dielectric surfaces with ultra-short laser pulses, Applied Surface Science, 186 (2002) 352-357.

[376] M. Bertolotti, F. de Pasquale, P. Marietti, D. Sette, G. Vitali, Laser damage on semiconductor surfaces, Journal of Applied Physics, 38 (1967) 4088-4090.

[377] C. Uzan, R. Legros, Y. Marfaing, R. Triboulet, CW laser-induced low-temperature decomposition of CdTe crystals, Applied Physics Letters, 45 (1984) 879-880.

[378] J.R. Meyer, M.R. Kruer, F.J. Bartoli, Optical heating in semiconductors: Laser damage in Ge, Si, InSb, and GaAs, Journal of Applied Physics, 51 (1980) 5513-5522.

[379] G. Rossbach, M. Feneberg, M. Roeppischer, C. Werner, N. Esser, C. Cobet, T. Meisch, K. Thonke, A. Dadgar, J. Blaesing, A. Krost, R. Goldhahn, Influence of exciton-phonon coupling and strain on the anisotropic optical response of wurtzite AlN around the band edge, Physical Review B, 83 (2011).

[380] A.S. Pine, Dresselh.G, Raman spectra and lattice dynamics of tellurium, Physical Review B-Solid State, 4 (1971) 356-371.

[381] H.M. Cheng, K.F. Lin, H.C. Hsu, W.F. Hsieh, Size dependence of photoluminescence and resonant Raman scattering from ZnO quantum dots, Applied Physics Letters, 88 (2006) 261909.

[382] J.F. Ready, Industrial applications of lasers, Academic Press, San Diego, CA, 1997.

[383] P. Rai-Choudhurry, MEMs and MOEMS technology and applications, SPIE Press, Bellingham, WA, 2000.

[384] C.T. Pan, H. Hocheng, Laser machining and its associated affects, in: H. Haocheng, H.-Y. Tsai (Eds.) Advanced analysis of non-traditional machining, Springer Science+Business Media, New York, NY, 2013.

[385] Y.-L. Zhang, Q.-D. Chen, H. Xia, H.-B. Sun, Designable 3D nanofabrication by femtosecond laser direct writing, Nano Today, 5 (2010) 435-448.

[386] S. Maruo, J.T. Fourkas, Recent progress in multiphoton microfabrication, Laser & Photonics Reviews, 2 (2008) 100-111.

[387] K. Kordas, K. Bali, S. Leppavuori, A. Uusimaki, L. Nanai, Laser direct writing of copper on polyimide surfaces from solution, Applied Surface Science, 154 (2000) 399-404.

[388] A. Pique, S.A. Mathews, B. Pratap, R.C.Y. Auyeung, B.J. Karns, S. Lakeou, Embedding electronic circuits by laser direct-write, Microelectronic Engineering, 83 (2006) 2527-2533.

[389] T. Inushima, N. Kusumoto, N. Kubo, H.Y. Zhang, S. Yamazaki, Phase transformation in amorphous silicon under excimer laser annealing studies by Raman spectroscopy and mobility measurements, Journal of Applied Physics, 79 (1996) 9064-9073.

[390] R. Tsu, R.T. Hodgson, T.Y. Tan, J.E. Baglin, Order-disorder transition in single-crystal silicon induced by pulsed UV laser irradiation, Physical Review Letters, 42 (1979) 1356-1358.

[391] N. Yue, Y. Zhang, R. Tsu, Ambient condition laser writing of graphene structures on polycrystalline SiC thin film deposited on Si wafer, Applied Physics Letters, 102 (2013) 071912.

[392] D.J. Ehrlich, R.M. Osgood, T.F. Deutsch, Laser chemical technique for rapid direct writing of surface relief in silicon, Applied Physics Letters, 38 (1981) 1018-1020.

[393] A. Pique, D.B. Chrisey, R.C.Y. Auyeung, J. Fitz-Gerald, H.D. Wu, R.A. McGill, S. Lakeou, P.K. Wu, V. Nguyen, M. Duignan, A novel laser transfer process for direct writing of electronic and sensor materials, Applied Physics A-Materials Science & Processing, 69 (1999) S279-S284.

[394] C.B. Arnold, P. Serra, A. Pique, Laser direct-write techniques for printing of complex materials, MRS Bulletin, 32 (2007) 23-31.

[395] K.K.B. Hon, L. Li, I.M. Hutchings, Direct writing technology - Advances and developments, CIRP Annals - Manufacturing Technology, 57 (2008) 601-620.

[396] W. Gao, N. Singh, L. Song, Z. Liu, A.L.M. Reddy, L. Ci, R. Vajtai, Q. Zhang, B. Wei, P.M. Ajayan, Direct laser writing of micro-supercapacitors on hydrated graphite oxide films, Nature Nanotechnology, 6 (2011) 496-500.

[397] J.A. Vanvechten, R. Tsu, F.W. Saris, Nonthermal pulsed laser annealing of Si - Plasma annealing, Physics Letters A, 74 (1979) 422-426.

[398] R.M. Osgood, H.H. Gilgen, Laser direct writing of materials, Annual Review of Materials Science, 15 (1985) 549-576.

[399] B.H. Seo, J. Youn, M. Shim, Direct laser writing of air-stable p-n junctions in graphene, ACS Nano, 8 (2014) 8831-8836.

[400] D.B. Chrisey, Materials processing: The power of direct writing, Science, 289 (2000) 879-881.

[401] D.B. Geohegan, A.A. Puretzky, G. Duscher, S.J. Pennycook, Photoluminescence from gas-suspended SiOx nanoparticles synthesized by laser ablation, Applied Physics Letters, 73 (1998) 438-440.

[402] Y.F. Lu, H.Q. Ni, Z.H. Mai, Z.M. Ren, The effects of thermal annealing on ZnO thin films grown by pulsed laser deposition, Journal of Applied Physics, 88 (2000) 498-502.

[403] X.Y. Chen, Y.F. Lu, Y.H. Wu, B.J. Cho, M.H. Liu, D.Y. Dai, W.D. Song, Mechanisms of photoluminescence from silicon nanocrystals formed by pulsed-laser deposition in argon and oxygen ambient, Journal of Applied Physics, 93 (2003) 6311-6319.

[404] J.M. Moison, C. Licoppe, Y.I. Nissim, F. Houzay, CW laser processing of semiconductor surfaces, Journal of Applied Physics, 59 (1986) 2444-2446.

[405] S.K. Bhattacharya, R.R. Tummala, Next generation integral passives: materials, processes, and integration of resistors and capacitors on PWB substrates, Journal of Materials Science-Materials in Electronics, 11 (2000) 253-268.

[406] W. Chen, H. Ahmed, Fabrication of 5-7 nm wide etched lines in silicon using 100 keV electron-beam lithography and polymethylmethacrylate resist, Applied Physics Letters, 62 (1993) 1499-1501.

[407] S.Y. Chou, P.R. Krauss, W. Zhang, L.J. Guo, L. Zhuang, Sub-10 nm imprint lithography and applications, Journal of Vacuum Science & Technology B, 15 (1997) 2897-2904.

[408] S.H. Ahn, L.J. Guo, Large-area roll-to-roll and roll-to-plate nanoimprint lithography: A step toward high-throughput application of continuous nanoimprinting, ACS Nano, 3 (2009) 2304-2310.

[409] Y.N. Xia, G.M. Whitesides, Soft lithography, Annual Review of Materials Science, 28 (1998) 153-184.

[410] R.D. Piner, J. Zhu, F. Xu, S.H. Hong, C.A. Mirkin, 'Dip-pen' nanolithography, Science, 283 (1999) 661-663.

[411] D.S. Ginger, H. Zhang, C.A. Mirkin, The evolution of dip-pen nanolithography, Angewandte Chemie-International Edition, 43 (2004) 30-45.

[412] J.L. Wilbur, A. Kumar, E. Kim, G.M. Whitesides, Microfabrication by microcontact printing of self-assembled monolayers, Advanced Materials, 6 (1994) 600-604.

[413] R.J. Jackman, J.L. Wilbur, G.M. Whitesides, Fabrication of submicrometer features on curved substrates by microcontact printing, Science, 269 (1995) 664-666.

[414] H. Sirringhaus, T. Kawase, R.H. Friend, T. Shimoda, M. Inbasekaran, W. Wu, E.P. Woo, High-resolution inkjet printing of all-polymer transistor circuits, Science, 290 (2000) 2123-2126.

[415] Y.N. Xia, M. Mrksich, E. Kim, G.M. Whitesides, Microcontact printing of octadecylsiloxane on the surface of silicon dioxide and its applicaiton in microfabrication, Journal of the American Chemical Society, 117 (1995) 9576-9577.

[416] N. Misra, L. Xu, Y. Pan, N. Cheung, C.P. Grigoropoulos, Excimer laser annealing of silicon nanowires, Applied Physics Letters, 90 (2007) 111111.

[417] J. Yuan, L.-P. Ma, S. Pei, J. Du, Y. Su, W. Ren, H.-M. Cheng, Tuning the electrical and optical properties of graphene by ozone treatment for patterning monolithic transparent electrodes, ACS Nano, 7 (2013) 4233-4241.

[418] J. Lu, X. Lim, M. Zheng, S.G. Mhaisalkar, C.-H. Sow, Direct laser pruning of CdS_xSe_{1-x} nanobelts en route to a multicolored pattern with controlled functionalities, ACS Nano, 6 (2012) 8298-8307.

[419] A. Ebina, K. Asano, T. Takahashi, Surface properties of clean, and with adsorbed oxygen surfaces of CdTe (110), (111), and (100) and of CdSe (0001) studied by electron-energy-loss spectroscopy and Auger-electron spectroscopy, Physical Review B, 22 (1980) 1980-1991.

[420] T. Sameshima, S. Usui, M. Sekiya, XeCl excimer laser annealing used in the fabrication of poly-Si TFTs, IEEE Electron Device Letters, 7 (1986) 276-278.

[421] K. Sera, F. Okumura, H. Uchida, S. Itoh, S. Kaneko, K. Hotta, High-performance TFTs fabricated by XeCl excimer laser annealing of hydrogenated amorphous-silicon film, IEEE Transactions on Electron Devices, 36 (1989) 2868-2872.

[422] C. Wang, M. Takahashi, H. Fujino, X. Zhao, E. Kume, T. Horiuchi, S. Sakai, Leakage current of multiferroic (Bi0.6Tb0.3La0.1)FeO3 thin films grown at various oxygen pressures by pulsed laser deposition and annealing effect, Journal of Applied Physics, 99 (2006) 054104.

[423] I.E. Ture, A.W. Brinkman, G.J. Russell, J. Woods, The effects of oxygen in Au-CdSe Schottky diodes, Physica Status Solidi A-Applied Research, 100 (1987) 681-691.

[424] R. Sobolewski, W. Xiong, W. Kula, J.R. Gavaler, Laser patterning of Y-Ba-Cu-O thin film devices and circuits, Applied Physics Letters, 64 (1994) 643-645.

[425] C. Levy-Clement, R. Tena-Zaera, M.A. Ryan, A. Katty, G. Hodes, CdSe-sensitized p-CuSCN/nanowire n-ZnO heterojunctions, Advanced Materials, 17 (2005) 1512-1515.

[426] Y. Yu, P.V. Kamat, M. Kuno, A CdSe nanowire/quantum dot hybrid architecture for improving solar cell performance, Advanced Functional Materials, 20 (2010) 1464-1472.

[427] S. Kirmayer, E. Edri, D. Hines, N. Klein-Kedem, H. Cohen, O. Niitsoo, I. Pinkas, P.V. Kamat, G. Hodes, Surface oxidation as a cause of high open-circuit voltage in CdSe ETA solar cells, Advanced Materials Interfaces, 2 (2015) 1400346.

[428] J. Li, C. Meng, Y. Liu, X. Wu, Y. Lu, Y. Ye, L. Dai, L. Tong, X. Liu, Q. Yang, Wavelength tunable CdSe nanowire lasers based on the absorption-emission-absorption process, Advanced Materials, 25 (2013) 833-837.

[429] A. Khandelwal, D. Jena, J.W. Grebinski, K.L. Hull, M.K. Kuno, Ultrathin CdSe nanowire field-effect transistors, Journal of Electronic Materials, 35 (2006) 170-172.

[430] Z. He, W. Zhang, W. Zhang, J. Jie, L. Luo, G. Yuan, J. Wang, C.M.L. Wu, I. Bello, C.-S. Lee, S.-T. Lee, High-performance CdSe:In nanowire field-effect transistors based on top-gate configuration with high-k non-oxide dielectrics, Journal of Physical Chemistry C, 114 (2010) 4663-4668.

[431] K. Hattori, A. Okano, Y. Nakai, N. Itoh, Laser-induced electronic processes on GaP (110) surfaces: Particle emission and ablation initiated by defects, Physical Review B, 45 (1992) 8424-8436.

[432] M. Mitsunaga, H. Shinojima, K. Kubodera, Laser annealing effect of carrier recombination time in CdS_xSe_{1-x} doped glasses, Journal of the Optical Society of America B-Optical Physics, 5 (1988) 1448-1452.

[433] L. Hu, H. Wu, Influence of size and surface state emission on photoluminescence of CdSe quantum dots under UV irradiation, Journal of Luminescence, (2016) Accepted. Available: http://dx.doi.org/10.1016/j.jlumin.2016.1004.1049.

[434] B. Fortin, F. Raoult, G. Rosse, Y. Colin, M. El Khadir, Analysis of the polycrystalline semiconducting film electrical resistance variation due to isothermal desorption and temperature stimulated desorption of oxygen, in: H.J. Möller, H.P. Strunk, J.H. Werner (Eds.) Polycrystalline semiconductors: Grain boundaries and interfaces, Springer-Verlag, New York, 1988, pp. 139-145.

[435] V. Babentsov, J. Riegler, J. Schneider, M. Fiederle, T. Nann, Excitation dependence of steady-state photoluminescence in CdSe nanocrystal films, Journal of Physical Chemistry B, 109 (2005) 15349-15354.

[436] A.K. Arora, A.K. Ramdas, Resonance Raman scattering from defects in CdSe, Physical Review B, 35 (1987) 4345-4350.

[437] V.V. Poborchii, A.V. Kolobov, K. Tanaka, An in situ Raman study of polarization-dependent photocrystallization in amorphous selenium films, Applied Physics Letters, 72 (1998) 1167-1169.

[438] J.M. Rabaey, A. Chandrakasan, B. Nikolic, Digital integrated circuits: A design perspective, Pearson, New York, NY, 2003.

[439] S.L. Hurst, Multiple-valued logic - Its status and future, IEEE Transactions on Computers, 33 (1984) 1160-1179.

[440] V. Gaudet, A survey and tutorial on contemporary aspects of multiple-valued logic and its application to microelectronic circuits, IEEE Journal on Emerging and Selected Topics in Circuits and Systems, 6 (2016) 5-12.

[441] A.K. Jain, R.J. Bolton, M.H. Abdelbarr, CMOS multiple-valued logic design. 1. Circuit implementation, IEEE Transactions on Circuits and Systems I-Fundamental Theory and Applications, 40 (1993) 503-514.

[442] Q. Chen, Y. Zhang, The reversal of the laser-beam-induced-current contrast with varying illumination density in a Cu2ZnSnSe4 thin-film solar cell, Applied Physics Letters, 103 (2013) 242104.

[443] F.J. Schultes, T. Christian, R. Jones-Albertus, E. Pickett, K. Alberi, B. Fluegel, T. Liu, P. Misra, A. Sukiasyan, H. Yuen, N.M. Haegel, Temperature dependence of diffusion length, lifetime and minority electron mobility in GaInP, Applied Physics Letters, 103 (2013) 242106.

[444] N.M. Haegel, Integrating electron and near-field optics: Dual vision for the nanoworld, Nanophotonics, 3 (2014) 75-89.

[445] A.K.H. Henning, T.; , C.G. Levey, C.P. Daghlian, J. Slinkman, J. Never, P. Kaszuba, R. Gluck, R. Wells, R. Bolam, P. Coutu, Applications of scanning probe microscopy to problems in microelectronic device failure analysis, in: Scanning Microscopy International Conference, Houston, TX, 1995.

[446] A.K.H. Henning, T.; , C.G. Levey, C.P. Daghlian, J. Slinkman, J. Never, P. Kaszuba, R. Gluck, R. Wells, R. Bolam, P. Coutu, Surface studies with the force-based scanning Kelvin probe, in: ndustrial Applications of Scanned Probe Microscopy Workshop, Gaithersburg, MD, 1995.

[447] K. Banerjee, S.J. Souri, P. Kapur, K.C. Saraswat, 3-D ICs: A novel chip design for improving deep-submicrometer interconnect performance and systems-on-chip integration, Proceedings of the IEEE, 89 (2001) 602-633.

[448] A.K. Datta, S. Munshi, Optical implementation of flip-flops using single-LCD panel, Optics and Laser Technology, 40 (2008) 1-5.

[449] P. Anzenbacher, Jr., P. Lubal, P. Bucek, M.A. Palacios, M.E. Kozelkova, A practical approach to optical cross-reactive sensor arrays, Chemical Society Reviews, 39 (2010) 3954-3979.

[450] C. Xu, E. Bakker, Multicolor quantum dot encoding for polymeric particle-based optical ion sensors, Analytical Chemistry, 79 (2007) 3716-3723.

[451] S.H. Jo, T. Chang, I. Ebong, B.B. Bhadviya, P. Mazumder, W. Lu, Nanoscale memristor device as synapse in neuromorphic systems, Nano Letters, 10 (2010) 1297-1301.

[452] G. Indiveri, B. Linares-Barranco, T.J. Hamilton, A. van Schaik, R. Etienne-Cummings, T. Delbruck, S.-C. Liu, P. Dudek, P. Hafliger, S. Renaud, J. Schemmel, G. Cauwenberghs, J. Arthur, K. Hynna, F. Folowosele, S. Saighi, T. Serrano-Gotarredona, J. Wijekoon, Y. Wang, K. Boahen, Neuromorphic silicon neuron circuits, Frontiers in Neuroscience, 5 (2011) 73.

[453] A. Hepp, H. Heil, W. Weise, M. Ahles, R. Schmechel, H. von Seggern, Light-emitting field-effect transistor based on a tetracene thin film, Physical Review Letters, 91 (2003) 157406.

APPENDIX I: THE CONTEXT FOR NANOWIRES

"My greatest concern is that the emergence of [nanotechnology] without the appropriate public attention and international controls could lead to an unstable arms race."

K. Eric Drexler, 2013 Radical Abundance:
How Nanotechnology Will Change Civilization

AI.1 Public Awareness and Literature Landscape

For years, most Americans, as well as the world, were largely unaware of what nanotechnology actually is or of its impact in our global society [1-8], which scant media coverage may have played a role [9], although nationally funded nanotechnology centers are combating this problem [10]. Researchers are now better informed on the issue [6], and even cite Dr. Feynman's 1959 speech on "Plenty of room at the Bottom" [11] as the origin of the nanoscale vision, but they still highlight the term's ambiguity [12]. Few may know of the pioneering work on metallic whiskers by Cobb and by Bell Laboratories Staff in 1946 and 1951 respectively [12, 13]. Whiskers are 1–5 microns in diameter and 1–500 microns in length [14] and were the precursor to nanowires. Nanowires are identical to nanowhiskers, except that their radius is usually within the 1–100 nm range, although a less common definition exists where the aspect ratio is below 100. Whisker research created the pathway to lead–free electronics [13-15], and to a world where nano–based devices appear in integrated chips aiming for tetrahertz processing speeds [16]. The concept of whiskers has appeared in literature since the 1940s, while one–dimensional (1D) nanowires were prevalent in literature for about the past 20 years. Web of Science's citation report™, which was conducted on 24 April 2016, shows the number of publications by topic as shown in Table AI.1. Note the almost exponential increase in the number of citations from the mid–1990s until now, with a subtle decline since the 2000s. Metallic nanowires increased the earliest and

most abruptly. Before the mid–1990s, there were occasional articles on this topic, while II–VI nanowires did not occur frequently until the early 2000s. While the source of the decline in total publications has not been explored, one explanation is changing terminology. For example, specifically mentioning insulating or semiconducting may be necessary to highlight novel growth strategies or devices. After the technique or application becomes common knowledge, the general term of “nanowire” (30,000+), “whiskers” (14,000+), or “nanowire arrays” (11,000+) may be used. These terms were not included in Table AI.1 because citation reports could not be generated for such a large number of results. Similarly, “quantum nanowires,” “organic nanowires,” and “one–dimensional nanowires” were not included for similar reasons and respectively generated 15,303, 10,457, and 11,622 records respectively. Regardless of the reason, it is clear that II–VI nanowires are relatively under–investigated compared to other nanowire materials, e.g., little was published about defects. As a result, II–VI nanowires could yield further insights and are worth additional investigation. While strong quantum confinement affects are typically observed for diameters below a few nanometers [17], a nanowire’s large surface–to–volume ratio may result in altered optical and electrical properties that are distinctly different from their molecular, thin film, and bulk counterparts (refer to Chapter 2). The large surface–to–volume ratio is ideal for chemical adsorption/surface passivation, which may be used in gas/chemical [18-22], force– [23], and bio–sensors [18, 24-26]. The large surface area may be passivated with chemical species or a semiconductor–based shell in order to alter optical properties [21, 22, 27]. Other properties may also be effected, such as polarization–dependence [28-30], electrical properties [21, 22, 31-33], diameter–dependent, thermal conductivities [34], and the potential for tunable super currents [35].

Table AI.1 Total articles, number of citations without self-citations, average citations per article, and h-index values for different keywords used to generate Web of Science™'s citation reports generated on 24 April 2016. The h–index indicates that *n* articles have at least *n* citations, e.g., an h–index of 20 means that at least 20 articles have at least 20 citations.

Category	Total Articles	Citations	Average Citations	h–index
II–VI Nanowires	521	12661	25.00	58
III–V Nanowires	1312	22591	25.43	80
Inorganic Nanowires	1956	62273	32.87	111
Insulating Nanowires	849	16700	19.92	60
Nanowhiskers	1423	23053	19.64	77
Organic Nanowires	9574	78483	24.53	140
Semiconducting Nanowires	2100	70591	34.87	110

It should be noted that substrate preparation, nanowire density and diameter, catalyst, and other growth conditions also play a role in altering these properties [36-43], where a major role is played by the defect configuration and density [44-49]. For example, oxide layers play important roles in transistor performance [50].

Nanowires are used in a number of applications including: batteries [51, 52], lasers [22, 53-56], light–emitting diodes (LEDs) [22, 57, 58], nano–generators [22, 59, 60], optical switches [61], photo–detectors [61, 62], photonic applications [63-65], piezoelectric and piezo–phototronic devices [22, 66-68], solar cell/photovoltaic devices [22, 69-75], thermoelectric applications [76, 77], transistor applications [20, 23, 25, 31, 46, 78, 79], and as optical waveguides [56]. These nano–sized devices have the potential for smaller grain boundaries, and for example, increased electron mobilities [80]. A significant research direction is the integration of these devices into more complex structures [81-84], such as nanowire circuits [85]. Such devices will be in need of thermal management. Large laser cooling, perhaps from an integrated optical source, could drastically cool the system, e.g., up to a 40 K reduction was reported [86].

Applications for nanowires are numerous and are continually expanding in research focus. Every few years, new observations are published. This is an exciting field that, despite about 20 years of sustained investigation, still has much insight to yield.

REFERENCES

[1] The Harris Poll, Nanotechnology awareness may be low, but opinions are strong: Regional and generational disparities in familiarity with and feelings toward nanotech are anything but small, in, 2012.

[2] The Project on Emerging Nanotechnologies, Poll reveals public awareness of nanotech stuck at low level, in, 2007.

[3] J. Besley, Current research on public perceptions of nanotechnology, Emerging health threats journal, 3 (2010) 1-8.

[4] D.M. Kahan, D. Braman, P. Slovic, J. Gastil, G. Cohen, Cultural cognition of the risks and benefits of nanotechnology, Nature Nanotechnology, 4 (2009) 87-90.

[5] M.D. Cobb, J. Macoubrie, Public perceptions about nanotechnology: Risks, benefits and trust, Journal of Nanoparticle Research, 6 (2004) 395-405.

[6] M. Siegrist, C. Keller, H. Kastenholz, S. Frey, A. Wiek, Laypeople's and experts' perception of nanotechnology hazards, Risk Analysis, 27 (2007) 59-69.

[7] M.-F. Chen, Y.-P. Lin, T.-J. Cheng, Public attitudes toward nanotechnology applications in Taiwan, Technovation, 33 (2013) 88-96.

[8] E. Senocak, A Survey on Nanotechnology in the View of the Turkish Public, Science Technology and Society, 19 (2014) 79-94.

[9] D.A. Scheufele, B.V. Lewenstein, The public and nanotechnology: How citizens make sense of emerging technologies, Journal of Nanoparticle Research, 7 (2005) 659-667.

[10] K.K. Runge, S.K. Yeo, M. Cacciatore, D.A. Scheufele, D. Brossard, M. Xenos, A. Anderson, D.-h. Choi, J. Kim, N. Li, X. Liang, M. Stubbings, L.Y.-F. Su, Tweeting nano: how public discourses about nanotechnology develop in social media environments, Journal of Nanoparticle Research, 15 (2013) 1381.

[11] R.P. Feynmann, There's Plenty of Room at the Bottom, Engineering and Science, 23 (1960) 22-36.

[12] N.K. Tolochko, History of nanotechnology, in: V. Kharvin, C. Bai, O.O. Awadelkarim, S. Kapitsa (Eds.) Nanoscience and Nanotechnology, UNESCO-EOLSS, Encyclopedia for Life Support Systems, Oxford, 2009.

[13] H.L. Cobb, Cadmium Whiskers, Monthly Review American Electroplaters' Society, 33 (1946) 28-30.

[14] G.T. Galyon, Annotated tin whisker bibliography and anthology, IEEE Transactions on Electronics Packaging Manufacturing, 28 (2005) 94-122.

[15] K.G. Compton, Filamentary Growths on Metal Surfaces - "Whiskers", Corrosion, 7 (1951) 327-334.

[16] S. Anthony, IBM creates first cheap, commercially viable, electronic-photonic integrated chip, in, 2012.

[17] D.D.D. Ma, C.S. Lee, F.C.K. Au, S.Y. Tong, S.T. Lee, Small-diameter silicon nanowire surfaces, Science, 299 (2003) 1874-1877.

[18] Y. Cui, Q.Q. Wei, H.K. Park, C.M. Lieber, Nanowire nanosensors for highly sensitive and selective detection of biological and chemical species, Science, 293 (2001) 1289-1292.

[19] Q. Wan, Q.H. Li, Y.J. Chen, T.H. Wang, X.L. He, J.P. Li, C.L. Lin, Fabrication and ethanol sensing characteristics of ZnO nanowire gas sensors, Applied Physics Letters, 84 (2004) 3654-3656.

[20] Z.Y. Fan, D.W. Wang, P.C. Chang, W.Y. Tseng, J.G. Lu, ZnO nanowire field-effect transistor and oxygen sensing property, Applied Physics Letters, 85 (2004) 5923-5925.

[21] Y.W. Heo, D.P. Norton, L.C. Tien, Y. Kwon, B.S. Kang, F. Ren, S.J. Pearton, J.R. LaRoche, ZnO nanowire growth and devices, Materials Science & Engineering R-Reports, 47 (2004) 1-47.

[22] Z.L. Wang, ZnO nanowire and nanobelt platform for nanotechnology, Materials Science & Engineering R-Reports, 64 (2009) 33-71.

[23] X. Wang, J. Zhou, J. Song, J. Liu, N. Xu, Z.L. Wang, Piezoelectric field effect transistor and nanoforce sensor based on a single ZnO nanowire, Nano Letters, 6 (2006) 2768-2772.

[24] F. Patolsky, C.M. Lieber, Nanowire nanosensors, Materials Today, 8 (2005) 20-28.

[25] A.K. Wanekaya, W. Chen, N.V. Myung, A. Mulchandani, Nanowire-based electrochemical biosensors, Electroanalysis, 18 (2006) 533-550.

[26] F. Patolsky, G. Zheng, C.M. Lieber, Nanowire sensors for medicine and the life sciences, Nanomedicine, 1 (2006) 51-65.

[27] J. Zhu, Z. Yu, G.F. Burkhard, C.-M. Hsu, S.T. Connor, Y. Xu, Q. Wang, M. McGehee, S. Fan, Y. Cui, Optical Absorption Enhancement in Amorphous

Silicon Nanowire and Nanocone Arrays, Nano Letters, 9 (2009) 279-282.

[28] C.X. Shan, Z. Liu, S.K. Hark, Photoluminescence polarization in individual CdSe nanowires, Physical Review B, 74 (2006) 153402.

[29] J.F. Wang, M.S. Gudiksen, X.F. Duan, Y. Cui, C.M. Lieber, Highly polarized photoluminescence and photodetection from single indium phosphide nanowires, Science, 293 (2001) 1455-1457.

[30] Z.Y. Fan, P.C. Chang, J.G. Lu, E.C. Walter, R.M. Penner, C.H. Lin, H.P. Lee, Photoluminescence and polarized photodetection of single ZnO nanowires, Applied Physics Letters, 85 (2004) 6128-6130.

[31] J. Goldberger, D.J. Sirbuly, M. Law, P. Yang, ZnO nanowire transistors, Journal of Physical Chemistry B, 109 (2005) 9-14.

[32] Q.H. Li, T. Gao, Y.G. Wang, T.H. Wang, Adsorption and desorption of oxygen probed from ZnO nanowire films by photocurrent measurements, Applied Physics Letters, 86 (2005) 123117.

[33] Q.H. Li, Y.X. Liang, Q. Wan, T.H. Wang, Oxygen sensing characteristics of individual ZnO nanowire transistors, Applied Physics Letters, 85 (2004) 6389-6391.

[34] D.Y. Li, Y.Y. Wu, P. Kim, L. Shi, P.D. Yang, A. Majumdar, Thermal conductivity of individual silicon nanowires, Applied Physics Letters, 83 (2003) 2934-2936.

[35] Y.J. Doh, J.A. van Dam, A.L. Roest, E. Bakkers, L.P. Kouwenhoven, S. De Franceschi, Tunable supercurrent through semiconductor nanowires, Science, 309 (2005) 272-275.

[36] T. Ma, M. Guo, M. Zhang, Y. Zhang, X. Wang, Density-controlled hydrothermal growth of well-aligned ZnO nanorod arrays, Nanotechnology, 18 (2007) 035605.

[37] M. Guo, P. Diao, S.M. Cai, Hydrothermal growth of well-aligned ZnO nanorod arrays: Dependence of morphology and alignment ordering upon preparing conditions, Journal of Solid State Chemistry, 178 (2005) 1864-1873.

[38] Y.Y. Wu, H.Q. Yan, P.D. Yang, Semiconductor nanowire array: Potential substrates for photocatalysis and photovoltaics, Topics in Catalysis, 19 (2002) 197-202.

[39] V. Schmidt, J.V. Wittemann, S. Senz, U. Goesele, Silicon nanowires: A review on aspects of their growth and their electrical properties, Advanced Materials, 21 (2009) 2681-2702.

[40] J.T. Hu, T.W. Odom, C.M. Lieber, Chemistry and physics in one dimension: Synthesis and properties of nanowires and nanotubes, Accounts of Chemical Research, 32 (1999) 435-445.

[41] C. Thelander, P. Agarwal, S. Brongersma, J. Eymery, L.F. Feiner, A. Forchel, M. Scheffler, W. Riess, B.J. Ohlsson, U. Goesele, L. Samuelson, Nanowire-based one-dimensional electronics, Materials Today, 9 (2006) 28-35.

[42] N. Wang, Y. Cai, R.Q. Zhang, Growth of nanowires, Materials Science & Engineering R-Reports, 60 (2008) 1-51.

[43] P.L. Gai, M.A. Harmer, Surface atomic defect structures and growth of gold nanorods, Nano Letters, 2 (2002) 771-774.

[44] L. Liao, Y.-C. Lin, M. Bao, R. Cheng, J. Bai, Y. Liu, Y. Qu, K.L. Wang, Y. Huang, X. Duan, High-speed graphene transistors with a self-aligned nanowire gate, Nature, 467 (2010) 305-308.

[45] K.H. Tam, C.K. Cheung, Y.H. Leung, A.B. Djurisic, C.C. Ling, C.D. Beling, S. Fung, W.M. Kwok, W.K. Chan, D.L. Phillips, L. Ding, W.K. Ge, Defects in ZnO nanorods prepared by a hydrothermal method, Journal of Physical Chemistry B, 110 (2006) 20865-20871.

[46] Y. Cui, Z.H. Zhong, D.L. Wang, W.U. Wang, C.M. Lieber, High performance silicon nanowire field effect transistors, Nano Letters, 3 (2003) 149-152.

[47] R. Konenkamp, R.C. Word, C. Schlegel, Vertical nanowire light-emitting diode, Applied Physics Letters, 85 (2004) 6004-6006.

[48] Y.C. Kong, D.P. Yu, B. Zhang, W. Fang, S.Q. Feng, Ultraviolet-emitting ZnO nanowires synthesized by a physical vapor deposition approach, Applied Physics Letters, 78 (2001) 407-409.

[49] M.W. Ahn, K.S. Park, J.H. Heo, J.G. Park, D.W. Kim, K.J. Choi, J.H. Lee, S.H. Hong, Gas sensing properties of defect-controlled ZnO-nanowire gas sensor, Applied Physics Letters, 93 (2008) 263103.

[50] S. Thiel, G. Hammerl, A. Schmehl, C.W. Schneider, J. Mannhart, Tunable quasi-two-dimensional electron gases in oxide heterostructures, Science, 313 (2006) 1942-1945.

[51] L.-F. Cui, Y. Yang, C.-M. Hsu, Y. Cui, Carbon-silicon core-shell nanowires as high capacity electrode for lithium ion batteries, Nano Letters, 9 (2009) 3370-3374.

[52] C.K. Chan, H. Peng, G. Liu, K. McIlwrath, X.F. Zhang, R.A. Huggins, Y. Cui, High-performance lithium battery anodes using silicon nanowires, Nature Nanotechnology, 3 (2008) 31-35.

[53] M.H. Huang, S. Mao, H. Feick, H.Q. Yan, Y.Y. Wu, H. Kind, E. Weber, R. Russo, P.D. Yang, Room-temperature ultraviolet nanowire nanolasers, Science, 292 (2001) 1897-1899.

[54] X.F. Duan, Y. Huang, R. Agarwal, C.M. Lieber, Single-nanowire electrically driven lasers, Nature, 421 (2003) 241-245.

[55] J.C. Johnson, H.Q. Yan, R.D. Schaller, L.H. Haber, R.J. Saykally, P.D. Yang, Single nanowire lasers, Journal of Physical Chemistry B, 105 (2001) 11387-11390.

[56] J.C. Johnson, H.Q. Yan, P.D. Yang, R.J. Saykally, Optical cavity effects in ZnO nanowire lasers and waveguides, Journal of Physical Chemistry B, 107 (2003) 8816-8828.

[57] J. Bao, M.A. Zimmler, F. Capasso, X. Wang, Z.F. Ren, Broadband ZnO single-nanowire light-emitting diode, Nano Letters, 6 (2006) 1719-1722.

[58] F. Qian, S. Gradecak, Y. Li, C.Y. Wen, C.M. Lieber, Core/multishell nanowire heterostructures as multicolor, high-efficiency light-emitting diodes, Nano Letters, 5 (2005) 2287-2291.

[59] Y. Qin, X. Wang, Z.L. Wang, Microfibre-nanowire hybrid structure for energy scavenging, Nature, 451 (2008) 809-813.

[60] S. Xu, Y. Qin, C. Xu, Y. Wei, R. Yang, Z.L. Wang, Self-powered nanowire devices, Nature Nanotechnology, 5 (2010) 366-373.

[61] H. Kind, H.Q. Yan, B. Messer, M. Law, P.D. Yang, Nanowire ultraviolet photodetectors and optical switches, Advanced Materials, 14 (2002) 158-160.

[62] C. Soci, A. Zhang, B. Xiang, S.A. Dayeh, D.P.R. Aplin, J. Park, X.Y. Bao, Y.H. Lo, D. Wang, ZnO nanowire UV photodetectors with high internal gain, Nano Letters, 7 (2007) 1003-1009.

[63] M.S. Gudiksen, L.J. Lauhon, J. Wang, D.C. Smith, C.M. Lieber, Growth of nanowire superlattice structures for nanoscale photonics and electronics, Nature, 415 (2002) 617-620.

[64] R. Yan, D. Gargas, P. Yang, Nanowire photonics, Nature Photonics, 3 (2009) 569-576.

[65] P.J. Pauzauskie, P. Yang, Nanowire photonics, Materials Today, 9 (2006) 36-45.

[66] Z.L. Wang, J.H. Song, Piezoelectric nanogenerators based on zinc oxide nanowire arrays, Science, 312 (2006) 242-246.

[67] L. Dong, S. Niu, C. Pan, R. Yu, Y. Zhang, Z.L. Wang, Piezo-phototronic effect of CdSe nanowires, Advanced Materials, 24 (2012) 5470-5475.

[68] Y.S. Zhou, K. Wang, W. Han, S.C. Rai, Y. Zhang, Y. Ding, C. Pan, F. Zhang, W. Zhou, Z.L. Wang, Vertically aligned CdSe nanowire arrays for energy harvesting and piezotronic devices, ACS Nano, 6 (2012) 6478-6482.

[69] M.D. Kelzenberg, D.B. Turner-Evans, B.M. Kayes, M.A. Filler, M.C. Putnam, N.S. Lewis, H.A. Atwater, Photovoltaic measurements in single-nanowire silicon solar cells, Nano Letters, 8 (2008) 710-714.

[70] B. Tian, X. Zheng, T.J. Kempa, Y. Fang, N. Yu, G. Yu, J. Huang, C.M. Lieber, Coaxial silicon nanowires as solar cells and nanoelectronic power sources, Nature, 449 (2007) 885-889.

[71] E. Garnett, P. Yang, Light trapping in silicon nanowire solar cells, Nano Letters, 10 (2010) 1082-1087.

[72] E.C. Garnett, P. Yang, Silicon nanowire radial p-n junction solar cells, Journal of the American Chemical Society, 130 (2008) 9224-9225.

[73] K.Q. Peng, Y. Xu, Y. Wu, Y.J. Yan, S.T. Lee, J. Zhu, Aligned single-crystalline Si nanowire arrays for photovoltaic applications, Small, 1 (2005) 1062-1067.

[74] B. Tian, T.J. Kempa, C.M. Lieber, Single nanowire photovoltaics, Chemical Society Reviews, 38 (2009) 16-24.

[75] Physics of nanostructured solar cells, Nova Science Publishers, Inc., New York, 2010.

[76] A.I. Hochbaum, R. Chen, R.D. Delgado, W. Liang, E.C. Garnett, M. Najarian, A. Majumdar, P. Yang, Enhanced thermoelectric performance of rough silicon nanowires, Nature, 451 (2008) 163-167.

[77] A.I. Boukai, Y. Bunimovich, J. Tahir-Kheli, J.-K. Yu, W.A. Goddard, III, J.R. Heath, Silicon nanowires as efficient thermoelectric materials, Nature, 451 (2008) 168-171.

[78] Y. Li, F. Qian, J. Xiang, C.M. Lieber, Nanowire electronic and optoelectronic devices, Materials Today, 9 (2006) 18-27.

[79] J. Goldberger, A.I. Hochbaum, R. Fan, P. Yang, Silicon vertically integrated nanowire field effect transistors, Nano Letters, 6 (2006) 973-977.

[80] J.F. Wager, Transparent electronics, Science, 300 (2003) 1245-1246.

[81] Y. Cui, C.M. Lieber, Functional nanoscale electronic devices assembled using silicon nanowire building blocks, Science, 291 (2001) 851-853.

[82] Y. Huang, X.F. Duan, Y. Cui, L.J. Lauhon, K.H. Kim, C.M. Lieber, Logic gates and computation from assembled nanowire building blocks, Science, 294 (2001) 1313-1317.

[83] Y. Huang, X.F. Duan, Q.Q. Wei, C.M. Lieber, Directed assembly of one-dimensional nanostructures into functional networks, Science, 291 (2001) 630-633.

[84] D. Whang, S. Jin, Y. Wu, C.M. Lieber, Large-scale hierarchical organization of nanowire arrays for integrated nanosystems, Nano Letters, 3 (2003) 1255-1259.

[85] N.A. Melosh, A. Boukai, F. Diana, B. Gerardot, A. Badolato, P.M. Petroff, J.R. Heath, Ultrahigh-density nanowire lattices and circuits, Science, 300 (2003) 112-115.

[86] J. Zhang, D. Li, R. Chen, Q. Xiong, Laser cooling of a semiconductor by 40 kelvin, Nature, 493 (2013) 504-508.

APPENDIX II: CHARACTERIZATION TECHNIQUES AND EXPERIMENTAL DETAILS

"To acquire knowledge, one must study; but to acquire wisdom, one must observe."
Marilyn vos Savant, *2001 In Courage: The Heart and Spirit of Every Woman: Reclaiming the Forgotten Virtue*

AII.1 Appendix Information Summary

Table AII.1 highlights the advantages and disadvantages of techniques used in this dissertation. In general, laser spot sizes are the limiting factor for optically characterizing *single* nanoparticles. Submicron laser spot sizes are generally found in Raman spectroscopy, which can characterize small diameter (e.g., ~30 nm) nanoparticle diameters with some difficulty. There are currently no ideal optical techniques for very small nanoparticles. In theory, large spot sizes could be used, but small nanoparticles are more prone to laser heating due to their lower thermal conductivities. Lowering the laser power reduces signal intensity and may require greatly increased collection parameters (which requires additional collection time per spectrum). And a large spot size increases the amount of non–sample being measured, e.g., substrate, which may obscure weak Raman peaks. Small laser spot sizes would be ideal but are governed by the optical diffraction limit, $d = \lambda/(2\ N.A.)$. Here, d is the diffraction–limited laser spot size or lateral resolution, λ is the laser's wavelength, $N.A.$ is the numerical aperture and is equivalent to $n \sin(\varphi)$, where n is the refractive index and φ is angle needed to focus the laser spot. For example, if $N.A.$ = 0.9 (100x objective lens) for λ = 180 nm, then the diffraction–limited spatial resolution is ~200. nm. The current smallest commercial wavelength is 193 nm (ArF), although development of photolithography using 13.5 nm is underway. Even if laser technology was improved to 5 nm (extremely unlikely), optical microscopes would still have relatively poor resolution, which makes it difficult to focus on nanoparticles with diameters of only a few nanometers. However,

other methods are being employed to develop microscopes that could potentially offer atomic spatial resolutions [87]. In research, instrument limitations are expanded when a need arises. Very small nanowires require excellent stabilization of the optical table and mechanical stability (e.g., of the stage and related gears). Lasers may be positioned over very small nanoparticles by observing laser scattering in order to counter poor optical resolution and a large laser spot size.

Electrical and some structural techniques are capable of single nanoparticle measurements. The problem with electrical measurements is the enormous time investment to create electrical contacts, say, for a single nanowire. It could take a week to create one chip with several devices, and after removing the mask required for electrode deposition, the nanowires could be accidently removed during the lift–off process. Electrical measurements in standard setups, where electrodes are placed at each end of a nanowire, are averaged values that depend on numerous factors including defect configuration and density, structural homogeneity (e.g., inclusions vs. occlusion), and passivation. And some electrical methods combine problems with optical characterization. Photocurrent, for example, requires optical stimulation of the nanoparticle to measure the current output.

Structural characterization has its own issues. X–ray diffraction (XRD) measures large sample areas, whereas, high–resolution tunneling electron microscopy (HRTEM) has sub-atomic resolution and a much, much smaller sample chamber. XRD allows determination of grain size via Scherrer's formula, and crystallographic determination, while the latter's sub–atomic resolution and diffraction pattern capability collect the same information in addition to identifying structural faults. TEM's and scanning electron microscopy's (SEM's) electron–dispersive spectroscopy (EDS) allows

quantitative determination of atomic percentages of each element in the electron beam's interaction volume with the sample. Although the SEM's maximum resolution is only on the order of tens of nanometers, it lacks the ability to collect crystallographic information.

Table AII.1 Comparison of advantages and limitations of characterization techniques.

Category	Technique	Advantages	Disadvantages	Refs.
Optical	Optical Microscopy *(OM)*	• inexpensive and quick • can detect micro–defects • "vision–based" surface roughness with appropriate instrumental additions (cameras, etc.) • includes bright and dark field[1] techniques and retro–reflection photoluminescence emission wavelength • great sensitivity for intensity and linewidth[2] operates under ambient conditions	• poor topological resolution • low resolution, e.g., sub–micron to nm (diffraction limited)	[1-4]
	Photoluminescence *(PL)* PL (*cont.*)	• low cost, except for low–temperature equipment, and can operate over a large range of temperatures and under different environments, e.g., inert gas • ability to measure single nanoparticles • temperature–dependent measurements • potentially non-destructive – depends upon laser power • measure absolute quantum yield • create 2D maps of nanostructures and collect time-resolved data	• Fourier transform has limitations such as weak signal loss, and spectral extension to NIR and MIR reduces multiplexing advantages • requires careful alignment of optics	[5-7]

[1] With dark field microscopy, the observed color is equivalent to the particle's emitted photoluminescence wavelength.
[2] The scattered intensity is proportional to the volume squared. Linewidth is sensitive to both electron–surface scattering and radiation damping.

Table AII.1 Continued.

Optical	Raman Spectroscopy	• potentially non–destructive – depends upon laser power • optical and structural information (exciton–phonon coupling, defects, polytype, etc.) • spectrally narrow features • operates under ambient conditions • quick measurements (for materials with reasonably strong Raman cross–sections) • small sample volumes (laser spot size) • identifies phonon modes typically at Γ point • temperature–dependent measurements • use baseline fitting for quantitative measurements (remove scattering differences) • no or little sample preparation • state does not matter (solid, liquid)	• requires careful alignment of optics • fluorescence can convolute weaker Raman signals • not useful for metals (by themselves) • excitation wavelength limited by commercial availability and size • multiple lasers, filters, etc. can become prohibitively expensive • relatively insensitive technique (parts per thousand) • requires excitation source and standard calibration • seemingly simple spectra requires technical knowledge to extract complex information	[8-13]
Electrical	Current–Voltage *(IV)*	• inexpensive • operates under ambient conditions; temperature–dependence is optional	• sample preparation and device construction • two–point vs. four–point probe usage and parameter extraction	[14-16]

Table AII.1 Continued.

Electrical	Photocurrent	• operates under ambient conditions; temperature–dependence is optional • defect mapping, e.g., LBIC, PL maps • use of local electric field enhancements to enhance sensitivity	• sample preparation and device construction	[17-19]
Structural	Scanning Electron Microscopy *(SEM)*	• excellent image resolution • couples with other techniques, e.g. EDS, EELS, detectors, and configurations, e.g. HAADF • resolves topology • backscattered electrons for analytical purposes, e.g. EDS of interaction volume • 3D stage rotation (x,y,z), and limited tilt (for up to 8 in. wafers and limited movement for 8–12 in. wafers) • 3D visualization (surface height visible but not accurately measurable)	• spatial resolution ~10s of nm • in moderate vacuum • samples must be conductive • grey scale images • EDS is not well suited for trace analysis; quantitative only for interaction volume • sample preparation • image resolution depends upon probe size, with a very small probe needed for high resolution • conductive/semiconducting samples or metallic coating/metallic tape for insulating samples • possible radiation damage, esp. from small probe diameters (higher resolution)	[20-23]

Table AII.1 Continued.

Structural	Tunneling Electron Microscopy/ High-resolution TEM *(TEM/HRTEM)*	• sub–atomic spatial and image resolution • allows indexing of growth direction(s) • couples with other techniques, e.g. EDS, EELS, and detectors • multiple modes, e.g. bright and dark field, phase contrast • 2D stage rotation (x,y), and limited tilt • information from backscattered, emitted, and secondary electrons	• sample thickness < ~100 nm • sample preparation (typically more involved than for SEM) • in high vacuum • expensive • requires special maintenance • grey scale images • EDS is not well suited for trace analysis; quantitative only for interaction volume • conductive/semiconducting samples or metallic coating/metallic tape for insulating samples • image resolution depends upon probe size, with a very small probe needed for high resolution • possible radiation damage to organic and inorganic materials, esp. for small probe diameters (higher resolution)	[24]

Table AII.2 Comparison of crystal structure properties for wurtzite (W) CdSe and zinc blende (ZB) ZnTe.

Space Group (Point Group)	**Crystal Structure**	**Semi-conductor**	**a (Å)**	**c (Å)**	**Site Symmetries**[3]	**Number of Vibrations**[c]	**Polarization Tensor**
$P6_3mc(C_{6v}^4)$[a]	W	CdSe	4.1367	6.7161	$C_1(12)$	$6m + 3m_v + m_0$	
$F\bar{4}3_m(T_d^2)$	ZB	ZnTe	6.009		$2C_{2v}(6)$	$6m + 3m_d + m_2 + m_3$	$(\alpha_{xx} + \alpha_{yy} - 2\alpha_{zz})$

[3] For example, a C_4^1 point group with site symmetries of $2C_4$, $C_2(2)$ signifies that this point group has two (2) distinct sites with C_4 symmetry, where C_n comes from $\frac{360^o}{n}$, with one (1) site per set, and two (2) equivalent sites per set with C_2 symmetry. If a symbol is absent, then it indicates a lack of symmetry.

AII.2 Nanowire Growth, Device Fabrication, and Characterization Information

AII.2.1 Making Nanowire Synthesis and Device Fabrication

All samples investigated in this dissertation were obtained from other sources. Bulk ZnTe samples were purchased from commercial vendors, while thin film and wires were provided through respective collaborations with the Army Research Laboratory (ARL) and the Haitao Zhang group in the Department of Mechanical Engineering and Engineering Sciences at UNC–Charlotte. CdSe nanowires and related devices were provided by the Weilie Zhou group in the Advanced Materials Research Institute at the University of New Orleans. CdSe nanowire growth and related device fabrication are briefly outlined below.

CdSe nanowires were grown in a vertical array through gold–catalyzed chemical vapor deposition, as described elsewhere [109], and were then dispersed in alcohol and drop cast onto a Si/SiO_2 chip, which consists of Si substrate coated with a 300–nm thick SiO_2 layer. After dispersal onto a chip, a thin poly–methyl methacrylate (PMMA) layer was spin coated onto the chip, followed by electron–beam lithography to open channels at a nanowire's ends. Exposed PMMA was removed by developing the chip. Afterwards, the chip was transferred to a thermal evaporator (Cressington–308R) for indium metallization (30 nm), followed by lift–off in acetone to obtain a finished device. The other end of the indium wire end was bonded to a large gold pad used for placement of a gold–coated electrical probe. The samples were air stabilized for at least a week prior to testing.

AII.2.2 Light–effect transistor (LET) Characterization

Optical gating through $P_g(\lambda_g)$ has two basic control parameters: wavelength, λ_g, and power level, P_g, under one–beam CW operation, but it can be readily extended to

other operation modes. For instance, multiple independent beams and pulsed illumination may be represented as $P_g(\lambda_{g1}, \lambda_{g2},\ldots,\lambda_{gN})$ and $P_g(t,\lambda_{g1}, \lambda_{g2},\ldots,\lambda_{gN})$ respectively. We fully characterize LET output and transfer characteristics under one-beam CW operation with two illumination conditions: (1) illuminating the center of the SNW with a focused CW laser ("focused illumination") with an optical diffraction-limited spot size at wavelengths of 633, 532, 442, or 325 nm; and (2) illuminating the LET uniformly with "white light" from a halogen lamp ("uniform illumination").

The novel LET concept requires performance metrics for evaluation and comparison against FETs; thus, FET figures of merit are adapted, such as the two important input–output relationships: (1) "*output characteristics*" or I_{ds} *vs.* V_{ds} under a constant illumination condition $P_g(\lambda_g)$, which is equivalent to the FET's output characteristic under a constant gate voltage V_g; and (2) "*transfer characteristics*" or I_{ds} *vs.* $P_g(\lambda_g)$ under a constant V_{ds}, which is equivalent to a FET's I_{ds} *vs.* V_g under a constant V_{ds}. A FET's gate voltage, V_g, is replaced by a LET's gate power $P_g(\lambda_g)$, which not only serves the same function of modulating *S–D* conductivity but it also offers an avenue to achieve novel functions beyond those in a FET. Characteristic (i) is shared by both LET and photo–detection applications, while characteristic (ii) is required for LETs and FETs as a measure of turn–on energy, and in particular, for LETs to realize novel functions.

AII.2.3 Optical and Electrical Measurements

Figure AII.1 displays an instrument schematic that illustrates the ability to collect optical and electrical measurements. CW lasers consisted of 532, 441.6, and 325 nm ported through a Horiba LabRAM HR800 confocal Raman system with an internal 632.8 nm laser (that traversed the same beam path shown in Figure AII.1), while

halogen light was introduced through the microscope's white–light illumination port. Characterization of ZnTe systems and single CdSe nanowires used a 100x objective lens with a numerical aperture (*N.A.*) of 0.9, which yielded a laser spot size is ~0.72 μm, and a spatial resolution equivalent to about half the spot size. Due to limited probe spacing for electrical measurements on CdSe–based devices, all illumination sources were focused through a 50x long working distance (LWD) objective lens (*N.A.* = 0.50), except 325 nm, which went through a 10x MPLAN objective lens (*N.A.* = 0.25). Laser powers in Chapter 4 (e.g., the LET) were limited to absolute powers of ~3 μW, as measured on the sample side of the microscope lens, to avoid potential laser–induced material modifications, while Chapters 5 and 6 indicate the optical powers used. The total power of the halogen light was estimated to be 69.1 μW. The optical powers were measured with a Thor Labs PM100D power meter, and six and ten averaged measurements were used for D1 and D2, respectively, to calculate average powers. Laser powers were altered through a combination of a standard, neutral–density filters in the Raman system and an adjustable, neutral–density filter in the laser path.

The optical beams are in backscatter configuration, relative to the sample surface (Figure AII.1; see Section 2.6 for Raman selection rules). A notch filter removes laser contributions before the PL and Raman signals are focused to the confocal aperture, dispersed by a spectrometer, and detected by a charge–coupled detector (CCD) array. Micro–PL (μ–PL) and μ–Raman, where μ typically represents the near diffraction–limited, laser spot, are fundamentally different but complementary optical techniques affected by material conditions (e.g., impurities and defects), wavelength-dependent light-matter interactions (e.g., absorption and carrier dynamics), and illumination conditions (e.g., power density and beam size). The primary role of Raman

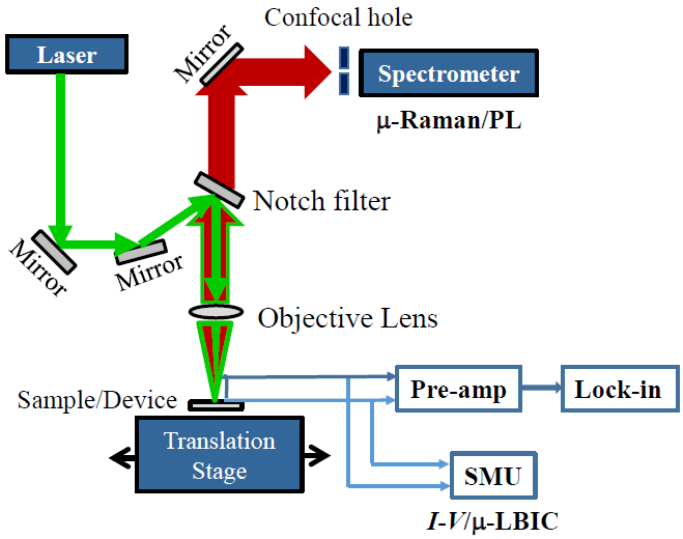

Figure AII.1 Schematic of instrument with ability to collect optical and electrical measurements. See this section for additional details.

spectroscopy, as discussed in Section 2.5, is to probe the perturbation to electronic susceptibility through changes in atomic polarization, while PL is directly impacted by free carrier recombination and diffusion [19, 183].

Two gold plated probes, which were used to conduct current from the device, enabled measurement of the photo–current or the laser–beam induced current (LBIC). (Electrical) I_{ds} vs. V_{ds} measurements were collected with a Keithley© 2401 low voltage sourcemeter® that was remotely operated with LabTracer v2.9 software via a GPIB connection. For currents below ~1 nA, a Stanford Research System SR570 current pre-amplifier was used in conjunction with the Keithley©. For sine wave modulation, e.g., Figure 4.5H, the laser was modulated with a mechanical chopper, and the photo–current was measured by an SR830 lock–in amplifier with a SR570 low noise current pre–amplifier.

AII.2.4 Estimation of Actual Power Absorbed

The laser spot size is estimated by the optical diffraction limit formula $1.22\lambda/N.A.$, where *N.A.* is the numerical aperture of the microscope lens. The fraction of the laser

power actually absorbed is estimated by taking the ratio of the nanowire diameter to the laser spot size. The estimated ratios for the 632.8, 532, 441.6, and 325 nm lasers are 5.18, 6.16, 7.43, and 10.1% for a nanowire with an 80 nm diameter (device D1). For halogen illumination, the fraction of actual absorbed light is estimated using the ratio of the nanowire's cross section to the total illumination area. For the 50x LWD (10x MPLAN) objective lens, the illumination area is ~279 (~1450) μm^2. The ratio for the 80 nm wide/10 μm long nanowire (D1) is ~3.2 10^{-6}, and the power estimation for light actually absorbed is ~0.22 μW (which is comparable to that for the focused laser beam). All the illumination powers mentioned in this dissertation were "applied powers," unless an actually absorbed power was explicitly stated.

REFERENCES

[1] E. M. Slayter and H. S. Slayter, *Light and microscopy*. Cambridge: Cambridge University Press, 1992.

[2] A. Lewis, M. Isaacson, A. Harootunian, and A. Muray, Development of a 500 A spatial resolution light microscope .1. Light is efficiently transmitted through lambda/16 diameter aperatures, Ultramicroscopy, 13 (1984), 227-231.

[3] D. B. Murphy, *Fundamentals of light microscopy and electronic imaging*. United States of America: Wiley-Liss, Inc., 2001.

[4] K. O. Greulich and G. Weber, The light microscope on its way from an analtyical to a preparative tool, Journal of Microscopy-Oxford, 167 (1992), 127-151.

[5] S. A. Empedocles, R. Neuhauser, K. Shimizu, and M. G. Bawendi, Photoluminescence from single semiconductor nanostructures, Advanced Materials, 11 (1999), 1243-1256.

[6] J. N. Demas and G. A. Crosby, Measurement of photoluminescence quantum yields - Review, Journal of Physical Chemistry, 75 (1971), 991-1024.

[7] T. H. Gfroerer, Photoluminescence in Analysis of Surfaces and Interfaces, Encyclopedia of Analytical Chemistry, (2006), 1-23.

[8] K. Kneipp, H. Kneipp, I. Itzkan, R. R. Dasari, and M. S. Feld, Ultrasensitive chemical analysis by Raman spectroscopy, Chemical Reviews, 99 (1999), pp. 2957-2975.

[9] A. C. Ferrari, Raman spectroscopy of graphene and graphite: Disorder, electron-phonon coupling, doping and nonadiabatic effects, Solid State Communications, 143 (2007), 47-57.

[10] R. Petry, M. Schmitt, and J. Popp, Raman Spectroscopy - A prospective tool in the life sciences, ChemPhysChem, 4 (2003), 14-30.

[11] A. C. Ferrari and D. M. Basko, Raman spectroscopy as a versatile tool for studying the properties of graphene, Nature Nanotechnology, 8 (2013), 235-246.

[12] E. B. Hanlon, R. Manoharan, T. W. Koo, K. E. Shafer, J. T. Motz, M. Fitzmaurice, et al., Prospects for in vivo Raman spectroscopy, Physics in Medicine and Biology, 45 (2000), R1-R59.

[13] G. Gouadec and P. Colomban, Raman Spectroscopy of nanomaterials: How spectra relate to disorder, particle size and mechanical properties, Progress in Crystal Growth and Characterization of Materials, 53 (2007), 1-56.

[14] S. K. Cheung and N. W. Cheung, Extraction of Schottky diode parameters from forward current-voltage characteristics, Applied Physics Letters, 49 (1986), 85-87.

[15] S. Hasegawa and F. Grey, Electronic transport at semiconductor surfaces - from point-contact transistor to micro-four-point probes, Surface Science, 500 (2002), 84-104.

[16] S. Hasegawa, I. Shiraki, T. Tanikawa, C. L. Petersen, T. M. Hansen, P. Boggild, et al., Direct measurement of surface-state conductance by microscopic four-point probe method, Journal of Physics-Condensed Matter, 14 (2002), 8379-8392.

[17] W. Qiu and W. Hu, Laser beam induced current microscopy and photocurrent mapping for junction characterization of infrared photodetectors, Science China-Physics Mechanics & Astronomy, 58 (2015), 1-13.

[18] Q. Chen, and Y. Zhang, Correlating multiple spatially-resolved techniques (LBIC/Raman/PL/Reflectance/SEM/AFM) in the study of microscopic inhomogeneity of thin-film solar cells: $Cu_2ZnSnSe_4$ as an example, in: 2014 IEEE 40th Photovoltaic Specialist Conference (PVSC) (2014), 3338-3340.

[19] F. Chen, Y. Zhang, T. H. Gfroerer, A. N. Finger, and M. W. Wanlass, Spatial resolution versus data acquisition efficiency in mapping an inhomogeneous system with species diffusion, Scientific Reports, 5 (2015), 10542.

[20] H. Seiler, Secondary-electron emission in the scanning electron microscope, Journal of Applied Physics, 54 (1983), R1-R18.

[21] M. T. Postek, Critical issues in scanning electron microscope metrology, Journal of Research of the National Institute of Standards and Technology, 99 (1994), 641-671.

[22] M. Varela, A. R. Lupini, K. van Benthem, A. Y. Borisevich, M. F. Chisholm, N. Shibata, E. Abe, and S.J. Pennycook, Materials characterization in the aberration-corrected scanning transmission electron microscope, Annual Review of Materials Research, 35 (2005), 539-569.

[23] D. R. Clarke, Image contrast in scanning electron microscope - Review, Journal of Materials Science, 5 (1970), 689-671.

[24] D. B. Williams and C. B. Carter, Transmission electron microscopy: A textbook for materials science. New York, NY: Plenum Press, 2009.

APPENDIX III: SUPPORTING INFORMATION FOR THE LIGHT–EFFECT TRANSISTOR

"Every great advance in science has issued from a new audacity of imagination."
John Dewey, 1929 The Quest for Certainty

AIII.1 Appendix Information Summary

Section AIII.2 contains universal *NOR* and *NAND* logic circuits constructed using two LETs and their respective truth tables. Section AIII.3 provides LET transfer characteristics with two beam illumination using 532 nm and halogen illumination. Figure AIII.3A contains the individual data points used to create the contour plot in Figure 4.5C, while Figure AIII.3B clearly demonstrates the extrapolation of the super–linear, linear, and saturated regimes from single to two beam illumination. Section AIII.4 illustrates the non–linear, dual–beam LET transfer characteristics with 633 nm and halogen illumination. Single beam illumination with 633 nm demonstrated non–linear behavior, which was also present under two beam illumination with halogen light. Section AIII.5 presents the proposed truth tables and symbols for three–terminal, *AND–AND* and *AND–OR* logic gates obtained using a single LET device. The three inputs are V_{ds} and two light beams. Proposed symbols are also suggested and their origins are described. Section AIII.6 provides parameters and assumptions used to estimate the (total) switch energies in Chapter 4. Finally, Section AIII.7 plots LET (D2) output and transfer characteristics in both current and gain (or quantum efficiency).

AIII.2 Proposed NOR and NAND Gate Construction and Truth Tables

NOR and *NAND* logic gates are universal, which means that they can be used to construct most other logic circuits. Because a LET behaves similarly to an n–MOSFET, similar *NOR* and *NAND* logic circuits and truth tables may be constructed as illustrated in Figure AIII.1. Logic inversion is possible given the high resistivity of an

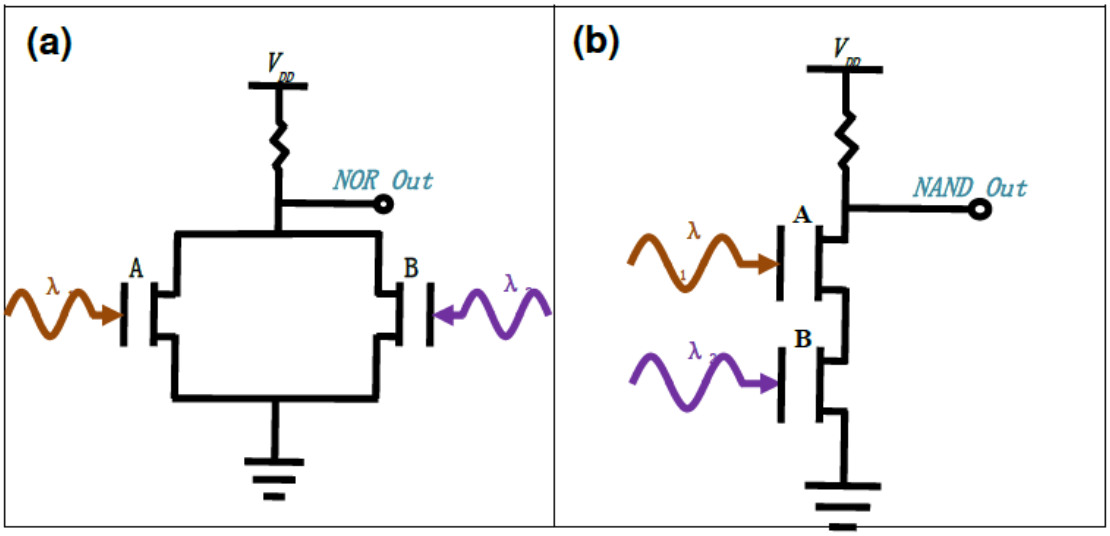

(c)

λ_1	λ_2	A NOR B
0	0	**1**
0	1	**0**
1	0	**0**
1	1	**0**

(d)

λ_1	λ_2	A NAND B
0	0	**1**
0	1	**1**
1	0	**1**
1	1	**0**

Figure AIII.1 Diagrams for **(a)** *NOR* and **(b)** *NAND* logic gates constructed with two LETs. Their respective truth tables are provided in **(c)** and **(d)** respectively, where off ("0") and on ("1") states are measured at the output port.

unilluminated LET (off state). In this case, the drive voltage, V_{DD}, goes directly to the output port. For the parallel LET devices in the *NOR* logic gate, Figure AIII.1A, illumination of either or both LET device(s), labelled as A and B, allows current to travel to ground, and yields an off state ("0") at the output port. An on state ("1") is only possible when both LET devices are off or unilluminated. A *NAND* logic circuit, on the other hand, contains two LET devices in series. Illumination of either LET device is insufficient for current to travel to ground, which results in an on state at the output port. Illuminating both devices, however, produces an off state at the output port. Truth tables for both of these gates are given in Figure AIII.1C and Figure AIII.1D respectively.

AIII.3 LET Transfer Characteristics with 532 nm and Halogen Illumination

LET transfer characteristics under two–beam (532 nm and halogen) illumination. Individual data points used to create the contour plot in Fig. 4.5C are plotted in Figure AIII.2A, while Figure AIII.2B provides additional data that clearly show extrapolation of the three operating regimes observed for single beam illumination to dual–beam conditions. The data in Figure AIII.2A consists of only three (four) measurements under combinations of 532 nm (halogen) illumination; this data was chosen for Figure 4.5 due to their high *R* values. Finally, halogen illumination produced greater current modulation than through laser power alone and is a direct result of the optical powers explored.

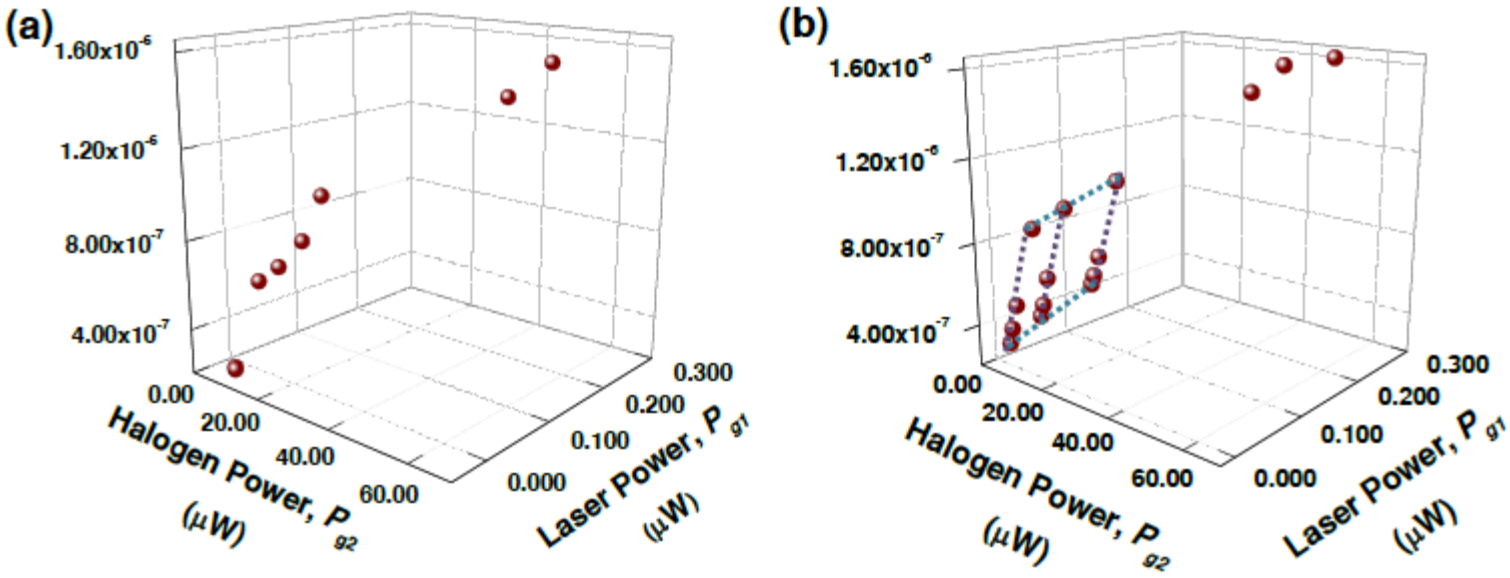

Figure AIII.2 Dual gate LET transfer characteristics for P_{g1}*(532 nm)* and P_{g2}*(halogen)* at V_{ds} = 4.98 V. The vertical axis is I_{ds}, and the horizontal axes are P_{g1}*(532 nm)* and P_{g2}*(halogen)* respectively. A 3D plot of **(a)** the original I_{ds} vs. (P_{g1},P_{g2}) used to generate R in Fig. 4.5C's contour plot, and **(b)** additional I_{ds} vs. (P_{g1},P_{g2}) data clearly demonstrating super–linear, linear, and saturated regimes. **(b)** Two–beam equivalent to the three operating regimes for single beam illumination shown in Figure 4.4. The dotted lines guide the eye in (b): The yellow line represents super–linear operation where P_{g2} (halogen) is varied with fixed P_{g1} (532 nm), while the light blue line illustrates linear operation where P_{g1} is altered under constant P_{g2}. The higher (P_{g1},P_{g2}) points, e.g. P_{g2} > 0.2 μW, are in the saturation regime.

AIII.4 Non-linear Dual Beam LET Transfer Characteristics with 633 nm and Halogen Illumination

Contour plot for dual–beam LET (D2) illumination demonstrating non-linear behavior using 633 nm and halogen beams. *R* is defined in Section 4.3. The non–linear behavior produced by 633 nm illumination allows for additional, interesting functionality beyond that offered by shorter wavelengths, e.g., 532 nm. Instead of switching between different laser powers, one only needs to modulate V_{ds}. For example, modulating V_{ds} at a constant power of 1.06 μW allows dynamic switching between all three regimes or functionalities. This, in principle, simplifies the operational principle.

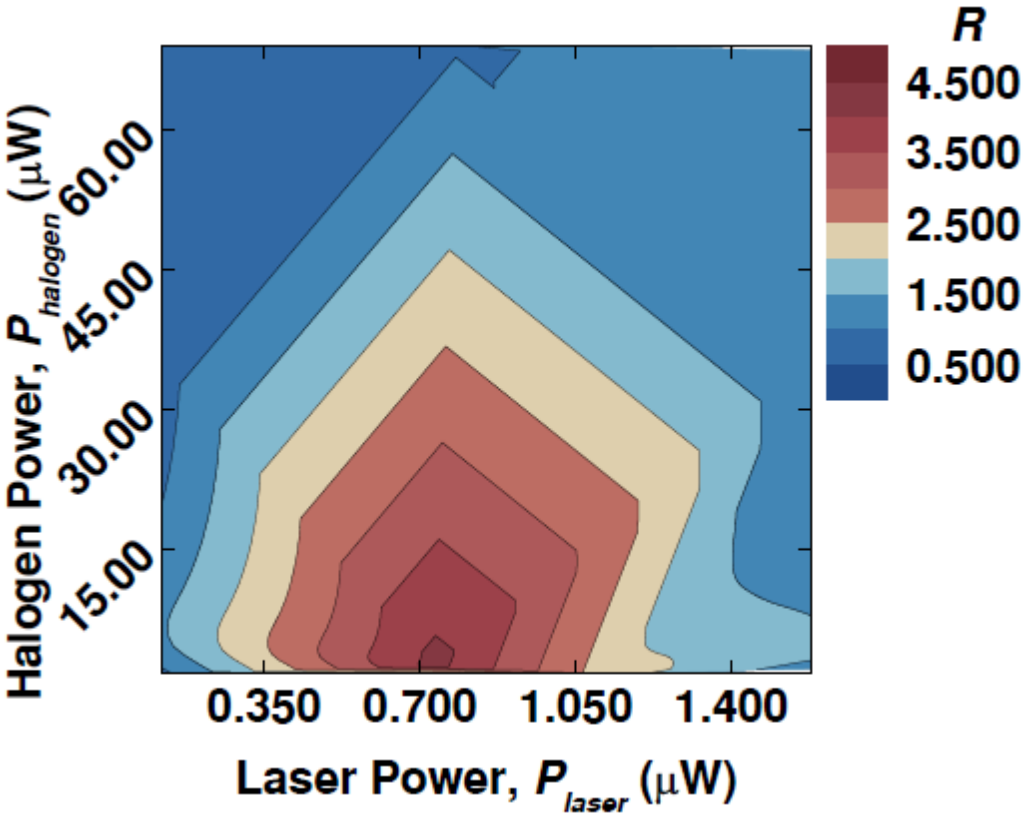

Figure AIII.3 Dual–gate LET transfer characteristics, represented as a contour plot, for P_{g1}*(633 nm)* and P_{g2}*(halogen)* at V_{ds} = 4.98 V. Two beam conditions produced non–monotonical behavior for both D1 (Figure 4.3A), and for D2 (this figure's data with P_{g2}*(halogen)* = 0).

AIII.5 Proposed Truth Tables and Symbols for AND-AND and AND-OR Logic Gates

Truth tables are in Figures AIII.4A–B and their proposed symbols are in Figures AIII.4C–D for hybrid electrical–optical devices employing three–input, *AND* and *AND–OR* logic gates (see Section 4.2). Changing between two logic functions simply requires altering both optical gate powers from the super–linear region to the saturation region, which was demonstrated in Figure 4.5A.

(a)

V_{SD}	$\lambda_{532\ nm}$	$\lambda_{halogen}$	*AxBxC*
0	0	0	**0**
0	0	1	**0**
0	1	0	**0**
0	1	1	**0**
1	0	0	**0**
1	0	1	**0**
1	1	0	**0**
1	1	1	**1**

(b)

V_{SD}	$\lambda_{532\ nm}$	$\lambda_{halogen}$	*Ax(B+C)*
0	0	0	**0**
0	0	1	**0**
0	1	0	**0**
0	1	1	**0**
1	0	0	**0**
1	0	1	**1**
1	1	0	**1**
1	1	1	**1**

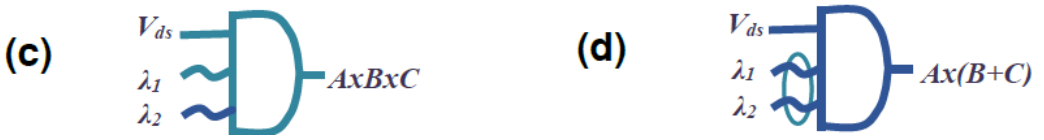

Figure AIII.4 Truth tables **(a)** and **(b)** and their proposed symbols **(c–d)** for hybrid electrical–optical, three–input logic gates *AxBxC* (*AND*) and *Ax(B+C)* (*AND–OR*), respectively, which are achieved using three inputs consisting of $A = V_{ds}$, $B = P_{g1}$ (beam 1), and $C = P_{g2}$ (beam 2). Straight lines represent electrical inputs or outputs, curved lines for optical inputs, and *OR* inputs are grouped.

AIII.6 (Total) Switch Energy Estimates

Section 4.6 provided switch energy estimates for photo–detectors (with M–S–M architecture), FETs, and LETs. Typically, only the switch energy is reported for FETs, where the values in Chapter 4 were obtained from Ref. [1]. Given the addition of an optical gate, terminology was altered to optical and electrical switch energies and their sum or total. The total switch energy provides a proper number for comparing these different devices. Experiments, however, often measure the power, such as the optical

or electrical power, where the latter is obtained by multiplying the I_{ds} and V_{ds}. Power is converted to time with *Energy* = *Power* x *time*, where *time* represents the average carrier lifetime.

Photo–detectors posses large dark currents typically on the order of 100 nA. As a result, large, often non–monotonical increases in optical power are required to increase the collected current by an order of magnitude (or decade of change). Ref. [2] provides representative results for an n–type, GaAs:Fe photo–detector with M–S–M architecture. The interdigitated finger electrodes possess identical finger widths and spacings of 3 μm. The optical power required to produced one, two, three, and four decades of change in the collected current, relative to the dark current, were 1.8 μW, 22 μW, 222 μW, and 2 mW respectively [2]. Assumming a typical carrier lifetime of 20 ps at room temperature, the corresponding optical switch energies are 0.04, 0.44, 4.44, and 40. fJ/switch (where femto = 10^{-15}). Due to this variability, an average value of 0.5 mW/decade (2 mW/4 decade) was assumed in the estimate reported in Chapter 4, and yields an average optical switch energy of 10. fJ/switch. The electrical switch energy was estimated next. The beginning of the current plateau occurred at V_{ds} = 3 V and was multiplied by the current (I_{ds} = 10^{-3} A) to derive a value of 60. fJ/switch. The total switch energy is 70. fJ/switch. Obviously, typical photo–detectors are not ideal transistors, which highlights the significant electrical advances offered by a LET.

LET values were obtained from the champion device (D2) in Chapter 4 (or Ref. [3]), where P_g = 0.11 μW at V_{ds} = 1.43 V produced $I_{ds} \approx$ 0.35 μA. Most semiconductors possess a typical carrier lifetime of 100 ps at room temperature, and was assumed here. Furthermore, a LET only absorbs about 6.16% of the “applied power.” This value stems from taking the ratio of nanowire diameter to laser spot size (see Section AII.2.4 in

Appendix III). The optical and electrical switch energies are 0.011 and 0.050 fJ/switch respectively, which yields a total switch energy of 0.061 fJ/switch. Finally, a LET's potential may be estimated using quantum conductance, G, which limits 1–D (electronic) ballistic transport (at the quantum scale) [4]. $G = nG_0$, where n are integers. The quantum impedance, Z_0, or AC resistance is $1/G_0$ or the inverse conductance, and yields Z_0 = 12.9 kΩ. Assuming I_{ds} = 1 μA, then $V_{ds} = Z_0$ x I_{ds} yields a minimum V_{ds} of 13 mV. The required optical gate power, or on–state consumption energy, is $P = V_{ds}$ x I_{ds} = 13 nW per LET device. Both the optical and electrical switch energies are 0.0013 fJ/switch, which yields a total switch energy of 0.0026 fJ/switch or 2.6 aJ/switch (atto = 10^{-18}).

AIII.7 Output and Transfer Characteristics Plotted in Current and Gain

LET (D2) output and transfer characteristics plotted with both current and gain (or quantum efficiency) appears in Figure AIII.5. There is no reason to suspect that the gain is limited to 1,000 in this unoptimized device (D2).

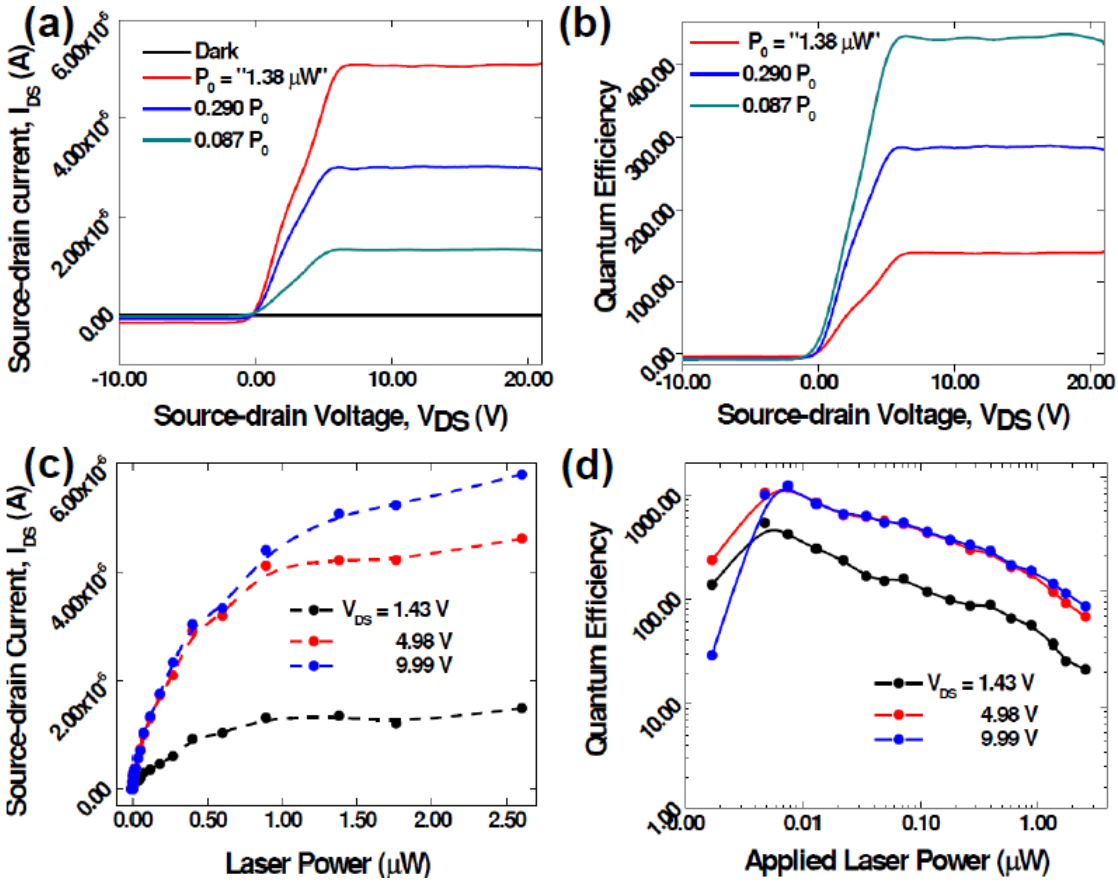

Figure AIII.5 Output and transfer characteristics of a CdSe–nanowire–based LET. **(a–b)** output characteristic plotted in current and gain. **(c–d)** transfer characteristic plotted in current and gain. In the gain plots, the estimated, laser powers used are the "applied powers." The gain was calculated with the estimated laser power actually absorbed by the nanowire channel, which was about 6.2% of the "applied power" (see estimation of actual power absorbed in Appendix II).

REFERENCES

[1] ITRS, International Technology Roadmap for Semiconductors (ITRS), in: ITRS, 2013.

[2] Z. Marks, B. Van Zeghbroeck, High-speed nanoscale metal-semiconductor-metal photodetectors with terahertz bandwidth, Optical and Quantum Electronics, 42 (2011) 771-776.

[3] J.K. Marmon, S.C. Rai, K. Wang, W. Zhou, Y. Zhang, Light-effect transistor (LET) with multiple independent gating controls for optical logic gates and optical amplification, Frontiers in Physics, 4 (2016) 1-10.

APPENDIX IV: SUPPORTING INFORMATION FOR ELECTRON–PHONON COUPLING IN MULTIDIMENSIONAL ZnTe SYSTEMS

"The good thing about science is its true whether or not you believe in it."
Neil deGrasse Tyson, 2011 Real Time with Bill Maher (Episode 201)

AIV.1 Appendix Information Summary

Section AIV.2 contains integrated peak area ratios for gallium phosphide (GaP) with low nitrogen doping, a prototypical sample used in electron–phonon coupling investigations, and bulk ZnTe samples. Section AIV.3 plots ratios of integrated peak areas normalized by square diameter for nanowires on silicon substrate and a TEM grid. Section AIV.4 contains higher order ratios of integrated peak areas for their lower order counterparts included in Chapter 5. Section IV.5 explores the laser power required to form Te–related compounds in bulk CdTe, which is used for comparison to laser–forming similar aggregates on a ZnTe wire. Section IV. 6 contains tabular summaries of PL and Raman spectra displayed in Chapter 5. Section IV.7 further discusses the standard EPC strength model. Section IV.8 generalizes the findings in Chapter 5 to other II–VI semiconductor compounds.

AIV.2 Integrated Raman Peak Intensity Ratios for GaP and Bulk ZnTe

The intent of this section is to provide a general sense of how accurate one could calculate the ratio of the integrated intensities for two Raman peaks. This exercise is to confirm that the large variations in the ZnTe results are not simply because of the experimental uncertainty, including evaluating the integrated intensity. A GaP sample (with a low level of N doping) was used as a prototype sample. The room–temperature bandgap of GaP is 2.26 eV, which is very close to that of ZnTe. 532 nm excitation yields a resonant Raman spectrum as shown in Figure AIV.1A. The ratio of its I_{TO}/I_{1LO} peak areas yields a narrow distribution of 1.5±0.05 (N = 30) under 2.4 μW of 532 nm light.

Bulk ZnTe values were collected under 1.62–2.64 μW and 26.0 μW at five different sites across each sample (N = 5). The small I_{TO}/I_{1LO} range (3.3%) found for GaP is much smaller than for B1 (ZnTe), where its I_{2LO}/I_{1LO} mean and uncertainty were 10.8±2.5 yields an uncertainty of 58.9% (N = 10). Figure AIV1.B plots two Raman spectra for B1 collected at the same measurement location under identical conditions, where the noise in the spectra resulted from subtracting out the PL contribution to leave only the Raman contribution. Peak integration clearly yielded very different I_{2LO}/I_{1LO} values, while graphically, the two spectra appear similar. Peak integration was carefully checked to ensure that the fitting parameter's width matched the peak's FWHM; however, the noisy 1LO will inevitably produce some variation. Impurities can also affect the I_{1LO}. Figure AIV1.C plots two Raman spectra for B4 (with ~2.46% Cd impurities) under a comparable laser power (to B1 and GaP), where noticeable differences in the I_{1LO} yield an I_{2LO}/I_{1LO} of 1.1±0.4 (N = 5). In contrast, samples B2 and B3 yield relatively consistent I_{2LO}/I_{1LO} values. The $I_{(n+1)LO}/I_{nLO}$ values for bulk ZnTe appear in Tables AIV.1 and AIV.2, where measurements were obtained at the same measurement locations from lower to higher laser powers. In general, the bulk ZnTe $I_{(n+1)LO}/I_{nLO}$ values (except B4) possessed relatively small uncertainties measured at individual measurement locations, while the composite or averages over five different measurement sites displayed greater uncertainty. This is because the values were not homogenous across different measurement sites, which could stem from local variations in defect densities. Site–to–site differences yield the relatively large, composite $I_{(n+1)LO}/I_{nLO}$ values reported in the "Avg." column in Tables AIV.1–2. These two tables also indicate a reduction in the site and average $I_{(n+1)LO}/I_{nLO}$ values with

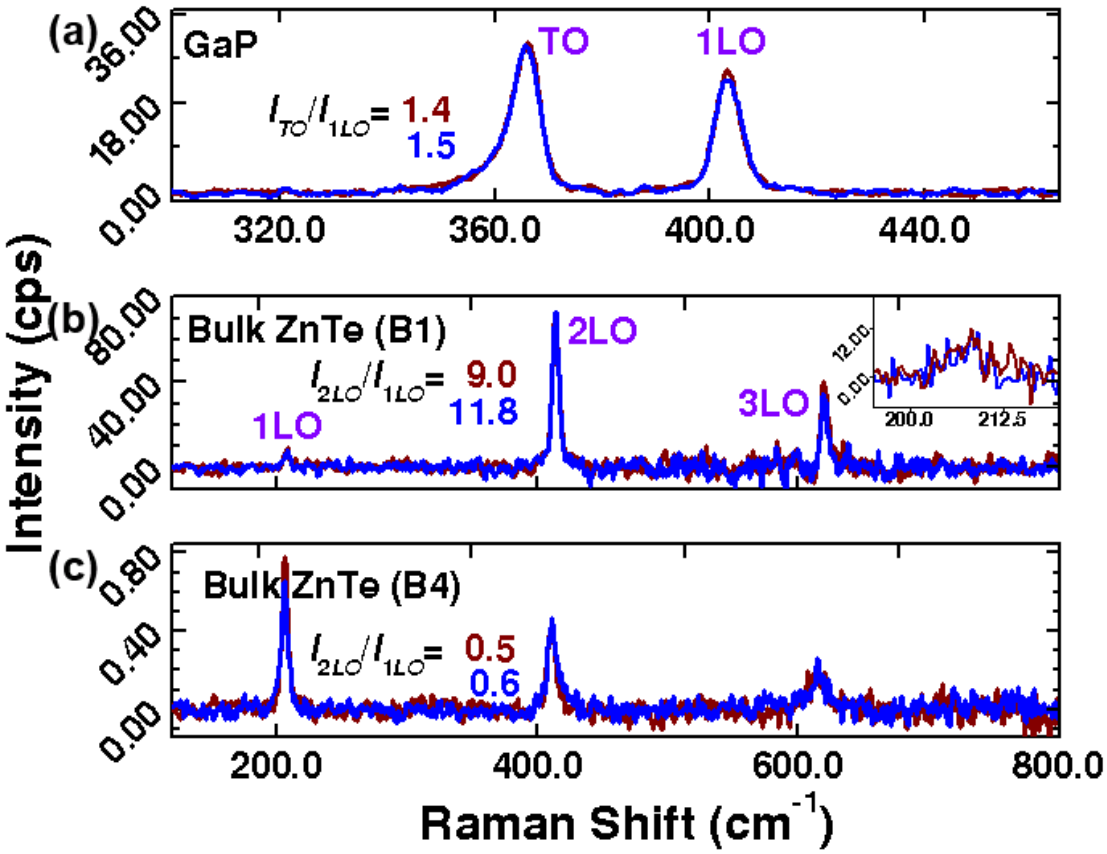

Figure AIV.1 Raman reproducibility of **(a)** low nitrogen–doped GaP and **(b)** B1 collected under 2.4 μW and 2.06 μW of 532 nm light respectively. The wine and blue colored lines are for two different spectra collected at the same measurement location. The ratio of GaP's (ZnTe's) I_{TO}/I_{1LO} (I_{2LO}/I_{1LO}) integrated peak areas yielded a distribution of 1.5±0.05 (10.8±2.5) for N = 30 (N = 10). The noise in (b–c) is from subtracting the PL contribution.

increasing laser power, which is consistent with Figure 5.7 (using a thin film sample). Table AIV.3 lists $I_{(n+1)LO}/I_{nLO}$ values collected under 1.62–2.64 μW of 532 nm light while laser heating with 10 s intervals under 155 μW; each measurement is performed after one, 10 s exposure at the same measurement location. It appears that laser heating with higher powers generally enhanced the mean $I_{(n+1)LO}/I_{nLO}$ (except for B3) relative to similar measurements collected prior to laser heating (e.g., see Table AIV.1), while the uncertainty demonstrated a small change (e.g., B3 and B4) or increased significantly (e.g., B2), where the latter could result from laser annealing defects. This is the first time that these findings have been reported, and further investigation is required to

determine their origin.

Table AIV.1 Mean $I_{(n+1)LO}/I_{nLO}$ value with uncertainty derived from standard deviation from the mean (N = 5) for four different bulk ZnTe samples collected under 1.62–2.64 μW of 532 nm light. B1 I_{2LO}/I_{1LO} values from N = 10, where most measurements did not yield strong 1LO and 4LO peaks.

Sample	Site 1	Site 2	Site 3	Site 4	Site 5	Avg.
			I_{2LO}/I_{1LO}			
B1	10.8±2.5	—	—	—	—	10.8±2.5
B2	2.5±0.1	2.4±0.1	3.2±0.3	3.1±0.2	2.8±0.1	3.7±2.0
B3	2.2±0.1	1.9±0.1	1.7±0.07	1.9±0.1	2.0±0.06	2.0±0.2
B4	0.8±0.7	0.7±0.2	1.1±0.4	1.1±0.5	0.5±0.2	0.8±0.5
			I_{3LO}/I_{2LO}			
B1	0.7±0.2	1.2±0.9	0.9±0.7	1.2±1.3	0.9±0.7	0.8±0.1
B2	0.4±0.2	0.7±0.6	0.5±0.1	0.3±0.1	0.7±0.5	0.5±0.4
B3	0.8±0.06	0.7±0.05	0.7±0.03	0.6±0.2	0.7±0.04	0.7±0.1
B4	1.0±1.6	0.5±0.2	0.8±0.4	0.7±0.4	1.3±0.6	0.9±0.8
			I_{4LO}/I_{3LO}			
B1	—	—	—	—	—	—
B2	—	—	—	—	—	—
B3	0.08±0.04	0.1±0.04	0.1±0.02	0.2±0.1	0.1±0.05	0.1±0.07
B4	0.7±0.8	1.2±0.6	1.0±0.9	0.2±0.1	0.3±0.2	0.7±0.7

Table AIV.2 Mean $I_{(n+1)LO}/I_{nLO}$ value with uncertainty derived from standard deviation from the mean for four different bulk ZnTe samples collected under 26.0 μW of 532 nm light.

Sample	Site 1	Site 2	Site 3	Site 4	Site 5	Avg.
			I_{2LO}/I_{1LO}			
B1	9.7±6.9	14.0±9.8	9.5±9.8	9.2±4.1	6.6±2.1	8.1±1.3
B2	3.4±0.2	3.3±0.1	4.0±0.7	3.6±0.2	3.1±0.1	3.0±0.3
B3	1.8±0.2	1.6±0.05	1.4±0.1	1.6±0.06	1.7±0.1	1.6±0.2
B4	1.1±0.8	1.1±0.7	1.1±0.5	0.8±0.25	0.7±0.2	1.0±0.5
			I_{3LO}/I_{2LO}			
B1	2.2±1.8	0.7±0.6	0.7±0.1	1.3±0.7	2.8±3.0	0.8±0.15
B2	0.5±0.1	0.6±0.1	0.5±0.1	0.5±0.06	0.5±0.25	0.4±0.05
B3	0.8±0.1	0.8±0.04	0.7±0.08	0.8±0.06	0.8±0.06	0.8±0.07
B4	0.3±0.1	0.7±0.4	0.3±0.15	0.4±0.2	0.5±0.4	0.4±0.3
			I_{4LO}/I_{3LO}			
B1	—	—	—	—	—	—
B2	0.2±0.02	0.3±0.05	—	0.1±0.1	0.5±0.26	0.3±0.2
B3	0.2±0.03	0.1±0.01	0.1±0.02	0.1±0.02	0.1±0.02	0.14±0.02
B4	1.0±0.7	0.4±0.26	0.7±0.2	1.0±1.2	1.1±0.9	0.8±0.7

Table AIV.3 Mean $I_{(n+1)LO}/I_{nLO}$ values with standard deviations (N = 5) collected under 1.62–2.64 μW of 532 nm light after laser heating after 10 s intervals under 155 μW. Eeach measurement was collected under the low laser power after one, 10 s exposure to the higher power at the same measurement location.

Sample	I_{2LO}/I_{1LO}	I_{3LO}/I_{2LO}	I_{4LO}/I_{3LO}
B2	6.7±4.4	0.4±0.1	—
B3	1.9±0.06	0.7±0.03	0.2±0.05
B4	1.0±0.7	0.4±0.3	1.3±1.1

AIV.3 Square Diameter Normalization of Integrated Peak Areas

Figure 5.5 plotted the integrated peak areas as a function of diameter to extract EPC strengths. For convenience, the I_{2LO}/I_{1LO} is replotted as a function of nanowire diameter on Si substrate in Figure AIV.2. An alternative method, which should, in principle, yield a slope with an identical numerical value involves normalizing each integrated peak area by the nanowire's square diameter, e.g., (I_{2LO}/d^2) vs. $(I_{1LO}/d^2) = I_{2LO}/I_{1LO}$. This was not true for nanowires on the Si substrate (Figure AIV.2B), while similar values were achieved with both methods for nanowires dispersed on a TEM grid (Figures AIV.2C–D). The I_{2LO}/I_{1LO}, I_{3LO}/I_{2LO}, and I_{4LO}/I_{3LO} values for the Si substrate/TEM grid in Figures AIV.2B–C (under 2.05/1.62 μW of 532 nm light respectively) are 9.7/0.9, 0.8/4.0, and 0.070.18, while nanowires on Si substrate in Figure AIV.2C, which were measured under a higher laser power (25.2 μW), produced values of 7.8, 2.2, and 0.13 respectively.

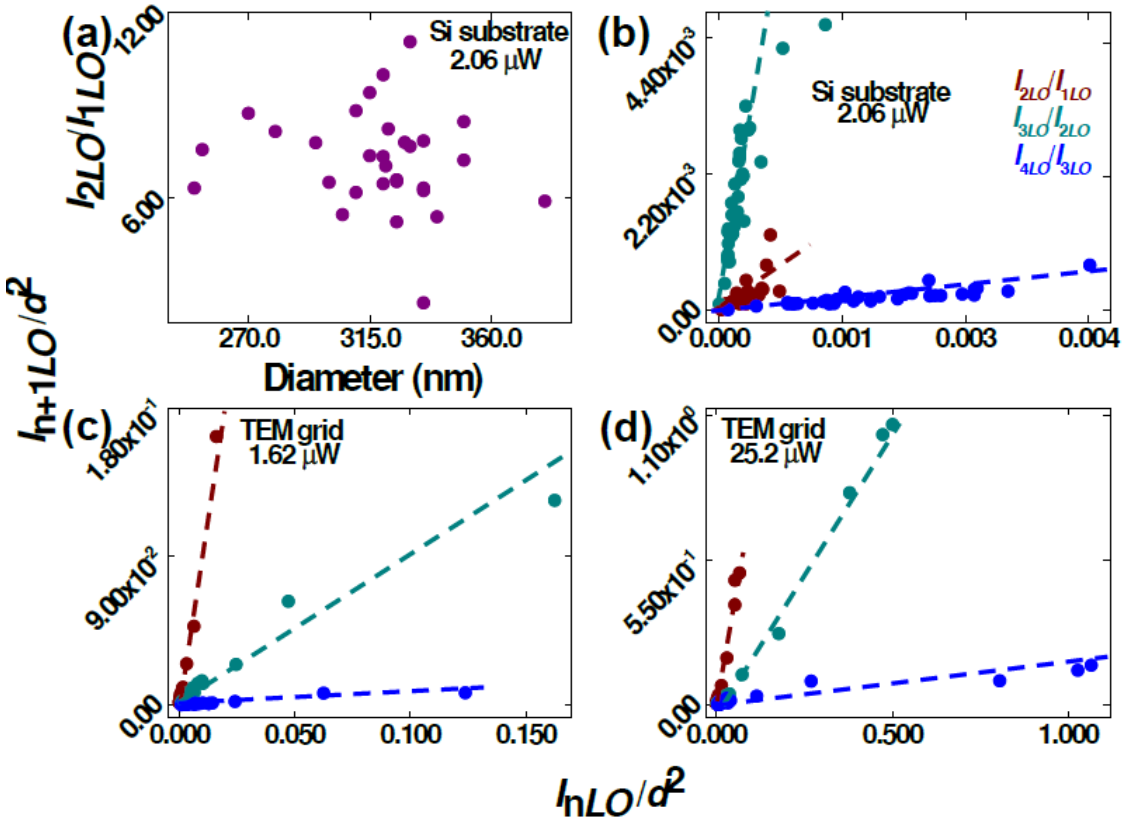

Figure AIV.2 Ratio of integrated peak areas for nanowires on Si substrate (a) for the I_{2LO}/I_{1LO} as a function of diameter, and (b) after being normalized the square diameter (2.06 μW). Nanowires on a TEM grid were also normalized using **(c)** 1.62 and **(d)** 25.2 μW of 532 nm light. Dashed lines are to guide the eye. The I_{2LO}/I_{1LO}, I_{3LO}/I_{2LO}, and I_{4LO}/I_{3LO} values for the Si substrate/TEM grid in (b-c) are 9.7±0.2/0.9±0.2, 0.8±0.03/4.0±0.5, and 0.07±0.005/0.18±0.02, while the corresponding values in (c) were 7.8±0.3, 2.2±0.04, and 0.13±0.009 respectively.

AIV.4 Higher Order Ratios of Integrated Peak Areas

Laser power, laser heating, and polarization dependencies of the I_{2LO}/I_{1LO} was graphed in Figures 5.6D, Figure 5.8B, and Figure 5.9B, respectively. Their higher order ratio of integrated peak areas, e.g., I_{3LO}/I_{2LO} and I_{4LO}/I_{3LO}, are plotted in Figure AIV.3.

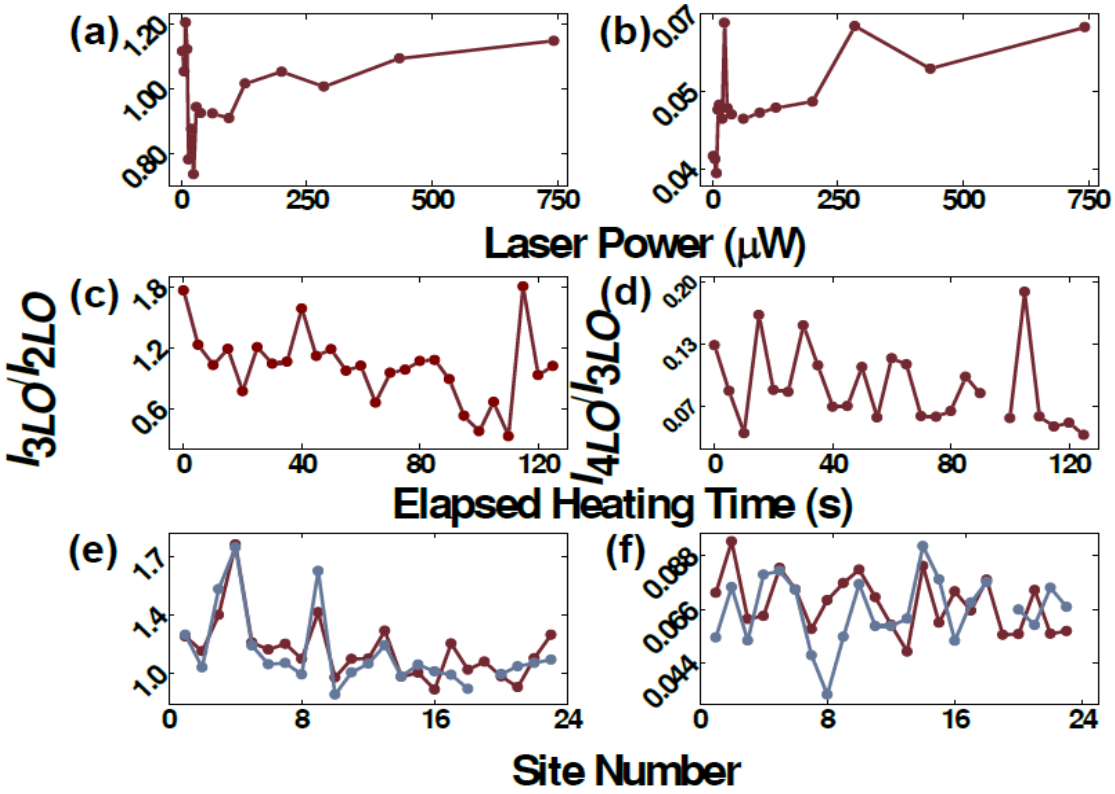

Figure AIV.3 Higher order ratios of integrated peak areas demonstrating **(a–b)** laser power dependence (Figure 5.6D), **(c–d)** elapsed heating time (Figure 5.8B), and **(e–f)** polarization dependence (Figure 5.9B). See text for additional details.

AIV.5 Laser Forming Te in Bulk CdTe

It is useful to compare the laser power used to form Te in ZnTe with that used for the same purpose with bulk CdTe. A 100x objective lens with *N.A.* = 0.9 was used to collected the measured Raman signal. Figure AIV.4A plots bulk CdTe Raman spectra under 65.1, 222, and 1,000 μW of 532 nm light. Initially, only CdTe's 1LO mode appears, while an E(TeO) mode appears and eventually surpassed the 1LO as the laser power was increased. CdTe's 1LO peak remained at 167.7 cm^{-1} until 222 μW, at which point, it down shifted to 164.5 cm^{-1} under 1,000 μW. CdTe's 1LO peak experiences a Raman shifts from 165.9 to 161.4 cm^{-1} as the laser power is increased from 11.91 μW

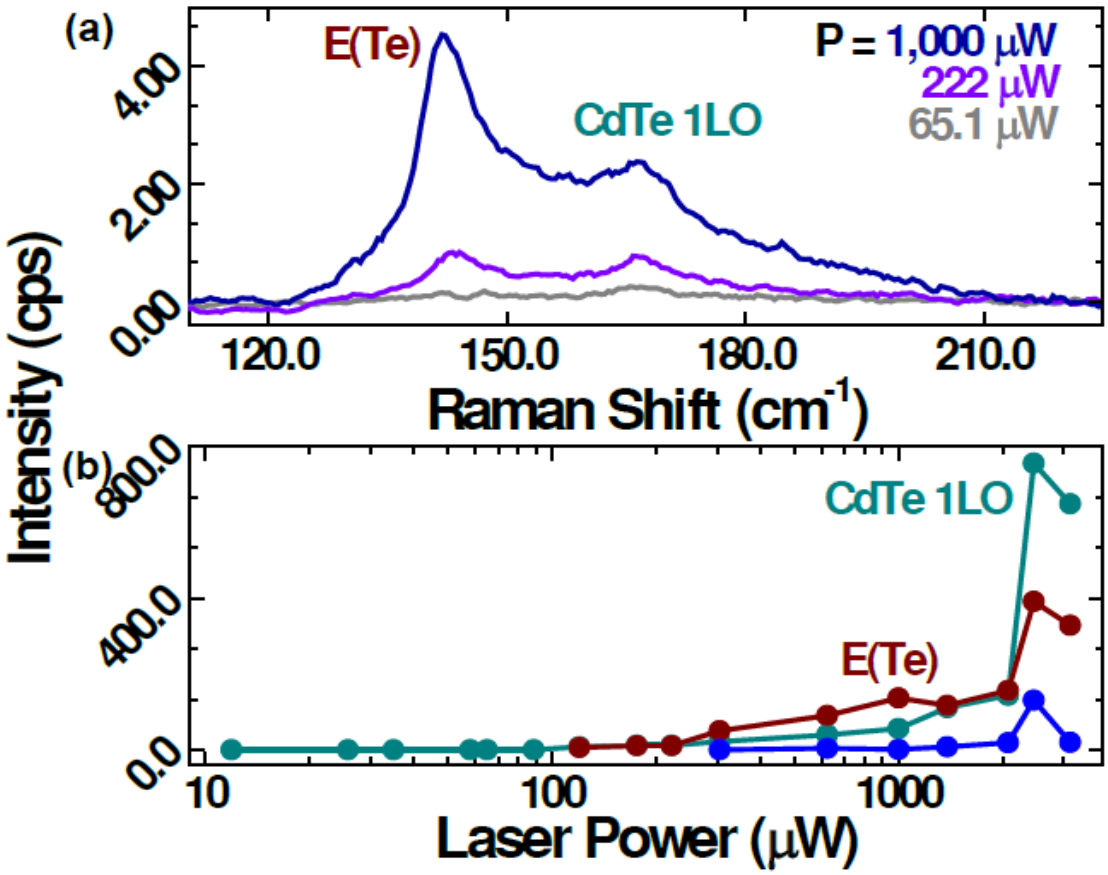

Figure AIV.4 Laser power dependence of Te formationin CdTe. **(a)** Raman spectra of bulk CdTe collected under 65.1, 222, and 1,000 μW of 532 nm light. **(b)** Integrated peak area for CdTe LO, E(Te), and an unassigned peak at ~260 cm^{-1} as a function of (532 nm) laser power.

to 3.13 mW of 532 nm, while the peak area increases from 0.4 to 649.5 cm^{-1} cps. At 65.1, 222, and 1,000 μW, the peak shift (peak area) was 167.6 (0.5), 167.6 (12.5), and 164.5 (56.1) cm^{-1} (cm^{-1} cps). The E(TeO) mode appeared under 120.3 μW, and resulted in Raman shift and peak area changes from 145.3 to 143.1 and 141.7 cm^{-1} under 222 and 1,000 μW respectively, while its peak area changed from 6.6 to 10.8 and 137.5 cm^{-1} cps respectively. Illumination with 12.72 mW yielded a peak shift and peak area of 159.6 cm^{-1} and 328.7 cm^{-1} cps respectively. Not shown is an unassigned peak that appears at 270.3 cm^{-1} under 305 μW of 532 nm light, which down shifted to 266.3 cm^{-1} under 1,000 μW; the peak shift continued shifting to 260.2 cm^{-1} under 19.8 mW. Figure AIV.4B plots integrated peak areas for CdTe's 1LO, E(Te), and an unassigned

peak as a function of laser power. It shows that both the 1LO and E(Te) increase in integrated peak area with increasing laser power, with intensity increases occurring at~300 and 2,000 μW.

AIV.6 PL and Raman Summary Tables

This section contains PL and Raman summary tables for data displayed in figures in the main text.

Table AIV.4 Raman summary table for bulk, thin film, and nanowire systems displayed in Figure 5.2. Only one set of bulk ZnTe data out of two shown in Figure 5.3.

Description	***n*·LO ZnTe**	**Peak Position** *cm^{-1}*	**Peak Area** *a.u.*	**FWHM** *cm^{-1}*
Bulk				
ZnTe RS	1	209.1	44.4	5.5
	2	415.2	544.8	5.3
	3	620.6	365.1	6.9
	4	826.9	25.1	7.4
ZnTe(100) Orangish	1	206.9	22.3	4.4
	2	412.6	77.8	5.3
	3	617.7	45.4	7.6
	4	824.1	4.9	12.0
ZnTe(100)	1	206.9	26.7	4.7
	2	412.6	68.8	5.4
	3	618.1	38.5	7.2
ZnTe(110)	1	205.5	45.3	6.1
	2	410.8	65.7	9.2
	3	614.7	19.5	6.7
Thin Film				
022811	1	205.6	18.8	5.0
	2	412.1	134.2	4.0
	3	617.7	127.6	5.3
	4	824.1	9.5	5.3
030211	1	206.0	8.8	3.0
	2	412.1	137.6	4.2
	3	617.7	132.9	5.8
	4	823.2	4.7	2.9
030311	1	204.7	3.4	1.2
	2	412.1	89.2	4.2
	3	618.1	89.1	5.9
	4	824.1	6.7	6.3
Nanowire				
d = 84 nm	1	205.5	46.0	4.0
	2	411.3	334.6	4.4
	3	617.3	441.5	6.5
	4	823.2	49.6	7.7
d = 223 nm	1	205.5	44.7	8.2
	2	411.2	325.4	4.4
	3	616.8	364.1	6.1
	4	824.1	14.6	5.9
d = 340 nm	1	205.5	28.6	4.1
	2	411.3	197.7	4.4
	3	616.8	246.3	6.0
	4	822.8	15.7	6.8

Table AIV.5 Tabular summary of integrated peak area ratios for bulk, thin film, and nanowire systems graphed in Figures 5.2 and 5.3. Only one set of bulk ZnTe data out of two shown in Figure 5.3.

Description	I_{2LO}/I_{1LO} *a.u.*	I_{3LO}/I_{2LO} *a.u.*	I_{4LO}/I_{3LO} *a.u.*
Bulk			
ZnTe RS	17.9	0.7	0.0(7)
ZnTe(100) Orangish	3.5	0.6	0.1
ZnTe(100)	2.6	0.6	—
ZnTe(110)	1.5	0.3	—
Thin Film			
022811	7.1	1.0	0.0(7)
030211	15.6	1.0	0.0(3)
030311	16.0	1.0	0.0(7)
Nanowire			
d = 84 nm	7.3	1.3	0.1
d = 223 nm	7.3	1.1	0.0(4)
d = 340 nm	6.9	1.2	0.0(6)

Table AIV.6 PL summary table for bulk, thin film, and nanowire systems shown in Figure 5.2.

Description	**Peak Energy** *eV*	**Intensity** *Cts* s^{-1}
Bulk		
ZnTe RS	2.26	956.27
ZnTe(100) Orangish	2.26	57.70
ZnTe(100)	2.26	3.6
ZnTe(110)	2.26	—
Thin Film		
022811	2.26	77.57
030211	2.26	68.30
030311	2.26	20.42
Nanowire		
d = 84 nm	2.27	11.7
d = 223 nm	2.26	11.9
d = 340 nm	2.26	12.3

Table AIV.7 Raman summary table for laser heating the nanowires in Figures 5.4E–F.

Description	***n*·LO ZnTe**	**Peak Position** *cm^{-1}*	**Peak Area** *a.u.*	**FWHM** *cm^{-1}*
d = 29 nm (25.2 μW)	1	207.1	295.9	4.6
	2	412.4	1,778.2	5.8
	3	617.5	1,943.0	7.5
	4	821.4	772.7	9.2
d = 29 nm (186.0 μW)	Te–related	140.8	9.1	4.8
	1	202.3	14.5	4.3
	2	406.8	119.5	10.8
	3	613.3	125.4	14.3
	4	811.6	74.1	20.0
d = 219 nm (25.2 μW)	1	207.1	88.5	4.8
	2	413.3	590.5	4.9
	3	618.3	722.9	6.4
	4	824.3	141.3	8.3
d = 219 nm (186.0 μW)	Te–related	139.5	42.1	3.0
	1	201.8	4.4	5.7
	2	409.8	16.7	9.3
	3	613.3	7.4	1.8
	4	818.1	3.8	1.3

Table IV.8 Tabular summary of mean integrated peak area ratios for nanowires on Si substrate and a TEM grid (Figure 5.5).

Description	I_{n+1LO}/I_{nLO}	**Exp. mean** *a.u.*	**Norm. slope** *a.u.*	**b–value** *nm^{-2}*
Si substrate (2.06 μW)	I_{2LO}/I_{1LO}	7.2	0.9	-3.6×10^{-5}
	I_{3LO}/I_{2LO}	0.9	3.6	9.2×10^{-4}
	I_{4LO}/I_{3LO}	0.12	0.2	-9.0×10^{-5}
TEM grid (1.62 μW)	I_{2LO}/I_{1LO}	7.4	9.7	-2.4×10^{-3}
	I_{3LO}/I_{2LO}	1.2	0.8	3.2×10^{-3}
	I_{4LO}/I_{3LO}	0.08	0.07	1.0×10^{-4}
TEM grid (25.2 μW)	I_{2LO}/I_{1LO}	6.2	7.8	-7.5×10^{-3}
	I_{3LO}/I_{2LO}	1.2	2.2	-1.9×10^{-2}
	I_{4LO}/I_{3LO}	0.4	0.1	7.5×10^{-3}

Table IV.9 Raman summary table of laser heating data for the 1.3–μm–diameter wire presented in Figure 5.8.

Description	***n*·LO ZnTe**	**Peak Position** *cm^{-1}*	**Peak Area** *a.u.*	**FWHM** *cm^{-1}*
0 s	1	206.3	391.0	70.4
	2	412.4	2690.2	547.1
	3	618.1	4751.0	646.3
	4	824.0	436.7	85.9
90 s	Te–141 cm^{-1}	142.9	17.2	2.6
	1	206.5	91.8	18.0
	2	412.5	595.2	92.5
	3	618.1	568.4	71.6
	4	823.6	71.5	7.4
95 s	Te–141 cm^{-1}	142.7	33.6	4.5
	1	207.5	19.5	3.3
	2	413.7	153.0	25.0
	3	619.3	162.2	19.8
	4	824.4	6.7	1.8
100 s	Te–141 cm^{-1}	143.2	12.9	3.3
	1	207.6	19.0	3.3
	2	413.6	128.4	21.9
	3	619.3	148.2	17.4
	4	825.4	17.2	2.0
105 s	Te–141 cm^{-1}	143.6	23.7	4.4
	1	208.0	30.0	3.0
	2	413.7	129.6	21.3
	3	619.4	134.3	16.7
	4	825.7	27.8	1.6
110 s	Te–141 cm^{-1}	143.7	43.3	4.0
	Te–161 cm^{-1}	161.4	211.8	5.4
	1	206.3	108.3	23.8
	2	412.7	246.7	33.6
	3	618.8	160.0	17.7
	4	823.9	13.9	2.0
125 s	Te–141 cm^{-1}	145.0	47.0	3.2
	Te–161 cm^{-1}	161.1	154.5	4.7
	1	206.6	54.0	11.9
	2	413.1	141.0	17.5
	3	618.8	110.2	12.4
	4	824.9	10.5	1.2

Table IV.10 Raman summary table from investigation into interface effects, such as at Au–ZnTe junctions, from Figure 5.10.

Description	***n*·LO ZnTe**	**Peak Position** *cm^{-1}*	**Peak Area** *a.u.*	**FWHM** *cm^{-1}*
Similar				
Au sphere	1	206.0	869.5	4.1
	2	412.1	4,049.7	4.4
	3	617.7	3,822.3	6.4
	4	823.2	314.9	7.3
Au–ZnTe junction	1	206.0	102.7	2.0
	2	412.1	1,523.2	4.3
	3	618.1	1,276.3	6.3
	4	824.5	95.5	7.3
ZnTe nanowire body	1	206.0	247.2	5.1
	2	412.1	1,844.8	4.6
	3	617.7	1,680.4	6.0
	4	823.6	89.3	4.0
Dissimilar				
Au sphere	1	204.2	165.2	5.6
	2	408.7	802.1	6.3
	3	612.2	547.9	8.5
	4	817.5	539.7	9.7
Au–ZnTe junction	1	204.7	345.1	5.6
	2	409.5	2,163.1	6.9
	3	614.7	2,526.7	9.2
	4	818.7	2,029.1	13.9
ZnTe nanowire body	1	205.6	476.0	4.1
	2	411.3	2,248.6	5.0
	3	616.0	3,228.1	7.4
	4	822.0	304.6	8.9

Table IV.11 Tabular summary of integrated peak area ratios for the investigation into material interface effects, e.g., Au–ZnTe, contained within Figure 5.10.

Location	I_{2LO}/I_{1LO} (a.u.)	I_{3LO}/I_{2LO} (a.u.)	I_{3LO}/I_{4LO} (a.u.)
Similar			
Au	4.7	0.9	0.08
Au–ZnTe	14.8	0.8	0.07
ZnTe body	7.5	0.9	0.05
Dissimilar			
Au	4.9	0.7	1.0
Au–ZnTe	6.3	1.2	0.8
ZnTe body	4.78	1.4	0.1

Table IV.12 PL summary table from investigation into interface effects, such as at Au–ZnTe junctions, from Figure 5.10.

Description	**Peak Energy** *eV*	**Intensity** *Cts s^{-1}*
Similar		
Au sphere	2.26	267.36
Au–ZnTe junction	2.27	163.16
ZnTe nanowire body	2.27	217.08
Dissimilar		
Au sphere	2.23	565.69
Au–ZnTe junction	2.24	248.00
ZnTe nanowire body	2.25	821.60

Table IV.13 Raman summary table from methanol exposure graphed in Figure 5.11.

Description	***n*·LO ZnTe**	**Peak Position** *cm^{-1}*	**Peak Area** *a.u.*	**FWHM** *cm^{-1}*
Before	1	206.1	10.4	4.1
	2	412.2	118.6	19.3
	3	617.7	82.1	10.9
	4	822.0	8.3	1.0
After	1	206.5	27.2	5.0
	2	413.4	52.5	5.8
	3	618.9	33.3	2.9
	4	821.9	3.5	1.6

Table IV.14 Tabular summary of integrated peak area ratios for methanol exposure (Figure 5.11).

Location	I_{2LO}/I_{1LO} (a.u.)	I_{3LO}/I_{2LO} (a.u.)	I_{3LO}/I_{4LO} (a.u.)
Before	11.4	0.7	0.1
After	1.9	0.6	0.1

AIV.7 Standard Nanowire EPC Model: Extended Discussion and Limitations

Derivation of the standard EPC model [1, 2] is discussed and ZnTe parameters are provided prior to discussing potential limitations with this model. Eq. 5.1 (in the text) provides a simple formula relating the 2LO and 1LO intensity ratio to the EPC strength described by Huang-Rhys factor S. The formula is based on a resonant Raman model that can describe the relative intensities between *n*–LO Raman peaks, and was initially developed by Albrecht [3]. *S* is related to the relative lattice relaxation between the

excited and ground state or the Δ term, Eq. AIV.1. Note that this equation is derived under the assumption that the hole is perfectly localized, while the electron is orbiting the hole with an effective Bohr radius a_0 [4]. In this equation: a_0 is the Bohr radius, ω_{LO} is the LO frequency, ε_∞ and ε_0 are the high frequency and static dielectric constants, $w = (3\pi^2)^{1/3}\, d/a_0$, d is the lattice spacing, [1, 4]. The resulting theoretical bulk ZnTe coupling strength, S_{bulk}, is 3.2 when: E_{ex} = 2.25 eV, ε_∞ (ε_0) = 7.28 (10.1), d (a_0) = 6.1 Å (5.2 nm), Γ = 65 meV (obtained from epilayer [5] measurements), and ω_{LO} = 205 cm^{-1}) [6-9]. As discussed in the text, the theoretical value is much below those observed for high quality ZnTe samples. However, samples containing defects and impurities produced coupling strengths closer to this theoretical value.

$$\Delta^2 = \left(\frac{24}{\pi}\right)^{1/3} \frac{e^2}{a_0 \hbar\omega_{LO}} \left(\frac{1}{\varepsilon_\infty} - \frac{1}{\varepsilon_0}\right) \frac{1}{w} \int_{x=0}^{w} \frac{x^4 \left(2 + x^2\right)^2}{\left(1 + x^2\right)^4} dx \qquad \text{(AIV.1)}$$

Deviations from this model are available in literature. As examples, experimental nanowire [8] (microcrystal [10]) resonant Raman spectra, collected at room temperature (80 K), included up to second– (third–) order LO peaks. While both studies demonstrated decreasing I_{2LO} with decreasing size/diameter, only the microcrystal spectra displayed non–monotonic changes in both I_{1LO} and I_{3LO} peaks as a function of particle size.) Third, thermal effects related to laser–induced heating were found to have a moderate effect. While the standard model does include temperature dependence, it is assumed to play a minor role, which contrasts the experimental observations presented in this dissertation. Further experimental exploration is required to lay the foundation for a generalized theory.

AIV.8 Electron–phonon Coupling

Electron–phonon coupling strengths can be altered in systems beyond ZnTe, such as CdSe– and ZnO–based, core and core/shell systems. Figure AVI.5 plots I_{2LO}/I_{1LO} for ZnTe peaks and E_{2HI}/E_{1LO} for ZnO peaks in ZnO and ZnO/ZnSe nanowire arrays; the ZnSe nanowires are compared to bulk ZnTe. In Figure AVI.5A, the ZnO/ZnSe nanowires demonstrate undulations similar to those in Figure 5.6D and Figure 5.7D for nanowires and thin films respectively. In contrast, bulk ZnSe shows a slight increase in I_{2LO}/I_{1LO} with increasing laser power but does not display an oscillatory relationship. It may be interesting to investigate bulk ZnTe for further generalization. In Figure AIV.5B, both ZnO and ZnO/ZnSe nanowires display a sharp decrease in E_{2HI}/E_{1LO}, while the value is relatively constant at higher laser powers with the core/shell structure displaying a lower value than the core. No oscillations were observed.

CdSe's I_{2LO}/I_{1LO} can also be modified through a laser–induced, structural transformation. Raman spectra were collected as a function of laser power from 4.97 μW to 2.67 mW of 532 nm light. Figure AIV.5A plots select spectra demonstrating changes. Each spectrum represents typical features observed over large power ranges, e.g., ~5–20 μW, >20–161 μW, and >161 μW –2.67 mW. At low laser powers, the I_{2LO}/I_{1LO} was 0.05, while this value increased to 0.10 and 0.30 at 260 μW and 2.67 mW (which represent factor of 2 and 6 enhancements) respectively (see Table AIV.12). The extrinsic perturbation of the electron–phonon coupling strength with laser power probably contributed to the experimental discrepancies reported for CdSe quantum dots, which range from 0.02 to 0.20 for high quality, single crystalline material [11]. More specifically, the 1– and 2–LO modes permanently shifted from 240.1 and 413.0 cm^{-1} to

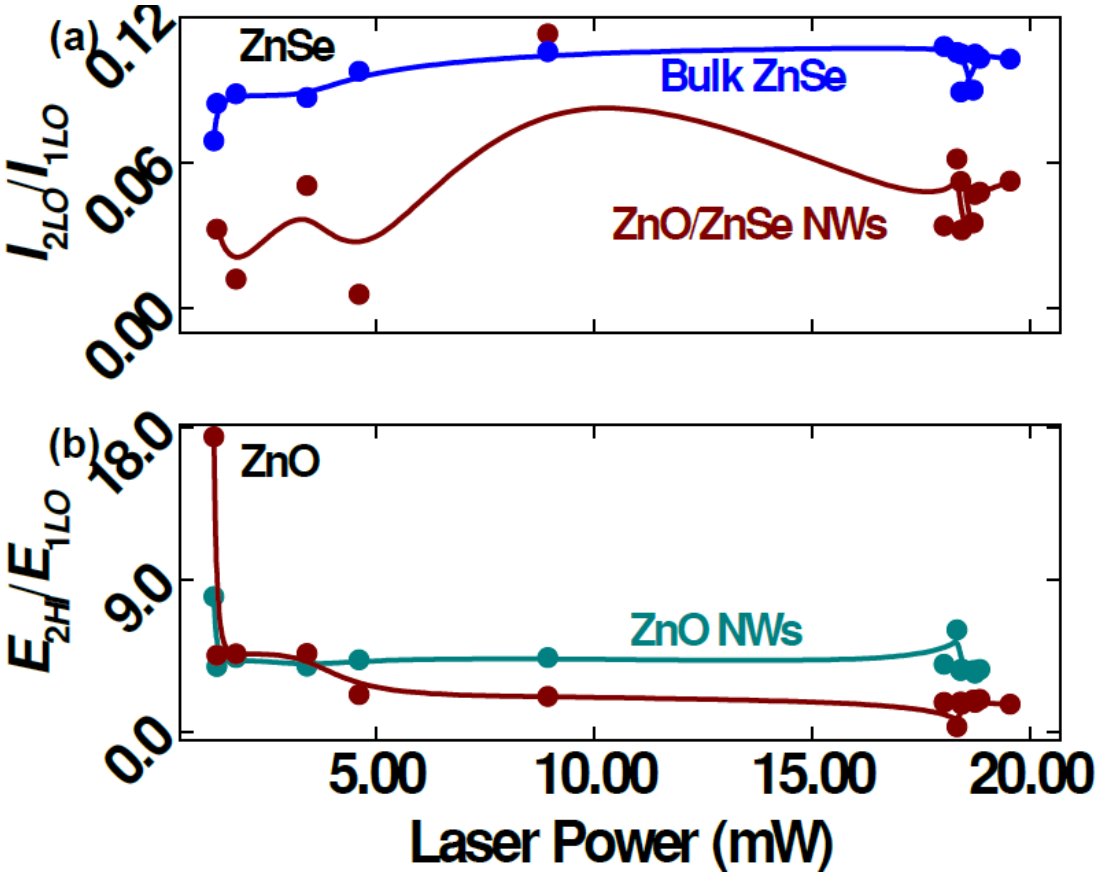

Figure AIV.5 EPC strengths in other II–VI systems. **(a)** Laser–power dependent spectra representative of findings collected with 4.97 μW to 2.67 mW of 532 nm light. **(b)** Raman spectra collected with 260 μW before and after exposure to 1.55 mW.

203.3 and 411.7 cm^{-1} respectively upon increasing the laser power, while the broad peak started at 169.6 and moved to 161.1 cm^{-1}. While the broad peak is also positioned similarly to that for cadmium telluride (CdTe), its existence was excluded by carefully preventing growth chamber contamination, and analyzing nanowire lattice spacings and diffraction patterns collected with TEM. Furthermore, laser heating the CdSe nanowire in Figure 6.3D decreased the I_{2LO}/I_{1LO} by –0.00105 n + 0.50, where n = 0–2 and represents the number of 100 s exposures to $P_w(532nm)$, while subsequent illumination yielded stable I_{2LO}/I_{1LO} values.

In Figure AIV.6, the broad feature, as demonstrated in Chapter 6, is sensitive to surface conditions, the 1LO shoulder at ~250 cm^{-1} was not previously reported for CdSe,

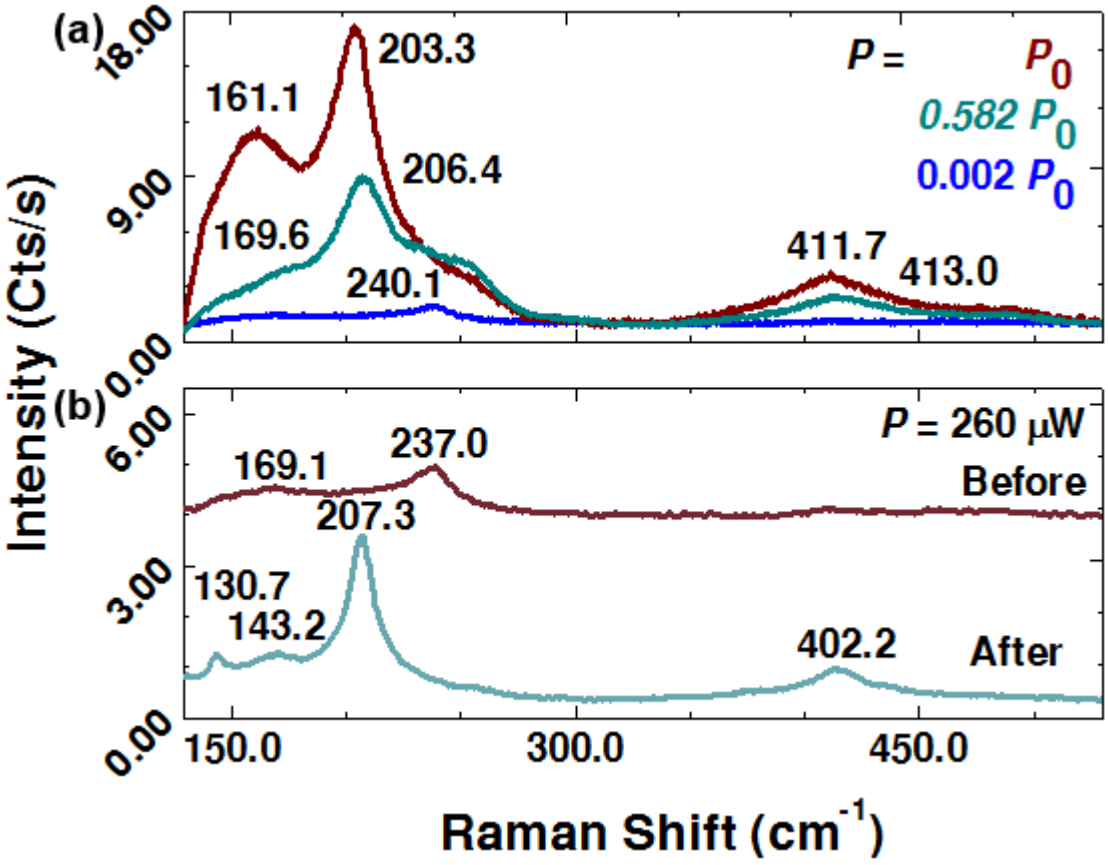

Figure AIV.6 Laser–induced Raman changes in a CdSe nanowire. **(a)** Laser–power dependent spectra representative of findings collected with 4.97 μW to 2.67 mW of 532 nm light. **(b)** Raman spectra collected with 260 μW before and after exposure to 1.55 mW.

while the ~240 cm^{-1} peak has been attributed to the following: thermal oxide [12], amorphous selenium (a–Se) [13, 14], and to cinnabar or wurtzite CdSe domains [15]. The small, 2LO shoulder at ~440 cm^{-1} matches the expected position for CdSe's thermal oxide [12], while the 1LO shoulder at ~240 cm^{-1} appears present in Ref. [12] but it was not discussed. The 1LO shift in particular, e.g., from 240.1 to 203.3 cm^{-1}, implies a structure transformation. The validity of the various literature assignments are briefly discussed. Assuming that the peak shift is from Se implies a photo–conversion process [16] involving excess selenium at macroscopic defects, such as at substitution and interstitial sites [17-19], but this assumption does not explain the absence of certain peaks, such as a CdSe–like, 1LO peak at lower laser powers, or the

Table AIV.15 I_{2LO}/I_{1LO} values for CdSe as a function of laser power (refer to Figure AIV.5).

Laser Power *μW*	I_{2LO}/I_{1LO} *a.u.*
Before	
4.97	0.07
19.3	0.05
30.1	0.08
55.8	0.05
160.6	0.02
260	0.10
453	0.01
1,554	0.07
2,670	0.30
After	
30.1	0.003
260	0.31
2,670	0.33

missing Se peak at ~140 cm^{-1}. Furthermore, the appearance of either (rather than both) the ~140 cm^{-1} peak or the 1LO shoulder extending to ~240 cm^{-1} (with a higher order, 2LO shoulder at 440 cm^{-1} that is difficult to observe visually) suggests that more than Se [13, 20] may be present. Assignment to thermal oxide is uncertain because it could not be decoupled from other effects. While Chapter 6 demonstrates that partial nanowire ablation removed both the broad feature and peak assigned to thermal oxide, the broad feature was sensitive to surface conditions, which suggested that it may not be related to the thermal oxide peak. Further investigation is required. A phase transformation may be a possible explanation for the large Raman shifts. As both wurtzite (WZ) and zinc–blende (ZB), CdSe crystal structures have similar free energies of formation [21], although ZB is the more energetically favorable configuration at low temperatures [22], a laser–induced phase transformation is not unreasonable. These hypotheses are tested with prolonged exposure to 1.55 mW of 532 nm light (Figure AIV.6B), which eventually forms a Raman peak at 143.2 cm^{-1}, while the intensity of the ~240 cm^{-1} peak was drastically reduced with $P\,(532nm) > \sim 0.5$ mW. Raman spectra

collected with 260 μW after exposure to high laser powers revealed 1– and 2–LO peaks at 207.3 and 402.2 cm^{-1} (compared to their initial values of 240.1 and 413.0) respectively. Raman spectra collected with 30.1 μW (not shown) presented 1– and 2–LO peaks at 208.2 and 415.6 cm^{-1} respectively, and are more reasonable values for CdSe. The Raman spectra collected with 260 μW is shown because its 2LO position is rather interesting. It is unclear if the laser–induced phase transformation is still occurring. The lack of recoverability under 30.1 μW could result from a phase transformation [15] from zinc–blend CdSe, with its 1LO at ~250 cm^{-1}, to wurtzite CdSe, while the continued presence of the 1– and 2–LO shoulders could stem from an incomplete removal of the thermal oxide. It is worth noting that the laser annealed peaks are “sharper” or more well defined, which implies an improved crystal structure such as through defect removal. Meanwhile, two new peaks appear at 125.4 and 144.1 cm^{-1}, where the 125.4 cm^{-1} peak is not resolved under higher laser powers. While both of these peaks are consistent with γ–Se [13], the dominate peak at ~245 cm^{-1} is clearly absent. Unfortunately, the origin of these two new remains unassigned.

REFERENCES

[1] A.P. Alivisatos, T.D. Harris, P.J. Carroll, M.L. Steigerwald, L.E. Brus, Electron-vibration coupling in semiconductor clusters studied by resonant Raman spectroscopy, Journal of Chemical Physics, 90 (1989) 3463-3468.

[2] J.J. Shiang, S.H. Risbud, A.P. Alivisatos, Resonance Raman studies on the ground and lowest electronic excited-state in CdS nanocrystals, Journal of Chemical Physics, 98 (1993) 8432-8442.

[3] S. Albrecht, L. Reining, R. Del Sole, G. Onida, Ab initio calculation of excitonic effects in the optical spectra of semiconductors, Physical Review Letters, 80 (1998) 4510-4513.

[4] R. Merlin, G. Guntherodt, R. Humphreys, M. Cardona, R. Suryanarayanan, F. Holtzberg, Multiphonon processes in YbS, Physical Review B, 17 (1978) 4951-4958.

[5] Y.M. Yu, S. Nam, K.S. Lee, Y.D. Choi, B. O, Photoluminescence characteristics of ZnTe epilayers, Journal of Applied Physics, 90 (2001) 807-812.

[6] L. Bornstein, Numerical Data and Functional Relationships in Science and Technology, in: O.W. OMadelung, H.; Schulz, M. (Ed.), Springer, Berlin, 1982.

[7] K. Sato, S. Adachi, Optical properties of ZnTe, Journal of Applied Physics, 73 (1993) 926-931.

[8] Q. Zhang, J. Zhang, M.I.B. Utama, B. Peng, M. de la Mata, J. Arbiol, Q. Xiong, Exciton-phonon coupling in individual ZnTe nanorods studied by resonant Raman spectroscopy, Physical Review B, 85 (2012) 085418.

[9] W.Y. Uen, S.Y. Chou, H.Y. Shin, S.M. Liao, S.M. Lan, Characterizations of ZnTe bulks grown by temperature gradient solution growth, Materials Science and Engineering B-Solid State Materials for Advanced Technology, 106 (2004) 27-32.

[10] S. Hayashi, H. Sanda, M. Agata, K. Yamamoto, Resonant Raman scattering from ZnTe microcrystals - Evidence for quantum size effects, Physical Review B, 40 (1989) 5544-5548.

[11] A.M. Kelley, Electron-phonon coupling in CdSe nanocrystals, Journal of Physical Chemistry Letters, 1 (2010) 1296-1300.

[12] D.P. Masson, D.J. Lockwood, M.J. Graham, Thermal oxide on CdSe, Journal of Applied Physics, 82 (1997) 1632-1639.

[13] S.N. Yannopoulos, K.S. Andrikopoulos, Raman scattering study on structural and dynamical features of noncrystalline selenium, Journal of Chemical Physics, 121 (2004) 4747-4758.

[14] M. Yashiro, Y. Nishina, Raman spectral studies on the crystallization processes of amorphous and liquid states in Se and Te: Proceedings of the International Conference on the Physics of Selenium and Tellurium, in: G. Gerlach, P. Grosse (Eds.) The physics of selenium and tellurium, Springer-Verlag, Heidelburg, Germany, 1979, pp. 206-208.

[15] S. Dhara, C.-P. Liu, S.-F. Chen, A.A. Eliseev, D.I. Petukhov, Resonance Raman spectroscopic study of shape-induced phase transition in CdSe nanoclusters, Journal of Raman Spectroscopy, 46 (2015) 1-3.

[16] V.V. Poborchii, A.V. Kolobov, K. Tanaka, An in situ Raman study of polarization-dependent photocrystallization in amorphous selenium films, Applied Physics Letters, 72 (1998) 1167-1169.

[17] G.P. Lindberg, R.E. Tallman, R. Lauck, M. Cardona, X. Liu, J.K. Furdyna, B.A. Weinstein, Effects of pressure on photo-induced formation of Se and Te clusters in II-VI compounds, Physica Status Solidi B-Basic Solid State Physics, 250 (2013) 711-715.

[18] K.H. Chow, G.D. Watkins, Optically induced migration of interstitial zinc in ZnSe: Caught in the act, Physical Review Letters, 81 (1998) 2084-2087.

[19] K.H. Chow, G.D. Watkins, Electronic structure and migrational properties of interstitial zinc in ZnSe, Physical Review B, 60 (1999) 8628-8639.

[20] P.J. Carroll, J.S. Lannin, Raman scattering of amorphous selenium films, Solid State Communications, 40 (1981) 81-84.

[21] S.H. Tolbert, A.P. Alivisatos, High-pressure structural transformations in semiconductor nanocrystals, Annual Review of Physical Chemistry, 46 (1995) 595-625.

[22] C.Y. Yeh, Z.W. Lu, S. Froyen, A. Zunger, Zinc-blende-wurtzite polytypism in semiconductors, Physical Review B, 46 (1992) 10086-10097.

APPENDIX V: SUPPORTING INFORMATION FOR LASER PROCESSED TUNING OF SEMICONDUCTOR NANOWIRES

"Discovery consists of looking at the same things as everyone else and thinking something different."
Albert Syent-Györgyi, Oct. 1985 Bridging the Present and the Future in IEEE Professional Communications Society conference record

AV.1 Appendix Information Summary

Sections AV.2–AV.3 respectively provide (1) additional information supporting wavelength–dependent device responses; and offers (2) supplemental optical and structural characterization supporting the laser processing of CdSe and CdSe/ZnTe SNWs in Figure 6.3. Wavelength–dependent electrical properties are first explored in Section AV.2, where two devices are investigated. The first device (D1) is different from that shown in Chapter 6 and possesses a 10.–μm–long, CdSe SNW. The second device (D2) is the device with a 10.–μm–long SNW used in Figure 6.2. First, wavelength–dependent behavior is investigated for a LET's turn–on voltage, $V_{D,on}$, or the V_{ds} point where current begins to increase, output and transfer characteristics, and under optical gating with dual–beam illumination. The wavelength–dependence of the $V_{D,on}$ is plotted as a function of $\lambda_g(P_g)$ in Figure AV.1 for pristine operation of D1 and D2, and is extracted from the output characteristics or I_{ds} vs. V_{ds} plots. The output characteristics are displayed in Figure AV.2 for D1 using λ_g = 633, 532, and 442 nm before and after gentle laser processing with $P_w(532nm)$ = 3.2–3.6 μW, where Tables AV.1–AV.2 summarize their I_{ds} and V_{ds} onsets for the first and second current plateaus, e.g., primary and secondary photoconductivity. Figure AV.3 plots the PL emission for 532 nm excitation for both D1 and D2. The PL emission intensity is altered by laser processing and generally correlates with the output characteristics, where a higher current correlates with reduced PL emission (presumably due to enhanced carrier

diffusion away from the measurement site). Figure AV.4 presents the transfer characteristics or I_{ds} vs. $P_g(\lambda_g)$ before and after laser processing for D1 and D2, where optical gating employed λ_g = 633, 532, and 442 nm for the former and λ_g = 532 nm for the latter respectively. While the relationship between output and transfer characteristics are straightforward, the wavelength–dependent effects resulting from illumination with multiple optical sources is more complicated. Figure AV.5 displays laser–written, multi–optical–gate function for dual–beam gating using $P_{g,1}(532nm)$ and $P_{g,1}(Halogen)$, and discusses its measure of optical amplification. R is defined in Section 4.3.

Second, Section AV.3 provides additional optical and structural information that supplements the results displayed in Figure 6.3. Figure AV.6 reproduces Figure 6.3B with three pristine PL measurements to demonstrate reproducibility. This graph also indicates that the intensity change resulting from laser processing is significant. Figure AV.7 magnifies the deep–level emission portion of the PL spectra shown in Figure 6.3. Supplemental investigation into the oscillatory nature is briefly explored with ultraviolet (325 nm) excitation in Figure AV.8. Meanwhile, the complete laser removal of the broad Raman feature is significant, and the Raman data is summarized in Table AV.4. The observed Raman trends are reproduced across a CdSe–SNW channel in an In–CdSe–In device (Figure AV.9), where one spot was lightly ablated. Another partially ablated, single CdSe SNW is investigated structurally using TEM in Figure AV.10, and reveals the laser–formation of a polycrystalline CdSe layer on the ablated site. To gain additional insight into the broad Raman feature, a wurtzite CdSe/ZnTe SNW is investigated in Figures 6.4 E–F. Figure AV.11 structurally characterizes this core/shell SNW, and reveals an absence of surface damage. To compare Raman spectra between

different ZnTe crystal structures, gentle laser processing is performed on a zinc–blende ZnTe SNW in Figure AV.12; its pertinent Raman information is summarized in Table AV.5.

AV.2 Supporting Information for Wavelength–dependent Electrical Responses

Wavelength–specific, turn–on voltages, $V_{D,on}$, are shown in Figure AV.1 for two pristine devices (D1 and D2). $V_{D,on}$ is obtained from the output characteristics and describes the V_{ds} point where the current begins to increase; the output characteristics for D1 will be shown subsequently. The wavelength–dependent, V_{ds} onset of the current plateau directly impacts this parameter, where D1 possesses higher $V_{D,on}$ voltages than D2. Wavelength–dependent output characteristics are also demonstrated in Figure AV.2 using these two devices, where for D1, the device was allowed to recover in ambient conditions for at least one week between measurements with different λ_g. For D2, different λ_g conditions were measured consecutively before and after gentle laser processing. Both devices employed $P_w(532nm)$ = 3.5 μW. In general, gentle laser processing resulted in negligible changes in the dark current, while the photocurrents were drastically altered. Figure AV.2A–B, Figures AV.2C–D, and Figures AV.2E–F respectively contain D1's output characteristics (I_{ds}–V_{ds}) before and after laser processing, where the was optically gated with λ_g = 633, 532, and 442 nm respectively. The inset contains photoluminescence (PL) maps overlaid onto optical images of the same device. The PL measurements were performed before and after gentle laser processing and visually illustrate PL changes along the same SNW, where a clear reduction in PL intensity is observed at the site of laser modification. Note that a complete PL recovery did not occur, which could result from laser annealing defect states, although the PL intensity did drastically recover between each set of laser

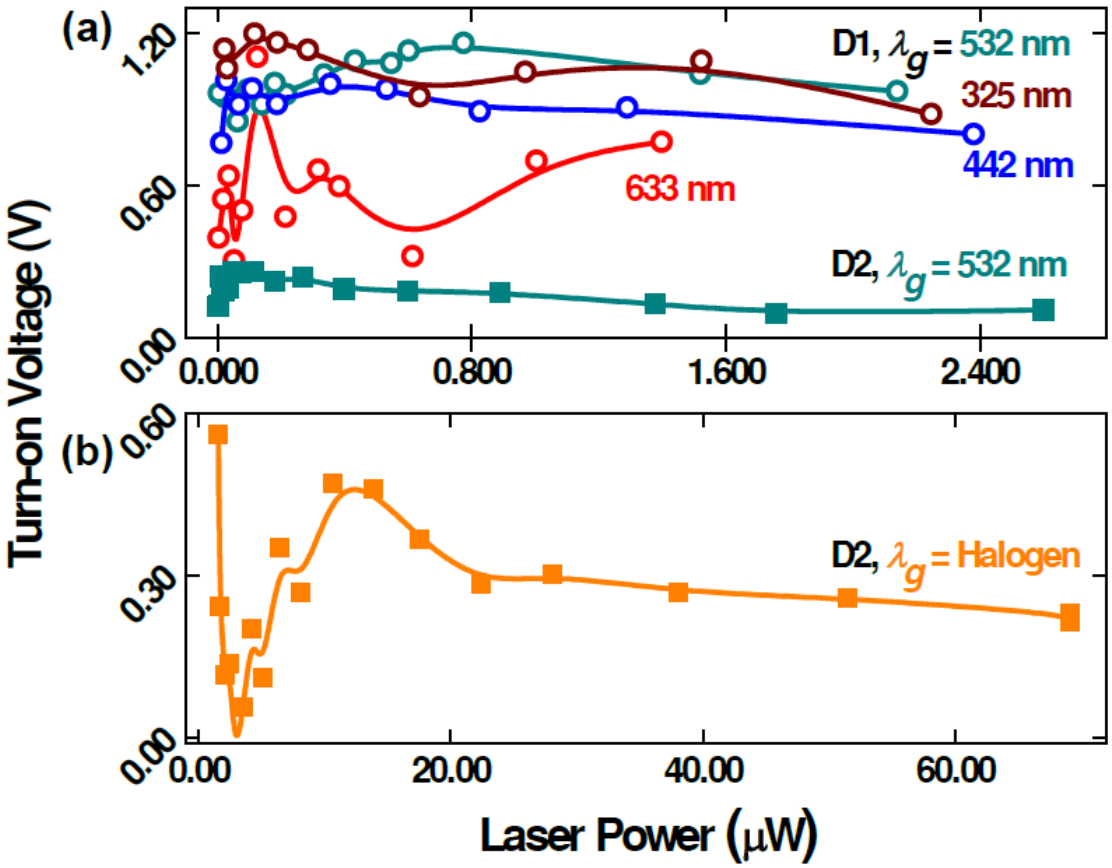

Figure AV.1 Wavelength–tunable turn–on voltages, $V_{D,on}$, were extracted from the output characteristics while operating two pristine devices: D1 (open circles) and D2 (solid squares). This parameter reflects the wavelength–dependent changes in the first current plateau's V_{ds} onset.

processing experiments. Figure AV.2 reveals two common trends: laser processing decreased the I_{ds}, as illustrated in Table AV.1, and shifted the V_{ds} onsets of the first and second plateaus typically to higher voltages as shown in Table AV.2. As previously demonstrated [1], different laser frequencies and wavelengths, $P_g(\lambda_g)$, can tailor the relative I_{ds} and V_{ds} onset of the two plateaus. Figure AV.2 extends this concept to demonstrate that laser modification or processing of the SNW also plays a significant role. This could result from the laser annealing of defect states or even the native oxide or amorphous layer on the nanowire's surface. Focused illumination increased rectification, while broad–band and broad–area illumination (with halogen light) altered the characteristics, such as through enhanced I_{ds}. More specifically, λ_g = 532 nm

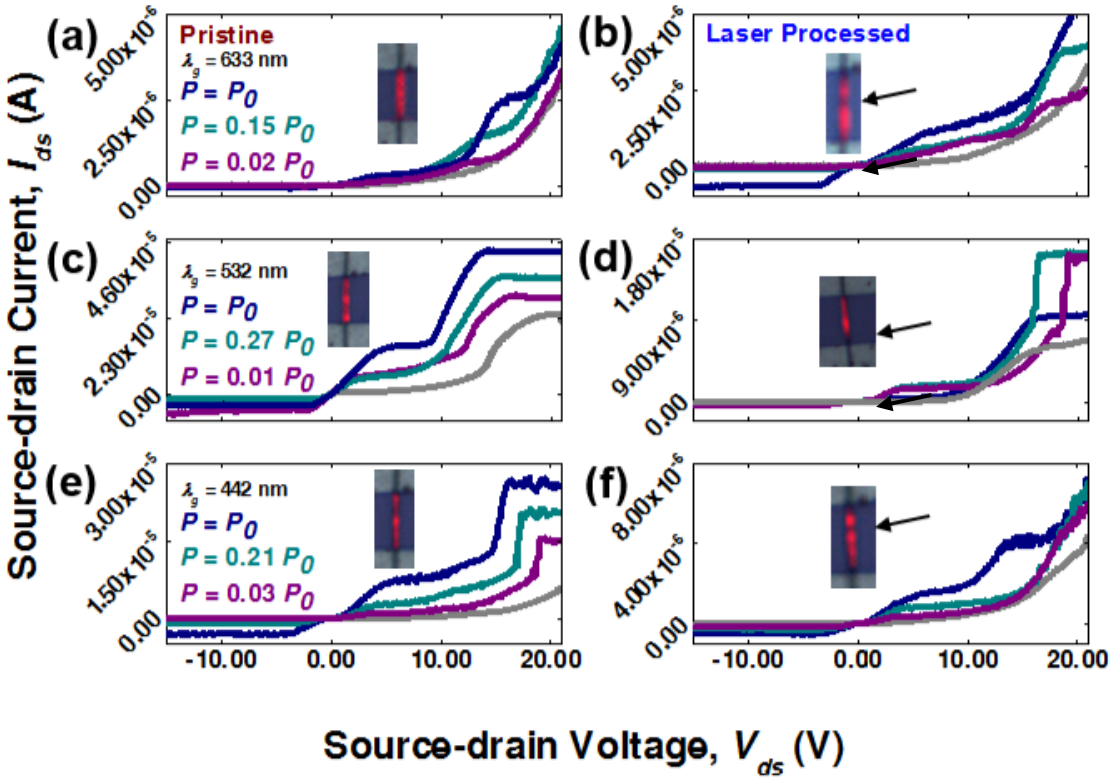

Figure AV.2 Wavelength–dependent output characteristics (from D1) collected from the same pristine and gently laser–processed device (with a 10–μm–long, CdSe SNW). The device was optically gated using λ_g = **(a–b)** 633, **(c–d)** 532, and **(e–f)** 442 nm with respective P_0 values of 1.40/1.35, 2.08/2.14, and 2.38/2.81 μW before/after gentle laser processing. Laser processing was performed with $P_w(532nm) \approx 3.5$ μW. The inset contains PL maps, collected with powers near P_0, overlaid onto optical images. Gentle laser processing produced visible PL changes that did not damage the SNW surface or alter the local crystal structure (as investigated with TEM/HRTEM and diffraction pattern analysis).

Table AV.1 Output characteristic summary from Figure AV.2. I_{ds} is reported for specific V_{ds} values before and after laser processing D1. Optical gating used the reported $P_g(\lambda_g)$ conditions.

$P_g(\lambda_g)$	V_{ds} V	I_{ds} (before/after) μA
λ_g = 633 nm P_g = 1.40/1.35 μW	-1.42 1.42 4.98	-0.014/-0.182 0.027/0.149 0.114/0.850
λ_g = 532 nm P_g = 2.08/2.14 μW	-1.45 1.45 4.96	-3.11/-0.13 4.45/0.26 13.80/1.44
λ_g = 442 nm P_g = 2.38/2.81 μW	-1.45 1.45 4.96	-0.83/-0.22 0.96/0.27 6.71/1.36.

Table AV.2 Output characteristic summary from Figure AV.2. Approximate V_{ds} onsets of the first and second Ids plateaus are reported before and after laser processing D1 using P_0 for each listed λ_g condition.

λ_g	First Plateau's V_{ds} onset (before/after) V	Second Plateau's V_{ds} onset (before/after) V
λ_g = 633 nm	~2.75/~4.75	12–14.5/17.25–20.
λ_g = 532 nm	1.75–42/2–3	13.25–16/15.5–19
λ_g = 442 nm	3–4/2.5–3.5	15.5–18.5/13.25 to >21

demonstrated transistor–like output characteristics in the pristine device, while gentle laser processing presented strongly rectified behavior, while for λ_g = 442 nm, the I_{ds} was drastically reduced, but the current plateaus were still visible. An interesting feature for λ_g = 633 nm is the conversion from a non–linear, laser–power dependence to a more linear dependence after laser processing. A relationship between carrier recombination and electrical behavior is briefly examined in Figure AV.3, which plots the PL intensity as a function of laser power before and after gentle laser processing. In general, the PL peak intensity increased in slope with increasing laser power under 532 and 442 nm light, while 633 nm light displayed an increase in exciton emission.

Together, these results strongly imply that: (1) wavelength–specific device responses may be laser processed for both optical and electrical signals; and (2) PL provides a quick and efficient means of optical feedback for laser processing electrical properties, which may be beneficial in a manufacturing environment. An example of gently laser–processed, wavelength–selective, electrical behavior involves switching λ_g from 532 nm to 442 nm to transition from diode–like to transistor–like output characteristics. This naturally leads one to question the possibility of selectively processing electrical behavior in the presence of multiple optical sources. But first, the transfer characteristics (I_{ds}–P_g) are explored, which are the foundation of a LET's multi–optical–gate function.

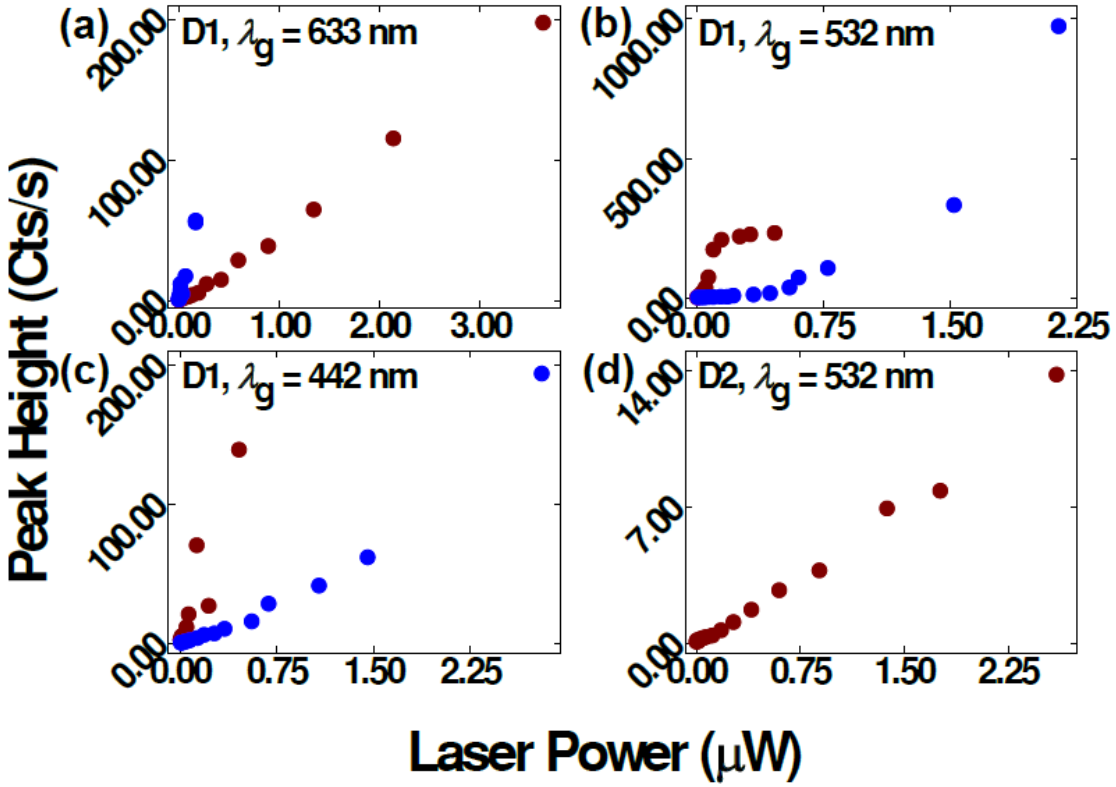

Figure AV.3 Laser–power–dependent PL intensities for pristine and laser processed devices (D1 and D2): D1 was illuminated using λ_g = **(a)** 633 nm, **(b)** 532, and **(c)** 442 nm light, while D2 used λ_g = 532 nm. Laser written PL intensities generally cover a larger power range as PL emission was collected during the laser writing process.

Transfer characteristics for D1 using λ_g = 633, 532, and 442 nm, and for D2 with λ_g = 532 nm is shown in Figure AI.4 before (red) and after (blue) gently laser processing the device, using $P_w(532nm)$ = 3.5 μW. The current changes reflect those in the output characteristics at these specific V_{ds} points, which were chosen as $V_{ds} \approx$ 1.4 and 5.0 V. As previously discussed, the oscillatory current under λ_g = 633 nm reflects non– linear behavior, while the relatively linear blue line represents the transition to a more linear power dependence. In general, laser processing enhanced the current at low voltages, except for 532 nm, which resulted in a decreased I_{ds}. Both D1 and D2, using λ_g = 633 and 532 nm respectfully, displayed large I_{ds} increases after laser processing. The transfer characteristics support the output characteristics in that wavelength–selective, electrical behavior may be laser processed. The next step is to explore multi–gate–

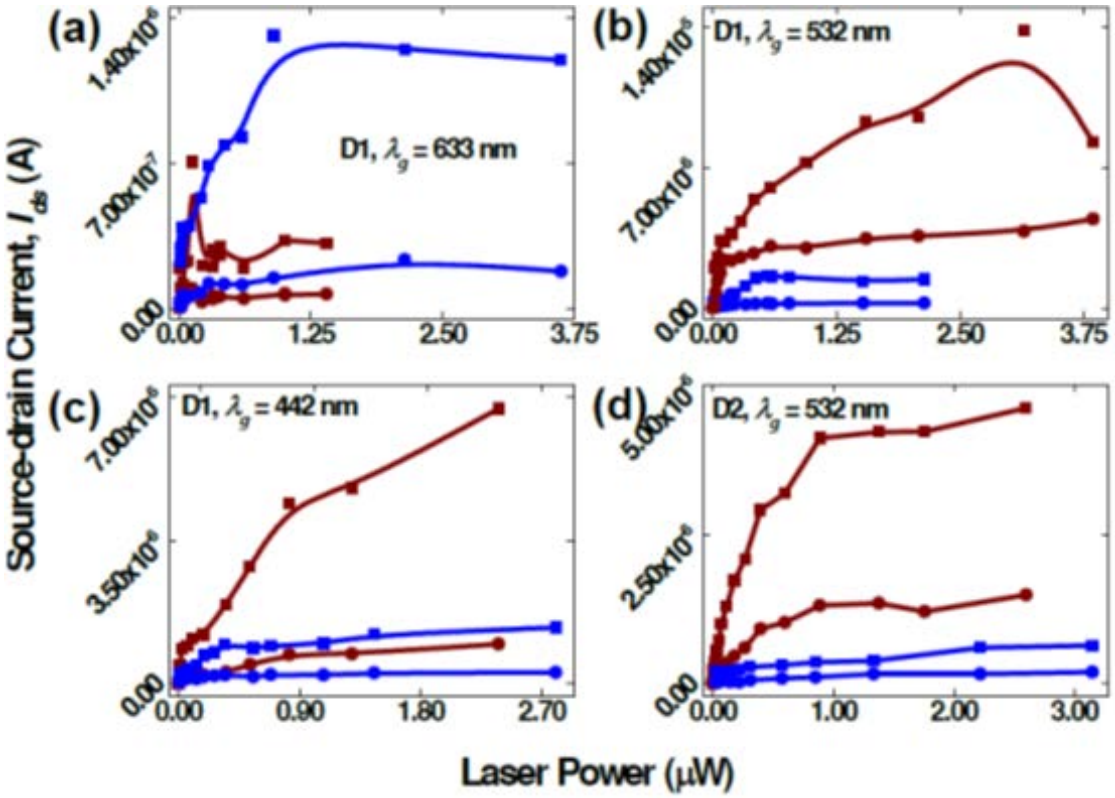

Figure AV.4 Transfer characteristics were measured at V_{ds} = 1.43 V (circles) and 4.98 V (squares) before and after gentle laser processing using $P_w(532nm) \approx 3.5$ μW. Device operation was performed as follows: D1 used λ_g = **(a)** 633, **(b)** 532, and **(c)** 442 nm, while D2 was under λ_g = **(d)** 532 nm.

functionality. To clearly demonstrate the effects, a current enhancement factor R is introduced by converting $I_{ds}(P_{g1},P_{g2})$ to $R(P_{g1},P_{g2})$, where $R = I_{ds}(P_{g1},P_{g2})/[\ I_{ds}(P_{g1}) + I_{ds}(P_{g2})]$. In other words, R is the current produced under simultaneous illumination normalized to the current produced under each independent illumination source. Figure AI.5 contains contour plots of R as a function of 532 nm and halogen power before and after laser processing the same device (D2). Before laser processing, a maximum R of ~10 occurred at the lowest optical powers, and had an implied gain of ~15. After laser processing, the maximum R was reduced by about an order of magnitude to ~1.5, where this reduced optical amplification was observed over smaller power ranges. Obviously, enhancing optical amplification is more desirable. The UV illumination studies, which will be discussed later, suggest that $P_w(325nm)$ may be one way to realize an increase.

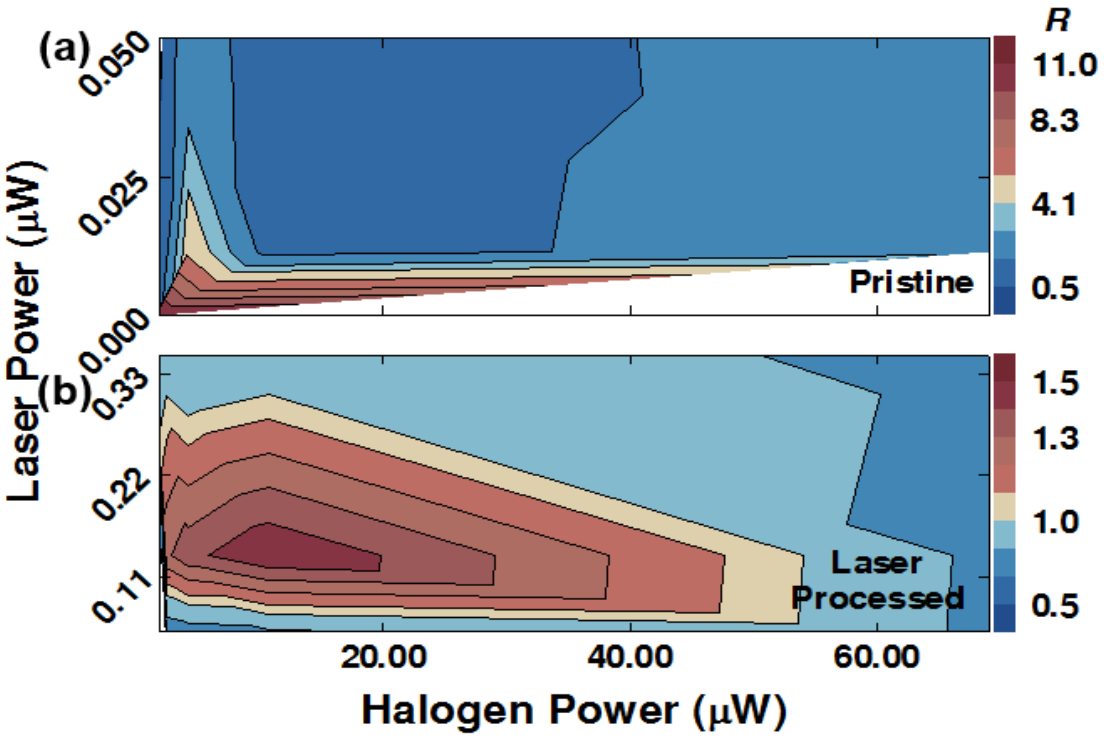

Figure AV.5 Dual–optical–gate amplification measured with the current amplification factor, R (see text). The two optical sources were P_{g1}(532 nm) and P_{g2}(*Halogen*), while transfer characteristics were collected before and after laser processing with P_w(*532nm*) ≈ 3.5 μW.

AV.3 Supplemental Structural and Optical Characterization

Figure 6.3 compares optical spectra for gently and irreversibly laser–processed, CdSe SNWs, and for a CdSe/ZnTe SNW. Additional optical and structural characterization is provided and discussed. First, the reproducibility of the PL measurements is demonstrated in Figure AV.6, where the increased exciton emission after laser modification is significant. Deep–level PL emission from Figure 6.3 is magnified to reveal changes in peak intensity and structure. The features are discussed in Chapter 6. Given the scant literature reports on oscillatory PL emission, it is useful to first review relevant references. Uniform oscillation was previously observed in PL spectra for silicon illuminated with light ≤ 3.2 eV [2, 3], and were speculated to originate from surface phonons. The references varied either the oxygen pressure or the particle diameter (through laser ablation times) and studied PL bands from 1.8–2.1 eV,

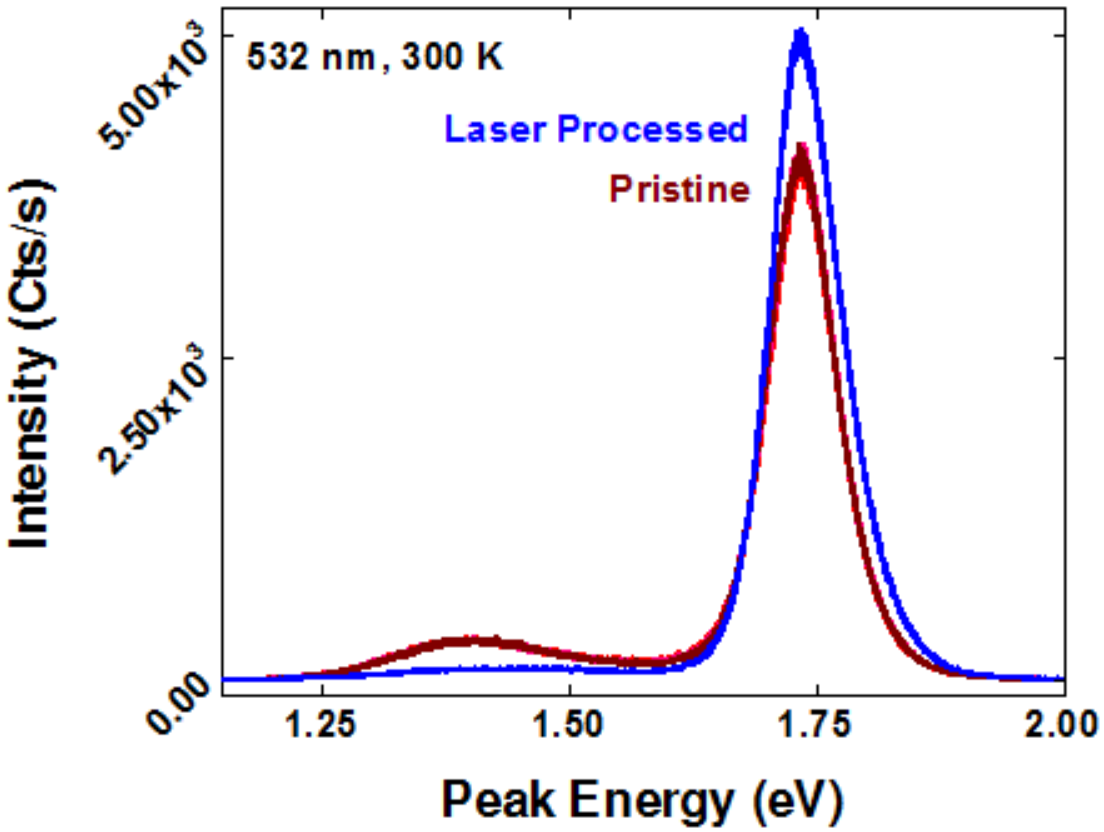

Figure AV.6 Demonstration of PL reproducibility and that intensity changes in PL emission are significant. Three initial measurements were collected and possessed with identical laser powers. Laser processing induced a drastic intensity change of ~1000. cps.

at ~2.55 eV, and at 3.2 eV. When the pressure of oxygen gas was altered during material growth, the 1.8–2.1 eV range was dependent upon the gas pressure and experienced intensity changes and peak shifts, while a broad peak at ~2.55 eV displayed negligible intensity and peak energy changes. The former was ascribed to confinement effects, while the latter to surface states. Laser ablation to form silicon oxide nanoparticles (with diameters of 1–10 nm) nanoparticles demonstrated an increase in emission at 3.2 eV with increasing ablation times. The oscillatory deep–level emission was attributed to phonon–assisted processes. The peak spacing between the oscillations varied from 97±9 meV when varying the oxygen partial pressure to 62±6 and 57±5 meV for the 3.2 and 2.55 eV bands, respectively, during laser ablation. Figure AV.8 investigates PL

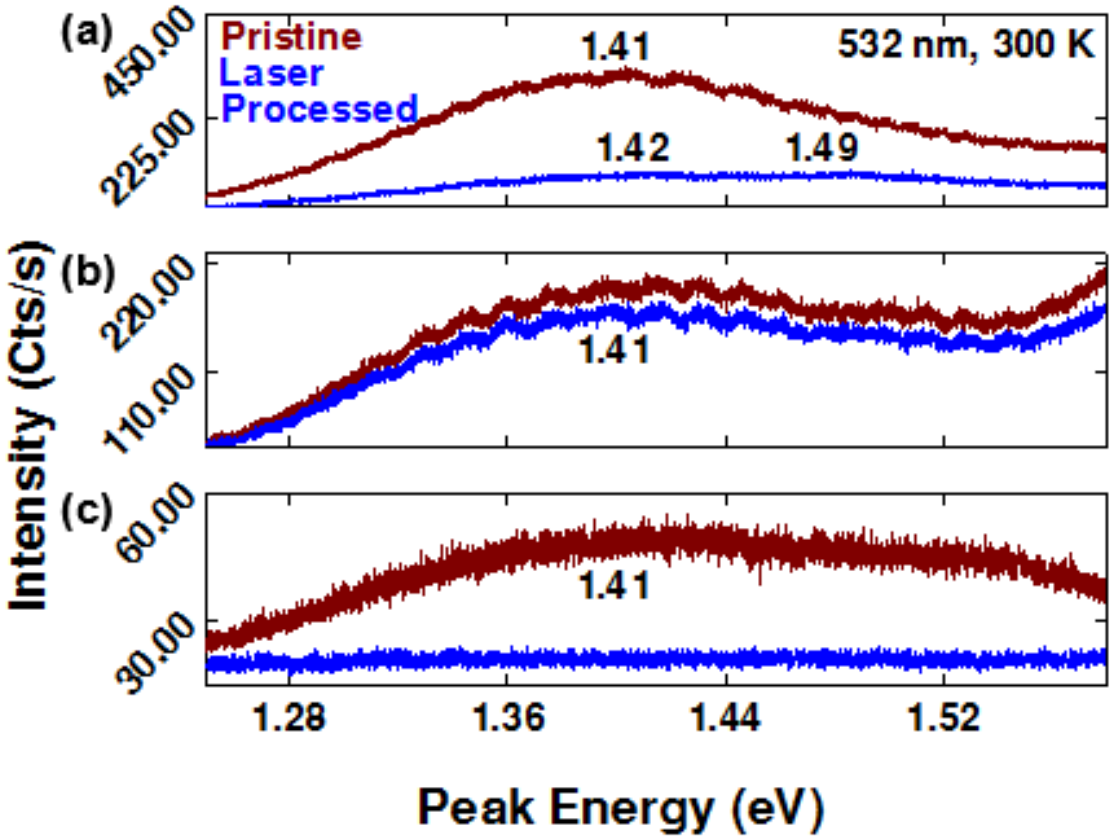

Figure AV.7 Magnification of deep–level emission from Figure 6.4 before and after **(a)** gently and **(b)** irreversibly laser–processing different CdSe SNWs, and **(c)** a CdSe/ZnTe SNW.

emission as a function of laser power and exposure time to 325 nm light for four semiconductor systems: ZnO SNW array, bulk ZnSe, a CdSe SNW, and a CdSe/ZnTe thin film. The bulk and thin film samples serve as references. In general, three PL bands are observed among all samples: low, medium, and high energy peaks at ~1.8–1.7 eV, ~2.3 eV, and ~3.1–3.2 eV respectively. A consistent peak spacing of ~50.–60. meV was observed for PL emission < ~1.75eV, although the oscillations were strongest in the CdSe samples. These values are near those reported for the silicon oxide nanoparticles formed through laser ablation, while interestingly, the peak spacing observed with 532 nm light was only ~20. meV. Further investigation is required to determine if these results stem from material difference (e.g., diameter or stoichiometric ratio) or illumination conditions.

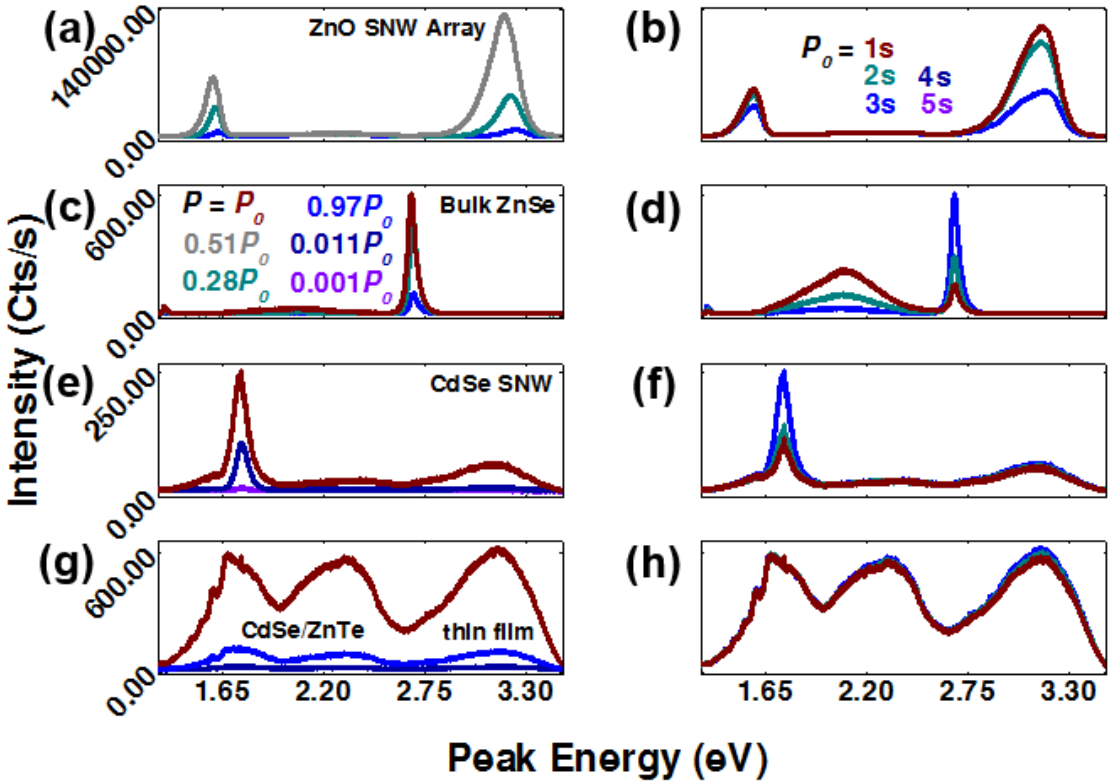

Figure AV.8 Investigating oscillatory PL emission with P_w(325 nm) = 2.976 mW (P_0). Laser–power–dependent and exposure–dependent (t = 1 s intervals) PL emission for **(a–b)** a ZnO SNW array, **(c–d)** bulk ZnSe, **(e–f) a** CdSe SNW, and **(g–h)** a CdSe/ZnTe thin film. The bulk and thin film serve as reference samples. The ability to enhance the low energy PL peak in CdSe SNWs may provide a mechanism for improving transistor function, and should be investigated further.

The ZnO and ZnSe systems provide useful insight and serve as samples containing and lacking an oxide in their respective material compositions. The ZnO SNW array exhibited a red shift of both low and high energy peaks as all three peaks increased in intensity with increasing laser power. Upon consecutive 1 s exposures to P_0 = 2.976 mW of 325 nm light, all three peaks experienced reduced intensities and peak broadening. For comparison, both the medium and high energy peaks in bulk ZnSe increased with laser power, while prolonged exposure enhanced the high energy peak at the expense of the medium energy peak. It is interesting that similar optical conditions produced very different results for these Zn–based, material systems. A single CdSe SNW was investigated next. Increasing laser power yielded a red shift of

all three peaks with enhanced deep–level emission below ~1.65 eV. Meanwhile, increasing its exposure to ultraviolet light actually increased the intensity of the low energy peak, while the other two peaks demonstrated negligible changes. For comparison, a CdSe/ZnTe thin film structure demonstrated no changes in PL emission when altering either the laser power or the exposure time. It is clear that CdSe SNWs are more susceptible to laser modification than their (relatively thicker) thin film counterparts, while the SNWs displayed different behavior from the ZnO SNW array and bulk ZnSe systems. While further investigation is required to better understand the origin of these changes, the similar peak energies and peak spacings hints that common origins may be shared between these material systems. As 325 nm illumination enhances deep–level emission, rather than removing it through laser annealing, a future step is to determine if $P_w(325nm)$ can enhance a LET's electrical performance.

Ablative laser processing did not change the oscillatory peak of the deep–level emission peak, but it did, surprisingly, result in the laser removal of the broad Raman feature. The Raman spectra in Figure 6.3D are tabulated in Table AV.3. In general, the peak area and the full width at half maximum (FWHM) decreased until a saturation point was reached, which was marked by the complete laser removal of the broad Raman feature. The Raman spectra in Figure 6.3B were collected across an In–CdSe–In device (Figure AV.9). The spectra were collected with 33.2 μW of 532 nm light after partial ablation with $P_w(\lambda_w)$ = 20.20 mW (t = 1.0 s). The pristine sites demonstrated a broad feature with a relatively low Raman shift of the 1LO peak, while the laser processed spot displayed complete removal of the broad peak and a simultaneous "sharpening" or intensity enhancement of the 1LO peak. These results match the trends observed in Figure 6.D for an irreversibly laser–processed, single CdSe SNW, while

Table AV.3 Tabulated Raman data for the pristine and laser–processed CdSe SNW in Figure 6.3B. Laser processing was performed with four, 100 s intervals with $P_w(532nm)$ = 0.397 mW, while Raman spectra were collected with 167.6 μW of 532 nm light. Values include peak position, peak area, and the full width at half maximum (FWHM) for CdSe's 1– and 2–LO phonon peaks and the broad Raman feature.

Exposure *n·100s*	***n*·LO CdSe**	**Peak Position** *cm^{-1}*	**Peak Area** *a.u.*	**FWHM** *cm^{-1}*
0	Broad peak	170.5	32.59	29.0
	1	203.3	30.24	22.7
	2	411.7	1.33	1.1
1	Broad peak	171.8	4.28	8.2
	1	206.4	29.44	13.2
	2	412.1	4.03	9.7
2	Broad peak	176.7	0.65	2.8
	1	206.4	37.09	8.9
	2	416.5	14.37	12.4
3	Broad peak	177.1	1.90	—
	1	206.4	43.06	10.3
	2	414.3	15.65	11.6
4	Broad peak	176.7	2.46	6.2
	1	206.4	40.95	9.1
	2	416.5	9.99	1.7

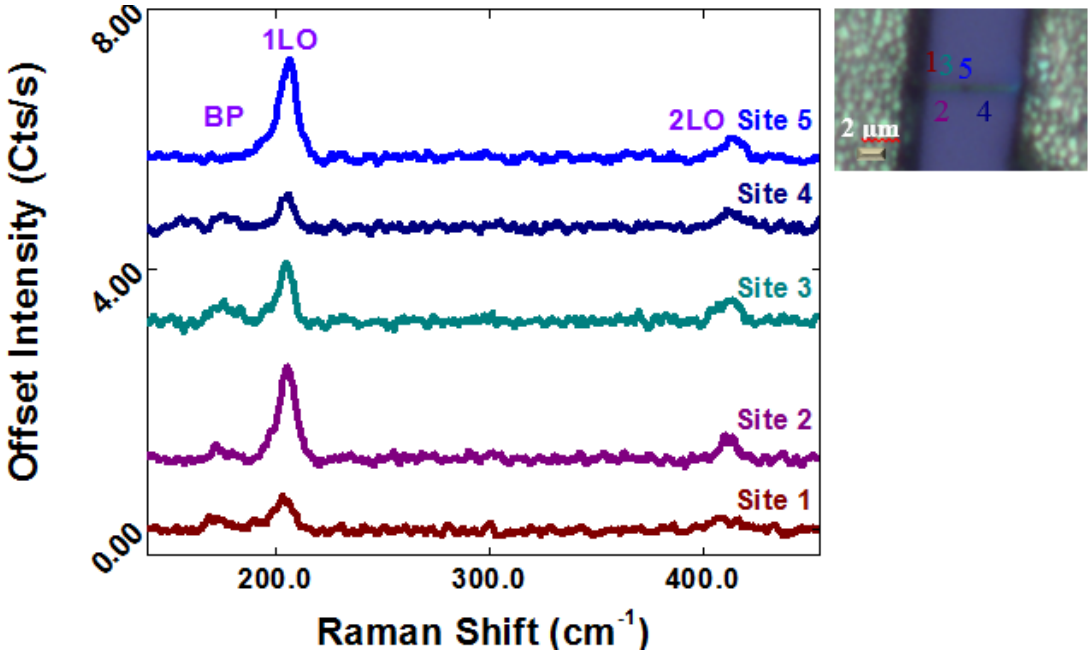

Figure AV.9 Reproducibility of Raman trends observed in Figure 6.3D. Raman spectra were collected across an In–CdSe–In device using 33.2 μW of 532 nm light after laser processing with $P_w(\lambda_w)$ = 20.20 mW (t = 1.0 s), which partially ablated the CdSe SNW (see optical image) and produced the electrical characteristics in Figure 6.1C. To the right, numbers on the optical image indicate the approximate spatial location of each measurement site. The ablated site corresponds to the blue spectra that does not possess a broad peak or "BP".

pristine sites display the broad peak with a reduced 1LO intensity. It is interesting that this device does not demonstrate a Raman–shifted 1LO for the ablated site compared to the pristine site, which contrasts the results in Figure 4D. This suggests that the Raman shifted 1LO may result from other phenomenon, such as from differences in initial surface conditions.

Laser ablation is investigated structurally for a CdSe wire that was irreversibly laser processed using $P_w(532nm)$ = 0.378 mW (t = 30. s). This SNW has a diameter of ~400 nm and is different than the one investigated in Chapter 6. The partially ablated SNW is structurally characterized with TEM (Figure AV.10) to reveal the formation of a polycrystalline CdSe layer at the ablation site. The bright field image in Figure AV.10C clearly reveals the structure, while the bright spots in the dark field image (Figure AV.10D) indicates the presence of polycrystalline CdSe. Figure AV10.E contains white lines that outline different polycrystalline regions at the ablation site, where the formation of polycrystalline material is consistent with the circular rings observed in the diffraction pattern in the inset of Figure AV10.B. In contrast, uniform lattice spacings are observed away from the ablation site (Figure AV10.F).

Figure AV.11 structurally characterizes a CdSe/ZnTe SNW with TEM. The SNW has a diameter of ~250 nm, and was laser processed with $P_w(532nm)$ = 0.366 mW (t = 0.25 s). No structural damage was observed with TEM although a noticeable reduction in PL intensity (using both 633 and 532 nm lasers) was observed after laser processing the structure. Ref. [4] previously characterized this structure and determined that spheres on the SNW surface are composed of ZnTe. The insets in Figures AV.11A–B were collected away from and at the illuminated site and indicate the presence of single crystalline and polycrystalline material respectively. Meanwhile, the bright field image

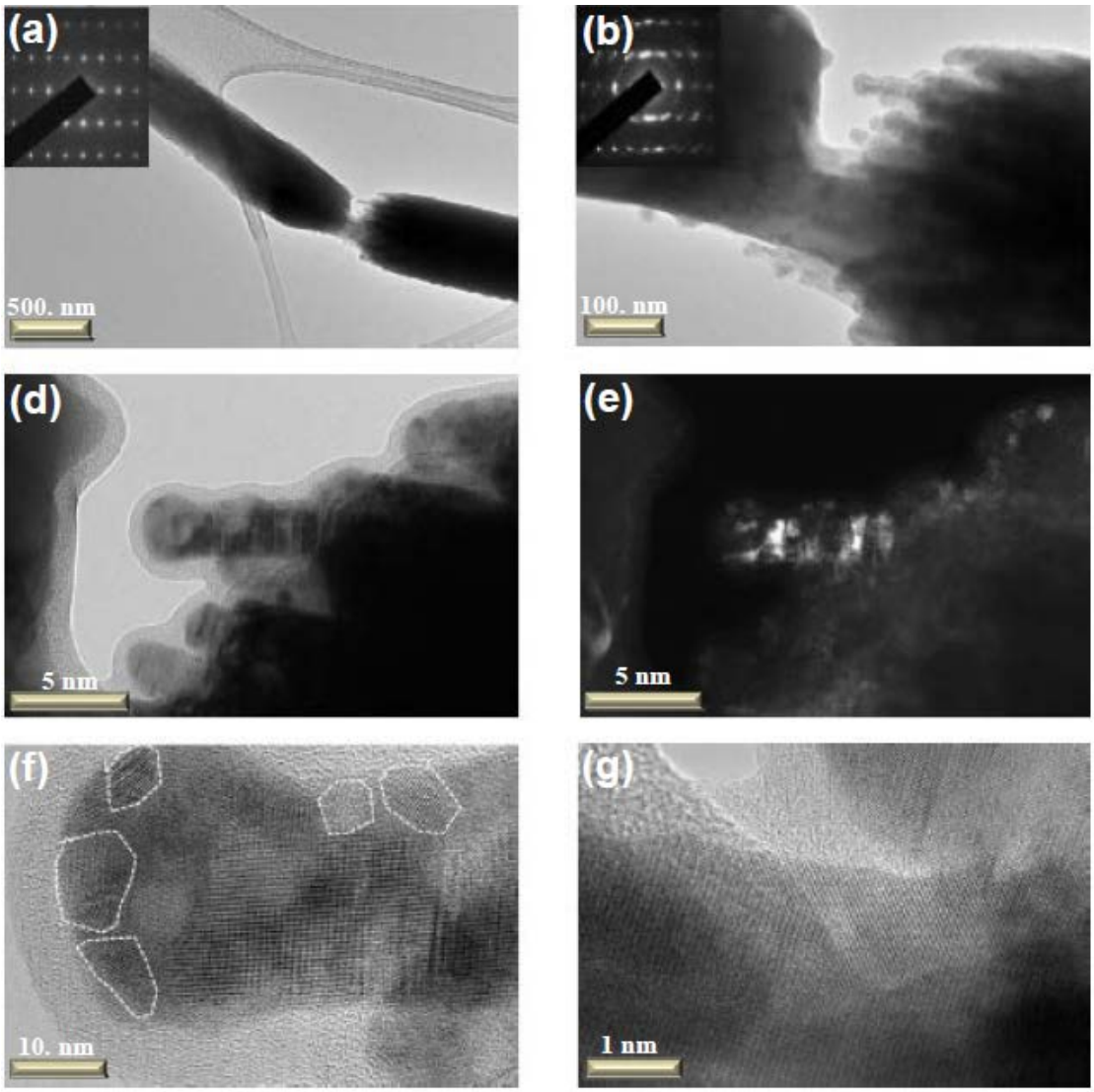

Figure AV.10 Structural characterization of a partially ablated, CdSe wire with a diameter of ~400 nm. Ablation was achieved with P_w(532nm) = 0.378 mW (t = 30. s). TEM images were collected at **(a)** 8 k (500 nm scale bar) and **(b)** 40 k (100 nm scale bar) magnification at the ablated site. **(c–d)** Bright and dark field images of a "finger" in the ablated site (120 k magnification; 5 nm scale bar). **(f–g)** High resolution TEM images (120 k magnification) showing the same finger and where the finger meets the SNW body respectfully. Scale bars are 10 nm and 1 nm respectively. (f) Select polycrystalline regions are outlined with dashed white lines.

in Figure AV.11C clearly resolves the structure, while the dark field image in Figure AV.11D indicates a homogenous material. The corresponding PL and Raman spectra appear in Figures 6.4E–F respectively, and indicate the formation of tellurium and a Raman peak at 252.0 cm^{-1}, which may be from amorphous selenium. As a reminder, the all–wurtzite (WZ), CdSe/ZnTe SNW in Figure 6.3F did not experience a shift of

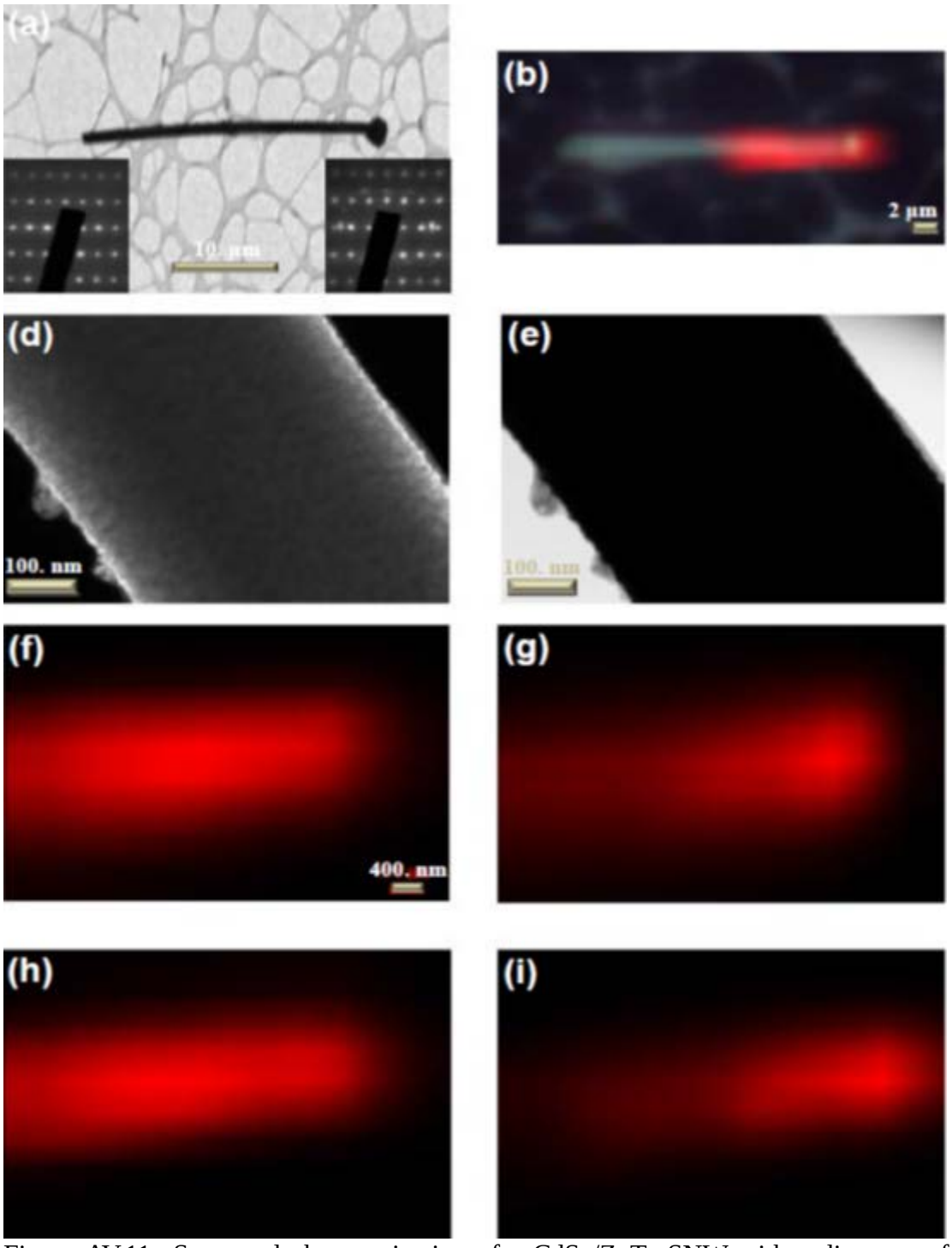

Figure AV.11 Structural characterization of a CdSe/ZnTe SNW with a diameter of ~250 nm. Laser processing was performed with $P_w(532nm)$ = 0.366 mW (t = 0.25 s). **(a)** TEM image of the SNW under 1 k magnification (10 μm scale bar). The two insets are diffraction patterns of the CdSe body (left) and of the ZnTe shell (right). **(b)** Optical image of the SNW with a PL map overlaid upon half of the structure (2 μm scale bar). **(c–d)** Bright and dark field images under 40 k magnification (100 nm scale bar) at the laser processed site. PL maps (with only relative intensity changes shown; 400 nm scale bars) were collected before and after laser heating using **(f–g)** 532 nm and **(h–i)** 633 nm light respectively, which are above and near CdSe's band gap respectively.

the 1LO peak, while only the 2LO peak was down–shifted by ~0.8 cm^{-1}. Its higher order replicas were not resolved due to the thin (~1 nm) ZnTe shell. This peak shift is likely a combined effect from both CdSe and ZnTe components, where CdSe provides the dominant contribution. For comparison, Figure AV.12 contains Raman spectra for a laser–written, zinc–blende (ZB) ZnTe nanowire using $P_w(532nm)$ = 0.243 μW (t = 0.5 s). Raman spectra were collected using 2.68 μW from a 532 nm laser, while pertinent Raman data is tabulated in Table AI.4. Gentle laser processing enhanced the peak areas and FWHM values, while only the 1– and 4–LO peaks were down–shifted by ~0.5 cm^{-1} and ~0.6 cm^{-1} respectively. As expected, the Raman shifts for the ZB ZnTe SNW are very different from the WZ CdSe/ZnTe structure.

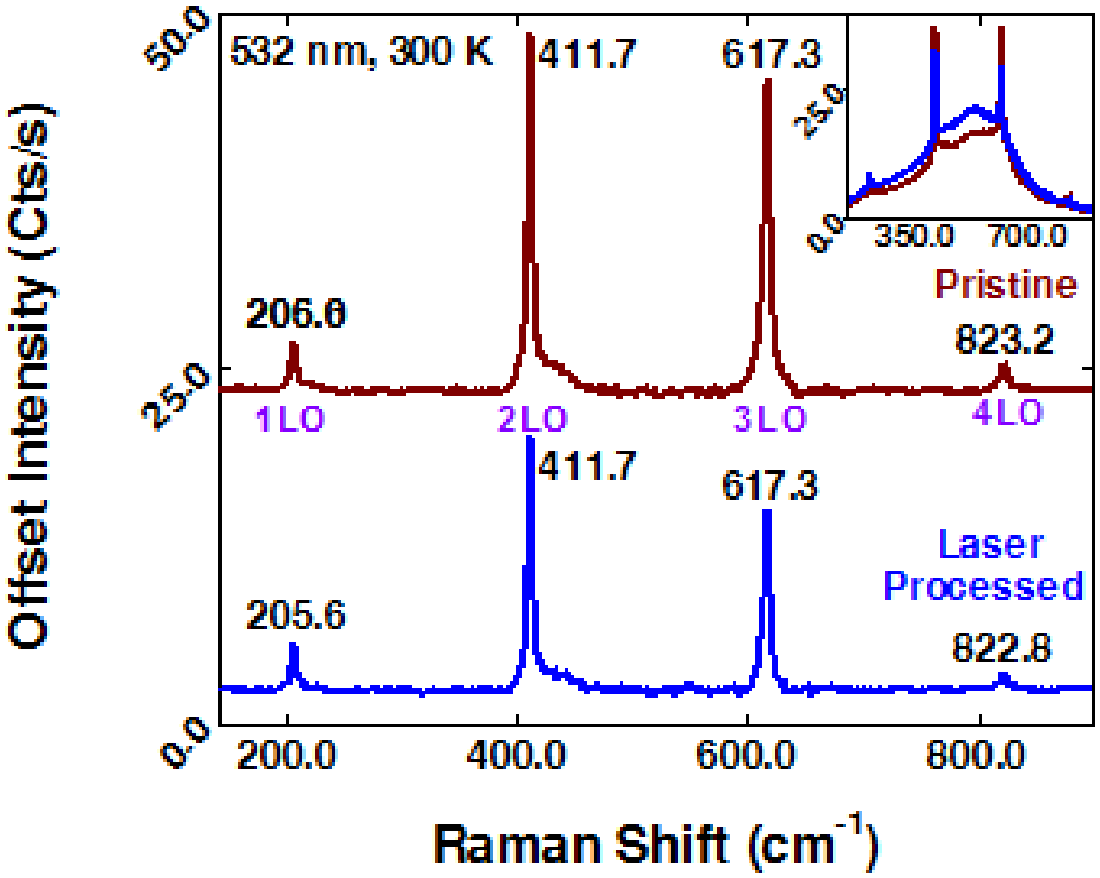

Figure AV.12 Raman investigation into gently laser written zinc–blende ZnTe for comparison with wurtzite results shown in Figure 6.4F. Laser processing was performed with $P_w(532nm)$ = 0.243 mW (t = 0.5 s), while the Raman spectra were collected under 2.68 μW or 532 nm light.

Table AV.4 Summary table of pertinent Raman parameters from Figure AV.12. The peak position, peak area, and FWHM are shown for all four of ZnTe's LO phonon modes before and after laser writing.

Exposure *0.5 s*	***n*·LO CdSe**	**Peak Position** *cm^{-1}*	**Peak Area** *a.u.*	**FWHM** *cm^{-1}*
Pristine	1	206.0	32.9	7.7
	2	411.7	177.9	4.7
	3	617.3	209.1	6.4
	4	823.2	19.2	28.7
Laser Processed	1	205.6	22.5	27.9
	2	411.7	129.0	27.7
	3	617.3	203.7	28.6
	4	822.8	13.6	28.7

Raman shifts were also investigated at the SNW body and Au–SNW junction for CdSe and CdSe/ZnTe SNWs in Figure 6.4. While the Raman measurements were repeated for both structures, the shift in the core/shell structure is intriguing. It is therefore useful to demonstrate its reproducibility. Figure AV.13 plots the Raman spectra collected at the Au–CdSe/ZnTe junction for two different SNWs. The shown spectra demonstrate large intensity differences, while the shape of the 2LO does appear to have some variation between samples. An interesting finding is a drastically different I_{2LO}/I_{1LO} at the Au–SNW junction for both CdSe and CdSe/ZnTe SNWs. A CdSe SNW (not shown) displayed I_{2LO}/ I_{1LO} values at the SNW body and Au–SNW interface, respectively, of 0.001 and 0.015, while the CdSe/ZnTe SNWs in Figures 6.5 and AV.13 yielded respective I_{2LO}/I_{1LO} values of 6.8 and 2.22 at the SNW body, which compares to respective values of 0.015 and 0.80 at the Au–SNW interface (light green and wine colored lines respectively). It appears that the gold interface drastically increased coupling strengths for the CdSe SNW, while it greatly reduces it for the CdSe/ZnTe SNW.

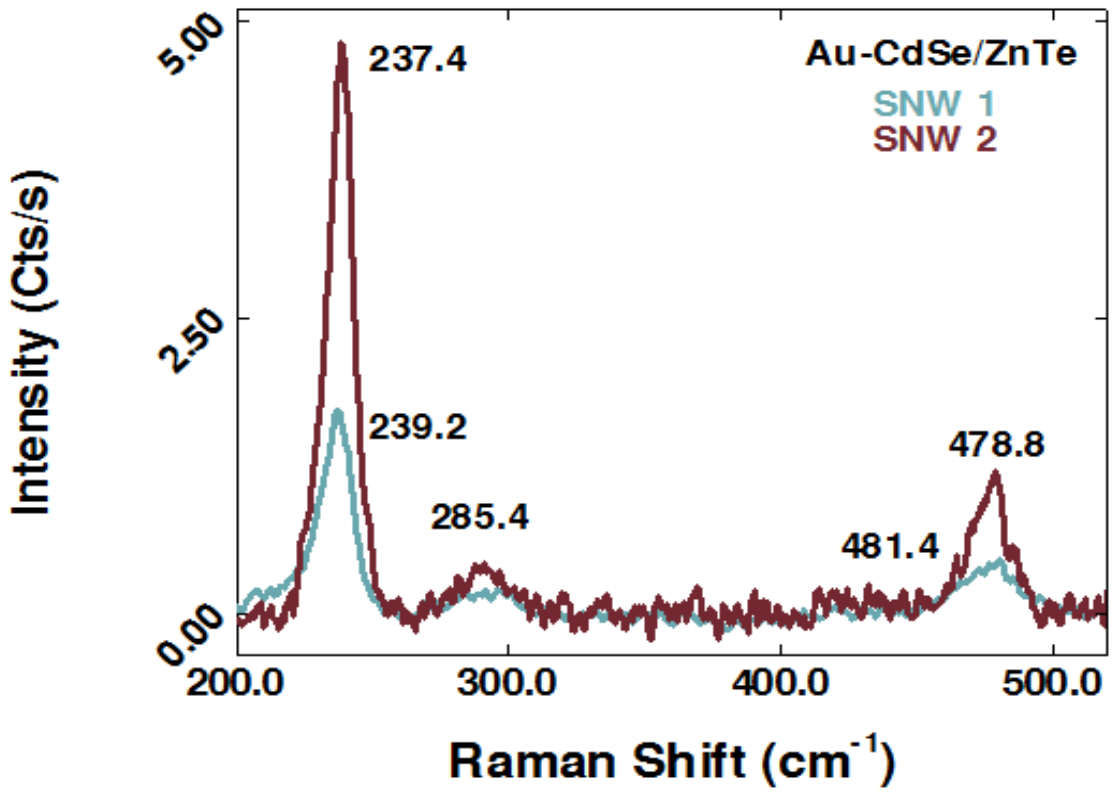

Figure AV.13 Raman spectra collected at the Au–CdSe/ZnTe junction for two different SNWs. The Raman spectra were collected with 207.5 μW of 532 nm light.

APPENDIX VI: ADDITIONAL RESEARCH WORK

"Always do more than is required of you."
General George S. Patton, Jr., Speech given in England to the U.S. Third Army, 5th June 1944

AVI.1 Appendix Information Summary

Appendix VI contains additional research work on the piezoelectric and piezophototronic effects in CdSe– and CdSe/ZnTe–nanowire–based devices.

AVI.2 Piezoelectric Devices

Figure AVI.1 explores the piezoelectric effect in CdSe [5] and CdSe/ZnTe [6] nanowire arrays, where the latter templates the shell's crystal structure [4]. CdSe and CdSe/ZnTe nanowire arrays are of interest because the former was demonstrated as a LET in Chapter 4, while the latter has photovoltaic applications and demonstrates the effect of a shell. Figure AVI.1A contains a device schematic, where the device's sandwich structure consists of a quartz slide with silver paste acting as the top electrode, which contacts the top of the vertical nanowire array, while the bottom electrode is formed with mica substrate. Kapton tape is also used to provide additional insulation for the electrical leads. Weights are placed on the quartz slide on the end opposite the measurement location, where PL spectra are collected with 70.70 μW of 532 nm light. The mechanical stimuli, or applied weight or load in this case, displaces non–centrosymmetric atoms in a wurtzite crystal structure, which produces the piezoelectric effect that manifests itself within an M–S–M device through altered M–S barrier heights [7, 8]. Figures AVI.1B–C plot output characteristics for the CdSe and CdSe/ZnTe nanowire arrays respectively. Although 532 nm and halogen light illumination and dark conditions were explored, similar results were obtained. This is because the relatively small illumination area (~1 μm spot size), compared to the much

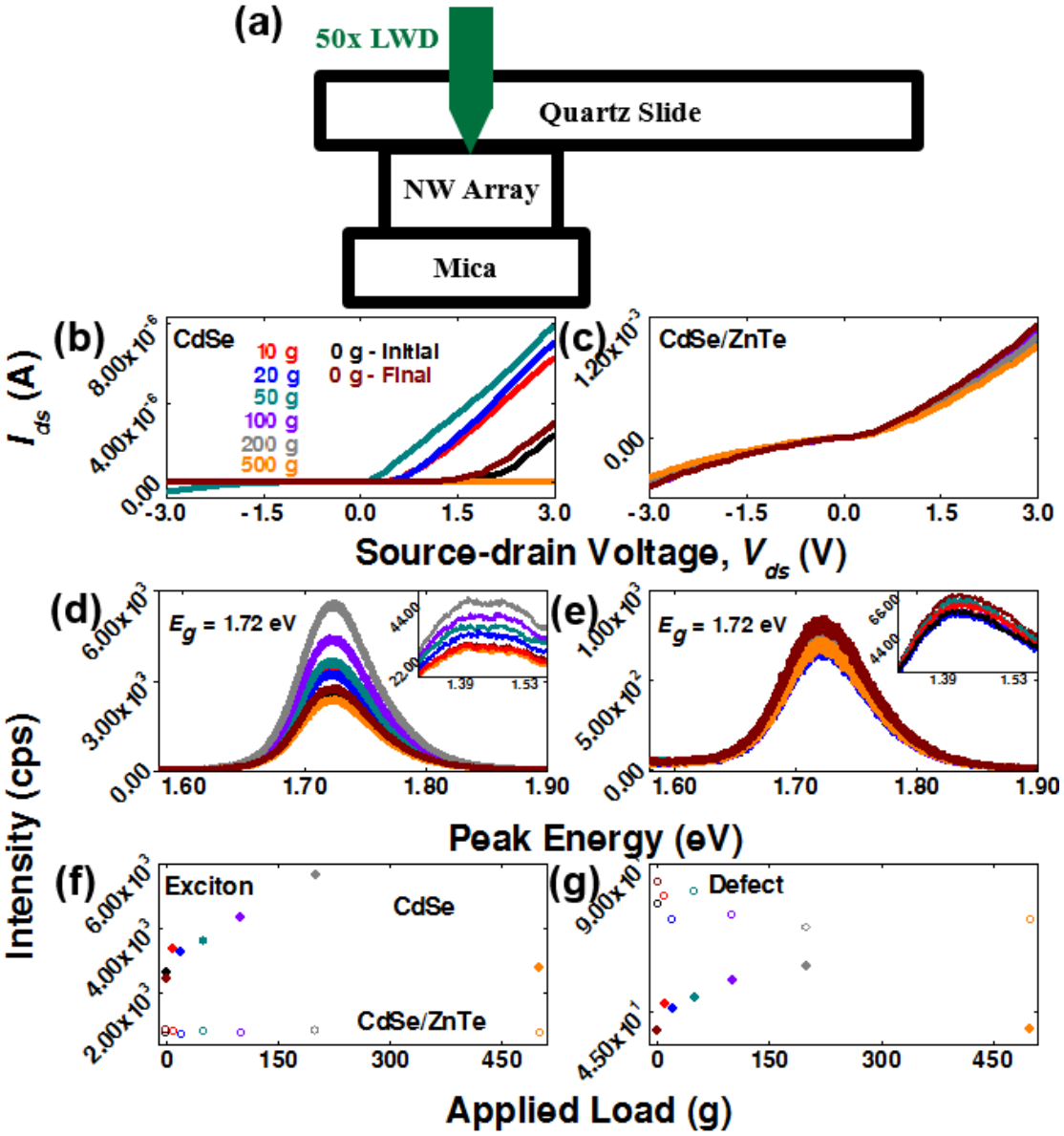

Figure AVI.1 Piezoelectric–enhanced electrical and optical properties in CdSe and CdSe/ZnTe nanowire arrays. **(a)** Schematic of device and its optical measurement using a 50x long working distance (LWD) objective lens (*N.A.* = 0.50). **(b–c)** Output characteristics under different applied loads. **(d–e)** Exciton and deep–level PL emission at 1.72 eV and ~1.4 eV respectively. The CdSe array has a second defect peak at ~1.5 eV. Measurements were collected with 70.70 μW of 532 nm light. **(f–g)** Exciton and deep–level (or defect) emission intensity, respectively, as a function of applied load on CdSe (solid circles) and CdSe/ZnTe (open circles) nanowire arrays.

larger device area on the order of square centimeters, could not yield sufficiently large differences in current modulation. Therefore, only dark current conditions are shown in these plots; however, a future step could employ illumination over the entire device's surface area similar to work performed for type–II, ZnO/ZnS nanowire arrays [9]. In

Figures AVI.1B, the CdSe array experiences an I_{ds} increase until saturation is achieved with a 50 g weight, after which point, the current reduces and even goes below the initial (0 g) value when the 500 g weight is applied. This behavior is well–known in ZnO nanowires [10]. In contrast, the CdSe/ZnTe nanowire array in Figure AVI.1B demonstrates four orders of magnitude increase in current, while comparatively small currently modulation was achievable by applying weights. It is clear that a mechanical gate affect both optical and electrical properties in CdSe–nanowire–based devices, while mechanical stimuli applied to the CdSe/ZnTe–based device had negligible effects, which could arise from efficient charge separation provided by the core–shell structure. There may, however, be specialized applications that require the large current modulation offered by the piezoelectric–enhanced, CdSe–based devices. Examples include sensor and memory applications, where tunable threshold voltages, which extended over ~2 V and could be optimized to extend even further, are particularly attractive for energy–efficient, multi–level memory applications [11].

PL is also investigated in Figures AVI.1D–E to correlate mechanical, electrical, and optical behavior, which is termed the piezophototronic effect [7, 8]. Exciton emission for both devices occurs at 1.72 eV with deep–level emission for both devices at ~1.4 eV, while the CdSe nanowire array displays a dominate, second peak at 1.49 eV. CdSe/ZnTe has lower emission intensities due to enhanced carrier separation [4, 6]. Application of weights effectively modulated PL emission for CdSe, while negligible changes were detected for the CdSe/ZnTe nanowire array, which qualitatively matches their respective output characteristics. In Figure AVI.1D, application of weight increased exciton and deep–level emission that saturated with the 100 g weight, compared to 50 g in the output characteristics, while exciton emission was quenched

with subsequent weight. It is worth noting that the 500 g weight quenched emission below the initial value, which reflects its electrical behavior. Figures AVI.1F–G plot exciton and deep–level emission intensities as a function of the applied load for CdSe (closed circles) and CdSe/ZnTe (open circles) nanowire arrays. An interesting finding is that deep–level emission was reduced with increasing load while exciton emission was generally enhanced. The inverse relationship between deep–level and exciton emission could be used as optical *NOT* logic gate. The correlated optical and electrical data in Figure AVI.1 also suggests the possibility of combining optical and electrical transistor concepts into a single device. An application example is the use of optical and electrical signals in transistor applications.

REFERENCES

[1] J.K. Marmon, S.C. Rai, K. Wang, W. Zhou, Y. Zhang, Light-effect transistor (LET) with multiple independent gating controls for optical logic gates and optical amplification, Frontiers in Physics, 4 (2016) 1-10.

[2] X.Y. Chen, Y.F. Lu, Y.H. Wu, B.J. Cho, M.H. Liu, D.Y. Dai, W.D. Song, Mechanisms of photoluminescence from silicon nanocrystals formed by pulsed-laser deposition in argon and oxygen ambient, Journal of Applied Physics, 93 (2003) 6311-6319.

[3] D.B. Geohegan, A.A. Puretzky, G. Duscher, S.J. Pennycook, Photoluminescence from gas-suspended SiO_x nanoparticles synthesized by laser ablation, Applied Physics Letters, 73 (1998) 438-440.

[4] K. Wang, S.C. Rai, J. Marmon, J. Chen, K. Yao, S. Wozny, B. Cao, Y. Yan, Y. Zhang, W. Zhou, Nearly lattice matched all wurtzite CdSe/ZnTe type II core-shell nanowires with epitaxial interfaces for photovoltaics, Nanoscale, 6 (2014) 3679-3685.

[5] L. Dong, S. Niu, C. Pan, R. Yu, Y. Zhang, Z.L. Wang, Piezo-phototronic effect of CdSe nanowires, Advanced Materials, 24 (2012) 5470-5475.

[6] S.C. Rai, K. Wang, J.J. Chen, J.K. Marmon, M. Bhatt, S. Wozny, Y. Zhang, W.L. Zhou, Enhanced broad band photodetection through piezo-phototronic effect in CdSe/ZnTe core/shell nanowire array, Advanced Electronic Materials, 1 (2015) 1400050.

[7] Z.L. Wang, Piezopotential gated nanowire devices: Piezotronics and piezo-phototronics, Nano Today, 5 (2010) 540-552.

[8] Z.L. Wang, Progress in Piezotronics and Piezo-Phototronics, Advanced Materials, 24 (2012) 4632-4646.

[9] S.C. Rai, K. Wang, Y. Ding, J.K. Marmon, M. Bhatt, Y. Zhang, W. Zhou, Z.L. Wang, Piezo-phototronic effect enhanced UV/visible photodetector based on fully wide band gap type-II ZnO/ZnS core/shell nanowire array, ACS Nano, 9 (2015) 6419-6427.

[10] Z.L. Wang, J.H. Song, Piezoelectric nanogenerators based on zinc oxide nanowire arrays, Science, 312 (2006) 242-246.

[11] S. Sahu, S. Ghosh, K. Hirata, D. Fujita, A. Bandyopadhyay, Multi-level memory-switching properties of a single brain microtubule, Applied Physics Letters, 102 (2013) 123701.

VITA

Jason K. Marmon completed Bachelor of Science degrees in Chemistry and Physics at Beloit College in 2006. Afterwards, he was awarded an Honors Term to study the Philippine weapons collection. This followed an undergraduate grant to study the chemistry and physics of ancient, bronze Chinese weaponry. He was also active in mentoring under–represented and first generation college/university students. After completing his undergraduate studies, he taught English in South Korea where he was both TESOL and TESOL teacher trainer certified, while continuing his international travels. Jason eventually returned to graduate studies at the University of North Carolina at Charlotte, where he pursued a doctorate in Nanoscale Science, and was a member of the IEEE – Eta Kappa Nu honor society (Kappa Pi chapter). He served the local Charlotte (NC) community as an Advisory Board Member and Loan Review Committee Member at the University City Branch of the State Employees' Credit Union since 2011 and 2013 respectively. Jason has had the privilege of sharing his research through publications and conference proceedings, as well as, through internationally, nationally, and locally through invited and contributed presentations.